UNIVERSITÉ DE GENÈVE
Département de physique nucléaire et corpusculaire

FACULTÉ DES SCIENCES
Professeur Martin Pohl

Performance of the AMS-02 Experiment for High Energy Gamma Ray Astrophysics

THÈSE

présentée à la Faculté des sciences de l'Université de Genève
pour obtenir le grade de Docteur ès sciences, mention physique

par

Sonia NATALE
de Rome, ITALIE

Thèse N 3890

GENÈVE
Atelier de reproduction de la Section de physique
2007

Alla Sera

Forse perche' della fatal quiete
tu sei l'imago a me sì cara vieni
o Sera! E quando ti corteggian liete
le nubi estive e i zefiri sereni,

e quando dal nevoso aere inquiete
tenebre e lunghe all'universo meni
sempre scendi invocata, e le secrete
vie del mio cor soavemente tieni.

Vagar mi fai co' miei pensieri su l'orme
che vanno al nulla eterno; e intanto fugge
questo reo tempo, e van con lui le torme

delle cure onde meco egli si strugge;
e mentre io guardo la tua pace, dorme
questo spirto guerrier ch'entro mi rugge.

Ugo Foscolo

Contents

Foscolo **3**

Résumé **1**

Introduction **15**

1 Cosmic Rays and Photons **19**
1.1 Cosmology . . . 19
1.1.1 Big Bang Nucleosynthesis . . . 19
1.2 Cosmic Rays Physics . . . 21
1.2.1 Cosmic-Ray Particles . . . 23
1.2.2 Fermi Acceleration . . . 27
1.2.3 Cosmic Ray Propagation . . . 29
1.2.4 Local Effects . . . 30
1.3 Search for Antimatter in the Cosmic Radiation . . . 32
1.3.1 Heavy Elements . . . 32
1.3.2 Antiprotons . . . 32
1.3.3 Positrons . . . 36
1.3.4 The Future . . . 37
1.4 Dark Matter properties . . . 37
1.4.1 Non baryonic Dark Matter . . . 38
1.4.2 Weakly Interacting Massive Particles . . . 39
1.4.3 WIMP Dark Matter Searches . . . 41

2 Gamma Astrophysics **50**
2.1 The Gamma Ray Universe . . . 50
2.2 Gamma Ray Astronomy . . . 51
2.2.1 The past missions . . . 55
2.2.2 The EGRET instrument . . . 56
2.2.3 The high-energy gamma-ray sky . . . 57
2.3 Diffuse galactic and extra-galactic emission . . . 58
2.3.1 Diffuse galactic emission . . . 58
2.3.2 Diffuse extra-galactic emission . . . 59
2.4 Active Galactic Nuclei . . . 59
2.5 Pulsars . . . 62
2.6 Gamma-Ray Bursts . . . 63

2.7 The Supernova Remnants . . . 64
2.8 Unidentified sources . . . 65

3 The AMS Detector 67
3.1 The AMS experiment . . . 67
3.1.1 Particle identification . . . 67
3.2 The AMS-02 detector . . . 71
3.2.1 Trigger . . . 90
3.2.2 Ground Data Handling and Remote Commanding . . . 92
3.3 The AMS-02 yields . . . 96

4 The AMS-02 Silicon Tracker 98
4.1 Introduction . . . 98
4.2 Silicon sensors . . . 100
4.3 Ladders . . . 103
4.4 The Ladder Front-End Electronics . . . 106
4.4.1 The Hybrids . . . 106
4.5 AMS-02 ladder production . . . 111
4.5.1 The ladder assembly and the University of Geneva assembly line . . . 113
4.5.2 Assembly Phase 1 . . . 116
4.5.3 Assembly Phase 2 . . . 120
4.6 Ladder bias . . . 121
4.6.1 AMS-01 case . . . 122
4.6.2 AMS-02 case . . . 123
4.7 Tracker Support Structure . . . 123
4.8 Tracker assembly and cabling preparation . . . 124
4.9 Tracker Electronics . . . 126
4.9.1 Tracker Electronics Production and Qualification . . . 127
4.10 Tracker Thermal Control System . . . 128
4.10.1 TTCS conceptual design and testing . . . 129
4.11 Performance tests . . . 132

5 Test Beam Setup @ CERN 133
5.1 Test Beam at CERN . . . 133
5.1.1 Location and Beam Features . . . 133
5.2 Previous Test Beams on AMS-02 Ladders . . . 137
5.3 2004 Test Beam . . . 147
5.3.1 Goals . . . 147
5.3.2 2004 Test Beam Setup . . . 147
5.3.3 Operation Mode . . . 152
5.3.4 DAQ System . . . 152
5.4 Mapping of the Magnetic Field . . . 153
5.4.1 MNP22/A Dipolar Magnet Features . . . 153
5.4.2 Method of Measurement . . . 154
5.4.3 Magnetic Field Determination . . . 156

5.4.4 Field Characteristics . . . 156
5.4.5 Magnetic Field Mapping Summary . . . 156
5.5 Electron Identification . . . 159
5.5.1 Threshold Čerenkov Detector . . . 159
5.5.2 Čerenkov Test Setup . . . 161
5.5.3 Performances of the two Detectors . . . 162
5.5.4 Particle Selection . . . 163
5.5.5 Counter C2 Usage . . . 166
5.6 Electron Identification Summary . . . 168

6 The Monte Carlo Simulation 169
6.1 Introduction . . . 169
6.2 The Event Generation . . . 169
6.2.1 Probe Spectrum and Energy Range . . . 170
6.2.2 The Generation Volume . . . 170
6.2.3 Trigger Simulation . . . 171
6.3 Electrons and Photons Simulation . . . 172
6.4 Electrons and Photons Reconstruction . . . 174
6.4.1 ECAL Reconstruction . . . 174
6.4.2 Tracker Clusters . . . 177
6.4.3 Hits . . . 179
6.4.4 Tracks . . . 179
6.4.5 Vertices . . . 180

7 Detector Performance for Electrons and Photons 183
7.1 Introduction . . . 183
7.2 Pulse Height Detection and Calibration . . . 183
7.3 Data and Montecarlo samples . . . 185
7.4 Preliminary analysis . . . 186
7.4.1 Pre-handling of data . . . 187
7.5 Detector performance . . . 188
7.5.1 Alignment . . . 188
7.5.2 Calibration . . . 189
7.5.3 Cluster Reconstruction . . . 189
7.5.4 Track Mirroring . . . 191
7.5.5 Hit and Track Efficiency . . . 191
7.5.6 Spatial Resolution . . . 193
7.5.7 Momentum resolution . . . 199
7.5.8 Photon Analysis . . . 205
7.5.9 Photon Energy and Angular Resolution . . . 214

8 Physics of High Energy Photons with AMS-02 223
8.1 Introduction . . . 223
8.2 AMS-02 Monte Carlo Simulation for Photon Detection . . . 224
8.3 AMS Gamma Fast Simulator . . . 226
8.3.1 ISS Orbit Simulation . . . 228

8.3.2 Celestial Coordinates . . . 229
8.3.3 Definition of the Orbit Elements . . . 230
8.3.4 Orbit Elements Dynamics . . . 231
8.3.5 Input Orbit Elements . . . 232
8.4 AMS Exposure Maps . . . 233
8.5 Astrophysical γ Ray Sources . . . 241
8.6 Detected Photons from a Point-like Source . . . 244
8.6.1 Point-like Source Sensitivity . . . 246
8.6.2 Photons from Diffuse Gamma Background . . . 247
8.6.3 Proton Background . . . 251
8.7 Upgrades to AMSFS . . . 251

Conclusions **256**

Acknowledgements **258**

Bibliography **260**

Résumé

Introduction

L'association récente de la Physique des Particules et de l'Astrophysique definít le domaine des Astroparticules. Les progrès techniques du siècle dernier ont permis le début de l'exploration complète du spectre électromagnétique et des autres particules que les photons qui sont appelées astroparticules. Aujourd'hui, les composantes du rayonnemment électromagnétique et du rayonnement chargé sont détectables tandis qu'il faudra encore attendre pour que les neutrinos ou les ondes gravitationelles le soient.

AMS, *Alpha Magnetic Spectrometer* (spectromètre magnétique de Alpha, Alpha étant l'ancien nom de la station spatiale internationale ISS), est un instrument qui sera installé en 2009 sur la station spatiale internationale ISS en cours de construction.
La station est sur une orbite autour de la Terre située entre 350 et 420 km d'altitude, inclinée de 51,6 degrés par rapport à l'équateur terrestre, et accomplit une orbite complète de la planète en 91 minutes, ce qui représente une vitesse de vingt sept mille kilomètres par heure. Un système de stabilisation par gravité permet à la station d'avoir toujours la même orientation par rapport au sol, c'est-à-dire que l'axe vertical de la station est toujours tourné vers le zénith.

AMS est la plus importante expérience de physique fondamentale approuvée sur la station. L'instrument est fixé (voir Fig. 1) sur la poutrelle principale de l'ISS, sur un support spécialement conçu à cet effet sur lequel l'armature métallique d'AMS-02 vient se fixer pour que l'instrument soit précisément positionné. L'axe du détecteur est incliné de 10 degrés par rapport à l'axe vertical de la station, c'est-à-dire le zénith, afin que l'instrument ait toujours devant lui l'espace libre, sans être gêné par les immenses panneaux solaires qui tournent pour être toujours orientés face au soleil. Cet axe est aussi celui du cône de sensibilité de 45 degrés (l'ouverture de l'instrument) c'est-à-dire la direction à l'intérieur de laquelle les trajectoires des particules cosmiques doivent se trouver pour être détectées et mesurées. La station spatiale fournit à AMS la puissance électrique nécessaire à son fonctionnement, soit 2 kW, et les télécommunications avec une bande passante moyenne de 2 Mbits/sec. A l'intérieur d'un module de la station, les spationautes pourront si nécessaire surveiller le fonctionnement du détecteur par l'intermédiaire d'un ordinateur, mais en fonctionnement normal tout le contrôle se fait depuis la Terre.

Figure 1: Le détecteur AMS-02 qui sera installé sur la Station Spatiale Internationale en 2009.

AMS-02 sera amené sur la station dans la soute de la navette spatiale américaine. Une fois la navette arrimée, le bras manipulateur de la navette saisira AMS-02 et le déplacera en direction du bras robot de la poutrelle qui saisira à son tour l'instrument et l'amènera jusqu'à son emplacement. Les spationautes feront une sortie dans l'espace pour amener précisément AMS-02 sur son support et le verrouiller, ainsi que pour connecter les prises électriques et le réseau de données.

Le déroulement de cette expérience est constitué en deux étapes. La première consiste en un vol de test et de qualification, qui eut lieu entre les 2 et 12 juin 1998: le détecteur était installé dans la soute de la navette spatiale Discovery, et la prise de données eut lieu durant les dix jours de la mission. Les buts de ce vol étaient de valider les technologies et les performances du détecteur, ainsi que d'obtenir une vision claire de la nature des rayons cosmiques sur une orbite similaire à celle que suivrait la station spatiale internationale. Cette mission, réalisée avec succès, permit à la collaboration AMS de s'engager dans la seconde étape: la finalisation et/ou amélioration du détecteur, pour un séjour minimum de trois ans sur ISS. L'installation d'AMS sur ISS n'aura pas lieu avant la premiere moitie de 2009.

Le détecteur AMS-01 et ses resultats

C'est sous la dénomination AMS-01 que l'on désigne la première étape de l'expérience AMS (Fig. 2). Les résultats produits par AMS-01 furent fructueux et au-dessus de toute attente. Le détecteur se comporta comme prévu, et l'acquisition des données se déroula sans problème. Un tableau clair de la population des rayons cosmiques les plus abondants fut établi. De plus, une recherche d'antimatière fut réalisée établissant une limite à la population en antihélium ($1.1 \cdot 10^{-6}$) inférieure aux valeurs trouvées jusqu'alors par des détecteurs embarqués sur ballons, et ce avec seulement dix jours de prise de données. Une étude se focalisa sur les antinoyaux avec $Z < -2$, fixant une limite au rapport antimatière/matière à $2.00 \cdot 10^{-5}$. Cette étude permit

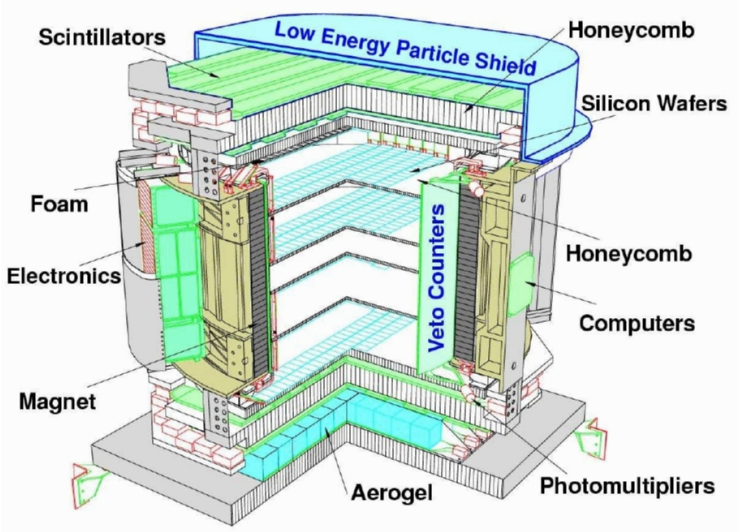

Figure 2: Le détecteur AMS-01 qui a volé en Juin 1998 sur la navette Shuttle *Discovery* (STS-91).

également de révéler les capacités du détecteur au silicium à identifier clairement les ions jusqu'à l'oxygène (fig. 3).

Le détecteur AMS-02

AMS-02 (Fig. 4) est un spectromètre magnétique, c'est-à-dire un instrument capable de mesurer les trajectoires des particules chargées électriquement qui le traversent et qui sont courbées par son champ magnétique. La courbure dépend de l'impulsion et de la charge électrique de la particule, tandis que le sens de la courbure dépend du signe de la charge électrique. Son but est d'acquérir les spectres des particules dans un domaine de rigidité allant jusqu'à quelques TV (la rigidité R correspond au quotient de la quantité de mouvement et de la charge électrique de la particule: $R = pc/Ze$). D'autres parties de l'instrument donnent des mesures de la charge électrique (sans le signe), de la vélocité (le rapport entre la vitesse de la particule et la vitesse de la lumière dans le vide), de l'énergie, ou encore donnent un signal différent selon la nature de la particule. L'ensemble des informations venant des différentes parties de l'instrument permet ainsi de déterminer la nature de la particule, son impulsion, et sa direction. On peut ainsi déterminer des flux et des spectres en énergie pour chaque type de particule, et éventuellement détecter des anomalies qui signalent la présence d'un phénomène nouveau. Le coeur d'AMS est constitué par un aimant supraconducteur de volume intérieur cylindrique de 1,114 mètres de diamètre et de 83 cm de haut, donnant une ouverture pour les particules de 0,8 m^2Sr. Le champ magnétique créé courbe les trajectoires des particules chargées électriquement qui traversent l'appareil. Huit plans de détecteurs de traces au silicium (TRK) mesurent avec précision des points sur cette trajectoire et permettent de la reconstruire géométriquement. Au-dessus et au-dessous

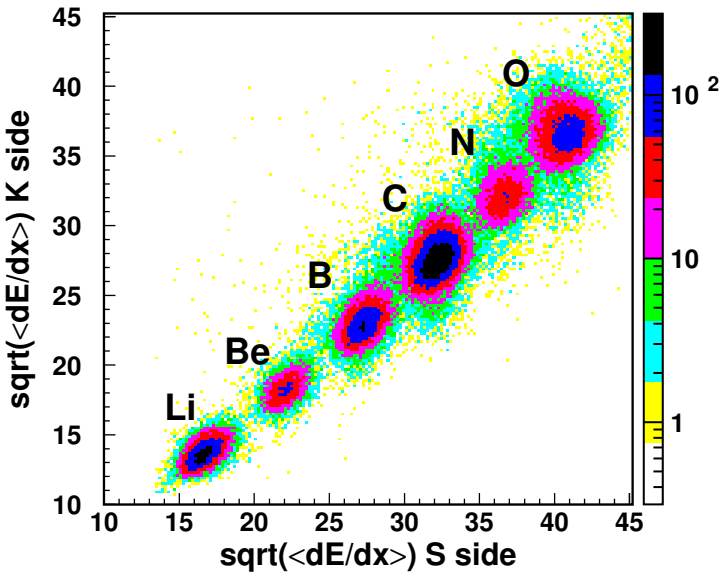

Figure 3: Performance du détecteur au silicium à identifier les ions jusqu'à l'oxygène.

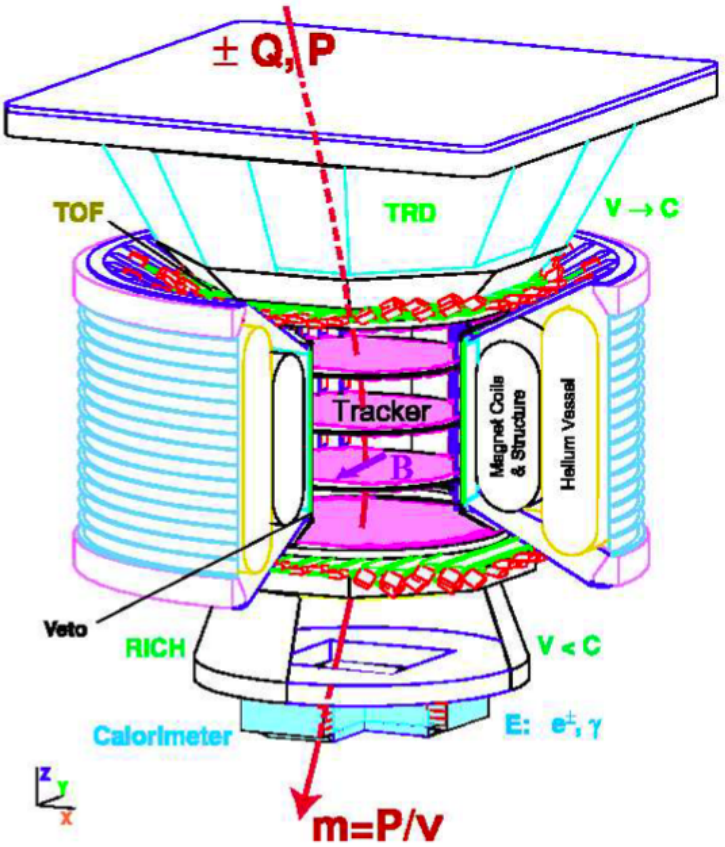

Figure 4: Le détecteur AMS-02 qui sera installé sur la Station Spatiale Internationale en 2009.

du détecteur de traces il y a deux plans de détecteur à scintillation, les compteurs Temps de Vol (TOF), qui signalent le passage d'une particule et donnent son sens de parcours. Le cylindre intérieur de l'aimant est aussi tapissé de Compteurs à Scintillation "Veto" (ACC) qui signalent lorsqu'une particule est désintégré par collision sur la matière en traversant le détecteur et donc de ne pas en tenir compte. Au-dessus des compteurs TOF supérieurs se trouve le Détecteur à Radiation de Transition (TRD) pour aider à l'identification des électrons et positrons. En-dessous du TOF inférieur on trouve tout d'abord le Compteur Čerenkov à Imagerie Annulaire (RICH), pour l'identification des nombres et numeros atomiques des noyaux, et enfin le Calorimètre Electromagnétique (ECAL) qui absorbe et mesure l'énergie des particules électromagnétiques et complète leur identification. L'instrument complet, avec une redondance des mesures cinématiques et des mesures d'identification des particules a ainsi de très grandes performances.

Perspectives physiques d'AMS-02

Ce spectromètre magnétique permet la mesure avec une grande précision et une haute statistique des particules cosmiques chargées électriquement, ainsi que des noyaux légers et des rayons gamma de haute énergie.

L'appareil utilise à la fois les techniques expérimentales développées en physique des hautes énergies et les techniques spatiales, réalisant un pont entre deux domaines de recherche: l'infiniment petit avec la physique des particules, l'infiniment grand avec l'astrophysique, pour arriver à percer les grands mystères de l'astrophysique:

- Existence des Univers d'antimatière: pour le savoir, il faut rechercher des noyaux d'anti-hélium ou d'anti-carbone, car ce derniers ne peuvent être produits qu'au coeur des étoiles d'antimatière. AMS est capable d'identifier un anti-noyau parmi un milliard de noyaux, soit une sensibilité cent fois plus forte que les expériences passées ou en cours.
  Répondre à cette question fondamentale pourrait bouleverser notre conception de l'Univers et de sa formation. Juste après le Big-Bang, la matière et l'antimatière formaient un plasma en expansion rapide et contenant une quantité égale de l'une et de l'autre. S'il n'existe plus d'antimatière primordiale (venant de l'origine de l'Univers) dans l'univers, il faut comprendre comment l'antimatière a pu disparaître. Inversement, si l'Univers est symétrique - c'est-à-dire si il contient autant de matière que d'antimatière - il faut comprendre pourquoi localement dans notre galaxie et dans celles qui nous entourent il n'y a que de la matière. En effet, les expériences faites jusqu'à présent excluent la présence d'antimatière dans l'amas de galaxies dont nous faisons partie. L'observation des étoiles lointaines avec des télescopes puissants ne permet pas d'apporter de réponse, car nous voyons alors seulement la lumière émise par l'étoile qui ne porte aucune indication sur le fait que l'étoile soit composée de matière ou d'antimatière. La détection d'un seul noyau d'antimatière dans l'espace, un antihélium ou un anticarbone par exemple, apporterait la preuve qu'il existe quelque part dans l'univers, hors de notre amas de galaxies, des

creusets où ces noyaux sont synthétisés : des étoiles d'antimatière dont le combustible élémentaire serait l'antimatière (des antiprotons) de l'univers primordial. AMS a été conçu pour détecter ces anti-noyaux avec une sensibilité cent à mille fois supérieure à celle des expériences existantes.

- La nature de la "matière noire": invisible, elle semble constituer 90% de la masse de l'Univers. On l'appelle ainsi car on détecte sa présence par la vitesse de rotation des bras des galaxies, mais on ne l'observe pas avec nos télescopes : cette matière ne rayonne pas de la lumière. On sait qu'il ne s'agit pas d'objets trop petits pour allumer leur feu nucléaire, ni de nuages de particules ordinaires. AMS pourrait détecter les annihilations des particules de matière noire et ainsi comprendre leur nature.
  En effet, l'observation du mouvement des galaxies par des grands télescopes, et en particulier celle de la vitesse de rotation des galaxies spirales, a provoqué une grande surprise: pour expliquer ces mouvements, il faudrait que ces galaxies aient une masse dix fois plus élevée que ce que nos grands télescopes observent, en particulier dans le halo de ces galaxies. En fait 90% de la masse totale de l'Univers ne serait pas vue par les instruments actuels et la nature de cette matière mystérieuse appelée " matière noire " n'est pas encore connue. Cette matière ne peut pas être de la matière ordinaire. Ce phénomène pourrait être dû à un nouveau type de particules massives, les WIMPs (Weakly Interacting Massive Particles). Dans le modèle théorique de physique des particules appelé modèle supersymétrique (MSS), le candidat pour le WIMP est une particule neutre appelée neutralino, qui est en plus sa propre antiparticule. Si ces neutralinos, qui sont activement recherchés, sont bien à l'origine de la matière noire, alors on doit pouvoir détecter leur annihilation lorsqu'ils entrent en collision entre eux dans le halo des galaxies. Ces annihilations se feraient en particulier en produisant des rayons gamma et des positrons qui se rajouteraient en excès au flux de particules cosmiques, excès qu'AMS pourrait détecter grâce à sa très grande sensibilité.

- Le fonctionnement de notre galaxie: les particules qui composent les rayons cosmiques sont produites dans les étoiles et éjectées, ou encore dans les interactions des particules avec le milieu interstellaire ou intergalactique. Pour comprendre les mécanismes de production, d'accélération, et de transport, les spectres en énergie de ces rayons cosmiques sont très importants. Ce sera une des tâches d'AMS de les mesurer.

- Les noyaux légers et leurs isotopes instables (qui jouent le rôle d'horloge cosmique par leur période de désintégration, un peu comme le Carbone 14 est utilisé pour la datation de fossiles sur la Terre) qui arrivent jusqu'à nous permettent d'étudier les temps de confinement dans la galaxie, et on peut ainsi comprendre les mécanismes dynamiques des galaxies. Là encore, AMS par ses capacités d'identification des particules qui le traversent permettra de gagner des ordres de grandeur sur les mesures existantes.

- Comprendre les phénomènes cataclysmiques dans les galaxies: parfois, un

point dans le ciel émet brusquement une grande quantité de rayons gamma, pendant quelques secondes ou quelques minutes. C'est une énergie équivalente à plusieurs milliers de fois la masse de notre Soleil qui est brusquement irradiée dans l'espace, venant du fond de l'Univers. AMS cherchera à comprendre quel mécanisme est à l'origine de tels cataclysmes cosmiques en observant les rayons gamma de haute énergie émis dans ces phénomènes.

Le détecteur de traces d'AMS-02

Le détecteur de traces est composé de détecteurs au silicium, avec des implantations de micropistes. Le principe de base de ces détecteurs repose sur les propriétés des jonctions $p-n$, les diodes.

Un détecteur au silicium avec implantations de micropistes consiste en un monocristal de silicium de type n, en général d'une épaisseur de 300 μm, avec des pistes implantées p^+ (fort dopage p) sur sa surface . Ces pistes, qui sont de l'ordre de 12 μm de largeur et qui sont implantées en surface, ne sont rien d'autre que des jonctions $p-n$. Le principe de fonctionnement est donc le suivant: la face munie des pistes p connectées à la masse, on applique une tension positive sur la face opposée. Dans ces conditions, les zones de déplétion occupant le volume autour des pistes (qui sont des jonctions $p-n$) s'étendent au fur et à mesure que la tension positive augmente, jusqu'à ce que la tension de déplétion soit atteinte. Tout le monocristal est alors vidé de ses porteurs de charge libres. L'énergie déposée par une particule chargée traversant le détecteur dans une telle configuration va induire la création de paires électron-trou. Le champ électrique au sein du détecteur permettra la récupération des trous au niveau des pistes: une localisation de la particule traversante est alors possible.
Les principales caractéristiques des détecteurs à micropistes sont la tension de déplétion, le courant de fuite des pistes, ainsi que les capacités entre pistes. La tension de déplétion permet d'identifier à partir de quelle tension le détecteur fonctionne correctement sur ses deux faces. Dans le cas d'AMS, une tension de dépletion maximale de 50 V a été choisie. Une marge de sécurité est adoptée, de sorte que la tension de fonctionnement est de 80 V.

Un module au silicium d'AMS (appelé *échelle*) est composé d'un alignement de sept à quinze détecteurs à micropistes double-face ($72.045 \times 41.36 \times 0.3$ mm^3). Les pistes sont connectées les unes à la suite des autres côté p, tandis qu'un câble flexible en Upilex permet la transmission des signaux côté n. Pour AMS-02, 192 échelles ont été produites. Ces modules sont répartis sur huit couches, totalisant une surface de détection de 6.39 m^2. Une structure (appelée *renfort*) faite de mousse en Airex et d'une couche en fibre de carbone permet de donner une rigidité à l'ensemble. Des pieds en aluminium, collés sur la fibre en carbone du renfort permettent de fixer les échelles sur l'une des huit couches de détection.
Les cartes de l'électronique d'amplification (appelées *hybrides*) sont connectées dans le prolongement du silicium, via des câbles en Upilex, pour chaque côté de détection

de l'échelle (le côté supérieur est appelé S, le côté inférieur K). Au total, 1024 canaux de lecture sont associés à une échelle. Les préamplificateurs, nommés VA, accomplissent la mise en forme du signal de façon continue.
L'assemblage des échelles nécessite un équipement particulier, ainsi qu'un environnement adéquat. Un système d'application de colle CAM/ALOT avec un microdoseur volumétrique est utilisé pour le collage de l'Upilex K. Les micropistes sont connectées les unes aux autres par microsoudure, tandis que l'alignement des détecteurs est contrôlé par une machine de métrologie Mitutoyo. La fragilité des détecteurs au silicium vis-à-vis des manipulations et des poussières nécessitent également un environnement d'une propreté extrême, d'où la nécessité de travailler dans une salle blanche.
La production est partagée par trois sites: G&A Engineering, une industrie italienne, l'Université de Perugia (Italie) et l'Université de Genève.
L'Université de Perugia, secondée par G&A, se spécialise dans les tests de validation des senseurs au silicium avant assemblage, tandis que Genève est le site par lequel tous les modules transitent, pour subir les dernières étapes d'assemblage: installation des hybrides dans une boîte en aluminium, collage des pieds qui permettront la fixation sur les plans. L'installation des échelles sur les plans s'opère en outre à Genève. Tout au long du processus d'assemblage, les échelles subissent des test électriques: mesure du courant de fuite à 80 V et 90 V, ainsi que des calibrages, pour notamment identifier les canaux bruyants ou inactifs. Une échelle présentant des défaillances durant le processus d'assemblage est écartée et si possible ultérieurement réparée.

Test faisceau avec électrons et photons

Les principaux objectifs du test en faisceau des échelles du détecteur de traces réalisé en septembre 2004, étaient les suivants:

- Etudier la réponse des échelles du détecteur de traces aux électrons et positrons de différentes énergies;
- Etudier la possibilité de détecter la conversion des photons en paire électron-positron;
- Mesurer la résolution en impulsion pour les particules chargées et la résolution en énergie et en angle pour les photons (produits via *bremsstrahalung* des électrons sur une cible de tungstène);
- Tester l'électronique prototype qui sera utilisée en vol.

Ce test s'est déroulé en collaboration avec le groupe responsable du calorimètre électromagnétique. Une seule des supercouches de ce calorimètre a été utilisée, l'électronique disponible ne permettant pas de tester le calorimétre complet.
Par rapport aux tests précédents, ce test a également la particularité de reproduire dans la mesure du possible la structure mécanique du tracker.

Le test a eu lieu au CERN dans le Hall Est. La zone mise à disposition était la zone T7 (Fig. 5). Le faisceau qui alimente cette zone est un faisceau secondaire

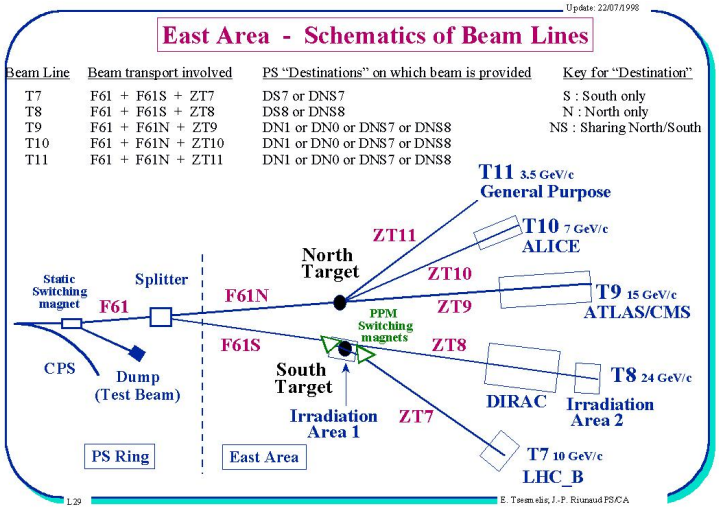

Figure 5: Schéma de la zone expérimentale du *PS* et géométrie des lignes de faisceau *T7*, *T8*, *T9*, *T10* et *T11*.

issu du faiseau de protons de 24 GeV/c de l'accélérateur PS (Proton Synchrotron) du CERN. Pour le test, il a fonctionné avec un faisceau d'une impulsion de 3, 5 et 7 GeV/c pendant une période de test d'environ 5 semaines. Afin d'enrichir le faisceau secondaire en électrons, un faisceau d'antiprotons et une cible riche en électrons ont été utilisés. Le matériel disponible dans la zone expérimentale comprenait un aimant dipolaire capable de générer des champs pouvant atteindre 1 T. La cartographie du champ magnétique de cet aimant a été effectuée. Elle montre une forte homogénéité du champ dans la partie centrale de l'entrefer tandis qu'en bordure des pôles, où se trouvaient la première et les deux dernières échelles, le champ varie sensiblement (selon z). Ces données ont été utilisées par le code de simulation du test faisceau et également par le code de reconstruction des traces. Deux détecteurs Čerenkov à seuil étaient également disponibles: à l'intérieur de la zone, un d'une longueur de 2 mètres (C2) a été positionné entre la sortie du faisceu et l'aimant, un autre Čerenkov (C1), d'une longueur de 4 mètres, était situé immédiatement en amont de la zone (avant le mur de blindage). L'étude des caractéristiques de ces détecteurs a été aussi réalisée. Elle a montré une bonne résolution et une bonne efficacité pour ce qui concerne C1 tandis que C2, même en fonctionnant moins bien, a permis d'améliorer la sélection des électrons par C1.

La Fig. 6 présente la configuration schématique du test faisceau. Les différents éléments qui y aparaissent sont:

- L'aimant dipolaire M;
- Les deux détecteurs Čerenkov C1 et C2. Ils sont indispensables à l'identification des électrons du faisceau;

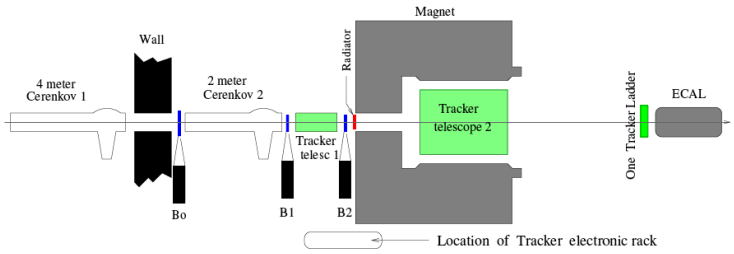

Figure 6: Configuration schématique du test faisceau en septembre 2004 au Cern.

- Les compteurs à scintillation B0, B1, B2 utilisés pour le Trigger;
- Un radiateur R en tungstène qui permet la production des photons de *bremsstrahlung* et leur conversion en paire électron-positron.
- Le téléscope T1 composé de 4 échelles. Il a permis de connaître la trajectoire des particules avant leur entrée dans l'aimant où elles étaient déviées par le champ magnétique.
- Le téléscope T2 qui était l'élément central du test faisceau. Il était composé de 11 échelles. Celui-ci est positionné dans l'entrefer de l'aimant et reproduit,

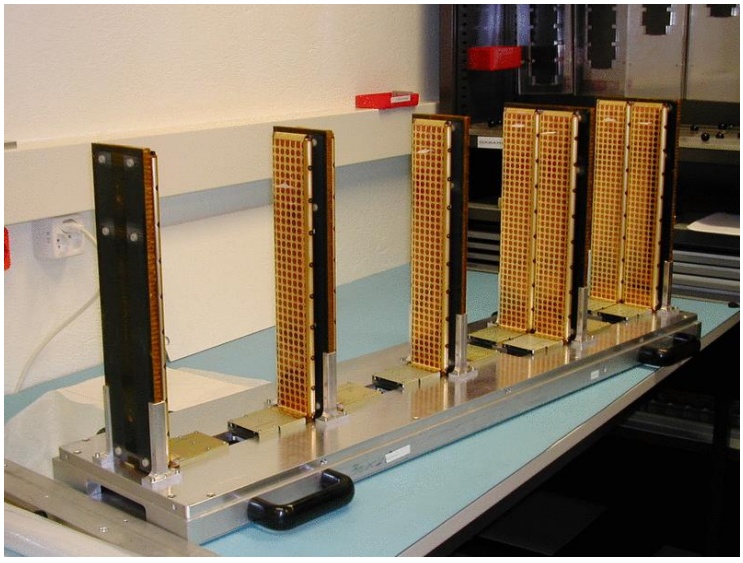

Figure 7: Le télescope T2 élément central du test faisceau.

dans la mesure du possible, la structure du tracker d'AMS-02. Comme on peut le voir sur Fig. 7, ce télescope reproduit la succession des 8 couches du détecteur de traces d'AMS-02 disposées sur cinq plans avec des espacements similaires. Le dernier plan contient deux échelles afin de recueillir davantage de particules. En effet, la composante principale du champ magnétique était

dirigée selon la verticale, une particule chargée arrivant dans la direction du faisceau était déviée dans le plan horizontal.

- En aval de l'aimant était également positionnée une des couches du calorimètre électromagnétique. Celle-ci était immédiatement précédée d'une échelle qui a permis de déterminer la position d'entrée de la particule dans le calorimètre.

Les résultats de ce test montrent que bien qu'AMS soit conçu fondamentalement pour l'observation des rayons cosmiques chargés, il présente un bon rendement pour la détection de rayons gamma, d'énergie plus grande que 1 GeV, avec une résolution en énergie ($\sigma(E)/E$) entre $2 \div 5\%$ et une résolution angulaire de $0.1\ ^o/2\ ^o$ (tracker/calorimètre) à 10 GeV, valeurs améliorant sensiblement à de plus grandes énergies.
En particulier, on a confirmé les résultats obtenus par la simulation dans l'intervalle d'énergie du photon de 1 à 6 GeV (où se concentrerait plus que 80% de la statistique) pour les résolutions angulaire et énergétique. On a validé de même la résolution spatiale intrinsèque des échelles de silicium, avec des valeurs de 10 et 30 μm pour les côté p et n des senseurs respectivement. Pour la première fois, on a vérifié la résolution en impulsion pour les électrons dans le détecteur de traces en utilisant les échelles et la configuration finale d'AMS-02 et un nouvel algorithme d'ajustement pour les traces. Cette résolution est de l'ordre de 1.6%.

Astrophysique des rayons gamma

Si les étoiles, comme par exemple le Soleil, émettent principalement de la lumière visible, les autres domaines du spectre électromagnétique se révèlent eux aussi très riches d'enseignement. Les astronomes y observent les horloges les plus précises de l'Univers: les pulsars. L'espace baigne dans un intense rayonnement millimétrique - le rayonnement cosmologique - que l'on pense être un vestige du "big-bang". Le rayonnement infrarouge nous révèle les étoiles naissantes, enveloppées dans un nuage de poussière. Les énigmatiques quasars sont des sources extraordinairement intenses de rayonnement ultraviolet. Grâce aux rayons X les astronomes observent les trous noirs en train d'avaler les étoiles qui furent leur compagnon. Enfin, les rayons gamma constituent la forme extrême du rayonnement électromagnétique. Les sources astrophysiques de rayonnement gamma sont toujours d'une violence fantastique, comme les supernovas ou les quasars, et les mécanismes d'émission impliquent généralement des particules à haute énergie. Contrairement à la majorité des autres domaines du spectre électro-magnétique, ce domain reste encore mal exploré. AMS-02 pourra aussi donner une contribution importante à ce sujet très interessant. Le relatif retard de l'astronomie gamma est dû au fait que le rayonnement gamma est très difficile à observer; tout d'abord parce que notre atmosphère constitue un écran totalement opaque au rayonnement gamma. Ceci est en fait plutôt heureux, car, comme on l'a bien appris avec la radioactivité, le rayonnement gamma est dangereux. Pour les astronomes, cela signifie qu'il faut s'affranchir de l'atmosphère en placant le détecteur dans un ballon ou, nettement mieux mais beaucoup plus onéreux, à bord d'un satellite.

La carte d'exposition du ciel d'AMS-02 et sa sensibilité aux pulsars

Pour obtenir des informations précises d'une source céleste dans le rayonnement gamma, il faut réaliser des poses très longues, typiquement de plusieurs jours à plusieurs semaines. Les observations de régions adjacentes du ciel peuvent être combinées afin d'en tirer un maximum d'informations. Des cartes d'exposition sont régulièrement réalisées montrant le temps total que les instruments ont passé à observer chaque région du ciel.

Pour établir des prédictions des flux de gamma provenant des sources et de l'émission diffuse, un programme de simulation rapide a été réalisé. Un simulateur rapide permet d'évaluer les performances d'un instrument sans pour autant nécessiter d'importantes ressources informatiques. La différence par rapport à la simulation complète (Monte Carlo) au moyen de GEANT consiste en l'utilisation des paramétrisations des acceptances et résolutions, sans tenir compte de toutes les interactions des particules dans le détecteur. Les éléments de base de l'algorithme sont:

- L'orbite: comme AMS sera sur l'ISS en orbite autour de la Terre, il ne pointera pas vers toutes les parties du ciel pendant des durées égales. Il faut donc simuler l'orbite pour pouvoir évaluer le temps d'observation pour chaque source.

- La source: en plus de sa position dans le ciel, il faut aussi connaître les propriétés de l'émission de la source, cést-à-dire son spectre. Le spectre peut être modélisé, ou bien venir des mesures ultérieures.

- Le détecteur: il est nécessaire de disposer d'une paramétrisation de l'acceptance et des résolutions du détecteur dont on veut évaluer la réponse.

Des données précises sur l'orbite de la Station Spatiale sont régulièrement diffusées et mises à jour sur Internet. Ces informations sont en fait les éléments képlériens de l'orbite: excentricité, anomalie moyenne, inclinaison, argument du périgée, etc. À partir de ces paramètres, on peut calculer la position de la station pour un temps t donné. Connaissant l'emplacement où AMS sera installé sur la station et son orientation, il est possible de déduire les coordonnées pointées par le détecteur. AMS pointe en permanence vers le ciel et est incliné de 12^o par rapport à la verticale pour éviter d'avoir une partie de panneau solaire dans son champ de vue. Le simulateur rapide utilise des cartes d'expositions en coordonnées galactiques pour représenter l'orbite. Ces cartes sont élaborées pour une certaine durée passée en orbite et donnent le temps (en secondes par an) passé par AMS à pointer une direction précise du ciel.
En particulier, les cartes d'exposition utilisées sont constituées en ignorant le temps passé par AMS au-dessus de l'Anomalie Sud-Atlantique (SAA de South Atlantic Anomaly). La SAA est une région de l'Atlantique sud où la ceinture de radiation entourant la Terre descend à basse altitude (environ 250 km). Dans cette zone, de

nombreuses particules (protons, électrons) peuvent faire déclencher les détecteurs de manière intempestive et on préfère souvent les désactiver.

A travers l'utilisation du "simulator" rapide on a calculé le nombre de photons par année d'opération et pour différentes sources du Catalogue d'EGRET, dans différentes bandes d'énergie. En outre, à travers une simulation spécifique on a calculé la capacité du détecteur AMS à détecter un signal d'une source qui émet un signal pulsé. Sur la base des caractéristiques du pulsar du Crabe on a trouvé que le nombre de photons necessaires pour distinguer ce signal du bruit de fond devrait être plus grand de 40.

Introduction

Since the beginning, particle physics investigations have been performed using particle accelerators: the higher the beam energy the deeper the matter can be probed. One of the most recent example of that is the LHC accelerator at CERN which will be operative in 2008; it will use superconductcting magnets, cooled by superfluid helium, to bend particles and it will be able to produce collisions at 14 TeV center-of-mass energy. This will be the higher energy reached by a laboratory device and will give to researchers the opportunity to produce heavy particles of new type: supersymmetric particles, the Higgs boson, mini black holes.
However the size, complexity and cost of a particle accelerator grows with its energy so particle physicists started to look at particles coming from the Universe.
This new branch of Physics is relatively new: it is the fusion between particle physics and astrophysics and it is referred to as Astroparticle Physics.
A black hole is an example of natural accelerator. It sucks stars and cosmic dust into giant swirl rotating around it; the falling matter heats up, resulting in enormous shock waves which propagate outward. At the shock fronts particles are accelerated in innumerably many kicks to higher and higher energies, until they finally escape into the void of intergalactic space. So we know that natural particle accelerators exist, but we do not know where they are. Charged cosmic particles have the disadvantage that they are deviated when they travel through cosmic magnetic fields loosing the information about their original direction. A localization of those kind of accelerating objects, is only possible with electrically neutral information carriers like photons or neutrinos. Both travel in straight lines. Photons can be detected easily, but can be absorbed by cosmic dust layers and matter. For neutrinos it is exactly the other way round.
In particular, the Gamma Ray Universe represents one of the most promising fields for the search of new physics. Among the past missions, the CGRO (Compton Gamma Ray Observatory), launched in 1991, opened a new window over the γ-ray astronomy. EGRET (Energetic Gamma Ray Telescope Experiment), one of the experiments operating on-board of CGRO, delivered to the scientific community new great discoveries and many troubling questions. The most important EGRET discoveries have been the confirmation that most cosmic rays are galactic, the estimation of the detailed map of the galactic diffuse radiation, the measurement of the diffuse, presumably extragalactic, high energy gamma-ray spectrum and the discovery of a new class of gamma-ray emitting Active Galactic Nuclei (the so-called gamma-ray blazars). Moreover, several sources detected by EGRET are still unidentified and the exploration of other astronomical fields (i.e. gamma ray bursts,

pulsars, dark matter, etc.) has to be completed.
This thesis summarizes my research activity, during a period of five years as PhD student, in the astroparticle experiment Alpha Magnetic Spectrometer (AMS-02). AMS is a particle detector designed to perform high precision measurements of the cosmic rays fluxes with the main goals of searching for anti-nuclei, as remnants of primordial anti-matter, and of measuring the faintest components of the cosmic flux, anti- protons, positrons and high energy photons. To fulfill the requirements of large acceptance, long exposure time and excellent particle identification needed to achieve the intended results, AMS will operate in space as an attached payload to the International Space Station (ISS), being the first full featured particle physics experiment to operate in the Earth orbit.
The core of the AMS-02 detector is a superconducting magnet, generating a very strong field, enclosing the silicon tracking system; the other main subdetectors are the time of flight (TOF) system, the transition radiation detector (TRD), the ring imaging Čerenkov (RICH) and the electromagnetic calorimeter (ECAL).
The AMS-02 accurate measurements of cosmic-ray nuclei, protons, antiprotons, electrons and positrons will be completed by high energy gamma rays detection. The experiment will detect γ-rays, either by reconstructing e^+e^- pairs generated by photons converted upstream the tracker (*conversion mode*), or based on direct identification of electromagnetic showers in ECAL (*calorimetric mode*). In order to use the latter techniques, the ECAL must be provided with a neutral "stand alone" trigger able to recover the photons not acquired by standard AMS-02 trigger based on TOF counters. Moreover an efficient method to reject the huge background to the γ-rays signal is required. The very good imaging capability of the calorimeter is helpful for background suppression purposes.
The AMS research group of University of Geneva participates to the construction and operation of the AMS-02 silicon tracker detector in collaboration with INFN-Perugia and RWTH-Aachen groups.
My contribution to the activity of the AMS-02 Tracker group started at the end of 2001 and touched many aspects of the detector construction such as the so-called *Phase 1* which took into account the assembly of silicon wafers into ladders, the responsibility of the commissioning of the subsequent *Phase 2* which includes the completion of silicon ladder assembly with their related electronics, the validation of both and the installation on the tracker planes. In 2002 and 2003, I participated to several beam tests performed on a few number of silicon ladders and aimed to study the detector capability to disantagle different chemical elements. During 2004 I took part to the organization of a test beam which used a beam of electron in order to produce photons via *bremsstrahlung*. In this case silicon ladders were arranged in a configuration mimicking the one of the AMS-02 Silicon Tracker detector ("mini-tracker"). The analysis of beam test data in order to estimate the silicon ladder performances to photons is presented in this thesis. My PhD thesis work continued with simulation studies devoted to the extraction of the *Exposure Maps* and the implementation of new algorithms to get a prediction of the AMS-02 sensitivity for pulsars. The above maps represent the effective integrated time, convoluted with detector acceptance, to detect photons from a specific point of the sky.

The outline of the thesis, organized in eight chapters, is as follows:

Chapter 1
An introduction to the Big Bang cosmology is given, together with the description of the most recent and important experimental measurements of the cosmological parameters. A review of the cosmic rays acceleration and propagation, anti-matter searches and dark matter scenario are presented.

Chapter 2
The gamma-ray Universe is briefly described showing an outline of the gamma ray sky on the basis of results reported by EGRET. The present knowledge about the diffuse gamma rays emission (galactic and extragalactic components) from both a theoretical and an experimental point of view is described.

Chapter 3
The AMS mission and its scientific goals are discussed. The working principles of AMS-02, each subdetectors, the trigger and the perspectives are presented.

Chapter 4
The main features of the the magnetic spectrometer (consisting of the superconducting magnet and the Silicon Tracker) are shown. The characteristics of the silicon tracker ladders are described in detail together with a review on the production phases, the related front-end electronics and the alignment system.

Chapter 5
After a brief description of the results from previous beam tests on AMS-02 silicon ladders regarding nuclei detection from helium up to the highest detectable charges, a detailed description of the goals, the set-up and the preliminary tests of the test beam performed in September 2004 using an electron beam, is reported.

Chapter 6
First the official AMS-02 simulation and reconstruction code is presented giving particular emphasis to the electron/positron signals. Then the equivalent reconstruction code developed for the 2004 beam test is detailed in its main components as the clusterization algorithms and the various corrections needed to recover DAQ failures during the data taking.

Chapter 7
The analysis of the 2004 test beam data is reported. Algorithms for the identification and reconstruction of electrons and photons in the silicon "mini-tracker" are described. The resulting performances, in terms of energy and angular resolutions, are shown.

Chapter 8

The AMS-02 gamma rays detection strategy is here described. The predicted performances for the *conversion* and *calorimetric mode* are discussed. In order to compute the expected number of gamma rays events from a given point in the sky, the detector exposure maps are needed. An original algorithm for the AMS-02 orbital simulation is presented and the corresponding exposure maps both for the tracker and the electromagnetic calorimeter over one year period, are shown. These exposure maps are then introduced as an input in the AMS-02 fast simulation code together with a set of γ-rays emission skymaps. Eventually, an estimate of the AMS-02 capability expected in the measurement of pulsars is given.

Chapter 1

Cosmic Rays and Photons

1.1 Cosmology

Our present understanding of the Universe is based upon the hot Big Bang theory, which explains its evolution from the first fraction of a second to our present age, around 15 billion years later. This theory is based on general relativity and there are three often cited observational facts strongly supporting it:

- the recession velocity of galaxies is proportional to their distance: the Universe is expanding (Hubble [1]);
- the cosmic microwave background (CMB), the afterglow of the Big Bang, discovered by Penzias and Wilson [2] as a very isotropic blackbody radiation at a temperature of about 3 K, emitted when the Universe was cold enough to form neutral atoms, and photons decoupled from matter, approximately 380 thousand years after the Big Bang.
- the relative abundance of light elements which were formed in nuclear reactions around a second to a few minutes after the Big Bang as explained by Gamov [3, 4];

Today, these observations are confirmed with great accuracy establishing the hot Big Bang as the preferred model of the Universe.

1.1.1 Big Bang Nucleosynthesis

One of the biggest success of the Big Bang theory is the correct prediction of the abundances of light nuclei (up to ^7Li) in terms of one parameter only, the baryon-to-photon ratio η, which is defined as the ratio of number densities:

$$\eta \equiv \frac{n_B}{n_\gamma} = \frac{n_b - n_{\bar{b}}}{n_\gamma} \tag{1.1}$$

In absence of baryon number violating processes and of any change in the total number of effectively massless degrees of freedom, this quantity remains constant.

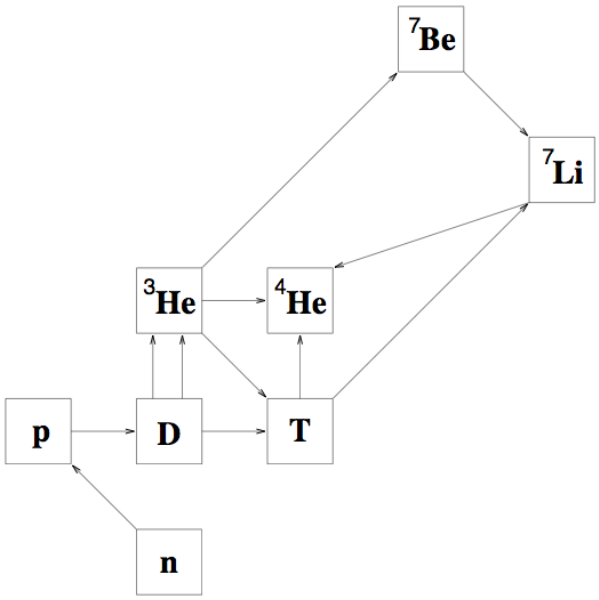

Figure 1.1: The twelve fundamental reactions which govern the production of the lightest nuclei during primordial Big Bang nucleosynthesis.

The whole primordial production is completed within the first three minutes after the Big Bang, at energies ranging from 10 MeV to 0.1 MeV.
At temperatures $T \gg 1$MeV neutrons and protons are in equilibrium with light nuclei, whose abundance, n, is exponentially suppressed, $n \sim exp(E_B/T)$, where E_B is the binding energy. Due to weak interactions, nucleons are in thermal equilibrium as long as the interaction rate is faster than the expansion rate, which is the case until $T \sim 0.8$MeV. Binding energies of light nuclei are typically in this range, but a significant production of light nuclei is delayed until $T \sim 0.1$MeV since they are broken up by photo-dissociation ($\eta^{-1} \sim 10^{10}$). When the weak interaction freezes out, for each neutron there are about six protons. Due to the relatively short lifetime of the free neutron ($\tau_n \sim 887$ s),the ratio n_n/n_p drops to 1/7. Deuterium can be produced through $p + n \rightarrow D + \gamma$ and is further processed by a network of reactions as depicted in Fig. 1.1. Practically all neutrons are finally transformed into ^4He and the mass fraction of primordial ^4He is predicted to be:

$$Y_p \equiv \frac{m_{He}}{m_n + m_p} = \frac{4n_{He}}{n_n + n_p} = \frac{2n_n}{n_n + n_p} \sim 0.25 \tag{1.2}$$

The production of heavier nuclei (^7Li, ^7Be) is relatively inefficient: there are no stable nuclei with masses 5 or 8, the Coulomb barriers are high, and 3α reactions are rare because the nucleon density is low. The primordial nucleosynthesis stops at this point; it is only during stellar nuclear fusion and supernovae explosions that further nuclei can be created much later.
From the experimental point of view, the measured abundances of ^4He are contaminated by non-primordial nuclei, so that the interstellar value of regions with low

metalicity represent an upper limit on Y_p. The extrapolated primordial component is evaluated to be [5]:

$$Y_p = 0.238 \pm 0.002 \pm 0.005 \tag{1.3}$$

in accordance with the prediction.
Primordial deuterium can be subsequently destroyed, whereas ^3He and ^7Li, can be both destroyed through stellar re-processing or produced in low-mass stars. Interstellar measurements indicate lower limits for the number ratio of the order $D/H \sim {}^3He/H \sim 1.5 \times 10^{-5}$.
^7Li can be determinated by observation of stellar atmospheres, and for old population II stars a ratio $^7Li/H = 1.6 \times 10^{-10}$ is obtained.
A single consistent η value can be chosen in order to explain the observed abundances (see Fig. 1.2) which span over ten orders of magnitude. Taking the different uncertainties concerning the primordiality of the nuclei into account, the allowed range [5] is:

$$1.2 \times 10^{-10} < \eta < 5.7 \times 10^{-10} \tag{1.4}$$

which can be translated into the critical baryon fraction:

$$0.004 < \Omega_B h^2 < 0.021 \tag{1.5}$$

This means that not only is the dark energy the dominating contribution to the energy content of the Universe, but also that the most important fraction of the matter density (80% or more) is a so far unknown from of non-luminous non-baryonic matter called *dark matter*.

1.2 Cosmic Rays Physics

The term *cosmic-rays*, in everyday language, refers to the ionizing particles that continuously penetrate our daily environment and interact with matter here on Earth. Their origin can be traced back to sources outside the Earth's atmosphere. This radiation is composed of secondary particles (mostly electrons and muons) produced in interactions between the Earth's atmosphere and the so-called *primary* cosmic-ray particles that impinge on it. These primary particles form an interstellar plasma that fills the Galaxy and is a part of what is called the interstellar medium (ISM). What is referred to as primary cosmic-rays might indeed be secondary particles in the sense that they can have been produced in interactions between the cosmic-ray plasma and other constituent particles of the ISM. However, the cosmic-rays must have primary sources of origin. These are believed to be located mainly inside the Galaxy, for energies below the so-called *knee* of the spectrum. The study of cosmic-rays allows the mechanisms of production and propagation of particles within our Galaxy to be investigated. The anti-proton and positron components of the cosmic radiation also gives the possibility to explore physics beyond the Standard Model, which otherwise may only be possible by using detectors located at particle accelerators.

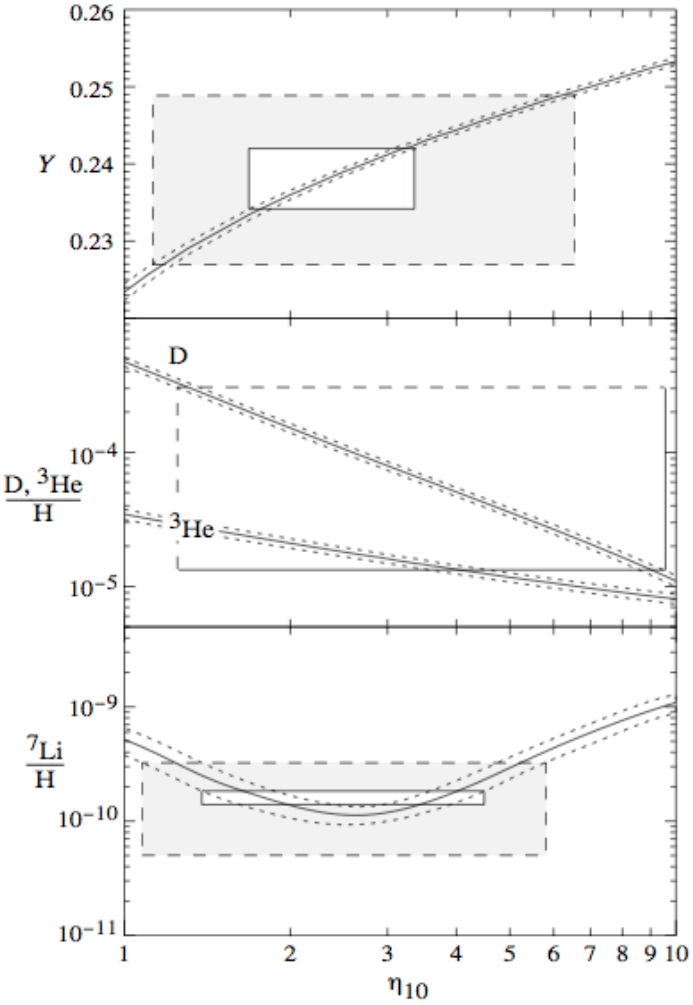

Figure 1.2: The abundances of the lightest nuclei as a function of $\eta_{10} \equiv \eta \times 10^{10}$, as predicted by the standard model of Big Bang nucleosynthesis [5]. The hatched and shaded boxes are the 1σ and 2σ experimental range. For ^3He and D a lower limit is given.

1.2.1 Cosmic-Ray Particles

Every second around 1000 charged cosmic-ray particles per square meter hit the Earth's atmosphere. About 90% of these are protons, 9% are alpha particles and 1% are electrons, and there are also a small abundance of heavier nuclei [6].

Cosmic rays were discovered in 1912 by Victor Hess and his colleague Werner Kohlörster when they were conducting an experiment in which a hot air balloon, carrying an electroscope, was used to measure the altitude dependence of the natural background radiation [7, 8]. At the time this radiation was thought to originate from the Earth. However, in Hess's experiment the electroscope discharged more rapidly as the balloon ascended in the atmosphere which meant that the ionizing radiation increased with altitude and therefore must originate from outside the Earth's atmosphere rather than from the ground. For some time it was believed that the radiation was of electromagnetic nature.

In 1929, an experiment of Walter Bothe and Kohlörster based on coincidence measurements using two Geiger detectors allowed the charged nature of cosmic rays to be determined [9]. A few years later (1932) Carl D. Anderson, using a cloud chamber, discovered the positron by measuring the curvature and the energy-loss of cosmic ray particles in a magnetic field [10]. This was the first experimental evidence of the antimatter predicted by Dirac. That discovery was an important milestone in the development of particle physics. In the following years many new particles were discovered in cosmic ray experiments, and cosmic rays provided the primary source of particles for high energy physics research.

With the advent of particle accelerators, cosmic rays lost their importance as a particle source. The study of the flux, composition, origin and propagation of cosmic rays has gradually grown into an independent field of research. However, during the last decades the interplay between cosmic ray physics and particle physics aims to answer fundamental physics questions connected to phenomena like neutrino oscillations, magnetic monopoles, dark matter and baryon asymmetry.
A wide range of experimental techniques are being used to pursue this scientific program. At ground-level, large area detector array experiments are constructed to measure air showers initiated by high energy cosmic rays. To study the primary cosmic ray particles before they interact in the Earth's atmosphere, high altitude balloons have frequently been used. At the altitudes reached by these balloon-borne experiments, there is however still an overburden of residual atmosphere where particle interactions can occur. The way to avoid this limitation is to use satellite-borne experiments.

Composition and Energy

The main component of the primary cosmic ray flux is hadronic in nature and seems to originate from within our Galaxy. The flux is approximately isotropic and ranges between 2 and 4 cm^{-2} s^{-1} at 1 astronomical unit. Galactic cosmic rays (GCR) are

mainly composed of hadronic particles with the abundance: 90% H, 9% He and 1% heavier nuclei. An electron component of $\sim 1\%$ and traces of anti-protons (0.001%) and positrons (0.1)% are also present [11].

Hadronic Component

The hadronic component of the cosmic radiation has an abundance of different nuclei which is almost the same as that in the solar system. This is illustrated in Fig. 1.3 where the relative abundance in the Solar system (dashed line) is compared to that of cosmic rays. Both compositions show a clear even-odd effect (nuclei with an even atomic number are more abundant than those with an odd one). This composition and the shape of the cosmic ray energy spectrum supports the assumption that most Galactic cosmic rays are synthetized in stars and liberated by supernova explosions.

Differences between Solar and GCR abundances are explained by spallation processes where carbon, oxygen and iron nuclei interact with the ISM as they travel through the Galaxy. The two groups of elements Li, Be, B and Sc, Ti, V, Cr, Mn are almost absent in the Solar system while a significant amount of them is found in cosmic rays. The observed abundances in cosmic radiation are interpreted as a result of the collisions of nuclei with the interstellar medium and the subsequent fragmentation of the primary nucleus into lighter elements. The products of these spallation processes are Li, Be, B, in case of primary carbon and oxygen, while Sc, Ti, V, Cr, Mn are produced by primary iron nuclei [12].
Collisions of primary cosmic ray nuclei with the ISM also cause production of long-lived radioactive isotopes, which can be used as cosmic ray "clocks". By comparing the observed abundances of these radioactive nuclei with the amount of stable secondary species in the cosmic radiation one can establish for how long cosmic rays are confined in the Galaxy and investigate the density distribution of the gas encountered by the particles. It has been deduced that an average GCR spends several million years wandering around our Galaxy before reaching Earth. Because of their charge, most cosmic rays propagating in the Galaxy have an energy low enough to be deflected by the interstellar magnetic field, and once they reach the Earth all directional information about their source has been lost [11].
The differential cosmic ray flux is shown in Fig. 1.4 as a function of energy. Above 10 GeV/nucleon the energy spectrum of primary cosmic rays can be described by a segmented power law spectrum:

$$\frac{dN}{dE} \propto E^{-\alpha}; \qquad \alpha = \begin{cases} 2.7 & E < 10^{16} eV \\ 3.0 & 10^{16} < E < 10^{18} eV \end{cases} \tag{1.6}$$

It spans over a large number of decades. For the highest energies (above 10^{19}eV) the is smaller. There are two breaks in the spectrum around 10^{15} to 10^{16}eV (the *knee*) and 10^{18} to 10^{18}eV (the *ankle*). Exactly what causes the knee is still unknown. Several explanations have been proposed. Some connect the steeping of the spectrum to different acceleration mechanisms or to a change in the GCR propagation which

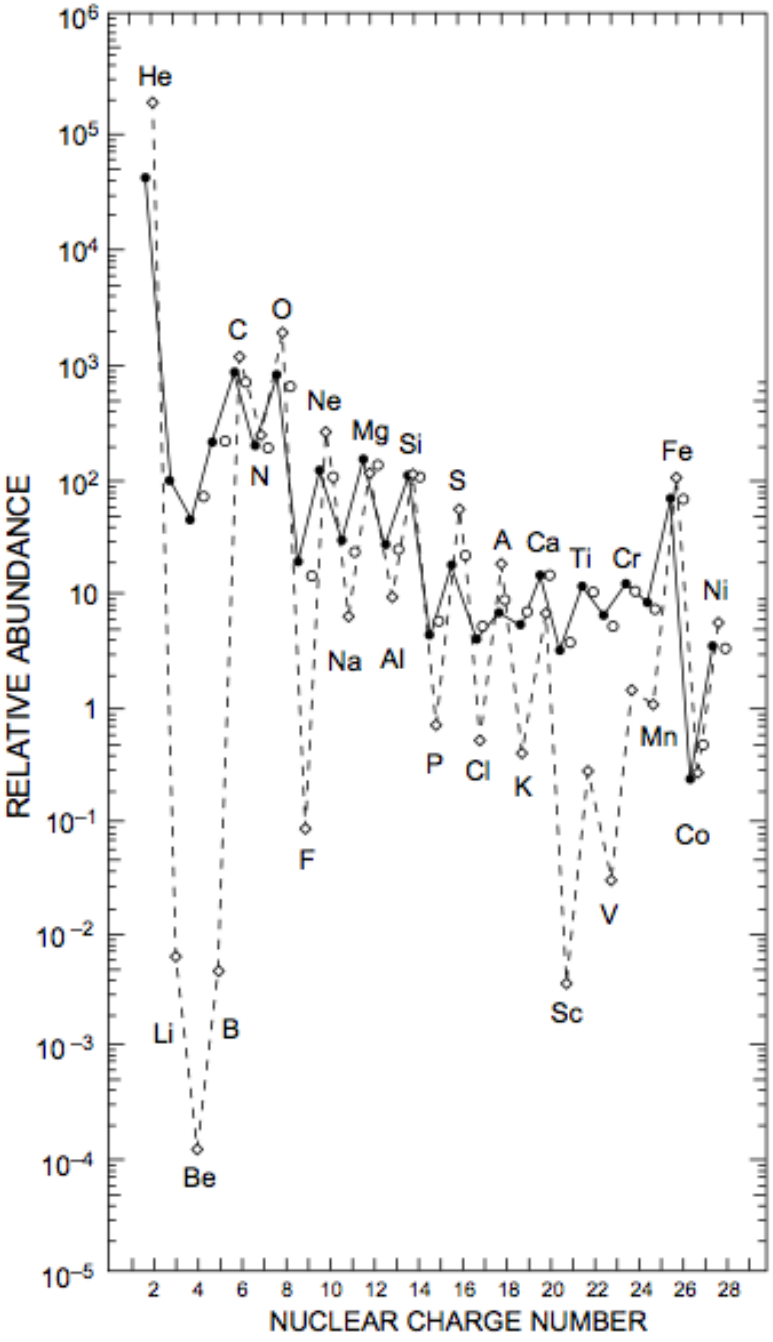

Figure 1.3: Relative abundance of cosmic rays (solid line) and of the elements present in the Solar system (dashed line). The numbers are normalized to the abundance of Si (= 100).

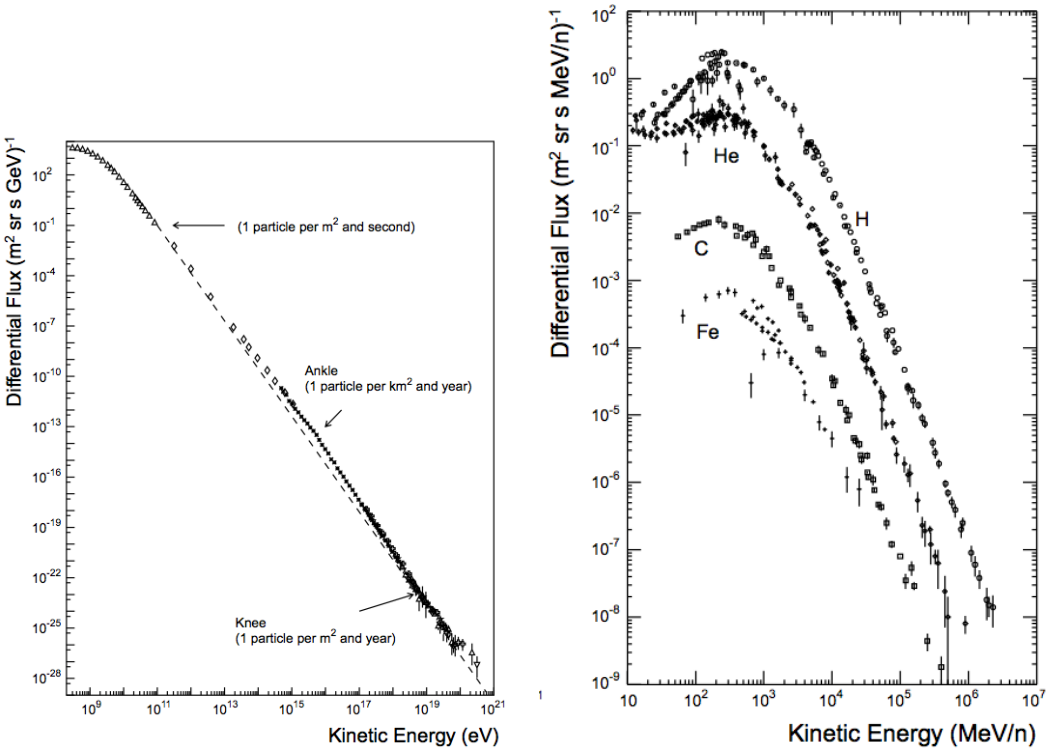

Figure 1.4: Energy spectra of cosmic rays. (a) Total spectrum [15], (b) Individual spectrum for components H to C [16].

leads to a more rapid escape from the Galaxy, others explain the knee in terms of different properties of the source itself [13].
The highest energy cosmic rays measured to date have had more than 10^{20}eV.

Electrons

Energetic cosmic rays that collide with the ISM can interact and produce a large variety of secondary particles, some of which will decay. Electrons can be produced in these decays (e.g. from pions via the decay $\pi^{\pm} \rightarrow \mu^{\pm}X \rightarrow e^{\pm}X$) which yield an equal number of positrons. However, the measured positron fraction $e^{+}/(e^{+}+e^{-})$, is found to be only a few percent in the explored energy interval (below ~ 50 GeV) [14]. This fact suggests that there are mainly primary sources of electrons in the Galaxy. The subject of cosmic ray positrons is discussed later in this chapter.

Like the hadronic component, electrons interact in the interstellar gas, but in addition to this they suffer significant energy losses when they interact with the interstellar magnetic field and the microwave background photons. These additional interactions, which include emission of synchrotron radiation and bremsstrahlung as well as inverse Compton scattering, causes the energy spectrum to be dependent on parameters such as: the average diffusion time in the Galaxy, the average strength of the Galactic magnetic field and the energy density of the background radiation. The energy losses due to inverse Compton scattering with the microwave background radiation also limits the lifetime for electrons and thus the distance they can travel. This implies that the sources must be intragalactic. Electrons (and positrons) are thus the only cosmic ray components for which extra-galactic contributions can be excluded at any energy [11].

1.2.2 Fermi Acceleration

Enrico Fermi developed a theory for stochastic acceleration of cosmic rays [17]. When cosmic ray particles "collide" with moving clouds of plasma, they gain or loose an amount of energy proportional to the plasma velocity and to the particle energy. Whether a particle gains or looses energy will depend on the relative velocity between the particle and the plasma (ν). Since there is no upper limit to the final energy but only a lower one ($E = 0$), there is however a net gain in the particle energy after many encounters. As the energy gained at each encounter is proportional to $(\nu/c)^2$, this mechanism is called *second order Fermi acceleration*. In many cases it leads to a power law energy spectrum of cosmic rays, but because of the quadratic dependence the process is quite slow and inefficient in comparison to what is needed to sustain the observed cosmic ray spectrum.
A similar stochastic acceleration process is believed to take place in shock-fronts that sweeps through the ISM with a velocity much faster than the speed of sound in the interstellar gas. The principle is very similar to the second order mechanism, but here an energy proportional to ν/c is gained each time the particle crosses the shock front. This mechanism is therefore referred to as *first order Fermi acceleration* (see Fig 1.5). With successive diffusive crossings of the front the calculated spectrum

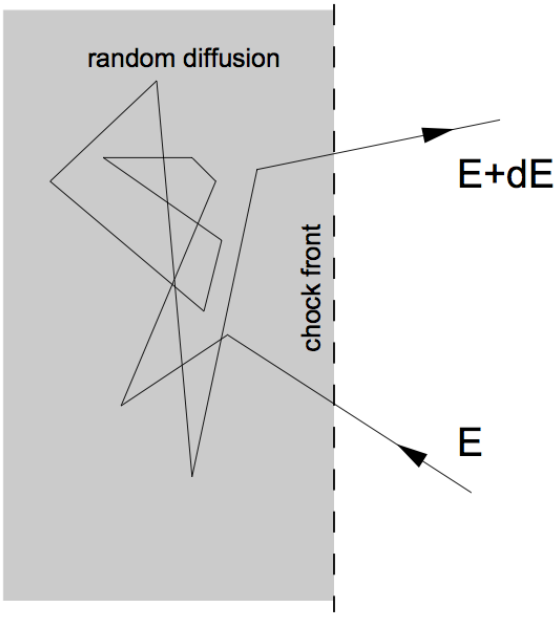

Figure 1.5: Schematic view of "first order" Fermi acceleration. A shock wave moves through the intergalactic medium with velocity v which is much faster than the speed of sound in the interstellar gas. It can be shown that, on average, the energy gained in each crossing (dE) is equal to $(3/4) \cdot E \cdot (v/c)$ [6].

reproduces reasonably well a measured power law spectrum with spectral index around -2. Taking into account that higher energy particles escape the Galaxy more easily, this index can be modified to the observed value of 2.7 [6].

First order Fermi acceleration is believed to be at work in many different types of shocks: the termination shock of the Solar and the Galactic winds, the acceleration shock near a super-massive black hole in the center of our Galaxy and the expanding envelopes of exploded supernovae. With the observed rate of supernova explosions in our Galaxy (approximately one every 50-100 years), only a few percent of the total energy released in a typical explosion ($\sim 10^{56}$J) needs to be transferred to cosmic rays to maintain the observed intensity [18]. The transfer rate of energy from supernovae to cosmic rays is balanced by the total power of the cosmic rays leaving the Galaxy, which is estimated to be of the order of 10^{47}W [19].
The supernova acceleration model works well below the knee, but it can not produce enough GCRs above 10^{18}eV [20]. Moreover, since the gyro-radius in the Galactic magnetic field at $\sim 10^{18}$eV is of the order of the size of the Galactic disk, a transition from Galactic to extra-galactic cosmic rays is expected to occur around this energy. Experimental evidence for such a transition is an important question [21, 22, 24].

1.2.3 Cosmic Ray Propagation

Once produced, cosmic rays propagate through the ISM, experiencing several physical processes: diffusion along magnetic field lines, scattering on magnetic field irregularities, interactions with the interstellar gas and radioactive decays. Cosmic ray propagation models take into account all these processes and attempt to explain the fluxes observed at Earth. Descriptions of two of the most frequently used models, the *Leaky Box Model* and the *Diffusive Halo Model*, are given below.
Both of these models rely on a general transport equation [6]:

$$\begin{aligned}\frac{\partial N_i}{\partial t} &= \nabla \cdot (D_i \nabla N_i) - \frac{\partial}{\partial E}[\frac{dE_i}{dt} N_i(E)] - \nabla \cdot \overline{u} N_i(E) + Q_i(E,t) - p_i N_i \\ &+ \frac{\nu \rho}{m} \Sigma_{K \geq i} \int \frac{d\sigma_{i,k}(E,E')}{dE} N_k(E') dE\end{aligned} \tag{1.7}$$

where $N_i(E,x,t)dE$ is the density of a given nuclear species of type i located at x and with energy between E and $E+dE$. The first term in the right side describes diffusion, D being the diffusion coefficient. The second term is related to the energy gains or losses and the third to convection with velocity u. The fourth is the source term and the fifth takes into account possible losses of nuclei by collision or decay (at rate p). The last term represents cascade and nuclear fragmentation processes (ν is particle velocity, ρ density, m particle mass and σ is the reaction cross-section).

Leaky Box Model

The simplest approach to the solution of the transport equation is the Leaky Box Model. Replacing the diffusion term by $-N/\tau_{esc}$ and neglecting collisions and all the other energy changing processes as well as convection, the solution for a point source is:

$$N(E,t) = N_0 exp(-t/\tau_{esc}) \tag{1.8}$$

in which τ_{esc} is interpreted as the mean time spent by cosmic rays in the Galaxy and consequently $\lambda_{esc} = \rho \beta c \tau_{esc}$, is the mean amount of matter traversed by a particle of βc velocity (ρ being the density of the interstellar gas).
λ_{esc} can be found by fitting the observed ratios of secondary to primary cosmic ray nuclei (e.g. $\overline{p}/p$). Several extensions to the Leaky Box Model have been proposed, which differ widely in the energy dependence of λ_{esc} and in the features of the containment box.
In the leaky box model the particles are evenly distributed in the Galaxy. Cosmic rays diffuse freely in a confinement volume, which could be either the Galactic disk or the halo, and they are reflected at the boundaries. They have constant probability per unit time of escaping into intergalactic space at each encounter with the boundary, governed by the characteristic escape time from the confinement volume.

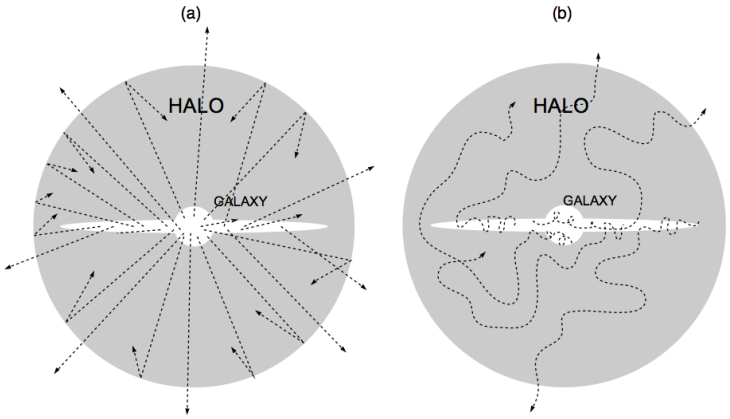

Figure 1.6: Illustration of different models for cosmic ray propagation in the Galaxy. (a) the Leaky Box Model, (b) the Diffusive Halo Model.

Fig. 1.6(a) illustrates the Leaky Box Model.

Diffusive Halo-Model

A completely different approach to the propagation problem is to consider a non-constant diffusion term in the transport equations [25, 26]. In these diffusion models the density of cosmic rays is not homogeneous and the isotropy of the Leaky Box Model is lost. Among them the Diffusion Halo Model (DHM) is the most used. In this model it is assumed that cosmic ray sources are located within the thin Galactic disk. The escape into the halo and eventually into the intergalactic space is driven by diffusion as depicted in Fig. 1.6(b). The velocity of the cosmic rays streaming away from the halo depends on the diffusion coefficient and on the halo size. The Diffusion Models deal with a more realistic physical scenario, while the Leaky Box Models are often preferred since for many purposes the results are equivalent but obtained through simpler calculations.

1.2.4 Local Effects

Solar Modulation

The plasma emitted from the Solar corona is called the *Solar Wind*. It consists of particles accelerated by Solar flares or shock waves driven by coronal mass ejection. The solar wind has speeds of about $\sim$ 350km/h. It reaches out beyond Pluto and carries the Solar magnetic field. This magnetic field in turn deflects low energy particles of extra-Solar origin and prevents them from reaching the Earth. The observed cosmic ray flux at Earth is therefore anti-correlated to the Solar activity. The effects can be seen for cosmic rays up to energies of tens of GeV. In order to estimate the Galactic cosmic ray flux in this region a good knowledge of the effects of the

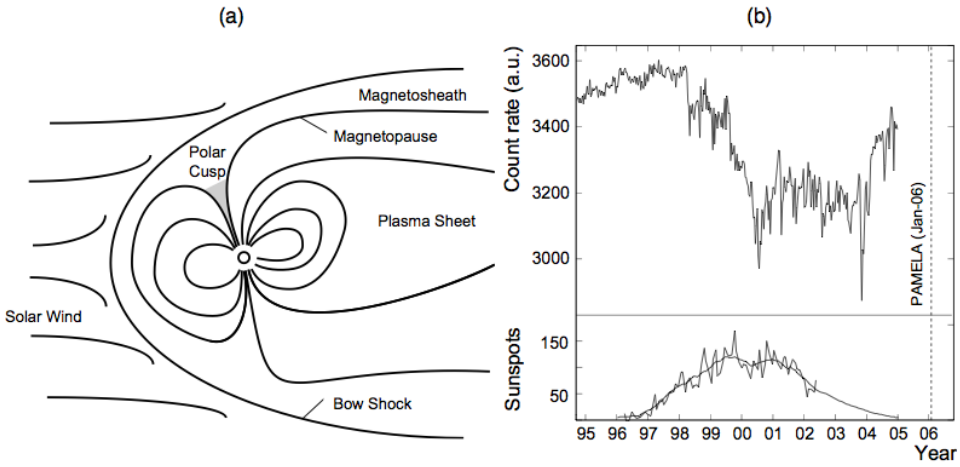

Figure 1.7: (a) The Solar wind forming the heliosphere will prevent some of the cosmic rays from entering the Solar system, (b) the number of observed sun-spots (bottom) and the measured atmospheric neutron flux (top). The anti-correlation between the number of sun-spots and the neutron flux [27] is clearly seen.

Solar activity is required. At energies below $\sim$ 10MeV the cosmic ray spectrum is dominated by solar particles due to this effect.
The Sun's activity shows a periodic behavior with an 11 year time interval. The number of sun-spots is an observable parameter used to monitor the Solar activity. By measuring the cosmic ray spectra over an extended period, information of the interstellar spectra and the effects on particles of different sign of charge (since the Sun reverses magnetic polarity every 11 years) can be collected. The solar activity is anti-correlated to the neutron flux on ground. Neutrons are used as a probe of low energy cosmic ray interactions in the atmosphere (see Fig. 1.7).

Geomagnetic Cut-Off

The radius by which a magnetic field of strength B deflects a charged particle is proportional to R/B and a factor that only depends on the incident angle between the particle's momentum and the direction of the magnetic field. R is the particle's rigidity defined by p/Ze (p being the particle momentum and Ze the charge). Thus, particles with the same rigidity and incident angle follow the same trajectory in a magnetic field.

The geomagnetic field deflects particles approaching Earth from outer space. For a given direction in the sky there is therefore a *cut-off* rigidity needed to overcome the geomagnetic field in order to reach the top of the atmosphere. The full solution of the problem is non trivial. However, the momentum needed for a vertically incident particle to reach the Earth's atmosphere depends on the geomagnetic latitude L_{geo},

and can be estimated by [28]:

$$R \geq \frac{14.9}{e} \cos^4 L_{geo} \qquad [GV] \tag{1.9}$$

(e is the electron charge). This equation takes into account that the cut-off is higher near the equator where the field lines are perpendicular to the motion of the particle, than at the poles where the magnetic field is parallel to the particle trajectory.

1.3 Search for Antimatter in the Cosmic Radiation

1.3.1 Heavy Elements

According to the Big-Bang theory, matter and antimatter should have been created in equal amounts in the first instants of the Universe. Thus, the evident asymmetry between matter and antimatter is a mystery. It has been suggested that this asymmetry is an effect of *CP* violation in combination with out-of-equilibrium expansion of the Universe and baryon number breaking mechanisms. However, the asymmetry could also be spatial in nature, i.e. regions of antimatter could exist alongside regions of matter. According to theories, any region of the Universe dominated by antimatter must be separated from matter dominated regions on the scale of clusters or super-clusters of Galaxies. Otherwise intense gamma radiation would be expected from annihilation processes on the border of between the regions. According to present understanding the electromagnetic interaction of matter and antimatter should be identical (the photon is its own anti-particle), and thus antimatter cannot be identified by optical or radio astronomy observations. The detection of anti-nuclei heavier than $\overline{He}$ would however indicate presence of bulk antimatter in our Universe (e.g. production through fusion in an "anti-star"), while finding $\overline{He}$ could also indicate the existence of primordial antimatter left over from the Big-Bang. No anti-nuclei have been found and the antimatter searches have only been able to set upper limits on the anti helium-helium ratio (Fig. 1.8) [29].

1.3.2 Antiprotons

Anti-protons have been observed in the cosmic rays since 1978 by balloon-borne experiments [26, 30]. Secondary anti-proton production occurs when cosmic ray nuclei undergo inelastic collisions with the constituents of the ISM. In order to produce at least one anti-proton in a proton-proton reaction and at the same time conserve baryon number and charge, a minimum of two additional baryons must be produced. An example is the reaction:

$$p + p \rightarrow p + p + p + \overline{p} \tag{1.10}$$

The production of anti-protons therefore requires high energies. From kinematic constraints, the production threshold is about 7 GeV for the interaction above.

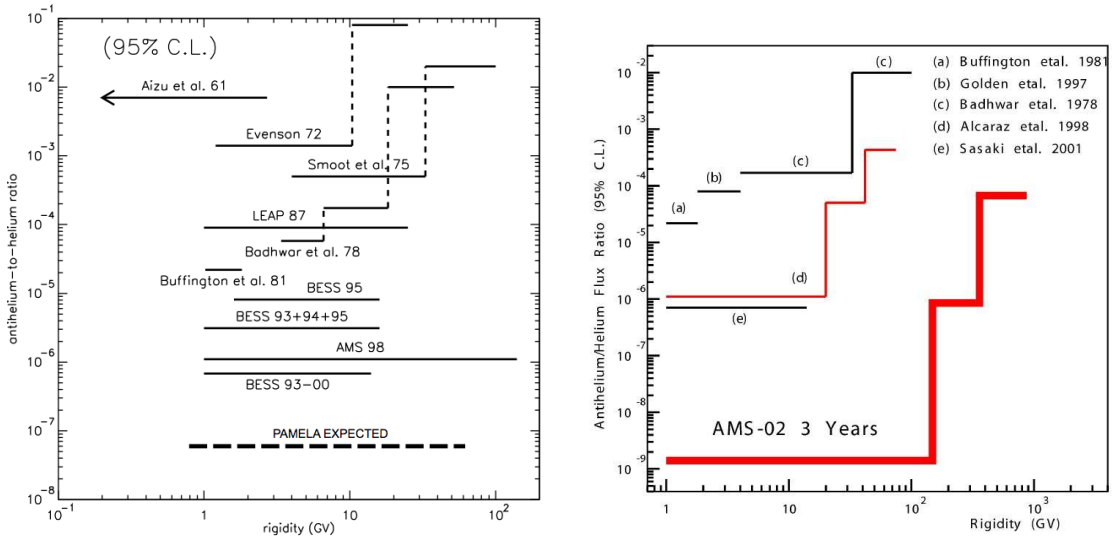

Figure 1.8: The ratio of anti-helium - helium in the cosmic radiation as a function of rigidity (momentum/charge). So far no experiment has been able to detect an anti-helium nuclei and thus only been able to set upper limits. On the right, the AMS-02 expectations are also shown.

One key feature, also due to the kinematics of anti-proton production, is that the anti-proton spectrum produced by such collisions sharply decreases below 1 GeV. This is often referred to as the *kinematic threshold* for anti-proton production. The spectrum of anti-protons has a characteristic shape with a maximum at ~ 2 GeV. This is the only strongly energy dependent production process in cosmic rays and this feature makes the anti-protons spectrum a unique probe of various phenomena. Anti-protons can also be created at lower energies in proton-nuclei or nuclei-nuclei interactions, via so-called "sub-threshold" production [31, 32, 33]. Fig. 1.9 shows the theoretical contributions to the interstellar anti-proton source density spectrum, from various interactions between cosmic ray particles and the ISM.
By measuring the spectral shape it is possible to measure the post-production acceleration or deceleration of the particles. Between 1 and 5 GeV the $\overline{p}/p$ ratio should have a characteristic rise. The shape and position of the rise tells us whether or not there is acceleration of the anti-protons in the ISM after they are produced and if they are produced by collisions in the ISM.

Determination of the energy spectrum of anti-protons is essential for understanding the propagation of cosmic rays as the interaction mean free path for anti-protons in interstellar space is much larger than the matter traversed by cosmic rays in the Galaxy. This is especially important when comparing propagation of light nuclei and anti-protons, since they have different production mechanisms even if they are both produced in collisions between cosmic rays and the ISM. The major difference is that anti-protons are primarily produced by cosmic ray protons while light nuclei are produced by spallation processes and depend strongly on the heavier nuclei

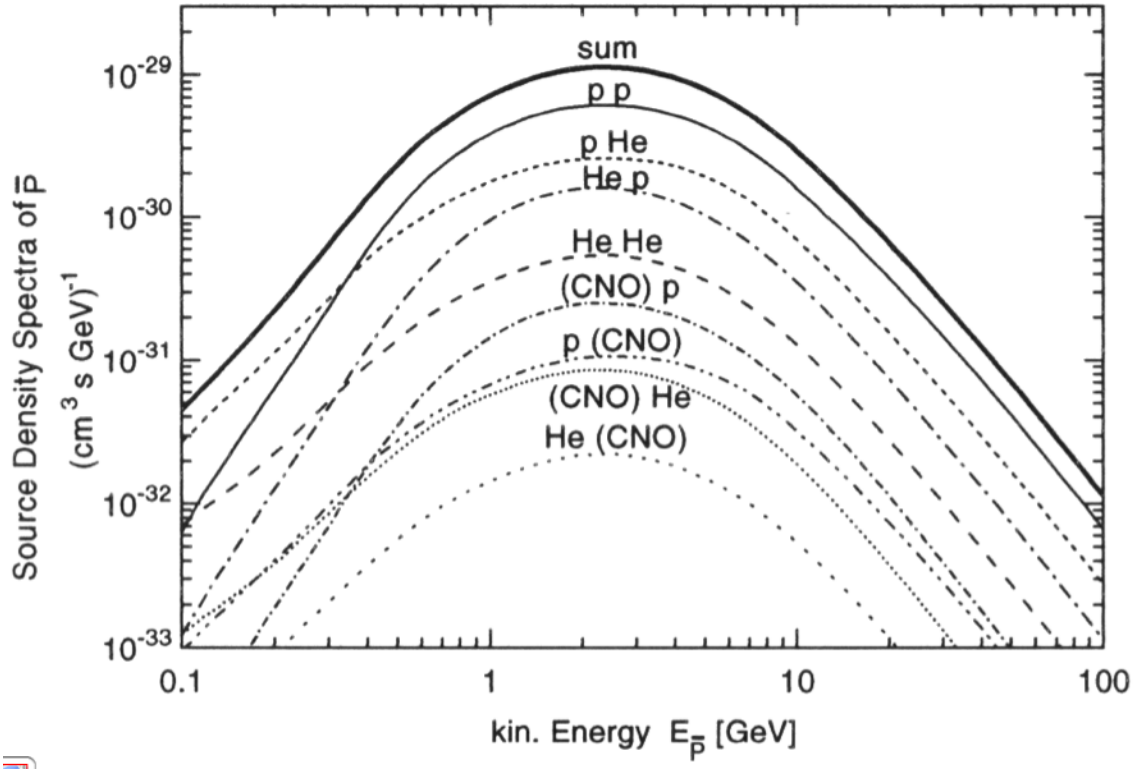

Figure 1.9: The interstellar anti-proton source density spectra resulting from the different interactions between cosmic ray particles and target particles of the interstellar gas [34].

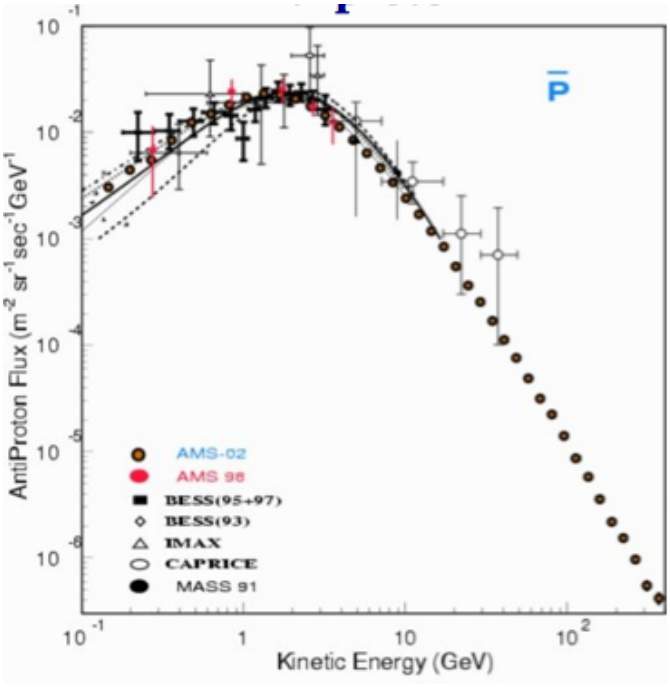

Figure 1.10: The measured anti-proton spectrum and AMS-02 expectations.

abundance and spectrum, which might have a different model of propagation.
"Exotic" *primary* processes for producing anti-protons, like the evaporation of mini black holes [35, 36, 37], or the annihilation of dark matter particles in the Galactic halo [38, 39, 40], have been suggested. One popular candidate for the latter is the lightest supersymmetric particle, the neutralino ($\tilde{\chi}^0$), which is stable due to R-parity conservation in some supersymmetric models. An accurate knowledge of the secondary anti-protons flux is crucial when trying to isolate an exotic primary contribution.

Fig. 1.10 shows a compilation of the current anti-proton measurements together with some theoretical models. The two solid curves are predictions of the interstellar secondary anti-proton flux based on the standard Leaky Box Model using different path lengths. The dashed curve represents a calculation of the secondary anti-proton flux derived from a diffusive model [40, 41] based on proton data from the CAPRICE-94 experiment [42]. The dotted curve is a prediction of the contribution from primary anti-protons produced by heavy neutralino (964 GeV) annihilation [43], which would be detected as a distortion to the secondary spectrum.
An experiment aimed at detecting anti-protons must be capable of charge identification and separation of anti-protons from the high background flux of electrons that decreases from about 10^3 times the anti-proton component at 1 GeV/c to less than 10^2 above 10 GeV/c.

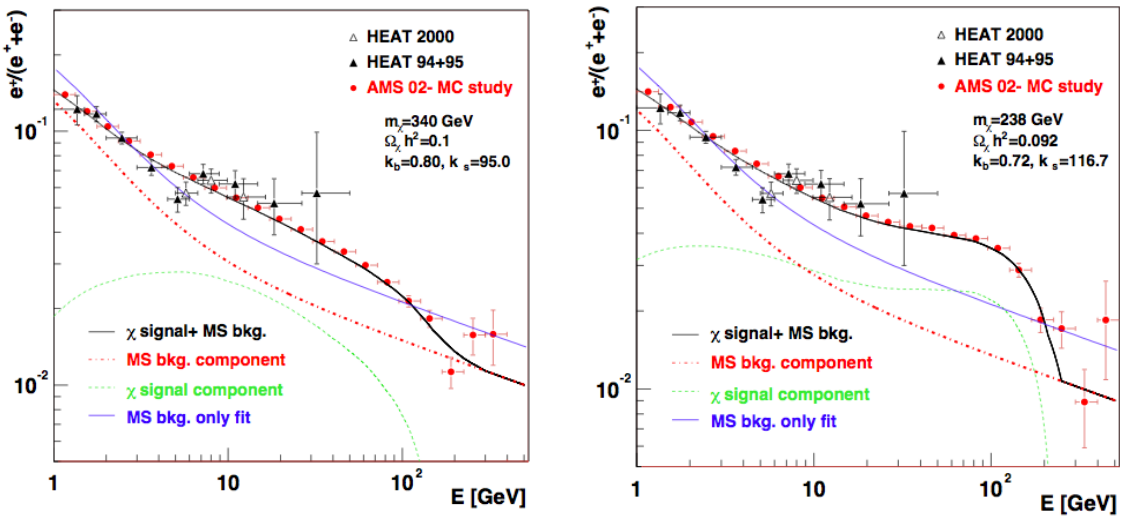

Figure 1.11: The measured positron charge ratio $e^+/(e^+ + e^-)$ and AMS-02 expectations. On the left side positrons primarily from hadronization are considered while on the right hard positron from direct gauge bosons decay are taken into account [23].

1.3.3 Positrons

While most of the observed electrons are believed to be of primary origin, the measured positron component is consistent with a pure secondary production. The main argument for this is that the measured positron fraction $(e^+/(e^+ + e^-))$, is found to be only a few percent. Moreover, the spectral power law index for positrons below 15 GeV is found to be about -3.1 [44] and consistent with secondary production. The theoretical positron energy spectrum can be estimated by starting from the pion and kaon production cross-sections and then applying propagation models which take into account the additional energy losses [45, 46, 47].

In Fig. 1.11 the experimental situation for positrons is shown. The measured positron charge ratio is displayed together with some theoretical predictions. The dashed line is from a calculation based on an older standard Leaky Box Model assuming a purely secondary origin of positrons [45]. The solid line is for secondary production using a diffusive model [46]. The dotted line is a prediction of a primary contribution based on the annihilation of neutralinos with a mass of 336 GeV [48]. Some data show an excess of positrons above the flux expected by the simple Leaky Box Model which may indicate a rise at energies greater than 15 GeV [49] even though the spectrum should be steepening in this region. Thus, clearly the positron spectrum is not understandable in terms of our conventional model for cosmic ray production and propagation.

One possible source of this excess is the annihilation of dark matter particles in

the Galactic halo. Other sources include magnetic pair production at pulsars and pair-production by gamma rays interacting with optical or ultraviolet photons [50]. Observation of positrons over a very large energy range should yield new insights into Galactic processes.

A difficulty in detecting positrons lies, as for anti-protons, in the charge identification and that the positrons have to be well separated from protons. The ratio between protons and positrons lies between 10^3 at 1 GeV/c and about 5×10^3 at 10 GeV/c and a reliable positron identification therefore requires a proton rejection factor greater than 10^4.

1.3.4 The Future

All data in Fig. 1.10 and Fig. 1.11 are consistent with a purely secondary origin for both anti-protons and positrons. However, most of the data comes from high altitude balloon experiments which are limited in statistics due to data collection times of $1 \div 2$ days. Therefore the steepness of the anti-proton and positron spectra at higher energies has so far limited the measurements to below $\sim$ 50 GeV. The balloon experiments also have to take into account the interactions occurring in the residual atmosphere ($\sim 5 g/cm^2$) above the experiments by estimations derived from simulations, which increase the systematic errors on the data points.

1.4 Dark Matter properties

Under the name of cold "Dark Matter" (DM) can be generally described any non relativistic component of the Universe which does not emit enough light to be detected. This would allow ordinary matter with low emission to account for *DM*, and indeed the presence of cold hydrogen gas in the halo has been suggested. However such gas should have reached hydrostatic equilibrium during the age of the galaxies and the equation of state combined to the gravitational potential, gives for the temperature [51]:

$$T = \frac{G M_P M(r)}{4k\pi} \cong 1.3 \times 10^6 K \tag{1.11}$$

where $M(r)$ is the mass contained within the distance r from the center of the gas cloud, G is the Newton constant of gravitation, k the Boltzmann constant and M_P is the Planck mass. This is not cold gas and would be detectable through X-ray emission.
Other possible sources of ordinary (i.e. baryonic) *DM*, are the so called *MACHOs* (Massive Compact Halo Objects), essentially remnants of late stages in star evolution, like white dwarfs, neutron stars and black holes, or forming stars that have not enough mass to ignite the nuclear reactions (brown dwarf/Jupiter-like objects). Searches for these candidates in our galaxy halo have been performed by different

collaborations (MACHO [52], EROS [53], OGLE [54]) using their gravitational lensing effect as a probe. Some tens of MACHOs were found with masses up to 0.1 to $0.4M_{sun}$, but they can only account for a maximum of 20% of the halo mass [55].
Though a part of existing *DM* is constituted by ordinary baryons, Big Bang Nucleosynthesis, Cosmic Microwave Background and Galaxy Red Shift Surveys data, show that the baryon contribution to the Universe energy density cannot exceed $\Omega_{bar} \approx 0.04$ while $\Omega_{mat} \cong 0.3$, so the main constituent of Dark Matter must belong to a non baryonic particle species, whose interaction other than gravitational with ordinary matter is ruled by the weak force, otherwise we would have observed it long ago.
This implies that they fell out of the thermal equilibrium condition at some time and now constitute a relic population distributed throughout the Universe.
To ensure that these relic particles survive until the present, without decaying into something that couples to photons, they must also be stable, or at least have a lifetime that is comparable to the age of the Universe.

1.4.1 Non baryonic Dark Matter

Several candidates for the role of non baryonic *DM* have been proposed over time, including primordial black holes (i.e. formed before the Big Bang Nucleosynthesis), massive neutrinos, axions and Weakly InteractingMassive Particles (*WIMPs*).
Primordial black holes require particular initial conditions for the cosmological model involved [56], and will not be treated here, but we will concentrate on the other three.

Neutrinos

Among the known neutral particles, only neutrinos are both weakly interacting and non baryonic; we also know them to be present as a relic background analogous to the Cosmic Microwave Background.
If neutrinos have a mass, as experiments on ν oscillation suggest [57, 58], their contribution to the energy density can be calculated as:

$$\Omega_\nu = \frac{\Sigma m_\nu}{94eV} h^{-2} \tag{1.12}$$

Oscillation experiments do not tell us the absolute neutrino masses, but only the squared mass difference between flavors, however the measured values ($\Delta \sim O(10^{-3}eV^2)$) suggest a lower limit of $\Omega_\nu \approx 0.001$ on the neutrino mass density parameter for $m = O(\Delta)$. If the neutrino masses are significantly larger than their differences, the contribution to Ω_{tot} could rise, however the results on tritium limits the sum of the masses of active neutrinos in the range 0.05 to 8.4eV, which yields an upper limit of $\Omega_\nu \approx 0.18$.
Particles that decouple from the primordial thermal bath while remaining relativistic (hot) like neutrinos do, damp the growth of perturbations so, for a total ν mass as small as 0.1eV this could have a potentially observable effect on the formation of structure [58].

Present cosmological observations (WMAP [60] plus 2dFGRS [59] data) have shown no convincing evidence of any effects from either neutrino masses or an otherwise non-standard neutrino sector, and impose more stringent upper limits ($\Omega_\nu < 0.013$ to 0.015 [61, 62]). Moreover, structure formation data rule out the possibility of Hot Dark Matter as the dominant component of Ω_{mat}, so *DM* particles must be cold ones.

Axions

A possible Cold Dark Matter (CDM) candidate is the *axion*: a particle introduced to solve the Strong *CP* problem, connected to the *CP* violating term of the *QCD* Lagrangian:

$$\mathcal{L}_{CP} = \Theta \frac{g^2}{32\pi^2} G^a_{\mu\nu} \tilde{G'}^{\mu\nu}_a \tag{1.13}$$

where $G^a_{\mu\nu}$ and $\tilde{G}^{a\mu\nu}$ are the gluon field strength and its dual, respectively, g is the weak coupling constant and Θ is a dimensionless parameter, whose value sets the magnitude of the effective term Eq. 1.13 of the Lagrangian.
The axion is a pseudo Nambu-Goldstone boson of the spontaneously broken Peccei-Quinn symmetry [63]. When the symmetry breaks the axions acquire an effective coupling to gluons that cancels the Θ parameter of equation Eq. 1.13, thus solving the problem.
Since axions are not produced thermally in the primordial plasma, they can be counted as *CDM* whatever their mass. In particular if $m_a \sim 10\mu$eV they could be the dominant component of *DM*. The cosmologically relevant mass range is explored by the experiments based on axion-photon interaction: in particular LLNL [64, 65] that currently excludes $m_a = 2.9$ to 3.3μeV and CARRACK [66, 67] which is being upgraded to probe the range 2 to 50μeV.

1.4.2 Weakly Interacting Massive Particles

Under the name of *WIMPs* are classified neutral particles other than neutrinos and axions that have the characteristics to make a good *DM* candidate we have met throughout our discussion; namely they are:

- non baryonic,
- long lived with respect to Universe age or stable,
- present as a relic population,
- massive (typically $m_\chi = 10GeV \div 1TeV$) hence,
- non relativistic at decoupling (CDM) and,
- their cross sections are approximately of order of the weak strength.

The relic energy density of *WIMPs* can be evaluated as [68]:

$$\Omega_\chi = \frac{T_0^3}{M_P^3 < \sigma_A v >} \cong \frac{0.1pb \cdot c}{< \sigma_A v >} \tag{1.14}$$

where M_P is the Planck mass, c the speed of light, T_0 the present day temperature of CMB, σ_A is the total annihilation cross section of a pair of *WIMPs* into SM particles and v their relative velocity. The angle brackets $< >$ denote thermal average. If the cross section is of the typical order for weak interactions, equation Eq. 1.14 yields a possibly dominant contribution to Ω_{mat}.

Supersymmetric WIMPs

Particles of this kind appear naturally in the context of Supersymmetric extensions to the Standard Model of particle physics. All SUSY models are based on the assumption that in nature exists an additional symmetry that connects fermions to boson partners of the same mass and vice versa: this allows for example to solve the scalar mass hierarchy problem, since the contribution of the partner particles to the Higgs mass correction have opposite signs and cancel each other [69].
When the symmetry is broken at some scale λ_{SUSY} the partner masses are no more equal and the cancellation is no more exact, so the Higgs fields mass acquire a radiative correction term of the order of the breaking scale: it follows that $\lambda_{SUSY} \sim O(TeV)$.
Even if we consider the minimal Supersymmetric extension to the Standard Model, i.e. the one where only strictly necessary additions are made (for instance two Higgs doublets are required), new interaction channels involving both particles and superpartners are opened. One such channel implies so small a lifetime for the proton that it should have disappeared from the Universe by now.
To overcome this difficulty, a discrete symmetry called *R-parity* was introduced in the theory; the corresponding multiplicative quantum number called R, is defined in terms of the particle spin, lepton number and baryon through the relation $R = (-1)^{3B+L+2S}$, that implies $R = 1$ for ordinary particles and $R = -1$ for the super-partners. If *R-parity* is a conserved quantity, Supersymmetric particles (also called *sparticles*), are forbidden to decay into ordinary ones, so the Lightest Supersymmetric Particle (LSP), is bound to be stable.
Moreover these stable particles cannot carry charge nor color, otherwise they would bind to ordinary matter producing anomalous isotopic masses [70], which is excluded by quite stringent experimental constraints [71].
The identity of the LSP depends on the parameters of the theory, but the most quoted one is the *neutralino*, linear combination of the $R = -1$ neutral sfermions [70], superpartners of the neutral electroweak gauge bosons W_3 and B and of the two neutral Higgs states, namely the wino $\tilde{W}$, the bino $\tilde{B}$, and the higgsinos $\tilde{H_{1,2}}$:

$$\chi = \alpha\tilde{W_3} + \beta\tilde{B} + \gamma\tilde{H_1^0} + \delta\tilde{H_2^0} \tag{1.15}$$

Depending on the value of the quantity $P = \alpha^2 + \beta^2$ it is further classified as gaugino ($P > 0.9$), higgsino ($P < 0.1$) or mixed [72]. Another property of the neutralino is

that $\chi = \overline{\chi}$, i.e. is a Majorana fermion.
Although the exact nature of the neutralino depends on the particular SUSY implementation, it is possible to find for each model a region of the parameter space that is consistent with a relic neutralino density consistent with cosmological observations.

1.4.3 WIMP Dark Matter Searches

The techniques to search for *WIMPs* fall essentially in two categories: direct detection, based on the measurement of the interaction of the *WIMP* with ordinary matter, and indirect detection that looks for the products of *WIMP* pair annihilation. In both cases the uncertainty in the *DM* density and velocity distribution affect the calculation of the expected signal rate. In particular, an higher density due to a cusp toward the galactic center or a clumpy distribution in the halo, as favored by numerical simulations [73] would increase the annihilation rate allowing indirect detection in a wider range of SUSY models while the velocity distribution uncertainties, though important for annihilation calculations too, mostly affect the direct search experiments [74].

Direct searches

Direct searches essentially look for the recoil of target nuclei due to interaction with the *WIMP*; natural radioactivity is a major noise source so the typical direct search experiment is performed in underground laboratories and requires the use of materials devoid of radioactive isotopes to a high degree and the weakness of the interaction forces to use large amounts of target material.
The experimental signatures of *WIMP* detection, that would prove its cosmological origin are the daily and annual modulations of the signal due to the Earth motion. Several experiments are being performed along these lines with different recoil detection techniques [75] among them the DAMA experiment that uses a 100kg NaI(Tl) target in the Gran Sasso laboratory has observed with a statistical significance of 6.3σ an annually modulated signal with the expected phase [78] over a 7 years observation period attributed to a *WIMP* signal by the collaboration. However the results of EDELWEISS [76] exclude the DAMA [77] result with a C.L. of 99.8%. Extended versions of current experiments are planned to further investigate on the subject (e.g. LIBRA [75]).

Indirect searches

Though *WIMPs* must be stable, nothing prevents them from annihilating with their anti-particle; indirect searches look for the annihilation products in the CR in order to detect an excess with respect to the abundance predicted by known production processes.
In the case of neutralino particle and anti-particle coincide and may annihilate into quarks ($\chi\chi \to q\overline{q}$), leptons ($\chi\chi \to \ell\overline{\ell}$), gauge bosons ($\chi\chi \to W^+W^-, Z^0Z^0$), Higgs bosons ($\chi\chi \to Z^0H^0_{1,2}, H^0_1H^0_2, ...$) and gluons ($\chi\chi \to gg$). These in turn decay or hadronize leading to final states containing e^+, $\overline{p}$, γ and ν [72].

Neutrinos

Neutralinos trapped into the core of celestial objects such as the bulge of the Galaxy, the Sun or even the Earth by gravity [79] would provide a typical signature in the neutrino channel. Among the final annihilation products, only neutrinos would be able to escape and the excess flux would be observed in a precise direction. Current neutrino experiments have put limits to the ν_μ flux due to this mechanism that tend to exclude the portion of parameter space favored by DAMA [80].

Gammas

The most distinctive feature of the γ-ray spectrum that can be observed as a consequence of neutralino annihilation is certainly the presence of sharp spectral lines. The loop-induced annihilation processes $\chi\chi \to \gamma\gamma$ and $\chi\chi \to Z\gamma$ [81] should produce mono-energetic photons, since the neutralinos involved in the process may be considered almost at rest. The energy of the photons is then calculated to be $E_\gamma = m_\chi$ and $E_\gamma = m_\chi(1 - m_Z^2/4m_\chi^2)$ respectively.
The rates of these processes are difficult to estimate because of uncertainties in the supersymmetric parameters, cross sections and halo density profile. However, in contrast to the other proposed detection methods they have the virtue of giving a direct measurement of the neutralino mass.
In practice the monochromatic spectral lines will suffer a smearing due to red-shift that can turn them into features of the continuum annihilation spectrum. As red-shift only stretches the observed wavelength of the photons, the smear is asymmetric and looks like a cutoff at about the value of the neutralino mass for $\chi\chi \to \gamma\gamma$ [81].
A second signature may be found in the continuum γ-ray spectrum, though less dramatic, in the form of a smooth bump at about one tenth of the neutralino mass. This signal is very low if compared with the flux measured by EGRET [83] (about 5 orders of magnitude), though these is the possibility that the bulk of EGRET flux may be due to unresolved AGNs. In this case AMS-02 [110], the GLAST [84] satellite or one of the air Cerenkov telescopes (e.g. VERITAS) [85], that will explore a quite complementary energy range would have good chances to pick up this kind of signal. Moreover it is possible that clumsy distributions of *DM* enhance the signal itself.

Anti-deuterons

Anti-deuterons are produced when an anti-proton and an anti-neutron produced in spallation processes in the Inter Stellar Medium (ISM) merge. The two anti-nucleons must be at rest with respect to each for fusion to take place, however, for kinematic reasons, a spallation reaction creates very few low-energy particles and low-energy secondary anti-deuterons are even further suppressed. The corresponding interstellar flux reaches at maximum (2 to 5) $\times 10^{-8} m^{-2} s^{-1} sr^{-1} GeV^{-1}$ for a kinetic energy of 4 GeV [86].
On the other hand, supersymmetric $\overline{D}$ are produced practically at rest with respect to the Galaxy since in neutralino annihilation, anti-nucleons are predominantly pro-

duced with low energies. This feature is further enhanced by their subsequent fusion into anti-deuterons. Below a few GeV/n, secondary anti-deuterons are quite suppressed with respect to their supersymmetric produced counterparts. This makes CR anti-deuterons a possible probe of supersymmetric *DM* capable to explore a significant portion of the supersymmetric parameter space.

Positrons

The CR also have a leptonic component made of electrons and positrons. The spectra of these particles have specific features, that come from energy losses due to electromagnetic interaction. In fact the dominant process that electrons and positrons undergo while propagating in the ISM, is *bremsstrahlung*, with contributions from ionisation interactions with the ISM itself under a few GeV and inverse Compton scattering with the CMB at higher energies. The net effect of those interactions is to decrease the electrons energy, so they concentrate at low energies and the spectrum is therefore much steeper than for hadronic CR [87].
Past experiments have measured the combined $e^{\pm}$ energy spectrum up to the TeV region [88, 89, 90, 91], showing that their intensity is about 1% of the proton one at 10 GeV and then decreases with energy according to a power law $E^{-\alpha}$ with spectral index $\alpha > 3.0$, higher than the ≈ 2.7 for protons.
The bulk of electrons is of primary origin, however there exists a secondary population of both electrons and positrons, which are produced in the interaction of Cosmic Rays with the ISM through the pion decay chain $\pi \rightarrow \mu \rightarrow e$. The measured value of the positron fraction $e^+/(e^+ + e^-)$ is of order 0.1 in the 1 to 10 GeV region.
An additional component of secondary positrons may be the result of the decay chains or hadronizations due to χ annihilation products. The actual shape of the spectrum depends on the preferred decay mode of the neutralino. If χ most of the times annihilates to $q\overline{q}$, the subsequent jets will broaden the energy spectrum of the final e^+s; if on the other hand the preferred annihilation channel is to W^+W^-, the positron spectrum will feature two peaks: the first corresponding to $m_\chi/2$, produced by direct $W^+ \rightarrow e^+$ decay, and the second, at lower and wider energy, from W decay into other leptons ($W^+ \rightarrow \tau^+(\mu^+) \rightarrow e^-$) and a contribution from the quark jets ($W^+ \rightarrow q \rightarrow \pi^+ \rightarrow e^+$) [48], omitting neutrinos.
Among the best results achieved by balloon-borne experiments are those of CAPRICE that determined the absolute positron flux in the interval 0.4 to 50 GeV [92, 93] and HEAT, that operated in a range 1.2 to 100 GeV in two successive flights [49, 94, 95]. Both are shown in Fig. 1.12 along with three possible Super-Symmetric (SUSY) positron spectra [96]. Measurements with higher statistics and over a wider energy range are required to better check the CR propagation models and to further investigate the existence of a primary neutralino-induced e^+ component.

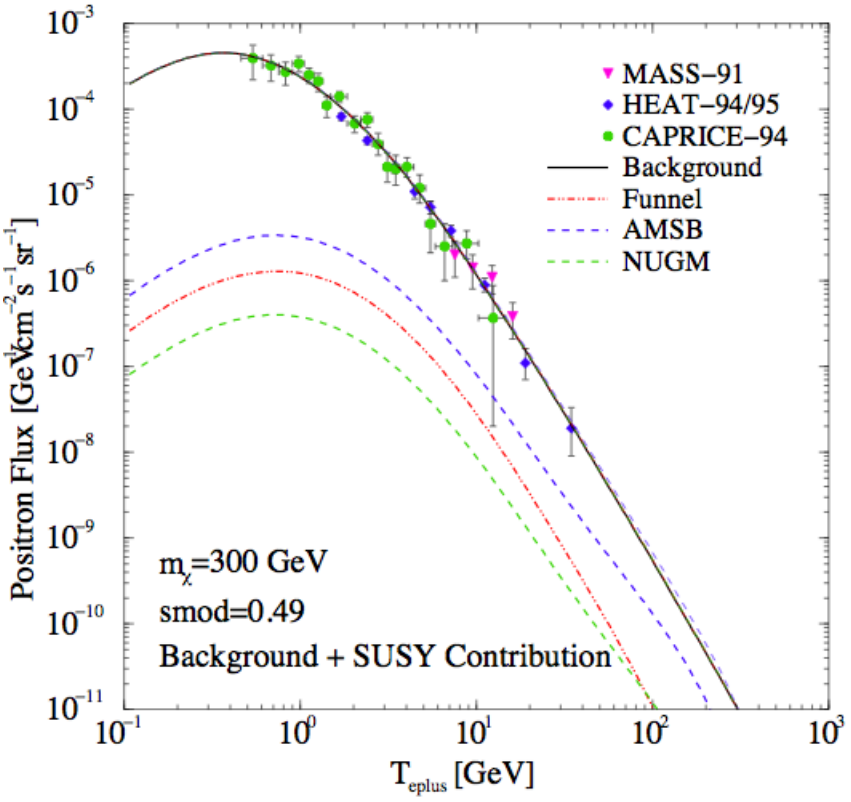

Figure 1.12: The solar modulated positron flux, as a function of the positron kinetic energy T_{e^+}. The black line corresponds to the calculated background, while the three colored lines to the signal for three particular SUSY models at a mass m_χ = 300 GeV [96]. The positron data from MASS [97], HEAT [94] and CAPRICE [92] are also shown.

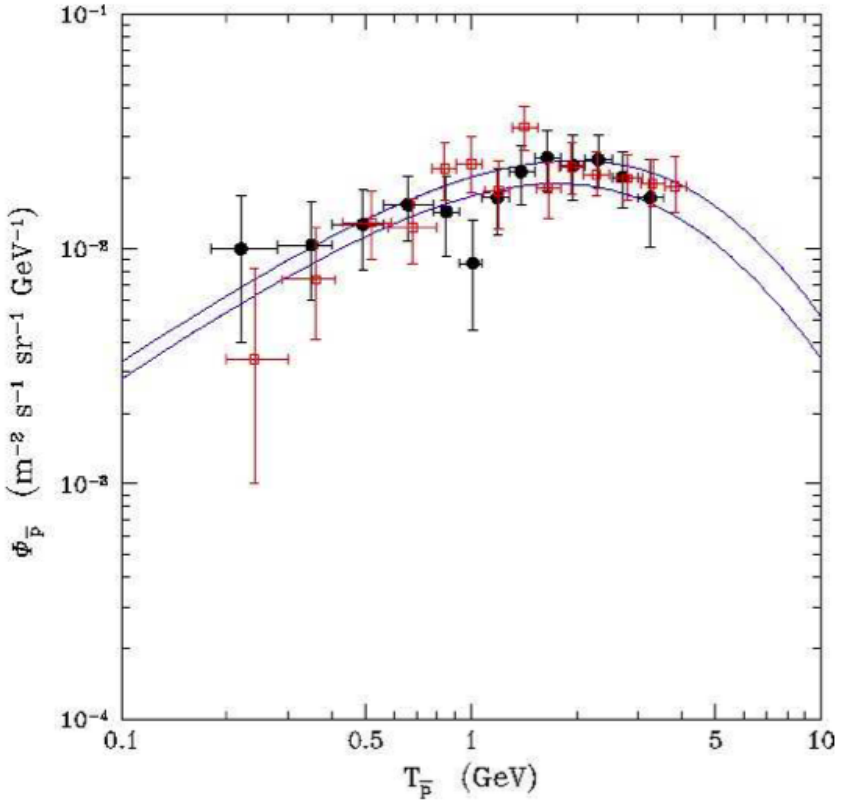

Figure 1.13: This plot from [104] shows the envelope of the top of atmosphere anti-proton spectra generated with the sets of diffusion parameters consistent with B/C ratio data in the framework of the Leaky Box propagation model. Data points are taken from BESS 95+97 [105, 106] (filled circles) and from BESS98 [107] (empty squares).

Anti-protons

The primary CR are mainly constituted by protons (∼90%) and helium nuclei (∼9%), with smaller components of heavier nuclei, electrons, positrons and anti-protons [6]. In particular, anti-protons are expected to be of secondary origin, i.e. produced in collision processes of the type $pp \rightarrow \overline{p}X$ in the ISM.
The first reports of the detection of CR anti-protons were published in 1979 by Golden and Bogomolov [98]. Shortly after these measurements, Buffington, Schindler and Pennypacker [99, 100] measured an unexpected large flux of $\overline{p}$ in the few hundred MeV kinetic energy range.
Subsequent measurements made at these low energies failed to verify this claim (PBAR [101, 102] and LEAP [103] experiments). The observed fluxes were approximately one decade below the Buffington's data level, and were near below the lower limit of sensitivity for these instruments.

In fact, the typical theoretical spectrum for $\overline{p}$ production in the ISM features a peak

at about 2 GeV (Fig. 1.13), that drops off on either side due to the process threshold at low energies ($E \geq 7m_p$) and to the steepness of the proton spectrum [108] at high energies. On the other hand, in neutralino annihilation events, the interacting particles are almost at rest and the produced anti-protons come from hadronization of those particles that were directly produced in the interaction. As such, SUSY $\overline{p}$ are expected to carry only a fraction of the total involved energy thus producing a detectable deformation in the $\overline{p}$ spectrum at low energy (Fig. 1.13).
A new generation of experiments was then designed, with greater sensitivity and enhanced particle identification capabilities, that started to get more accurate measurements in the nineties; in particular the balloon-borne experiments BESS and CAPRICE, and the space experiments such as PAMELA [109] and AMS [110].
Since the first flight in July 1993 [111] to the one performed during the recent solar minimum period [107, 106], BESS has identified hundreds of anti-protons in the range 0.18 to 4.20 GeV; CAPRICE on the other hand performed measurements at energies both lower [112] and higher [113] than $\sim$ 5 GeV up to $\sim$ 50 GeV (with modifications of the experimental apparatus between flights).

These experiments detected the distinctive peak at 2 GeV, thus confirming the secondary origin of most cosmic anti-protons, but the errors on the measurements (Fig. 1.14) are still too large to disentangle potential primary (*DM*) anti-protons from the secondary ones (spallation processes).
The evaluation of the *DM* induced contribution to the anti-proton flux is at present a field of active theoretical research that presents several difficulties on both aspects of background characterization and signal modelisation.
On the side of the background, the main problem is represented by the limited knowledge of the CR propagation mechanism, that determines the details of the $\overline{p}$ producing interactions between primary protons, hence their spectral features.
For instance it has been suggested [82] that, in p-nucleus interaction, the production of $\overline{p}$ is possible even when the impinging p has energy below the threshold of the process due to collective nuclear effects. This would enhance the low energy region of the spectrum (even more so if the produced $\overline{p}$ looses energy in escaping the target nucleus).
The consequent flattening of the low energy spectrum would then drown the χ annihilation signal and the anti-proton flux and $p\overline{p}$ ratio resulting from experiments would be consistent with secondary production during CR propagation through the Galaxy.
More accurate measurements of the secondary CR fluxes are necessary to refine these models. Apart from a direct observation of $\overline{p}$ and e^+ fluxes, most useful information may be gathered independently from the determination of the abundances of spallation products relative to that of the original nuclei (e.g B/C) and from the unstable to stable isotope fraction of elements (e.g. $^{10}Be/^{9}Be$), that are critically influenced by the propagation mechanism.
On the other hand, the signal itself is not univocally determined, since different SUSY breaking mechanisms produce neutralinos with different weights of the bino ($\tilde{B}$), wino ($\tilde{W}$) and higgsino ($\tilde{H}^0$) components which implies different annihilation

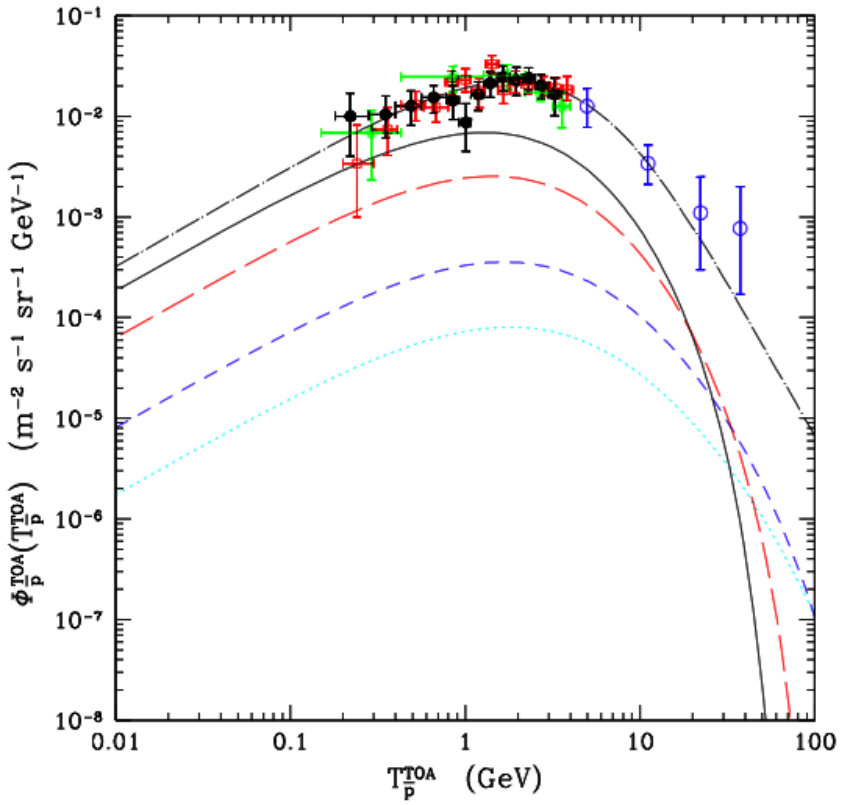

Figure 1.14: Primary top of atmosphere anti-proton fluxes as a function of the anti-proton kinetic energy, in the eMSSM [114]. The solid line refers to m_χ = 60 GeV, the long-dashed line to m_χ = 300 GeV, the dotted line to m_χ = 500. The astrophysical parameters correspond to a median choice. Solar modulation is calculated for a period of minimal solar activity. The upper dot-dashed curve corresponds to the anti-proton secondary flux [104]. The markers are results from BESS95-97 (full circles [107]), CAPRICE (empty circles [113]) and the precursor flight of AMS (stars [115]).

.

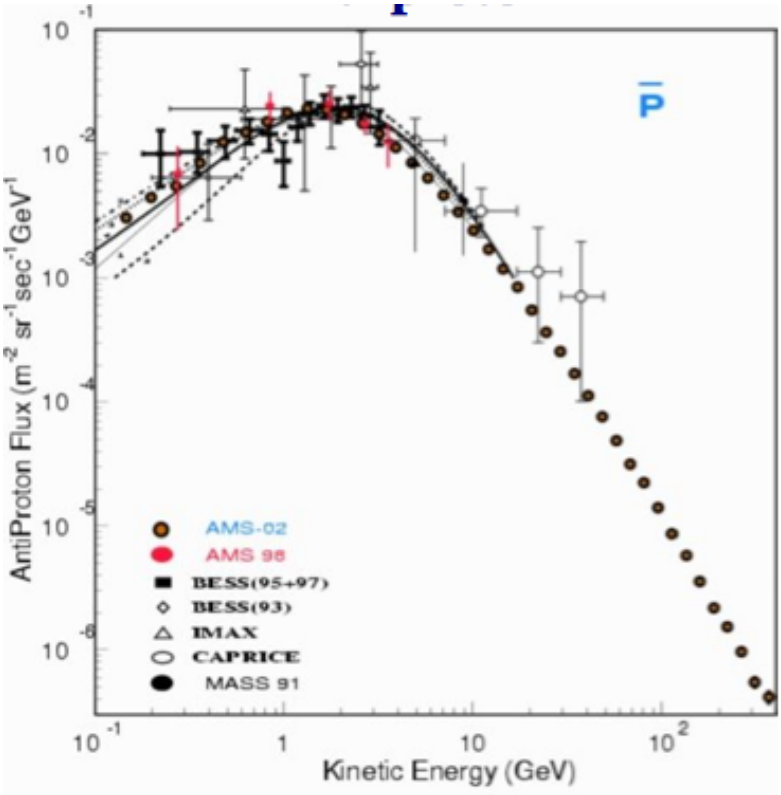

Figure 1.15: The Solar modulated anti-proton flux, as a function of kinetic energy. The black line corresponds to the calculated background, the three colored thick lines to the total signal for the three SUSY models at mass $m_\chi = 300$ GeV. The thin lines correspond to the SUSY contributions alone. The data from BESS [107] and CAPRICE-98 [113] are also shown.

cross sections and branching ratios. Even within models of the same class, different choices of the various parameters would produce neutralinos of different masses, which also alters the signal spectrum. In Fig. 1.14 SUSY induced $\overline{p}$ fluxes are reported for different values of m_χ.
Moreover, the density profile of *DM* in the Galaxy is not fully understood at present. Different assumptions on the density profile lead to significant variations of the corresponding signal flux. For instance a cuspy χ distribution towards the galactic center could enhance the SUSY $\overline{p}$ flux by $\sim$30%. Such enhanced fluxes can then be observed even at energies above a few GeV as a $\sim$10% contribution to the total flux. Such a signal is however comparable to the uncertainties introduced by the propagation models [104] used in the calculation.
Although a comprehensive analysis of the problem is unfeasible, given the number of involved parameters, it is possible to develop a consistent picture of both signal and background by applying a set of conservative assumptions and then coherently developing the calculations.

Model	Bino fraction	Wino fraction	Higgsino fraction
Funnel	$> 99.6\%$	$< 0.05\%$	$< 0.05\%$
AMSB	$< 0.02\%$	$> 98\%$ for $m_\chi > 100$ GeV	$> 2\%$ for $m_\chi > 100$ GeV
NUGM	$< 0.01\%$	$< 0.2\%$	99.8%

Table 1.1: The lightest neutralino composition for the three SUSY models in term of the bino, wino and higgsino fractions.

An example of this procedure are the top of atmosphere (TOA) signals reported in Fig. 1.15 [96]. The colored lines correspond to three SUSY scenarios characterized by different Super-Symmetry breaking mechanisms. On the same plot are also reported the available experimental data from BESS [107] and CAPRICE-98 [113].

The three schemes produce neutralino realizations in which one of the components is largely dominant over the other as detailed in Tab. 1.1, and are therefore suitable to be used as benchmarks to evaluate the visibility of SUSY signals.
The fluxes were obtained by simulating the production process with the PYTHIA [116] Montecarlo package giving as input the corresponding cross sections; the SUSY parameters were chosen respecting the present constraints from accelerator data and the displayed curves in Fig. 1.15 refer to the specific case of neutralino mass $m_\chi = 300$ GeV.
The neutralino density distribution in the galaxy was described by the so-called Burkert profile [117]:

$$\rho_B(r) = \frac{\rho_B^0}{(1 + r/a)(1 + (r/a)^2)} \tag{1.16}$$

with the length scale parameter $a = 11.7$ kpc, that assumes a quite conservative density increase towards the galactic center.
The resulting cosmic spectra were then propagated to the Top of Atmosphere by means of the Galprop code [118], including the effects of solar modulation implementing the one parameter model based on the analytical force-field approximation by Gleeson&Axford [119] for spherically symmetric model.
In all the above cases, an antiparticle signal from a SUSY model would be extremely small and practically unobservable.

Chapter 2

Gamma Astrophysics

Nowadays, the gamma astronomy is a very exciting field of research. Due to that, more and more performant detectors have been and are built. Those instruments improve our knowledge on the astrophysics objects making observations both from the ground and from space. In fact, the energy is the crucial factor which distinguishes these two approaches. The Earth atmosphere plays a role as a filter to prevent gamma rays to reach us. The interaction of those photons with the atmosphere produces a light (of fluorescence or by Čerenkov effect) proportional to their energies: the higher is the incoming photon energy the bigger will be the number of generated secondary particles. As a consequence, ground detectors are devoted to the study of very high energy photons, typically more than 100 GeV, while flight detector can access energies less than 1 TeV.
Another factor to be taken into account is the primary cosmic ray flux which decreases as the energy grows. In fact at 10 GeV, this flux is about 8 particles per squared meter and second while at 10 EeV it is 0.6 particles per squared kilometer, sr and century. Again this implies different choices on the detector applications. In space, small detectors are used as a compromise between their cost and the particle flux. On the ground, cheaper and larger detectors make up for a lower particle flux. The timeline of the past, current and future experiments relevant for gamma astrophysics is shown in Fig 2.1 while their sensitivity as a function of the photon energy is presented in Fig. 2.2.

2.1 The Gamma Ray Universe

Whenever charged particles are accelarated they emit photons. Thanks to the development of highly sensitive detectors and the possibility to operate them at increasing higher altitude, in the past century the sky observation has been extended to all frequencies of the electromagnetic spectrum. In particular, in the gamma energy range (the most wide, extending above 500 keV, i.e. frequency $\nu \geq 3 \times 10^{19} Hz$) the Universe appears extremely violent and rapidly changing. This was the discovery that revolutionized both the modern astronomy and the notion of a relatively stable Universe. Because of their relatively small interaction cross-sections, γ-rays can provide a direct view into highest-energy processes. Produced at distant sources,

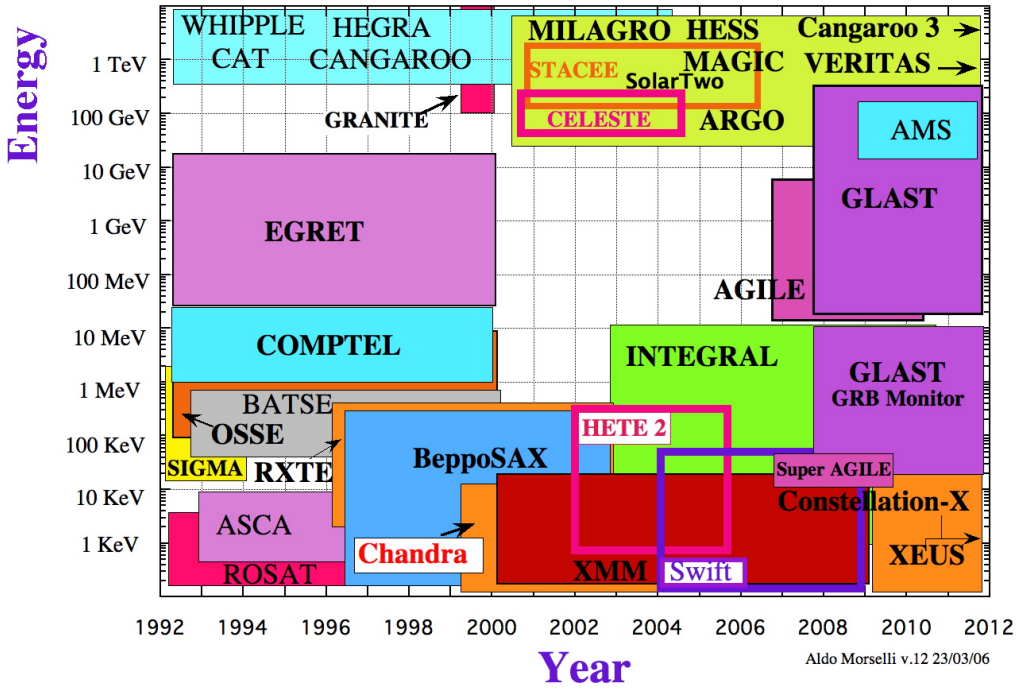

Figure 2.1: Timeline of the past,current and future experiments for gamma ray astrophysics.

the high energy photons travel through the central plane of galaxy with only 1 % probability of being absorbed. The high energy domain embraces astrophysics, astronomy and particle physics: the astronomical observations allow to reach the large scale application of basic physical laws. The main processes that can generate γ-rays involve acceleration of charged particles to high energy and their interaction with the surrounding medium and magnetic field where they are produced or injected. However the increased interest and the effort in new high-performance missions is mainly due to the unsolved emission processes that could explain many discovered galactic and extra-galactic sources.

2.2 Gamma Ray Astronomy

The γ region of the cosmic electromagnetic radiation has been the last explored. In fact in the past decades the development of technologies for space-based instruments gave a boost to our knowledge of the high energy Universe. Most of the pioneering work in the γ-ray astronomy has been made by balloon instruments [120] while nearly all historical discoveries have been achieved by satellites [121]. Three important reasons explain why many years have been necessary to overcome the technical difficulties:

- The Earth atmospheric transparency to electromagnetic radiation is highly energy dependent. In particular the electrons and nuclei in the atmosphere,

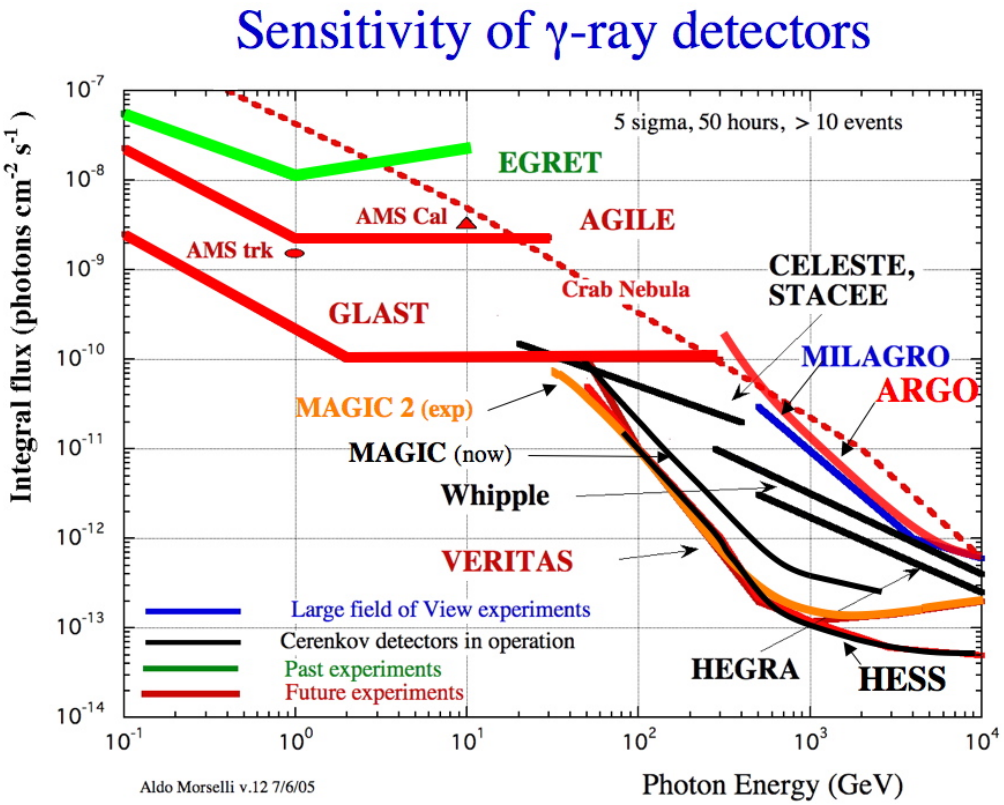

Figure 2.2: Sensitivity of past,current and future experiments for gamma ray astrophysics as a function of the photon energy.

involved in both absorption and scattering processes, prevent a ground based astronomy from γ region up to very high energies ($\sim$ 1 TeV). In fact the probability that a photon reaches the Earth surface without interacting is about 3×10^{-10}.

- The flux of γ rays from most sources is very low and decreases with energy. For example *Vela*, one of the most bright sources, has a flux of $1.3 \times 10^{-5} photons \cdot cm^{-2} \cdot s^{-1}$ integrated over 100 MeV, and an energy dependence described by a power law as $E^{-1.89}$; other examples of periodic sources are shown in Fig. 2.3. This means that the main problem in gamma-ray source detection is the sensitivity for point-like and diffuse sources, that leads to large area instruments and to an all-sky monitoring with time scale from few hours to days. Given the impossibility to put very large area detectors in space, the emission in TeV band is studied with ground-based telescopes.

- The charged particles can interact inside the detectors and generate photons that can be misinterpreted as gamma rays. The flux of these particles is larger than the photon flux by many orders of magnitude. This background can be removed employing detectors capable of efficiently discriminate against charged and neutral particles.

Two types of observations are used in order to perform Gamma Ray Astronomy:

Space observations

Cosmic ray observatory satellites have the same structure as particle detectors used at accelerators. They directly detect primary particles and make us able to determine their charge, mass and energy. To do that they are usually constituted as a collection of different and very specialized sub-detectors. For example, if a magnetic field is present, a tracker can measure the rigidity:

$$R = \frac{pc}{Ze} \tag{2.1}$$

and sometimes also the particle energy loss dE/dx being a function of Z^2 and velocity β. Scintillators are used to measure particle flight time from which we can extract particle velocity. Finally a calorimeter is able to measure particle kinetic energy. The measured energy is equal to the total incoming energy if the primary particle is totally absorbed. The AMS-02 detector will be presented in the next chapter.

Ground observations

Ground detectors can be grouped in three groups: atmospheric Cerenkov detectors, shower particle detectors and fluorescence detectors. As a 1 GeV photon interacts with the atmosphere, it generates a shower of charged particles. If those charged particles have a velocity larger than the light velocity in the atmosphere, they produce Čerenkov light which can be detected by ground detectors (Hess [124] and

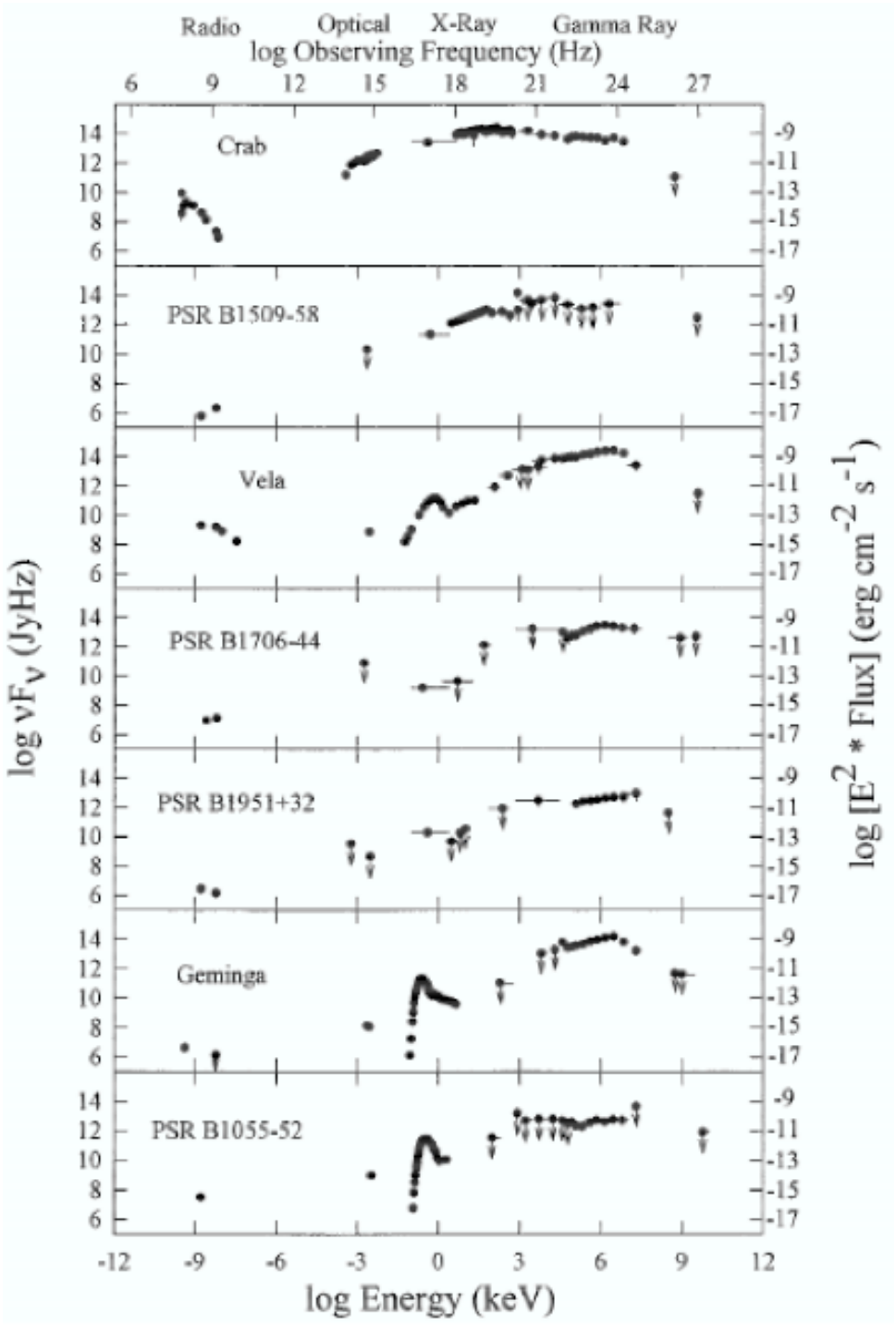

Figure 2.3: Spectral power law of pulsars detected with EGRET [123].

MAGIC [125]).
Very high energy particles produce showers which can reach the Earth surface. In that case those particles can be directly detected by detectors on the ground. Best conditions for this kind of detection are attained at very high altitude because of the closer distance to the shower and the larger fluxes. The typical threshold for those detectors is 1 TeV (Tibet [126] and Milagro [127]).
If the particle energy is more than 10 EeV (10^{19} eV), fluorescence detectors are also used. In fact, very high energy particles excite the air Nitrogen atoms which emit a light during their de-excitement. This light can be collected by image telescopes typically called fluorescence telescopes.

2.2.1 The past missions

The first satellites that allowed detection of cosmic γ-rays from the Milky Way above 100 MeV were Explorer 11 [128, 129] (launched in 1961) and OSO-III [130, 131] (launched in 1968). In the same period, the first Gamma Ray Burst (GRB) was discovered by the network of Vela satellites [132]. As the photon interaction cross section at energies above 10 MeV is dominated by pair production, most detectors employ tracker/converter layers or spark chambers to reconstruct the direction of incoming photons, and a calorimeter to measure their energy. The results obtained with early instruments were often limited by low statistics and large systematic errors.

A major step in galactic γ-ray astronomy was reached by the satellite missions SAS-II (1972) [133] and COS-B (1975) [134], carrying on board a spark chamber detector and a scintillator dome, working as a veto for charged particles. The two missions allowed the study of the galactic diffuse emission and thanks to an increased statistics with respect to the previous experiments, an accurate map of the Milky Way was also provided showing a spiral structure with the arms and the emission in the disc. In particular SAS-II [135] contributed to the detection of the Crab and Vela pulsars and of Geminga subsequently identified as a pulsar, while COS-B allowed the creation of the first source catalog, classifying about 25 objects and among them the first extra-galactic gamma-ray source, the quasar 3C273 [136].

After a pause of about 15 years because of the Challenger tragedy, the CGRO (Compton Gamma Ray Observatory) revolutionized the γ-ray astronomy with exciting discoveries. It was launched in 1991 carrying on board four instruments covering the energy range from 0.01 MeV up to 30 GeV: OSSE [137] (Oscillating Scintillation Spectrometer), optimized for detection of hard X-rays, BATSE (Burst and Transient Source Experiment) [138], for the monitoring of gamma ray bursts, COMPTEL (Compton Telescope) [139], for the observation of low energy γ-rays (1-30 MeV) and EGRET (Energetic Gamma Ray Telescope Experiment) [140], operating between 30 MeV and 30 GeV, described in more detail in the following section.

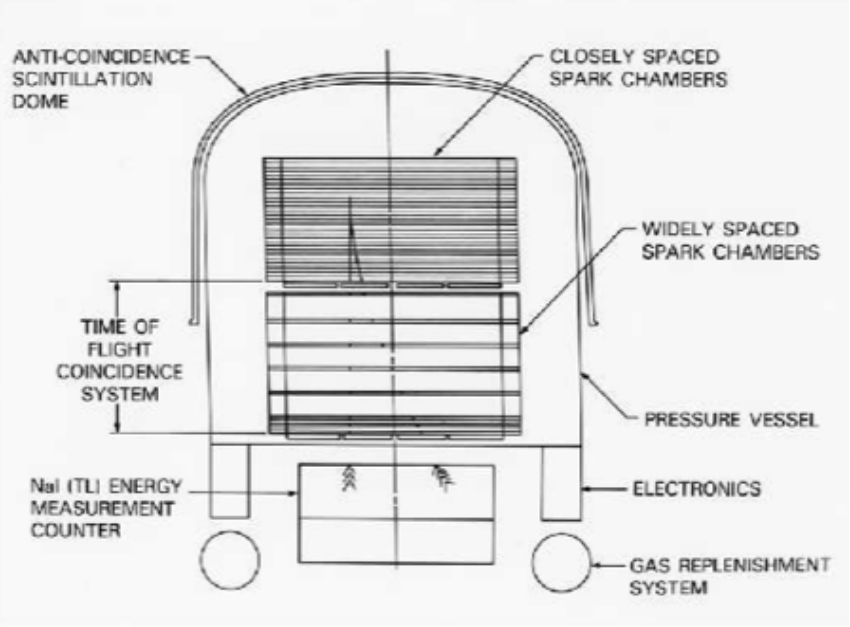

Figure 2.4: A schematic view of the EGRET instrument.

2.2.2 The EGRET instrument

The EGRET telescope monitored the sky in the years from 1991 to 2000, providing a first sensitive survey of the full γ-ray sky.
It was orbiting at 450 km altitude having an orbit inclination of 28 degrees, a precession period of 53 days and an orbital period of 90 minutes.

EGRET was composed by the following instrumentation for γ-ray detection (Fig. 2.4): two spark chambers equipped with high-Z material converter layers to allow photon conversion to e^+e^- pair or Compton scattering and to measure the photon direction; a calorimeter of NaI(Ti) crystals resulting in a total of 8 radiation lengths for the energy measurement, and an anti-coincidence system to veto charged particles. The anti-coincidence system played an important role in the rejection of the cosmic ray background, and it worked successfully since the γ-rays outnumbered background photons of a factor 10^4. The instrument was sensitive to fluxes larger than $\sim 3 \times 10^{-7} photons \cdot cm^{-2} \cdot s^{-1}$ ($E > 100 MeV$, for two week exposure). With respect to the past missions the telescope had a better angular resolution and a larger effective area, about $1500 cm^2$ between 0.2 GeV and 1 GeV on axis, decreasing to about one-half at 18^o off-axis. In Tab. 2.1 the instrument performances are shown, more details can be found in [141].

Thanks to its performance EGRET increased by a factor of 10 the number of identified objects and improved the knowledge of the diffuse gamma component. Moreover it detected also about 270 sources not identifed yet.

Parameter	EGRET
Energy range (MeV)	20 - 30000
Energy resolution (FWHM)	∼20 %
Effective area (cm^2)	1200 at 100 MeV 1600 at 500 MeV 1400 at 3000 MeV
Position location	5 - 10 arcmin
Field of view	$\sim$ 0.5 sr
Continuum sensitivity (for 10^6 s) (cm^2 s^{-1})	5×10^{-8} ($>$ 100 MeV)

Table 2.1: Main EGRET characteristic properties.

2.2.3 The high-energy gamma-ray sky

During its lifetime of approximately 9 years, EGRET detected about 2 million photons with energies above 100 MeV, allowing the study of the galactic and extra-galactic components of the diffuse radiation and the analysis of high energy point sources. About 300 point-like sources above 100 MeV were collected in the Third EGRET Catalog (*3EG*) [142] and they are shown in Fig. 2.5.
Different kinds of sources were detected and most of them ($\sim$ 60%) are unidentified (i.e. with no observed counterpart at other wavelengths). The majority of the objects away from the galactic plane have extra-galactic origin and have been classified as active Galactic Nuclei (AGN), almost all of them falling in the blazar class. Moreover, the EGRET telescope detected also 6 GRBs in coincidence with BATSE.

The most important EGRET discoveries can be summarized as follows:

- the discovery of a new class of gamma-ray emitting AGNs, the so-called gamma-ray blazars [144]. One of the best studied sources of this type was 3C279 [145]. Because of its brightness at all wavelength bands it was possible to measure its multi-wavelength spectrum quasi simultaneously from radio to gamma-ray energies;

- the observation of high energy gamma-rays emission from GRB940217 for over an hour, with some gamma rays having energies over 18 GeV [146];

- the observation of an increased fraction of pulsar electromagnetic radiation [147] at gamma-ray energies from 7 sources and the observation of Geminga pulses at E$>$ 100MeV [148];

- the confirmation that cosmic rays are galactic, at least up to the *knee* region [149];

- the detailed map of the galactic diffuse radiation and the measurement of the neutral pion bump in the high energy gamma-ray spectrum [150];

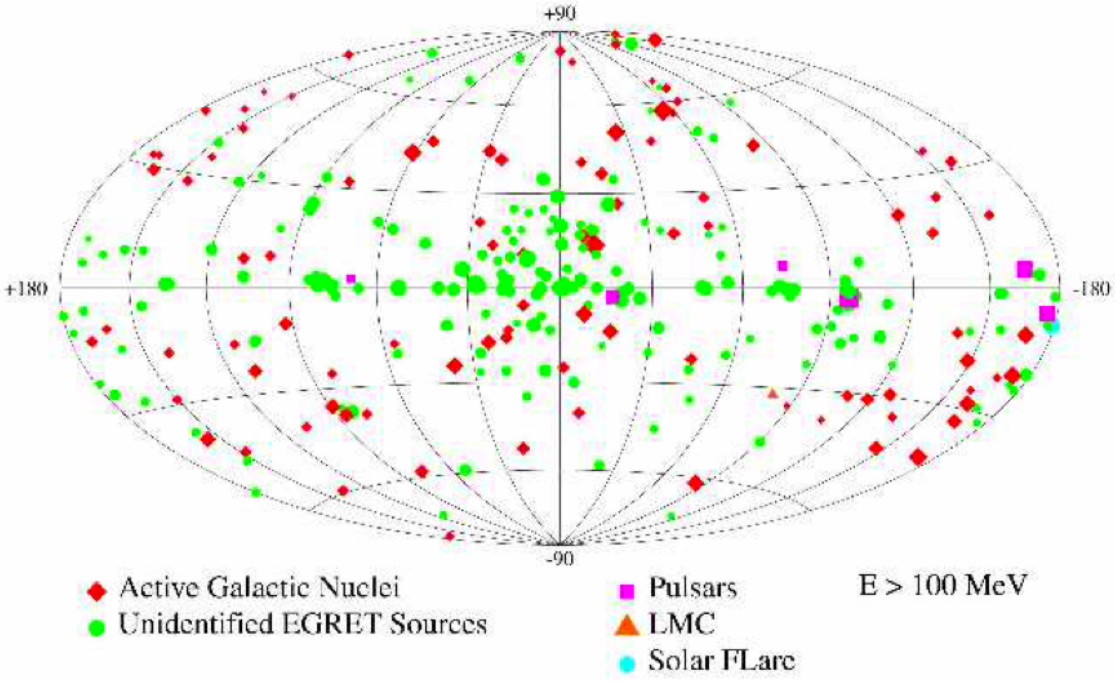

Figure 2.5: Point sources detected by EGRET at $E > 100$MeV (Third EGRET Catalog). Latitude and longitude coordinates are shown by AITOFF projection [143].

- a measurement of the diffuse, presumably extra-galactic, high energy gamma-ray spectrum [83];

In the next sections the most relevant fields of investigation in gamma-ray astronomy will be described.

2.3 Diffuse galactic and extra-galactic emission

CGRO allowed the first observation of the diffuse γ-ray emission in the energy band between 0.01 MeV and 30 GeV. This was the bulk of the emission detected by EGRET ($\sim$ 90% of photons). It can be divided in an isotropic extra-galactic component and in a component that dominates in the galactic plane.

2.3.1 Diffuse galactic emission

The diffuse galactic emission can be explained by the interaction of cosmic rays (CRs) with the interstellar medium. The spatial distribution of diffuse galactic-rays is usually described as "the gradient", that is a plot of the decline of the γ-ray emissivity per H-atom in the Galactic plane versus the galactocentric radius [151]. This approach implicitly assumes that gas interactions (i.e. π^0 production and bremsstrahlung) dominate over Inverse Compton scatting in the Galactic disk. To

investigate the γ-ray emission originating from π^0-decay and bremsstrahlung, one needs prior knowledge of the distribution of interstellar gas (neutral and molecular hydrogen) in the Galaxy.
The measured spatial and spectral distributions of the diffuse emission within 10^o from the Galactic plane have been compared to phenomenological models using realistic simulations [152]. The agreement is excellent except for an unexpected excess of emission above 1 GeV, that could be reproduced if the model prediction is scaled up by a factor 1.6. This underestimation cannot be explained neither by a bad calibration of the EGRET instrument, nor by spectral changes in the π^0 decay emission, nor by unresolved point sources (e.g. pulsars) that can at most contribute from 10% up to 40% to the observed deficit.
As the observation of Magellanic Clouds resolved the debate on the origin of cosmic-rays in the GeV energy, revealing their galactic origin, to explain the bulk above 1 GeV, one has to think about which kind of galactic accelerator would be able to produce cosmic rays with a source power of $10^{41} erg/s$. Recent observations of non-thermal X-ray synchrotron emission from Supernova Remnants (SNR), producing a spectrum of electrons with an injection index from 1.8 to 2.2, could explain the observed excess [153].

2.3.2 Diffuse extra-galactic emission

The presence of an isotropic, extra-galactic, diffuse emission of γ-rays above 30 MeV, was already detected by SAS-II and confirmed by the CGRO mission. The origin of this emission is not well understood. However, as most of the extra-galactic point sources are blazars, it was suggested that an unresolved population of these objects exists and could produce the diffuse extra-galactic background [154]. Presumably, also a contribution from the galactic halo has to be taken into account. The spectrum of the extra-galactic diffuse component measured by EGRET is well described by the relation:

$$\Phi(E) = (1.5 \pm 0.04) \cdot 10^{-8} \left(\frac{E}{377 MeV}\right)^{-2.07 \pm 0.03} photons \cdot cm^{-2} \cdot s^{-1} \cdot sr^{-1} \cdot MeV^{-1} \quad (2.2)$$

in good agreement with SAS-II data.

2.4 Active Galactic Nuclei

Before the launch of CGRO in 1991, the only known extra-galactic source of high energy γ-rays was 3C273 which had been detected with the COS-B satellite 20 years before [155]. A large fraction of identified sources discovered by EGRET at energies above 100 MeV belongs to a subclass of Active Galactic Nuclei (AGN), the blazars, characterized by an intense and variable emission from the inner nucleus, and a substantial fraction of those sources which remain unidentified in the EGRET catalog are likely to be AGNs as well.
AGNs are very different from the "normal" galaxies that are, typically, an assembly

of stars emitting as a black body. In fact they show bright nuclei and are dominated by non thermal emission from radio to gamma. Another fundamental difference is their observed variability: the emission changes significantly on a short time scale [156]. Since the typical variability period is of the order of 1 day, the size of the emitting region, at red-shift $z = 1$, has to be smaller than $\sim 1.3 \times 10^{10}$km, which is roughly the size of the solar system. The observed luminosities (typically $1.9 \times 10^{46} erg \cdot s^{-1}$) suggest the presence of a compact and bright source. The most efficient process known to explain the source emitting power is the release of gravitational energy in a deep gravitational potential:

$$L_{acc} = \varepsilon \dot{m}_{acc} c^2 \tag{2.3}$$

where L_{acc} is the luminosity of the source, ε the efficiency of the process in the conversion of gravitational energy into radiation ($\sim 10\%$), $\dot{m}_{acc}$ is the mass accretion rate and c the light speed. The accretion rate has a limit, called Eddington limit, that can be calculated from a balance between the gravitational force and the radiation pressure. For a spherical accretion, the luminosity at the Eddington limit is:

$$L_{Edd} = \frac{4\pi G m_P c}{\sigma_T} \cdot M = 1.3 \times 10^{38} \frac{M}{M_{sun}} erg \cdot s^{-1} \tag{2.4}$$

where G is the gravitational constant, m_P is the proton mass and σ_T is the Thomson cross-section. L_{Edd} is the maximum luminosity of a source of mass M, which is powered by a spherical accretion of gas. One can, now, invert the argument. If a source with observed luminosity L is radiating at the Eddington limit, the mass would be:

$$M_{Edd} = 8 \times 10^5 \frac{L}{10^{44} erg \cdot s^{-1}} M_{sun} \tag{2.5}$$

This is a minimum mass and the source could actually be radiating at much less than the Eddington limit. As an example, a Seyfert galaxy has typical luminosity $L \sim 10^{46}\ erg \cdot s^{-1}$ so the AGN mass in those galaxies must be at least $10^6\ M_{sun}$; for quasars, $L_{QSO} \sim 10^{48}\ erg \cdot s^{-1}$ and the AGN mass in those systems must be at least $10^8\ M_{sun}$. In general, if the AGN emits at the Eddington limit, its mass has to be of the order of 10^6 to $10^{10} M_{sun}$. All these observations lead to assume that the engine of the AGN is a super-massive black hole. There is another feature typical of about 5% of the AGNs: the presence of a collimated emission of plasma in relativistic jets. Inside the AGN family there is a wide sub-classification mainly based on morphological properties of the objects, their spectrum features, their frequency and the direction of the jet with the line of sight:

- Radio galaxies (divided in *Lobe Dominated* and *Core Dominated*) emitting mainly in radio wavelength by synchrotron emission of relativistic electrons.

- Seyfert galaxies (divided in Seyfert I and II) are spiral galaxies with a compact and very bright nucleus ($\sim 10^{46} erg/s$), characterized by prominent optical emission lines, corresponding to highly ionized gas, with a high velocity around 10000 km/s.

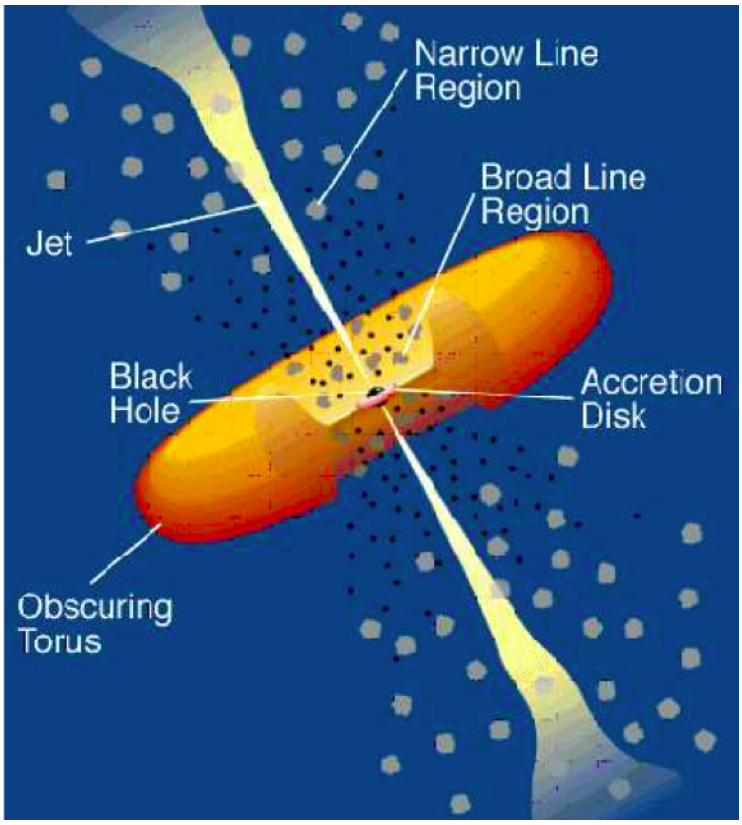

Figure 2.6: AGN: a schematic view of the standard model [157].

- Quasars were the brightest in the AGN family ($\sim 10^{44}$ to 10^{48} erg/s), according to their visual magnitude, these galaxies are nearly 10000 times brighter than our whole galaxy. Their spectra exhibit strange properties: emission lines are strongly red-shifted. The environment is characterized by the presence of a chaotic gas at such temperature that hydrogen ionization is possible.

- Blazars are the AGN subclass that dominates the observation at gamma energy. They are bright, star-like objects that can vary rapidly in their luminosity with peaks in the emission during flaring periods. It is believed that the Blazars emission is associated to a jet of relativistic matter directly pointing to the observer, this can explain the intense flux of energy, that could not be associated to an isotropic emission. The apparent luminosity, assuming isotropic emission, is 10^{48} to $10^{50} erg/s$.

With this wide subdivision there is agreement in accepting the unified model shown in Fig. 2.6 [157]. According to this model, AGNs are caused by a super-massive black hole, working as central engine that absorbs the plasma, gas and dust used as combustibles. The matter rotating at the center of the galaxy generates an accreting disk (extended from 1 to $30 \times 10^{14} cm$) surrounded by a torus of dust and absorbing matter; this central region radiates thermally from infrared to X-rays.

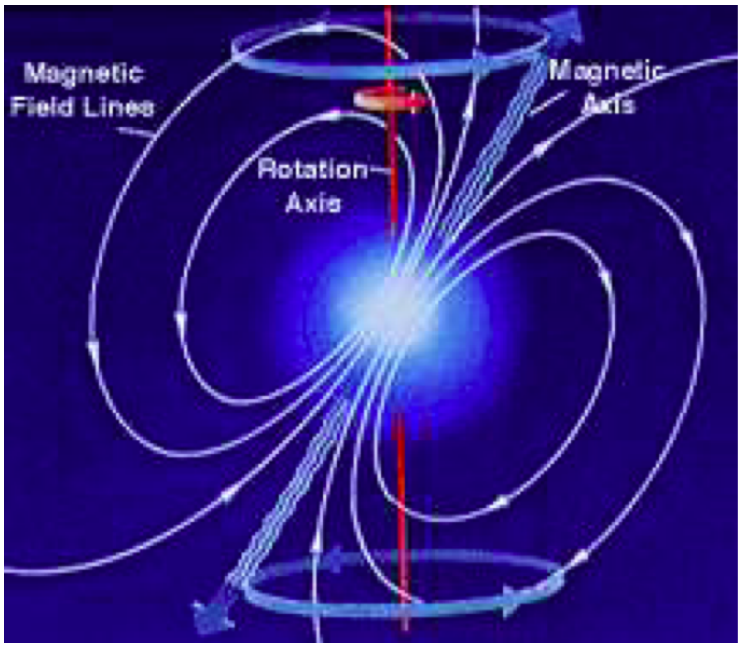

Figure 2.7: A diagram of a pulsar showing its rotation axis, its magnetic axis, and its magnetic field [163, 164].

Following the "modern" classification schemes, AGNs can be divided into two categories, on the basis of their radio properties: radio-loud objects, with a luminosity $L_{5GHz} > 10^{24} WHz^{-1}sr^{-1}$, or radio-quiet objects, for which $L_{5GHz} \leq 10^{24} WHz^{-1}sr^{-1}$. About 10% of all AGNs are radio-loud, the rest are radio-quiet AGNs. Radio-loud AGNs emit collimated beams or jets of plasma, while radio-quiet AGNs do not show large scale kilo-parsec jets. In general collimated relativistic particles contribute to non thermal emission via inverse Compton scattering of energetic leptons on photons (leptonic model) or via hadrons by photo-production (hadronic model). Recent comprehensive review about all aspects of AGNs and their observational properties can be found elsewhere [158, 159, 160].

2.5 Pulsars

The first identified gamma-ray sources belong to the class of pulsars. Pulsars were discovered mostly in the radio, but they emit in the entire electromagnetic spectrum. In particular, gamma ray emission was first observed in Crab and Vela by SAS-II [161]. The power spectra of most of the γ-ray pulsars [162] are extremely flat with maximum power often coming in the GeV energy range as shown in Fig. 2.3. Pulsars are neutron stars (NS), i.e. the relics of the intermediate mass star evolution. NS are high density (up to $10^{15} g/cm^3$) compact objects (radius $\sim 10km$), rapidly rotating around a central axis. The intense rotating magnetic field accelerates charged particles on the NS surface. These particles flow outward emitting synchrotron radiation and interacting via inverse Compton scattering with produced photons. The

beamed γ-rays radiation from the rotating object produces a pulsed emission with a period equal to the rotation period of the star (from few seconds to milliseconds). There are two models describing this mechanism: the *polar cap* [163] and the *outer gap* [164]. A scheme of a pulsar is shown in Fig. 2.7.

2.6 Gamma-Ray Bursts

Gamma-ray bursts are powerful flashes of gamma-rays that light up suddenly in the sky out-shining any other source. The first observation of GRB was obtained, by accident, by military VELA satellites, employed in defense of the international treaty that forbade nuclear explosions in space [165]. After this discovery many other missions were designed to study specifically those explosive events, among them was the BATSE instrument, on CGRO followed by the most successful X-ray mission BeppoSAX [166]. They allowed a precise localization of GRB X-ray afterglow [167], that is the emission following a gamma burst in other parts of the spectrum, ranging from waves to X-rays. Thanks to the observation of the GRB counterpart at optical and longer wavelengths host galaxies were identified and the measurement of the red-shift confirmed their cosmological. Such observed intense explosions require that a huge energy (10^{51} to $10^{53} erg$), corresponding to a sizeable fraction of a solar mass, which is emitted in a short time ranging from few milliseconds to about 10^3 seconds.
The GRB temporal durations in the BATSE energy band have a bimodal distribution of long bursts with $t > 2s$ (representing in majority) and short bursts with $t < 2s$. The resulting spectra are very hard and peak at energies of a few hundreds keV, following a power law described by a spectral index that varies during the burst.
The observations made during the past years cannot fully explain the phenomena associated to these intense bursts showing a complex typology of light curves.
At the moment many questions are unsolved about the nature of their progenitors, the hypotheses range from the collapse of the core of a massive star to a binary system of two merging neutron stars or a neutron star-black hole, but recently it has been noticed that they are associated with massive stars. These models suggest that the final formation of a few solar mass black hole, surrounded by a debris torus whose accretion provides a release of gravitational energy sufficient to power a burst. A presumably collimated fireball [169] of $e^{\pm}$ pair is accelerated to relativistic speed (Lorentz factor $\gamma > 100$) from the high internal pressure until most of its initial energy is converted into bulk motion. After this phase the fireball becomes transparent. An internal engine working intermittently is required to explain the observed duration. As the produced shells (several fireballs) have different γ, then the faster can catch up with the slower ones producing shocks responsible for the intense burst. All shells interact with the circumstellar medium generating the emission that could explain cosmological distances support the mentioned fireball scenario, whose a descriptive picture is shown in Fig. 2.8. Progress has been made in understanding how the GRB and afterglow radiation arises in term of a relativistic

fireball, but the debate concerning the nature of central engine and the identity of GRB progenitors is still open [170, 171, 172].

2.7 The Supernova Remnants

A star is a system that tends to maintain a balance between two fundamental forces: the gravitational attraction and the radiation pressure. When this system approaches the final state of its evolution, it can trigger one of the most energetic and spectacular explosive events, a Supernova, that can out-shine an entire galaxy during the peak light output. The explosion marks the end of a massive star ($> 8M_{sun}$) that collapses under the effect of the unbalanced gravitational force, leaving a neutron core and an expanding shell of matter known Supernova Remnants (SNR). During the collapse, the huge pressure produced from the degenerated gas of neutrons transforms the inner nucleus into a shield upon which the external shells rebound generating shock waves of supersonic speed. This event results in the release of a very large amount of energy and in the ejection into the interstellar space of the star envelope caused by the blast waves [173, 174].

Supernova remnants are generally powerful radio and X-ray sources. In fact near the core of the neutron star a very large magnetic field is generated, within which the relativistic electrons move emitting synchrotron radiation. Furthermore the shock waves generated from the ejected matter can ionize the surrounding gas, this is why the observed Supernova explosions are important, in particular:

- The interstellar medium, within which the explosion takes place, is strongly modified by the "hole" that rapidly expands up to several hundreds of light years diameter: we can derive that Supernovae explosions have affected the distribution of dust and gas in our Galaxy.
- The shock waves, generated during the explosion, can accelerate cosmic rays or trigger the formation of new stars from the existing interstellar clouds. In fact the amount of heat and pressure released from a supernova explosion can create new regions of star birth by compressing the surrounding interstellar medium.
- Supernovae are the primary suppliers of heavy elements. Elements necessary for life, such as carbon and oxygen, as well as heavier elements like iron, are produced by nucleosynthesis in the interior of the star and during the explosion they are redistributed through the interstellar environment.

SNRs are believed to be the sources of hadronic cosmic rays up to energies of approximately ($Z \cdot 10^{14}$ eV) [175]. Collisions of cosmic-ray nuclei with the interstellar medium produce neutral pions which subsequently decay into γ-rays. The luminosity of γ-rays from secondary pion production may be detectable by the current generation of satellite-based and ground-based experiments, particularly if the objects are in a high density region of the interstellar medium. EGRET has detected

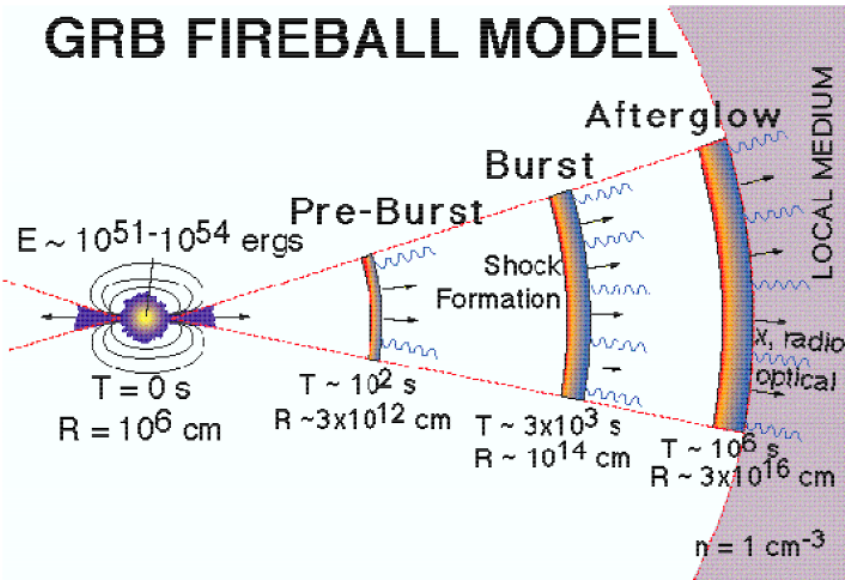

Figure 2.8: Cartoon for the Fireball Model [169].

signals consistent with the positions of shell-type SNRs. However EGRET observations alone are not sufficient to confirm the presence of high energy hadronic cosmic rays and the EGRET poor angular resolution cannot allow a good identification of a SNR shell.

2.8 Unidentified sources

About two out of three sources detected by EGRET have not been identified. To obtain information on the nature of the emitter, object class correlation studies are needed. Spectral features, spatial, temporal and physical characteristics are investigated. Their distribution show a clustering in the galactic plane, while high-latitude unidentified sources above 1 GeV are rare. As most identified sources are pulsars or blazars, the first hypothesis was to associate the unidentified sources to this objects [176]. Recent studies show the possibility of a distinction between unidentified sources at mid-latitude and brighter sources close to the galactic plane, the former ones are associated with the Gould Belt [177] of massive and late-type stars, interstellar gas and molecular clouds, while the latter ones are related to extra-galactic objects, isotropically distributed with at least one local galactic component. As a point source detection depends strongly on the exposure, the source flux and the background in the surrounding regions, we can conclude that a major drawback of EGRET was a nonuniform detection sensitivity. The study of these sources by crossed observations at different wavelengths with increased sensitivity is one of the hardest challenges of modern astronomy. A recent view of the current status of identification of the high-energy γ-ray sources is given in [178].

Chapter 3

The AMS Detector

3.1 The AMS experiment

The *Alpha Magnetic Spectrometer* (AMS) is a particle detector aimed at high precision measurements of cosmic ray fluxes in space. It will be part of the scientific program on board the International Space Station (ISS) (Fig. 3.1), where it will collect data for three years.

The AMS experiment's main goals are:

- search for cosmic antimatter nuclei;
- search for dark matter signatures;
- measurements of cosmic ray spectra in the energy range from a few GeV up to 1 TeV;
- detection of high energy γ-rays.

The precursor experiment AMS-01 (Fig. 3.2) was boarded on the space shuttle Discovery, flight STS-91 for 10 days in June 1998; the detector has been operative for about 180 hours, collecting over one hundred million cosmic ray events [179].
The improved version of the detector, called AMS-02, will be installed aboard the ISS. In addition to a refined silicon tracker (TRACKER) and a re-designed Time Of Flight (TOF) and anti-coincidence system (ACC), a proximity focusing Ring Imaging Cherenkov (RICH) detector will replace the threshold Cherenkov counter of AMS-01, and two additional subdetectors, a Transition Radiation Detector (TRD) and an Electromagnetic Calorimeter (ECAL), will be added to improve the proton-electron separation capability of the instrument.

3.1.1 Particle identification

In order to measure the fluxes of cosmic ray particles, the detector has to be able to measure their charge, velocity and rigidity:

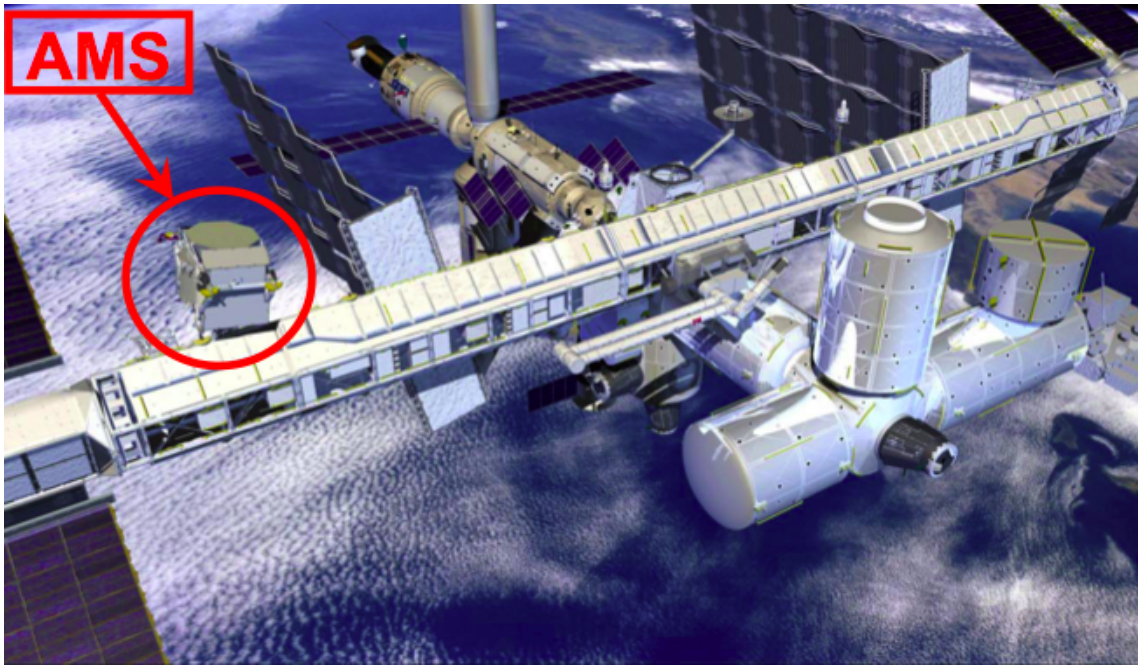

Figure 3.1: View of the AMS-02 detector as it will be installed on the ISS.

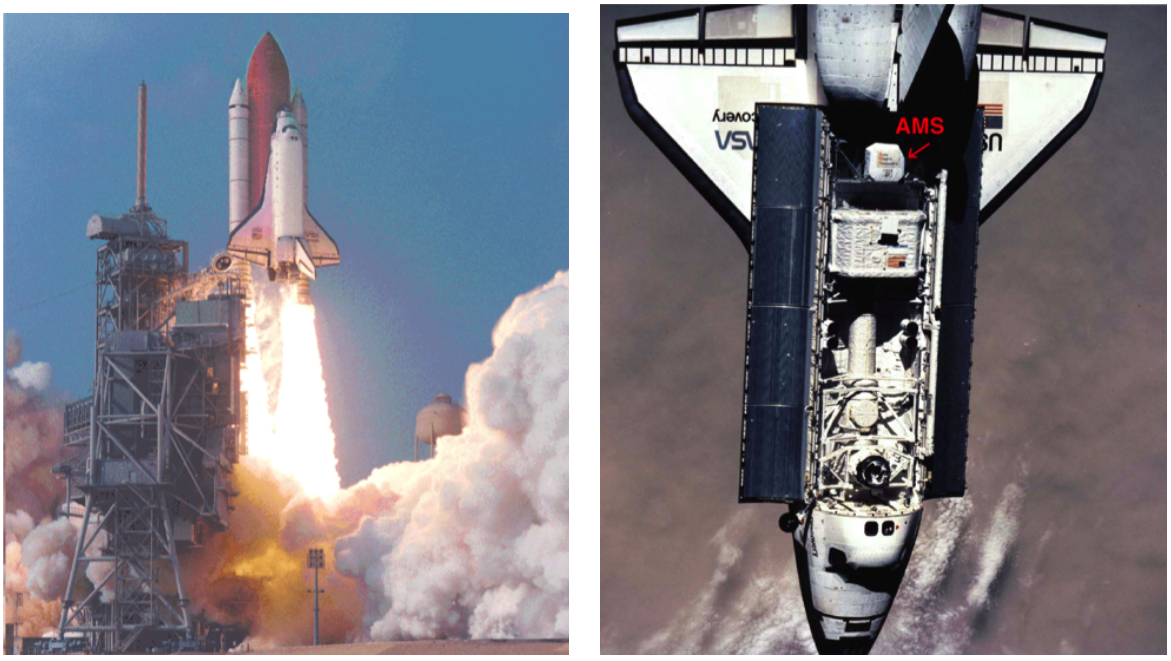

Figure 3.2: The launch and on-board installation of the AMS-01 detector.

$$R = \frac{pc}{|Z|e} = \gamma\beta\frac{mc^2}{|Z|e} \tag{3.1}$$

where p and Ze are the relativistic momentum and the particle charge respectively, m is its mass, c is the speed of light, $v = \beta c$ is the particle velocity and $\gamma = (1-\beta^2)^{-1/2}$ is the Lorentz factor.

When Z, β and R are known, it is possible to obtain the particle mass m from Eq.3.1 and the particle identification is complete. In practice, due to experimental uncertainties on those parameters, mass discrimination between two given particle species may be allowed only in some rigidity or energy range. In particular, it is easier to separate electrons from protons ($m_p \sim 1837 m_e$) than protons from deuterons ($m_d \sim 2m_p$), and the latter are better separated than any other pair of nuclear isotopes.

A particle with charge $|Z|$ and rigidity R, moving through a region where a uniform magnetic field B exists, will follow a helix with radius of curvature:

$$r = \frac{R}{Bc}\sin\theta \tag{3.2}$$

where θ is the angle between the particle momentum and the magnetic field. If the field is not perfectly homogeneous, as in the case of the AMS detector, the trajectory is more complicated but, in any case, it depends only on the particle instantaneous rigidity and the local magnetic field. Hence, if the field is known, in order to measure the particle rigidity one has to reconstruct its trajectory, taking into account the energy loss within the detector (that will decrease the instantaneous radius of curvature).

The tracking system of AMS is a silicon microstrip detector made of N planes ($N = 6$ for AMS-01, $N = 8$ for AMS-02) that are able to measure the (x,y) particle coordinates of the crossing points and its energy loss by the ionization of the active material. If the spatial resolution of the tracking system is σ_{pos} and the magnetic field strength along the particle trajectory is $s_{mag} = \int \vec{B}\cdot d\vec{l}$, the relative uncertainty on the rigidity is:

$$\frac{\Delta R}{R} \sim \frac{R\sigma_{pos}}{s_{mag}}\frac{1}{\sqrt{N+4}} \tag{3.3}$$

that is, the "deflection" $\eta = 1/R$, is Gaussian distributed.
It is customary to define the *Maximum Detectable Rigidity* (`MDR`) the rigidity for which the measurement uncertainty is 100% (that is $\Delta R/R = 1$). The `MDR` for protons is 150 GV in AMS-01 and will reach 1 TV in AMS-02. When the particle rigidity is comparable with the `MDR` of the instrument (i.e. the error on the deflection becomes of the order of the deflection itself which still remains proportional to R) , it becomes likely that a wrong deflection sign will be attributed to the trajectory ("spillover"). The spillover causes two problems: first, it produces fake antiparticles;

second, it leads to a distortion of the measured rigidity spectrum, that will appear steeper due to disappearance of events from the highest rigidity bins.
When the particle rigidity is known, in order to obtain the momentum it is necessary to measure its charge. The sign of the charge is found by looking at the track curvature (measured by the tracker) and the direction (obtained by the TOF system) in the magnetic field, while its absolute value is given by the energy loss in the active parts of the detector. Given a particle with charge Z and velocity βc, the average energy loss after a path length $d\xi = \rho dx$ through a medium with density ρ, atomic and mass numbers Z and A respectively, is given by the corrected Bethe-Bloch formula [180]:

$$-\frac{dE}{d\xi} = Kz^2\frac{Z}{A}\frac{1}{\beta^2}\cdot[\frac{1}{2}\log\frac{2m_ec^2(\beta\gamma)^2T_{max}}{<I>^2} - \beta^2 - \frac{\delta(\beta\gamma)}{2}] \tag{3.4}$$

where m_e is the mass of the electron, T_{max} is the maximum kinetic energy which can be imparted to a free electron in a single collision, I is the excitation energy and $\delta(\beta\gamma)$ is the density effect correction to ionization energy loss. Eq. 3.4 can be used to infer the particle charge $|z|$ from the energy deposition measurements in the TOF and tracker layers if the particle velocity β is known.
Two techniques can be used by AMS-02 to determine the particle velocity: measurements of the time of flight and of the Cherenkov cone opening angle.
The first method is used by the TOF system: a particle with velocity $v = \beta c$ takes a time $t = l/v$ to cover a distance $l = L/\cos\theta$ between the upper and lower TOF planes (L is their distance and θ is the trajectory colatitude angle, i.e. phi angle in spherical coordinates). The time of flight is given by:

$$t = \frac{L}{\beta c\cos\theta} \tag{3.5}$$

and its uncertainty σ_t is Gaussian. The uncertainty on β will be:

$$\sigma_\beta^2 = \frac{L^2}{c^2}(\frac{\sigma_t^2}{t^4\cos^2\theta} + \frac{\sigma_\theta^2\sin^2\theta}{t^2\cos^4\theta}) \sim \frac{L^2}{c^2}\frac{\sigma_t^2}{t^4\cos^2\theta} \tag{3.6}$$

since the second term inside the parenthesis can be safely neglected both in AMS-01 and AMS-02 thanks to the excellent angular resolution of the tracker. The time resolution of the TOF system is of the order of 0.1 ns, hence the time measurement can be used to infer the particle velocity up to about $\beta \sim 0.95$.
At higher β a direct measurement can be done exploiting the RICH detector of AMS-02, that will have a relative precision of $\Delta\beta/\beta \sim 0.1\%$. The Cherenkov radiation, produced by charged particles with velocity greater that the local phase velocity of light in the medium, is emitted over a surface of a cone whose axis is the particle momentum direction. The cone opening angle 2α depends only on the refractive index n of the medium and the particle velocity:

$$\cos\alpha = \frac{1}{\beta n} \tag{3.7}$$

Below the threshold given by:

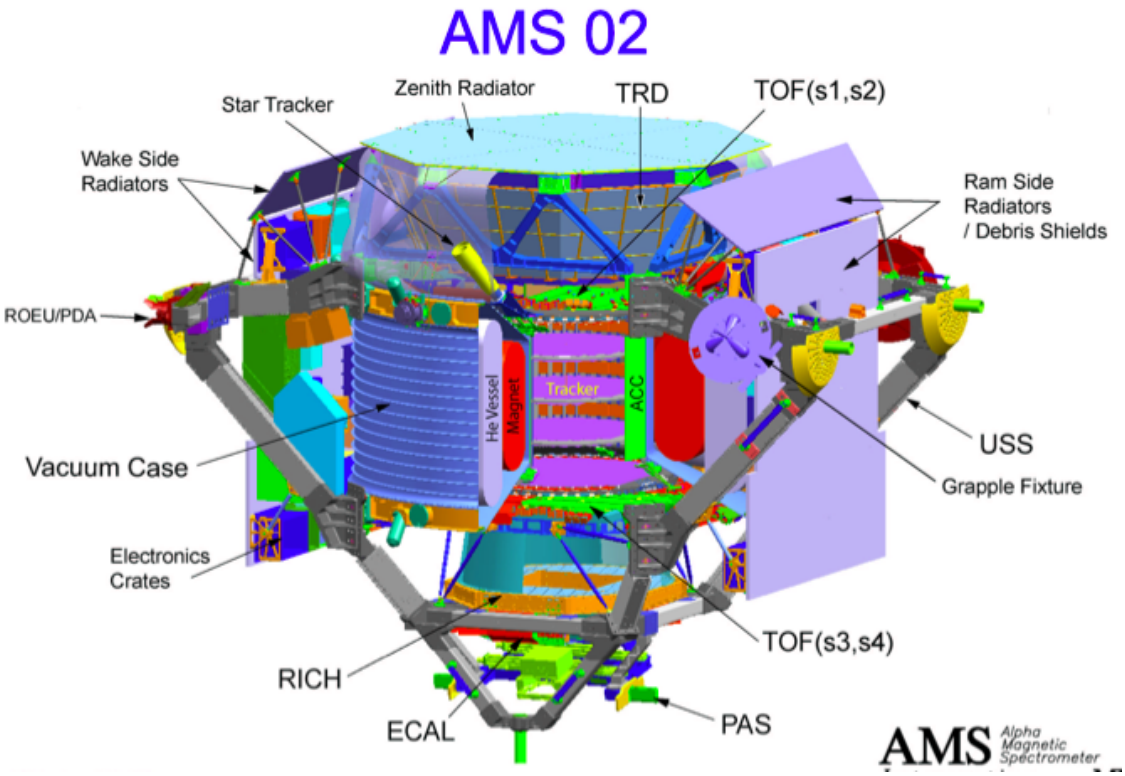

Figure 3.3: The AMS-02 detector.

$$\beta_{min} = 1/n \tag{3.8}$$

there is no Cherenkov emission at all.

3.2 The AMS-02 detector

The AMS-02 detector will be installed on board the International Space Station (ISS), where it will operate for at least 3 years, at an altitude of 430 km on a $\pm 51^o$ orbit.

The AMS-02 detector is based on a superconducting magnet generating a magnetic field intensity six times stronger than the AMS-01 permanent magnet. The threshold Cherenkov counter will be replaced by a Ring Imaging Cherenkov (RICH) counter to increase the velocity and the charge resolution; two completely new detectors will be added: a Transition radiation Detector (TRD), on the top of AMS-02, and an Electromagnetic Calorimeter (ECAL), below the RICH. They will improve the detector sensitivity to high energy electrons and photons, and the hadron/electron rejection capability.

A schematic view of the AMS-02 detector is shown in Fig. 3.3.

From top to bottom its main elements are:

- A twenty layers Transition Radiation Detector (`TRD`) to separate hadrons/electrons;
- Four layers of scintillators (`TOF` system) which perform time of flight and dE/dx measurements. The fast response of this detector is also used as input for the charged particle trigger;
- A superconducting magnet, which provides a dipolar field of 0.86 T, for a bending power of $BL^2 = 0.86Tm^2$;
- Eight layers of double side silicon microstrip detectors (`TRACKER`) providing an accurate measurement of the particle trajectory in both bending and non bending coordinates. The dE/dx measurement in silicon will be used to identify particles charges up to Iron;
- Anticoincidence counters (`ACC`), used as a veto, which ensure that only particles passing through the magnet aperture will be accepted.
- A ring Imaging Cherenkov (`RICH`), which measures the velocity and the charge ($|Z|$) of particles. The foreseen accuracy of this independent velocity measurement will enable AMS to unambiguously determine the particle mass for proton and nuclei up to tens of GeV in kinetic energy per nucleon.
- A 3-D sampling Electromagnetic Calorimeter (`ECAL`) made of $16.7X_0$ of lead and scintillating fibers to accurately measure the energy of the electromagnetic component of the cosmic radiation. Based on shower shape and an e/p separation of $\sim 10^4$ is expected up to the TeV energy range.

Already from this schematic description the guiding concept of multiple independent measurements of the particle properties can be appreciated. The particle absolute charge ($|Z|$) is independently measured four times in the `TOF`, up to eight times in the silicon `TRACKER` and by a different physical principle also in the `RICH`. The particle velocity is measured, with different accuracy, in the `TOF` and `RICH` detectors and at the same time the `TRD` response depends on the particle boost factor γ. The rigidity measurement in the `TRACKER` and the energy deposit in `ECAL` (or `TRD`) can be combined to cross-calibrate the response of the two detectors and improve e/p separation.

However, the particle charge sign (which is the crucial quantity in the matter/antimatter separation) is uniquely determined from the `TOF` measurement of the particle arrival direction and the bending sign in the magnetic field, as reconstructed in the tracking device. The magnet and the tracking system are in this concern the real core of the AMS instrument, and much effort has been put in their design to get a stable and performing system, also considering the extreme conditions of space environment.

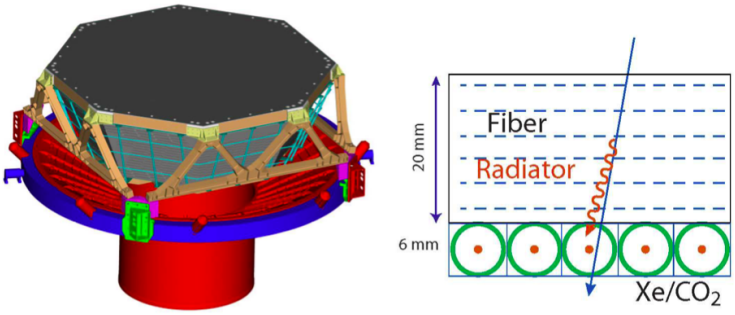

Figure 3.4: Schematic view of the TRD on top of the magnetic case (left) and operating principle of the AMS TRD detector (right).

The Transition Radiation Detector

Transition radiation is the electromagnetic radiation emitted when charged particles cross the boundary between two media with different dielectric properties [181]. Even if the probability for a particle to emit a transition radiation photon at a single interface is relatively small, ($\mathcal{O}(10^{-2})$), the use of a multi layer structure can significantly enhance the photon yield and result in a detectable signal. In AMS-02, transition radiation photons are generated in twenty layers of 21 mm fleece radiator (polypropylene/polyethylene) interleaved with 6 mm diameter straw tubes which detect X-ray photons. The detection principle, as well as the TRD structure on top of the magnet vacuum case, are presented in Fig. 3.4.

The use of the fleece radiator enhances the single layer emission since the impinging particle goes through several fibers that constitute the fleece itself, thus actually passing many dielectric interfaces in the single radiator module. Another improvement with respect to more classical designs is represented by the straw tubes, homogeneously distributed among the radiator, removing the necessity of an external detector for the emitted photons. The constituent modules (in total 328, each containing 16 straw tube chambers working in a proportional regime and filled with Xe/CO_2 (80%/20% gas mixture) are supported by a conical octagonal aluminum-honeycomb/carbon-fiber structure, such that the lower and upper four layers are oriented parallel to the AMS-02 magnetic field while the middle 12 layers run perpendicular to provide the detector with 3D tracking capabilities.

To verify the e/p separation performance of the AMS TRD system, a full 20 layer prototype has been exposed to the CERN T9, X7 and H6 beam lines to record electrons, muons and pions up to energies of 100 GeV and protons at energies up to 250 GeV [182]. The energy spectra measured for all wires in isolated track events are reported in Fig. 3.5: for both protons and electrons the dE/dx peak at ~ 2 keV is clearly seen. However, for electrons the signal enhancement above ~ 6 keV due to the radiated photon is evident. These results have been used in order to tune the Monte Carlo description of the detector response.

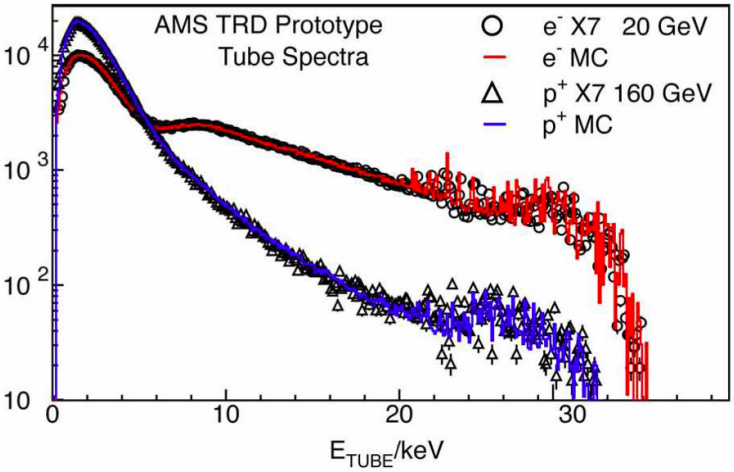

Figure 3.5: Single track energy spectra as measured for electrons and protons in a TRD tube. The larger energy deposit, due to the transition radiation photons, is clearly evident for electrons.

The Time of Flight Detector

The Time of Flight (TOF) system design is based on the experience gained with the AMS-01 detector [183]; as in the former case it is composed of four approximately circular planes consisting of scintillator paddles 12 cm wide and 1 cm thick, one pair of planes above the magnet (the upper TOF) and the other pair below (the lower TOF). Each plane has a sensitive area of 1.2 m^2 and, within each plane, the paddles are partially overlapped to avoid geometrical inefficiencies. Adjacent planes are arranged so that their paddles run in mutually perpendicular directions (Fig. 3.6).

This arrangement has been chosen in order to optimize background rejection at trigger level and to help in offline track reconstruction, providing an estimate of the position where the particle enters and leaves the volume occupied by the TRACKER. Each paddle is instrumented with two or three Photomultiplier Tubes (PMTs) at each end. The main modification with respect to AMS-01 concerns the light guides, that had to be curved in order to align the PMTs with the stray magnetic field, which in the proximity of the TOF system is still intense enough to influence the PMT performance significantly. The TOF system features a very fast and reliable response to the energy loss of charged particles, well suited to provide the general data acquisition system with the fast trigger signal, used as reference time for the event. The overlapping and crossed paddle geometry allows a spatial granularity of about 12×12 cm^2 , with a $\sim$ 100% efficiency and a gate of 50 ns for trigger purposes. The design resolution in the time of flight measurement is $\sim$ 120 ps, with a capability of discrimination between downward/upward going particles at the level of 10^9. The TOF counters were tested in ion beams at CERN in 2002 and 2003. The time of flight measurements between counter pairs resulting from the beam test are in good agreement with the expected ones for ions with $|Z| \geq 2$, while for $|Z| = 1$

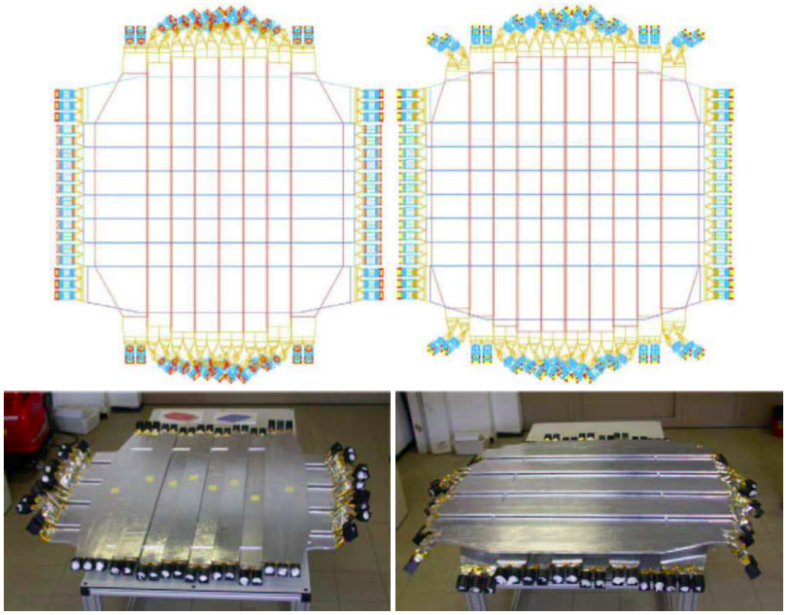

Figure 3.6: Top Panel: schematic design of the upper (left) and lower (right) TOF planes. Bottom Panel: assembled paddles on the upper (left) and lower (right) TOF planes.

species one observes a performance degradation due to the use of the curved light guides. The TOF resolution is shown in Fig. 3.7 as a function of the impinging ion charge.

The Superconducting Magnet

AMS-02 will operate with a six times stronger magnetic field, compared to AMS-01, created by a superconducting magnet system. The AMS collaboration has chosen to use a superconducting magnet system, as it is the only way to generate the required magnet flux density within the mass and power constraints of the Space Shuttle during the launch and of the ISS during operation. The AMS-02 magnet will be the first large superconducting magnet to be used in space.
The magnet system of AMS-02 consists of a pair of large coils together with two series of six smaller racetrack coils circumferentially distributed between them (Fig. 3.8 left side). The two main coils form a Helmholtz pair; they are used to generate the main part of the transverse magnetic field. The twelve smaller race-tracks are included to increase the magnitude of the overall dipole field, to reduce the magnitude of the stray field outside the magnet and to reduce the magnetic dipole moment to almost zero.
The nominal bending power of the magnet system in this configuration is $BL^2 = 0.78\ Tm^2$ [184] compared to $0.14\ Tm^2$ for AMS-01.
All coils are located inside a vacuum tank and operate at 1.8 K using super-fluid Helium. The free bore of the system has a diameter of 1.1 m, while the external

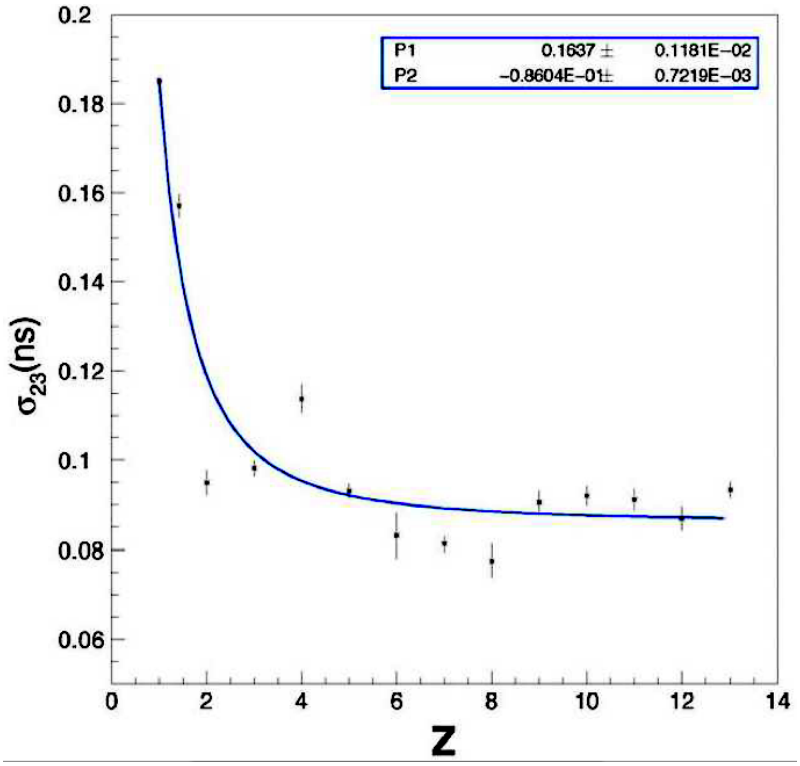

Figure 3.7: Time of flight resolution as a function of the ion charge for a pair of TOF counters as measured during test beam.

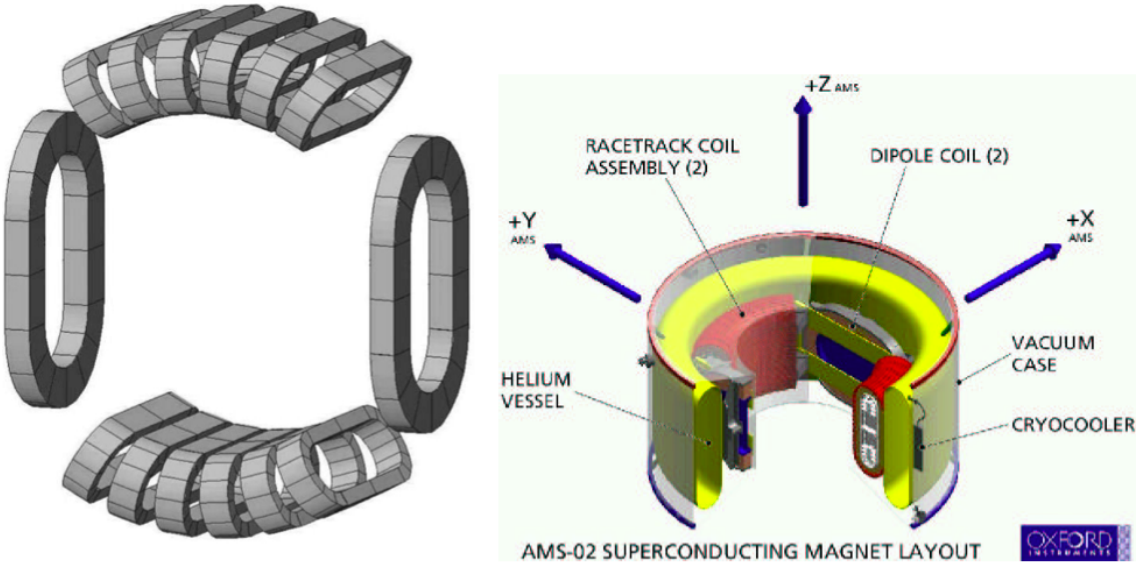

Figure 3.8: The AMS-02 superconducting magnet system.

diameter of the vacuum tank is 2.7 m, with a height of 1.55 m.

The coils are electrically connected in series, and operate with a current of 459 A in the "*persistent mode*": once a constant current has been established, a superconducting switch will cut off the power supply and the current will circulate with zero energy dissipation. At this stage no power is required to maintain the current loop. All magnets are wound from the same kind of conductor: a NbTi/Cu superconducting wire embedded in a high purity aluminum stabilizer. A total of 55 km of strand is required for the whole system. The operating temperature is below 10 K, requiring 2500 liters of liquid helium for evaporation cooling (the He vessel is filled with super-fluid He at 1.8 K before the launch). The coils are thermally connected to the tank through pipes filled with pressurized super-fluid He. This material has the highest heat conductivity among all materials, and high density. Helium will circulate also in the cooling circuit, and finally will be vented into space. The large volume of 2500 liters is needed to be able to operate for three years without refilling.

The Tracking System

The main differences between the AMS-01 and AMS-02 (Fig. 3.9) `TRACKER` are the number of support planes (6 and 5 respectively) and the read-out planes (6 and 8 respectively), the geometrical acceptance (from about 0.015 to 0.36 m^2sr), and the arrangment of silicon detectors on layers.

Decreasing the number of supporting planes results in a smaller amount of matter to be traversed by the particles, thus reducing the effect of multiple scattering on the trajectory. This is the main source of loss of precision in momentum measurements

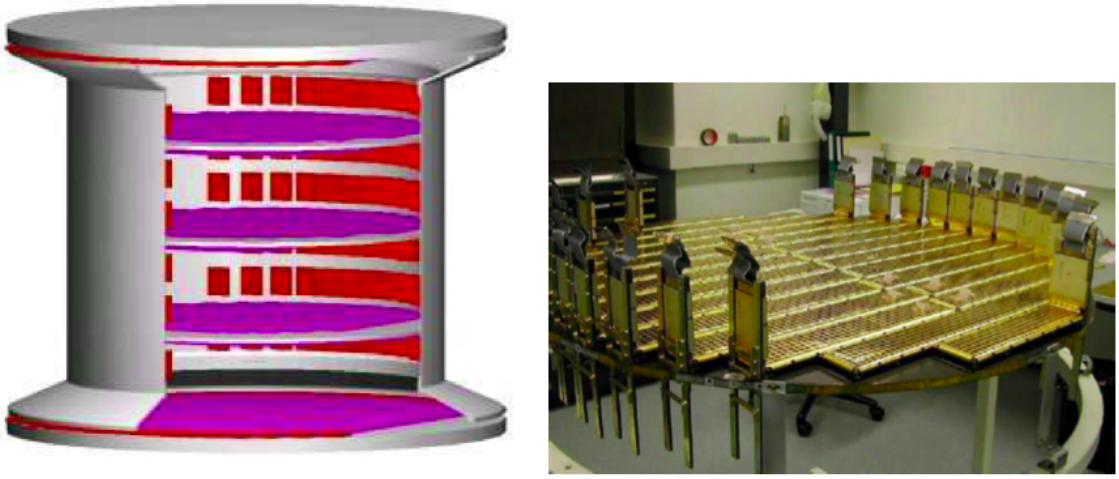

Figure 3.9: The AMS-02 silicon tracker detector.

at low rigidities.
The increment of the number of read-out (x,y) planes is obtained equipping both sides of the three internal planes with ladders; this guarantees a better measurement of the particle energy loss and an improvement in the reconstruction of the trajectory. In addition to a refinement in the ladder production and to the stronger magnetic field, the net result is a better measurement of the particle momentum. An estimate of the AMS-02 proton and helium rigidity resolution ($\geq$ 5 hit tracks) is presented in Fig. 3.10 [185]. Position resolution of 30 (10) μm were used for the x (y) coordinates with a detection efficiency of 90% in the silicon detectors. The estimated resolution is about 1.5% for 5 to 10 GeV protons, and the `MDR` is in the range of 1 to 2 TV.

A more detailed description of the AMS-02 Tracking System will be presented in the next chapter.

Laser Alignment System

Space based particle detection systems have to cope with a far wider range of environmental conditions than those at accelerators. This concerns notably the vibrations during the transport before deployment and the rapid periodic changes in the thermal settings due to solar radiation and cooling while in the shadow of Earth. With the AMS-02 silicon tracker, charged particle tracks are traced at 8 space points in a $\sim$1 m^3 sized B-field to an accuracy better than 10 μm. With AMS-01 it was found that the carbon fiber tracker support structure is stable at the 15 μm level but that excursions up to 30 μm occured. These excursions were correlated with changes in the thermal conditions following changes in spacecraft attitude [186, 187]. For long observation periods, the overall system stability is especially important in that it limits the ultimate momentum resolution for high rigidity particles and can

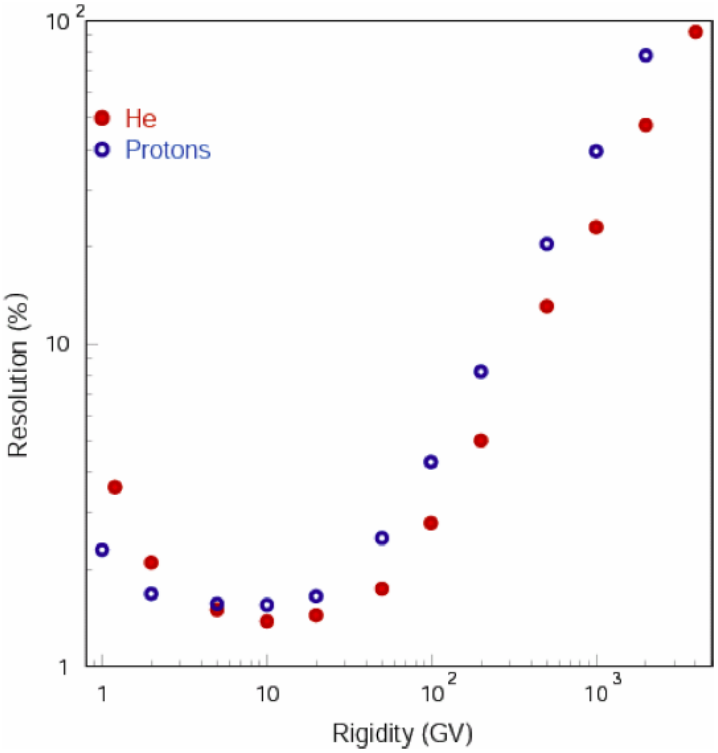

Figure 3.10: Rigidity resolution of protons and He in AMS-02.

introduce dominating systematic errors in the pointing accuracy of the AMS tracker for converted photons, particularly from astrophysical point sources. Sub arcminute precision pointing of weak sources is possible provided sufficiently frequent checks of the tracker geometry can be performed with laser beams and stiff cosmic tracks without going to a zero field condition. The alignment system, developed by RWTH-Aachen, provides optically generated signals in the 8 layers of the silicon tracker that mimic straight (infinite rigidity) tracks.
It has been shown with AMS-01 [186, 188, 189] that these artificial straight tracks allow the tracing of changes of the tracker geometry with a position (angular) accuracy of better than 5 μm (2 μrad). The system uses the same silicon sensors for both particle detection and control of the alignment. It serves to generate position control data within seconds at regular time intervals while the ISS flies into the shadow of the Earth or comes back into the sunlight. As shown in Fig. 3.11, the AMS-02 `TRACKER` is equipped with 20 pairs of alignment control beams.

The beams are narrow (diameter < 0.5 mm) and of small divergence (< 1 mrad). The beams enter the tracker volume through 2×5 beamport boxes (LBBX) mounted on the outer face of the two outer tracker support planes. The photons of these beams are generated with laser diodes mounted outside of the tracker volume and are brought practically loss free to the LBBX via mono-mode optical fibers. The wave length of these beams, 1082 nm, has been chosen such as to penetrate all 8

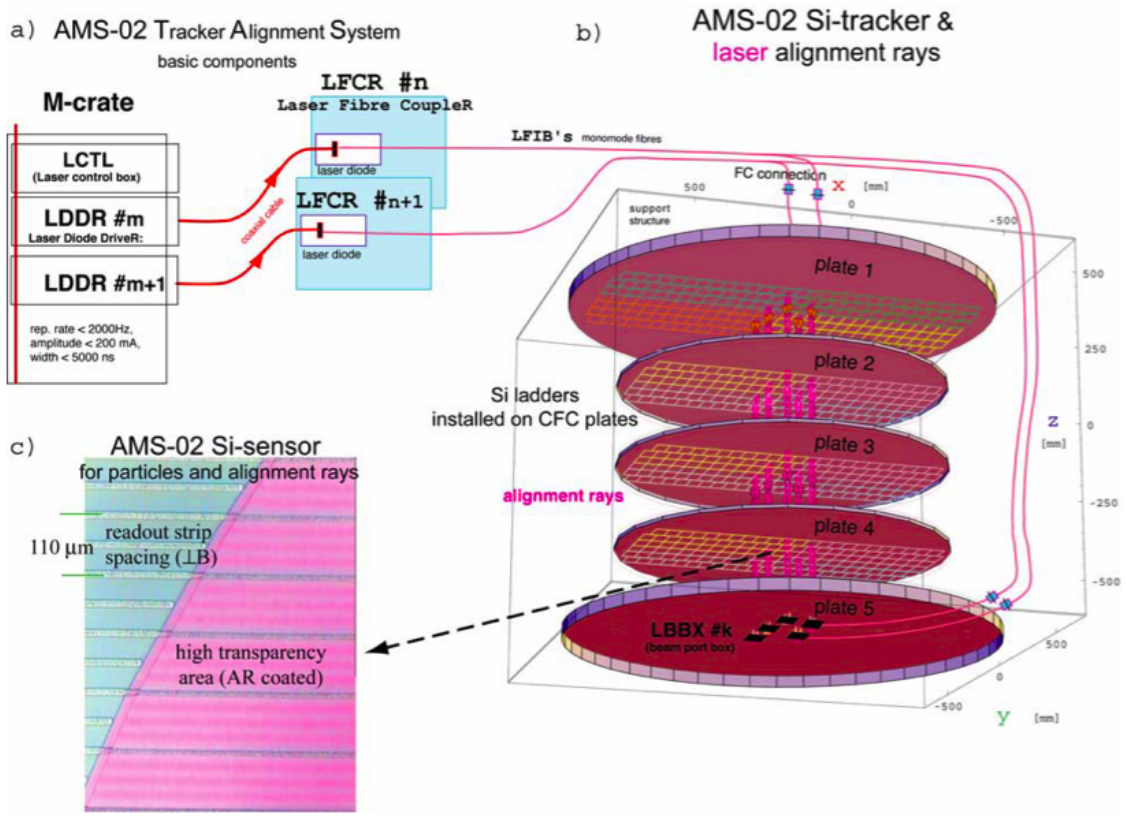

Figure 3.11: AMS-02 silicon tracker laser alignment system overview (a). Geometry of upward and downward going laser beams (b). Microphotograph of an Anti Reflective area (c).

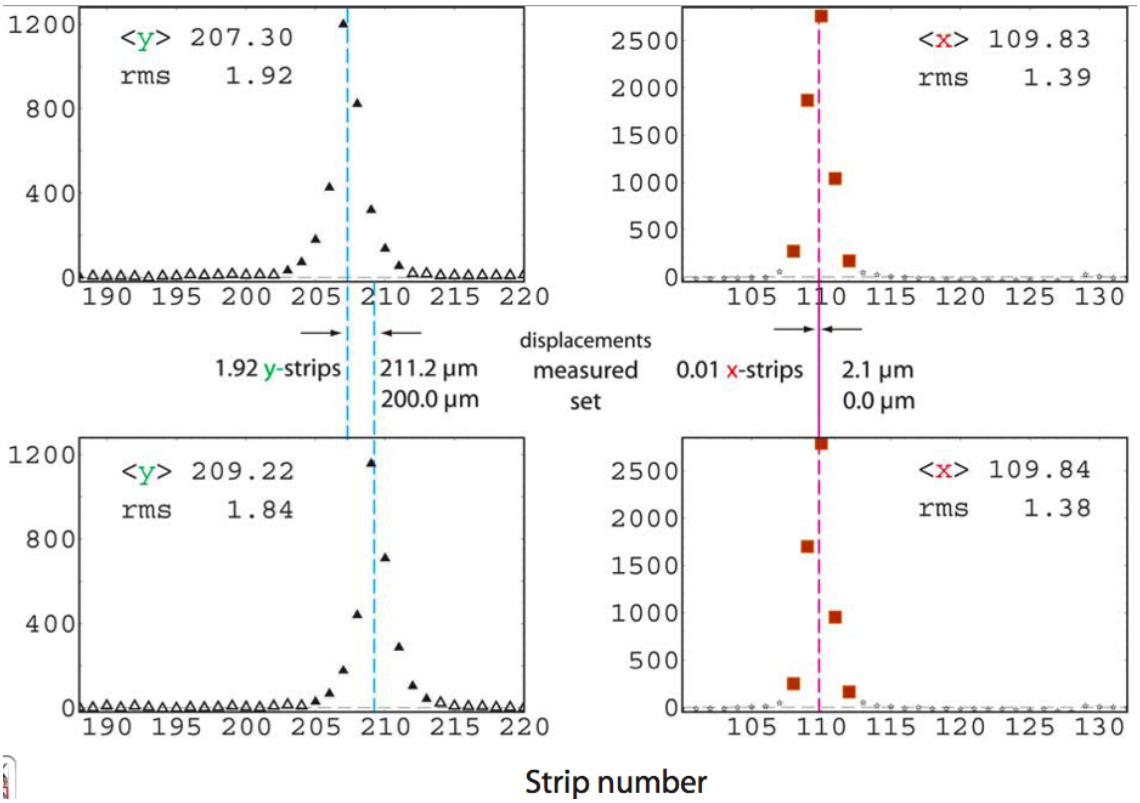

Figure 3.12: Single pulse laser beam profiles observed with the standard AMS-02 readout chain on flight ladders for the y (plots on the left) and x (plots on the right) coordinates. Between the upper and lower measurements the beam was stepped by 200 μm in y. In y coordinate the reconstruction precision is dominated by the stepping accuracy. In x it is better than 3 μm.

Si detector layers of the tracker. At this wavelength only a small fraction of the generated photons are absorbed (10% in the 300 μm-thick Si sensor), however the reflection at the Si surface has to be suppressed in order to overcome the intensity limitations in recording the alignment beams due to the strong effective attenuation (factor of $\sim$10 per Si layer) caused by the high refractive index (dielectric constant) of Si. Furthermore the transparency of the Si particle detector surfaces is obstructed by the aluminized readout strips. In consequence, the tracker sensors on the alignment beams have been equipped with anti- reflective coatings (SiO2 and Si3N4) optimized for the wavelength chosen (residual reflectivity 1%). In addition, the readout strip metalization width was reduced to 10μm in the coated areas and the passive implants not metallized. These modifications have resulted in a transparency of the alignment sensors of 50% [190] and the 8^{th} layer of the tracker receives about 0.8% of the intensity coming out of the LBBX.

As shown in Fig. 3.12, the laser beam spot covers 10 (5) strips on the p- (n-) side of the sensors. Position changes are determined concurrently for both coordinates

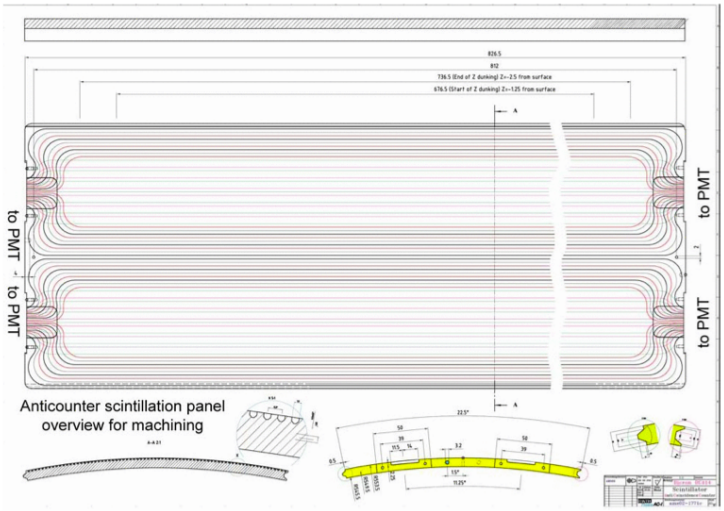

Figure 3.13: ACC scintillation panel drawing. The edges are dovetailed to ensure that no dead space is left.

from changes of the measured centroids of the laser profiles. Alignment beams are arranged in pairs in order to distinguish between changes in beam geometry and sensor displacements. Fig. 3.12 also shows that, with only a single laser pulse, displacements of 200 μm can be measured with a precision of a few μm. Laser alignment will be performed in parallel with data taking. This allows any possible changes in the tracker geometry, from rapid thermal deformations to long term drift, to be identified and corrected offline.

The Anti-Coincidence System

The Anti-Coincidence Counter (ACC) system forms a barrel around the silicon tracker of AMS-02. Its purpose is to flag events produced by particles crossing the detector from its sides, by δ-rays or showers produced by triggered particles, and by back-scattering of the electromagnetic calorimeter. In these cases, the detector would record informations resulting in bad track fit, charge and velocity resolution.
The ACC system consists of 16 scintillation panels (Bicron BSC414) of 8 mm thickness that cover completely the side wall of the tracking volume. Each paddle is 220 mm wide, and placed side to side by means of dovetail joints to completely avoid geometrical inefficiencies (Fig. 3.13). Since the ACC will be located inside the magnetic field, the readout PMTs cannot be placed in direct contact with the paddles; a wavelength-shifting fiber system is used instead to route the scintillation light out of the tracking volume, where the PMTs are oriented along the residual stray field lines ($\sim$ 1.2 kG). The fibers, of 1 mm diameter, are embedded inside grooves milled into the scintillation panels and are collected into two output ports of 37 fibers each at both ends of the counters.
The power system and the read-out electronics are very similar for the TOF and the ACC phototubes. The ACC anode signals will be routed to the scintillator front-end

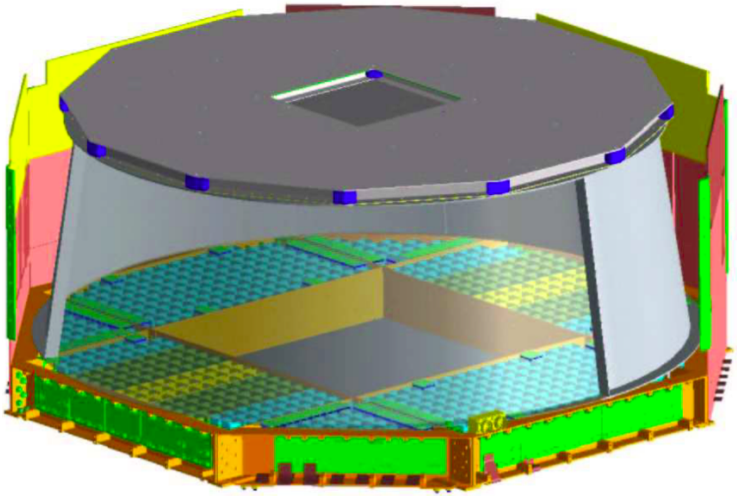

Figure 3.14: The main structural components of the RICH detector.

anti-coincidence board, that will send the discriminated signal to the trigger electronics. Since the ACC signals will also be used to check for back-scattering from the calorimeter, they will be used at the first level trigger stage in conjunction with the signals coming from the TOF and the ECAL system.

The Ring Imaging Cherenkov detector

The Ring Imaging Cherenkov (RICH) counter is designed to provide the experiment with a precise measurement of the charged particle velocity, needed to perform isotope separation in a wide energy range (Fig. 3.14). The RICH will also provide AMS with an extra electron-proton separation, needed to achieve the required rejection factor in positron and anti-proton identification. Moreover, the RICH will be able to supply AMS with an independent measurement of the particle electric charge up to Iron ($Z = 26$).

The detector main components are the Čerenkov radiator, the light detection system and the external conical reflector. Particles crossing the radiator layer with energy above the Cherenkov threshold will cause the emission of optical photons, eventually reaching the pixel plane (directly or after being reflected by the conical mirror) placed about half a meter below the radiator. In the middle of the pixel plane there is a square hole in order to avoid having material in front of the electromagnetic calorimeter. The photon detection system consists of a set of 680 multi-anode PMTs (Hamamatsu R7600-M16); the multi-anode structure (4×4 pads) together with the small PMT cross section ($25 \times 25\ mm^2$) provide the required accuracy in the photon position determination.

The overall reconstruction efficiency for events above the Cherenkov threshold (2 to 3 GeV/n depending on the aerogel refraction index) is estimated to be larger that 70% for unit-charge particles and above 80% for $Z > 1$ [191]. The reconstruction inefficiencies regard mainly partially contained events with a large fraction of the Cherenkov photons falling into the ECAL region of the detection plane. This

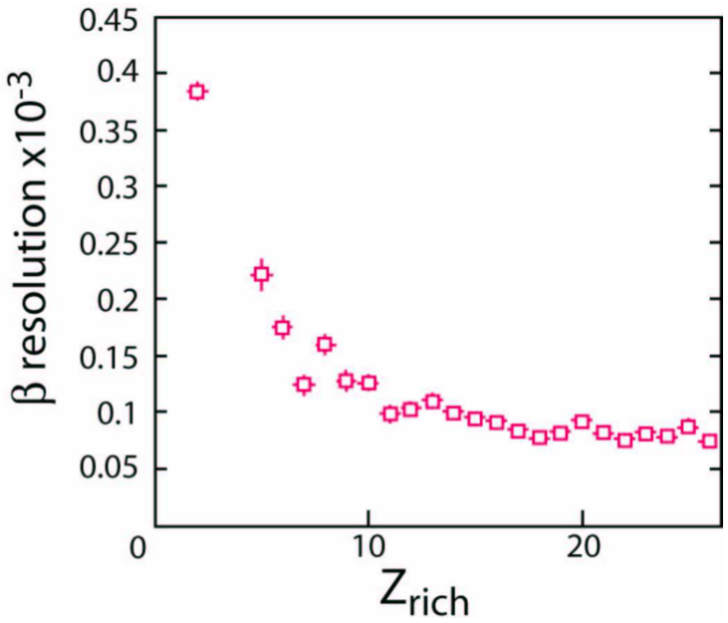

Figure 3.15: Dependence of the velocity resolution on the charge of the nuclei as obtained with a RICH prototype in a beam test.

sample can be partially recovered with the substitution of few aerogel tiles, in a central square, by another radiator with higher refraction index, e.g. NaF, so that the Cherenkov angles are big enough to avoid the central region. With the current configuration the RICH will provide AMS with a velocity resolution of about $\sim 0.1\%$ for protons.

In order to validate the detector design, the performance of a RICH prototype has been tested with cosmic muons and with an ion beam at CERN [192]. In Fig. 3.15 the measured velocity resolution as a function of the ion charge is shown.

Electromagnetic calorimeter

The AMS-02 electromagnetic calorimeter (ECAL) has to fulfill two main requirements:

- a good e/p separation given that 90% of cosmic rays is composed of protons, and
- a very accurate measurement of the electromagnetic particles energy loss.

In order to reach these goals one needs to have a calorimeter with both a large number of radiation lengths and a small number of hadronic interaction lengths. In addition to this, a fine lateral and longitudinal segmentation is also advisable; in fact, the former improves the e/p separation and the latter allows a more precise energy measurement, by refining the shower longitudinal profile measurement.
Other constraints to be taken into account are:

Volume	$64.8 \times 64.8 \times 16.65 cm^3$
Density	$6.9 \pm 0.2 g/cm^3$
Radiation length (X_0)	$\sim 17\ X_0$
Molière radius (R_M)	$\sim 30 \times 30\ R_M$
Hadronic length depth	~ 0.75

Table 3.1: AMS-02 `ECAL` characteristics.

- a radiation hard electronics and an electric power limited to 100 W;
- mechanics to sustain acceleration up to 27 g and a limited weight;
- a good thermal insulation to keep constant the fiber and photomultiplier gains (temperature gradient about $\pm 5^o$C).

The main features of `ECAL` are described in Tab. 3.1

The electromagnetic calorimeter is a sandwich of lead and scintillator fibers with $648 \times 648\ mm^2$ active surface and 166.5 mm thickness. It is composed by 9 superlayers, 18.5 mm thick each, disposed as follow: 11 lead foils of 1 mm thickness interleaved with 1 mm diameter scintillator fibers. Fibers run in one direction only inside a single superlayer. In order to obtain a 3-D imaging of the longitudinal and lateral shower development, superlayers are stacked with fibers alternatively parallel to x-axis (5 superlayers) and y-axis (4 superlayers): this structure is called *pancake* (Fig. 3.16).
Lateral and longitudinal sampling is done at 72 and 18 points respectively.

Each superlayer is read out by 36 four anode PMTs, arranged alternatively on the two opposite ends in order to read out each fiber without any dead zone in the detection geometry. The effective readout granularity is not given by the distance between two neighboring fibers, because each PMT collects the information from a group of 35 fibers, which form a readout *cell* (or *pixel*) of size 9×9 mm^2, half the superlayer thickness. A total of 324 photomultipliers (1296 anodes) are used (Fig. 3.17).

The fully equipped calorimeter weigh 638 kg. The main goal of this detector, which has $\sim 17 X_0$ depthness, is:

- to measure energy shower of electrons, positrons and photons;
- to disentangle electromagnetic from hadronic showers, thanks to the fine grain 3-D reconstruction of the shower;

The energy measurement of an electromagnetic particle is given by the sum of the electromagnetic shower particle energies produced by the mother particle energy loss when crossing a dense medium.
When charged particles from the shower cross scintillator fibers, emission of light

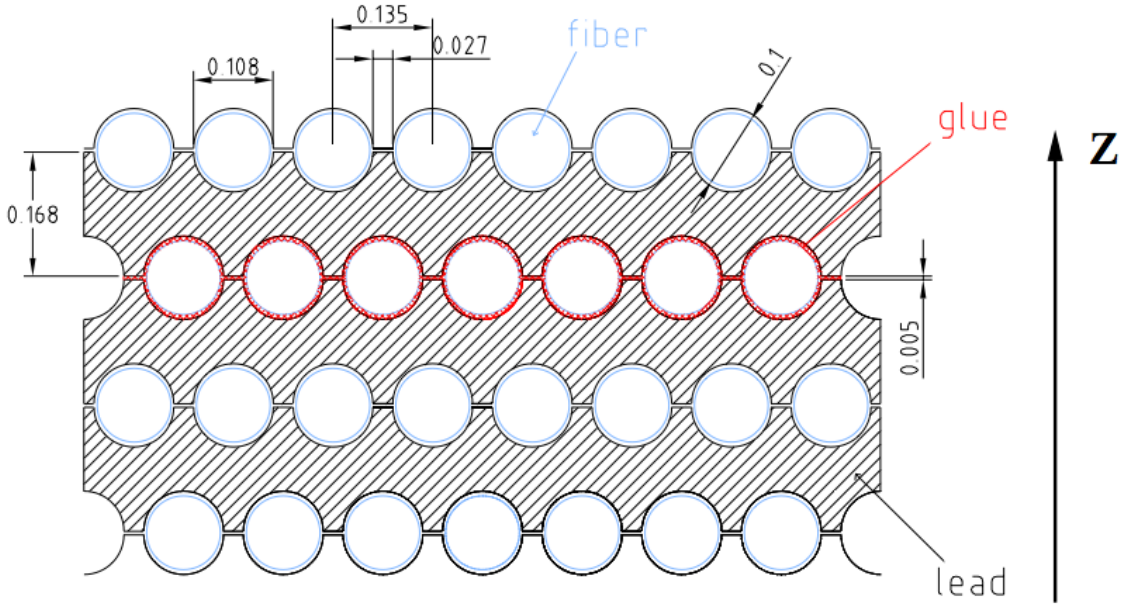

Figure 3.16: View of an ECAL superlayer (units are centimeters). Lead, fibers and glue volume ratios are 1/0.58/0.15. The average density is 6.9 ± 0.2 g/cm^3, which has to be compared with the lead density, 11.35 g/cm^3.

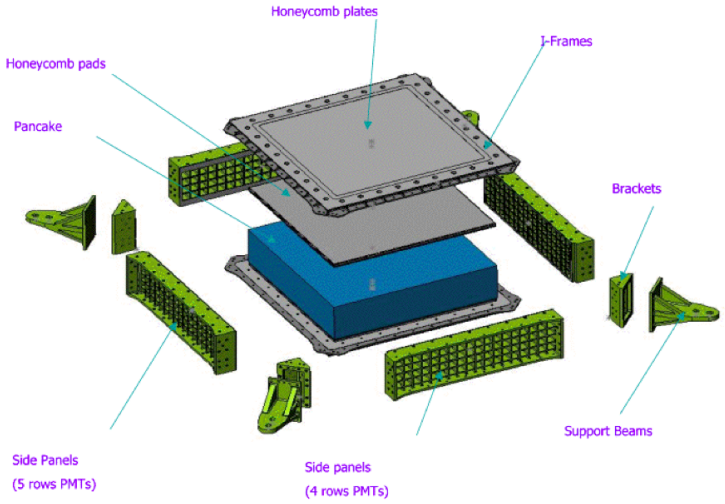

Figure 3.17: Exploded view of the ECAL.

occurs. The light is then guided by the fibers themselves and collected on photomultipliers which convert it into a measurable electric current. This current is proportional to the incoming particle energy.

If the particle impinging angle is normal to the calorimeter surface, the shower development is completed in about 16 radiation length or 0.75 hadronic length distance. The longitudinal profile is reconstructed on 18 points (10 points in yz-plane, 8 points in xz-plane) while for the lateral side each anode size corresponds to about half Molière radius.
Several discriminating variables (maximum shower height, energy fraction inside a distance of 2 cm around the shower axis,.....) allow for a e/p separation factor of $\sim 10^3$; adding the `TRACKER` information this factor moves to $\sim 10^4$.

Concerning the energy resolution, it is typically less than 4 - 3% in the range 10 GeV $\div$ 1 TeV; the angular resolution is around few degrees for the same energy range. Further details on energy and angular resolutions, important for photon reconstruction by `ECAL`, will be given in Chap.8.

To realistically assess the `ECAL` performances and validate the concepts design, a qualification model of the `ECAL` has been exposed to the `CERN SPS` beam line `H6A` with muons, 120 GeV protons and anti-protons and $e^{\pm}$ with energies in the range 3 to 180 GeV.
The shower shape (lateral and longitudinal shower development) and energy leakage have been analyzed on the beam test data as a function of the beam energy, for different geometry of the interactions and nature of the incident particles.

As a result, the effective radiation length, the energy and angular resolution as well as the electron/hadron discrimination have been verified to behave according to the `ECAL` design. In Fig. 3.18 the measured energy and angular resolutions for electrons are presented as a function of the particle energy.

The calorimeter also provides a standalone photon trigger capability to AMS for photons with energies down to 2 GeV. Further details are given in Sec. 3.2.1.

Star Tracker

Unlike charged particles, which are deflected in the solar, galactic and intergalactic magnetic fields, the direction from which neutral particles arrive indicates their point of origin. To correlate these sources with phenomena observed in other bands of the electromagnetic spectrum, it is necessary to know the precise direction in which the detector is pointing when the gamma ray arrived. Because the space station is a large and flexible structure it is necessary to make this measurement with a device attached directly to AMS-02.

Within AMS, the highest angular precision is provided in the measurement of gamma rays which convert in the upper layers of the detector and the resulting e^+e^- pair is then measured in the silicon tracker.

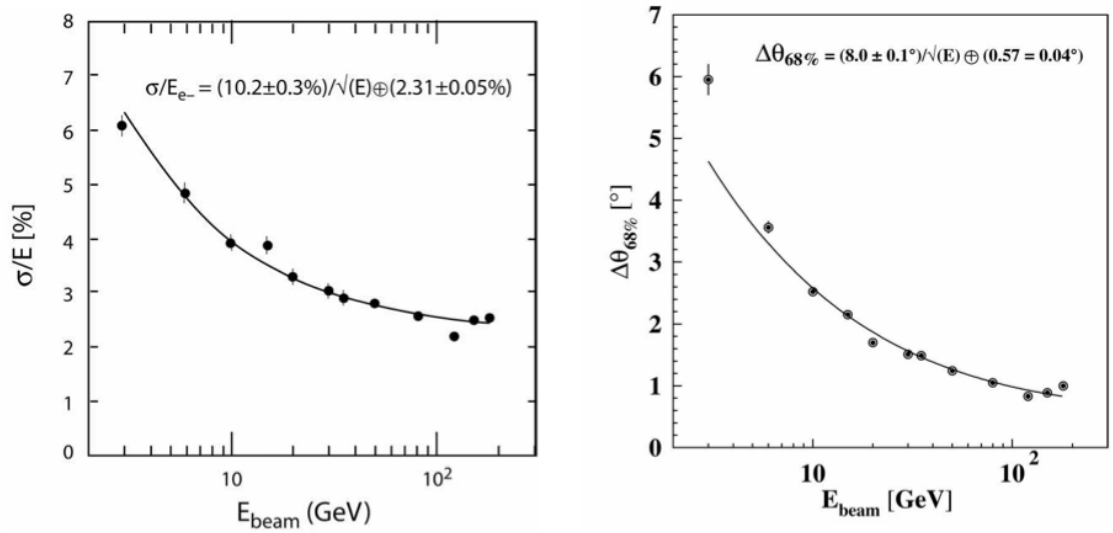

Figure 3.18: Energy (left) and angular (right) resolution measurements of ECAL for different electron beam energies. The curves corresponds to the fitted parameterization.

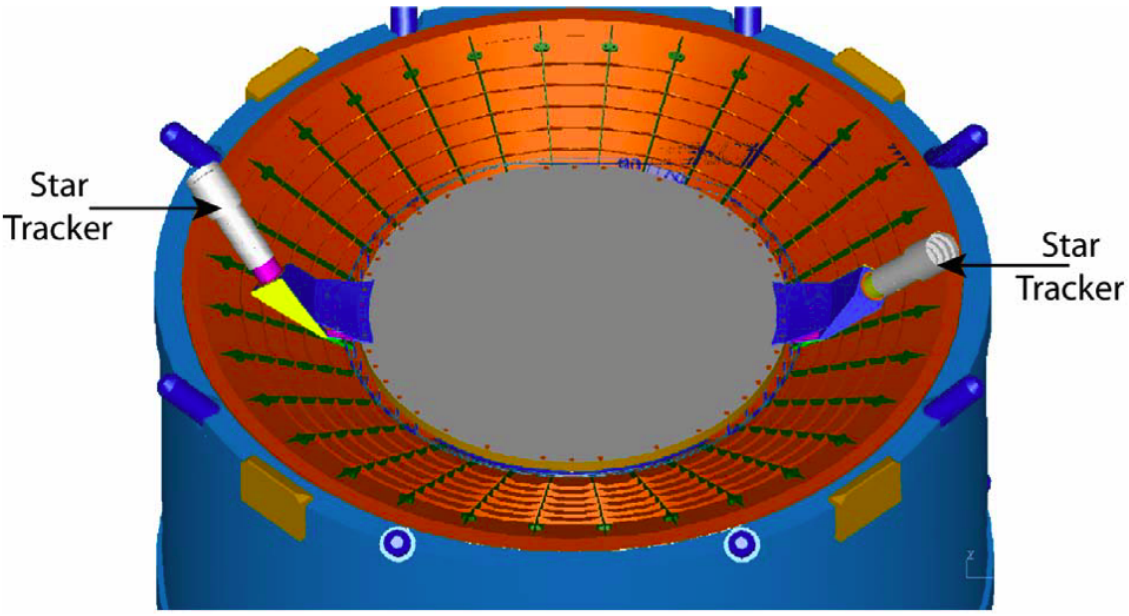

Figure 3.19: Star Tracker telescopes mounted to the silicon tracker structure.

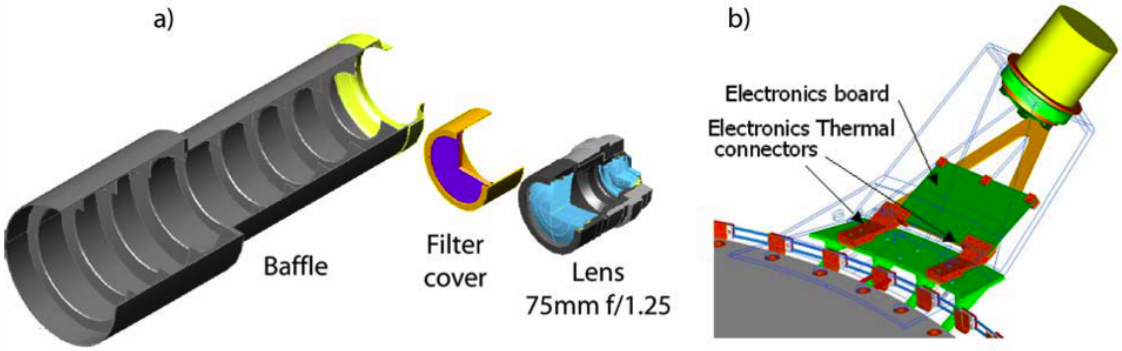

Figure 3.20: Star Tracker optics (a) and support (b).

To avoid any systematic shifts, the measurement must be made directly with respect to the silicon tracker structure. Two AMICA (Astro Mapper for Instrument Check of Attitude) Star Trackers (AST) are thus mechanically mounted on the tracker structure.
As shown in Fig. 3.19, it consists of a small optical telescope mounted on each side of the upper silicon tracker which acquires the images of stars and compares these with an on-board astrometric star catalogue. With this information, the attitude of AMS can be determined within an accuracy of a few arcseconds at rates up to 20 Hz.
Each telescope consists of an optical system, a low noise frame-transfer charge coupled device (CCD), a support and a baffle to limit reflected daylight.
The CCD has 512×512 pixels, each 16×16 mm^2 (Fig. 3.20). The cameras have been oriented so as to maximize their view towards space, avoiding both the rotating solar panels as much as possible and attached radiators and the central parts of the space station. In addition, having two cameras pointing in opposite directions ensures that at least one will always have a clear view of space without solar interference. The front end electronics uses a correlated double sampling technique to suppress noise.

GPS

In addition to the directional correlation provided by the star tracker, the physics accessible by measuring gamma rays also requires the precise temporal correlation to a few microseconds of measurements by AMS-02 and other instruments. Timing information is provided by the space station, but owing to the limitations of the low rate data link (LRDL) and the processing required within AMS, the reference time accuracy would be a few tenths of seconds, which is insufficient.
Within AMS, short time intervals (up to a few seconds) can be measured accurately (with submicrosecond precision) by the trigger system. However they are subject to long term drift and lack an absolute reference, to address these issues, a global positioning system (GPS) will be deployed on AMS-02. Two patch type antennae will be mounted on an upper USS member pointing in different directions to ensure

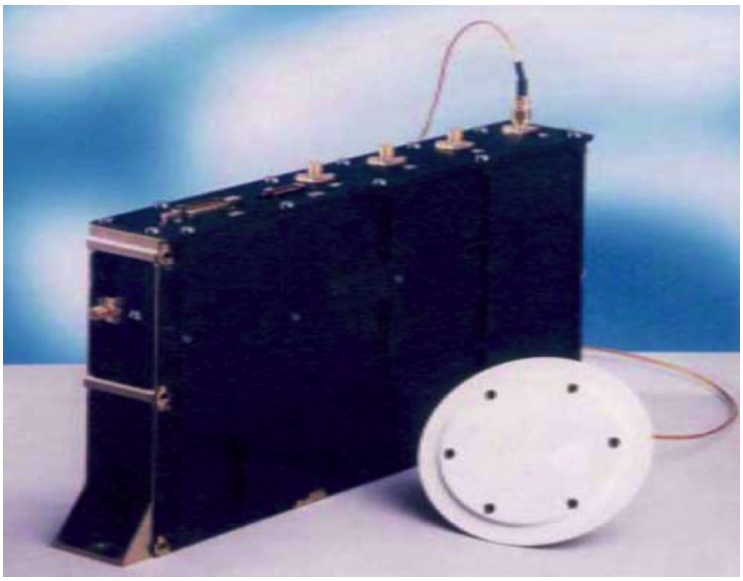

Figure 3.21: TOPSTAR 3000 D unit and a GPS patch antenna.

that the signals from a sufficient number of GPS satellites can always be acquired. Fig. 3.21 shows the unit and an antenna.
To reach the required accuracy, the software running in the unit has been specially adapted to include all the corrections required when traveling in low earth orbit.

3.2.1 Trigger

The *trigger* is the digital/analog signal which starts the data acquisition (DAQ) chain. By extension, this term is often used to represent the logic conditions required for it to be generated by the electronics.
In high energy physics experiments it is customary to define three types of trigger logics, depending on the type of data they act on: the *first level trigger* (including a pre-trigger called *fast trigger*) is generated imposing conditions on fast signals only (i.e. on logic signals coming from discriminators); the *second level trigger* is generated after the first level trigger if digitized data of any single subdetector satisfy the required conditions, and the *third level trigger* follows the second level trigger signal when the digitized data of the whole detector are checked against the desired set of conditions.
The general tasks of the AMS-02 trigger system are:

1) provide fast start signal for the readout system in response to crossing particles of certain types with certain kinematic parameters (direction, momentum, velocity). The decision is be based on the analog signals from "fast" (PM-equipped) detectors like TOF, ECAL and ACC;

2) confirm or reset the readout sequence based on more complicated analysis of the signals (analog or digitized) from fast detectors and digital information

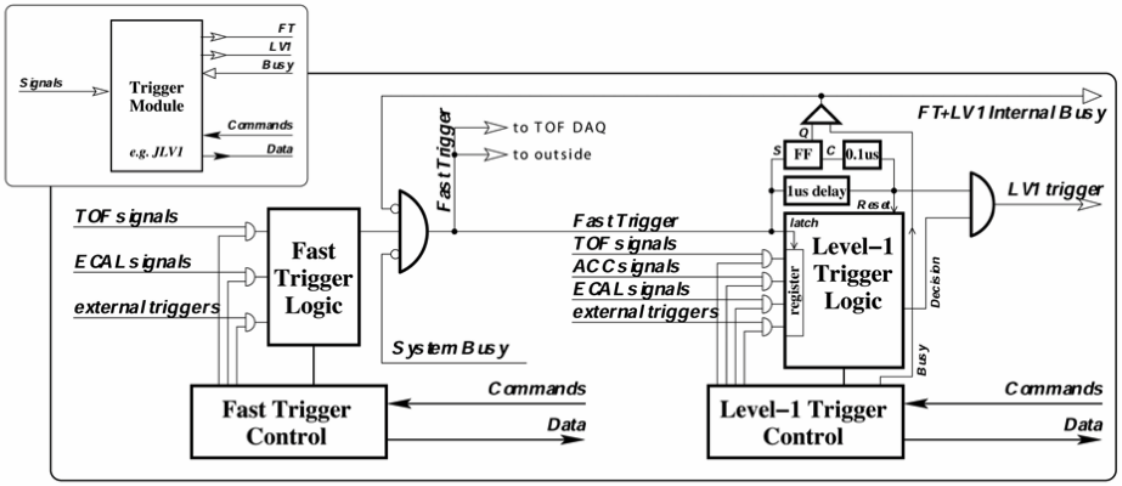

Figure 3.22: Fast(FT) and Level-1 (LV1) Trigger Scheme.

from slow detectors (TRD and TRACKER).

In AMS-02 two kinds of triggers (Fig. 3.22) are implemented: one for charged particles, and one for photons.

In the first case the validation (acquisition) of the event is done combining the response of TOF, ECAL and ACC. In this combination the TOF has to send to the trigger box the signals used to create the fast trigger signal: this is the very first step of the data acquisition electronics. This signal is used by the TOF electronics as the "time zero", which the scintillator time signals are referred to. The TOF system could also use the energy loss measurement to send to the trigger box a special flag for ions events, that can be used at *third level* to disable the anti-coincidence counters veto, that would suppress higher charges whose flux is low.

The trigger for photons is a stand-alone ECAL trigger. The AMS-02 calorimeter has an excellent imaging capability which allows to implement a very efficient trigger for photons with energies down to few a GeV and to reject most of the background (protons and electrons), increasing the total trigger rate only by a few percent.

The trigger is made in two steps: a fast decision, available within 180 ns, given by the count of PMTs above threshold in the 6 central (2^{nd} to 7^{th}) superlayers of the calorimeter and a Level 1 trigger decision, well before 1 μs, obtained with a fast reconstruction of the particle direction.

The photon direction is calculated using the distances between the centers of gravity of the three superlayers belonging to the same projection. Particles with an inclination larger than 20 degrees are rejected, ensuring the trajectory passed cleanly through the magnet bore. The expected ECAL trigger efficiency in AMS-02 for unconverted photons of different energies is shown in Fig. 3.23. The efficiency is 90% at 2 GeV and more than 99% for energies larger than 10 GeV. The trigger rates for photons and for the most relevant backgrounds, as deduced from Monte Carlo studies based on the data collected by AMS-01 [193, 194, 195, 196] and others [83],

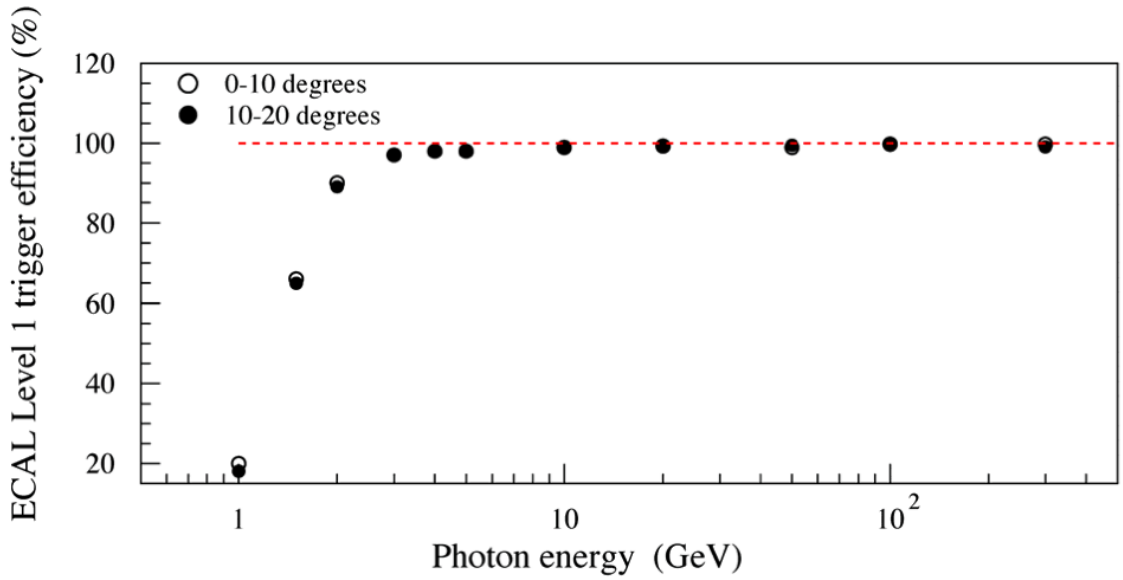

Figure 3.23: ECAL Level 1 trigger efficiency for different photon energies and angles.

are shown in Fig. 3.24. Particles firing the AMS charged trigger, which include converted photons, are not included in this background rate.

The ECAL standalone trigger also provides an electron trigger that recovers the inefficiency introduced by the ACC on high energy electrons with backsplash from the calorimeter.

3.2.2 Ground Data Handling and Remote Commanding

The long duration of AMS-02 mission on the International Space Station (ISS) makes the operation of the ground data handling complex fundamentally different from that one of AMS-01. Data analysis will be performed during the flight on a continuous basis. Physicists will need access to scientific, calibration and monitoring data continuously. Fig. 3.25 shows the AMS-02 Ground Data Handling and Remote Commanding System. The ground based computing equipment can be conceptually divided into three functional units: the Ground Support Computers (GSC), the Payload Operations and Control Center (POCC) and the Science Operations Center (SOC).

The GSC receive control and science data from Huntsville Operations Science Center (HOSC) and buffer these data along with NASA ancillary data for transmission to POCC and SOC. These computers will have to run continuously, thus system reliability is the vital issue. The system should be able to store about 2 weeks of data. Two identical systems will be installed and run simultaneously and independently. Thus, in case of a computer failure, the data transmission will be continued without interruption.

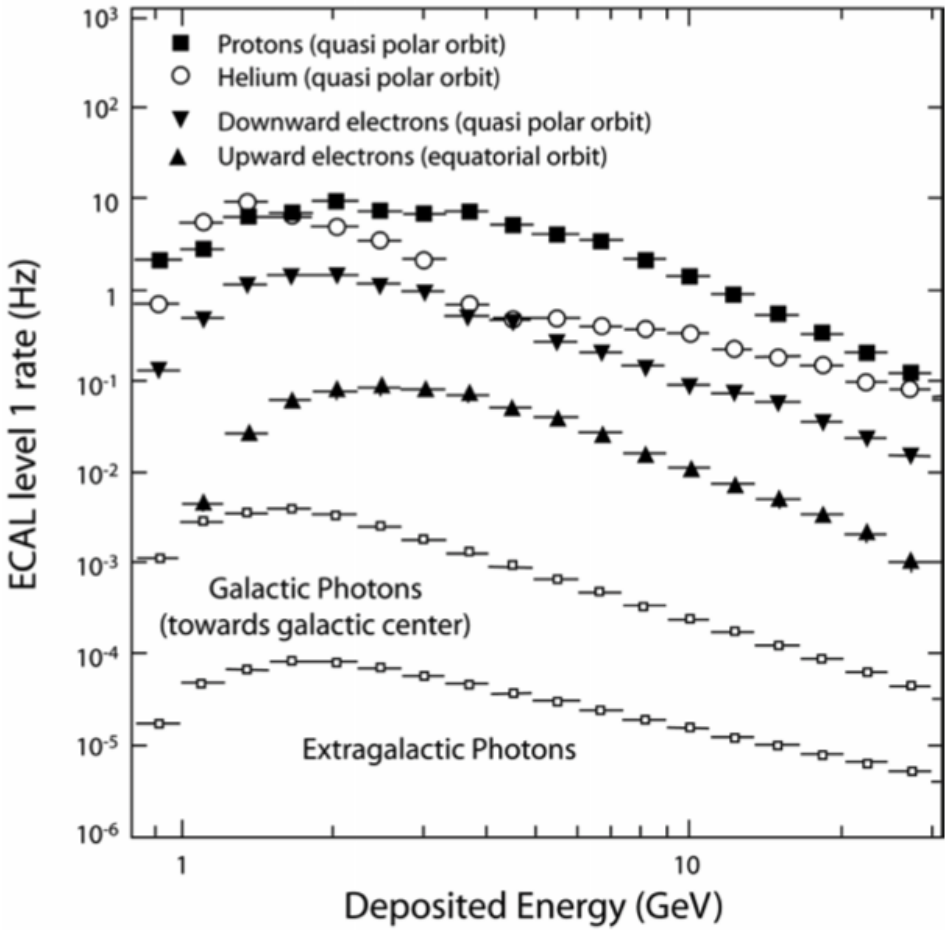

Figure 3.24: Expected ECAL stand alone trigger background and photon rates.

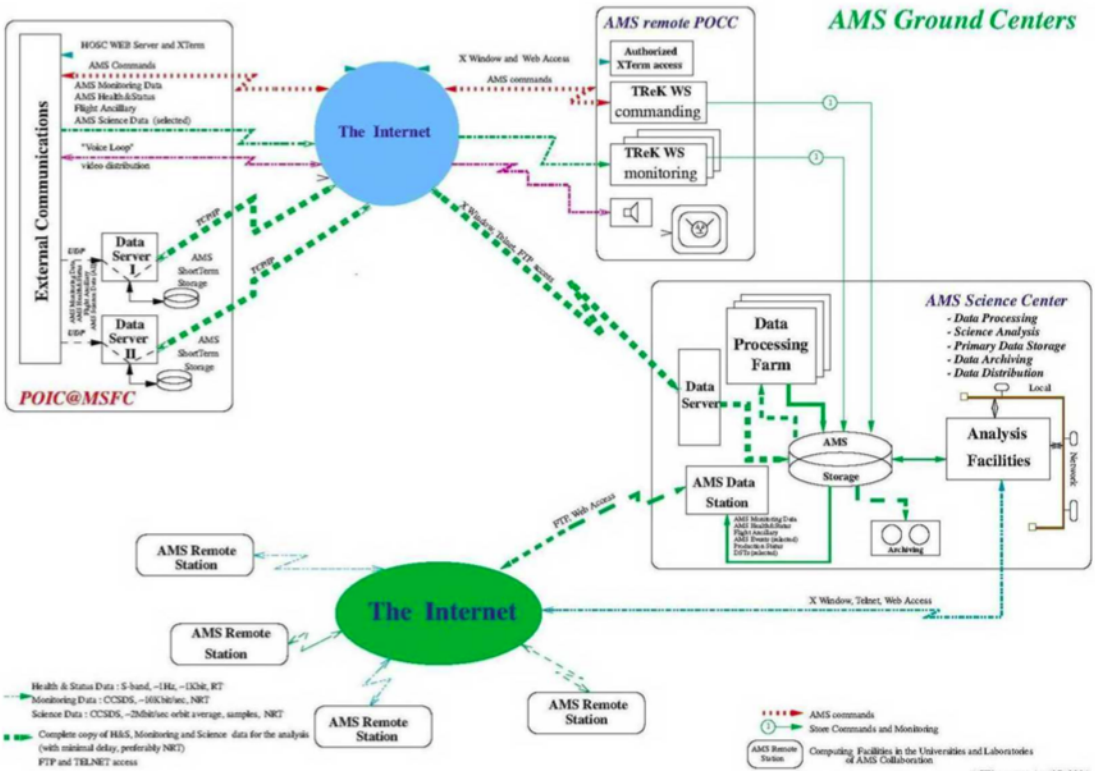

Figure 3.25: Data transmission from `NASA-MSFC` to AMS Ground Control Centers via the Internet.

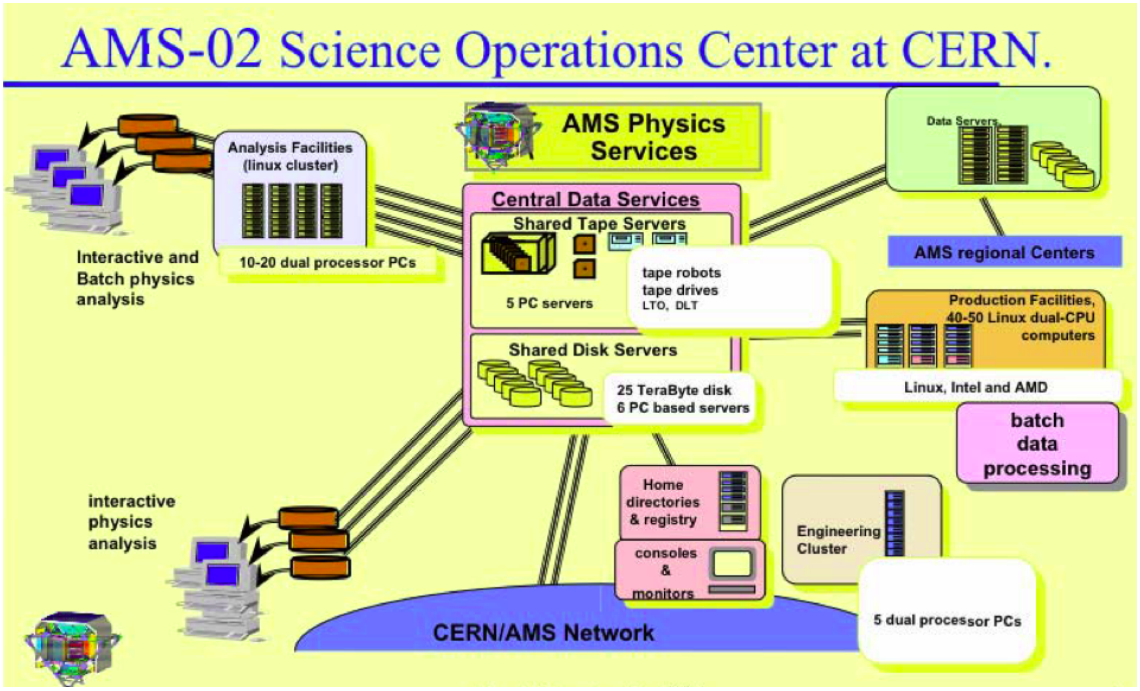

Figure 3.26: The AMS Science Operations Center(SOC) at CERN.

The POCC is where AMS operations will take place, including commanding, storage and analysis of housekeeping data and partial science data analysis for rapid quality control and feedback. After a check out period when AMS is first installed on the space station, the POCC will be located at CERN, with a backup location at MIT. The commanding and detector control will be done from this one single place. However, detector monitoring programs can be run by experts from different geographical locations at their home institutes.

The SOC (Fig. 3.26) receives and stores all AMS science and housekeeping data ensures full science data reconstruction, calibration and alignment and keeps data available for physics analysis. All data is archived. A SOC prototype has been setup at CERN and is in use for AMS-02 Montecarlo simulation. The SOC event reconstruction facility will ensure the full reconstruction of about 10% of the input events with an average time delay of no more than half an hour and the full reconstruction of 100% of the events with a typical delay time of less than one day. The complete Ground Data Handling and Remote Commanding System is scheduled to be up and running six months before AMS launch to support AMS testing and the early installation of AMS Crew Operation Post computer (ACOP) on the ISS.

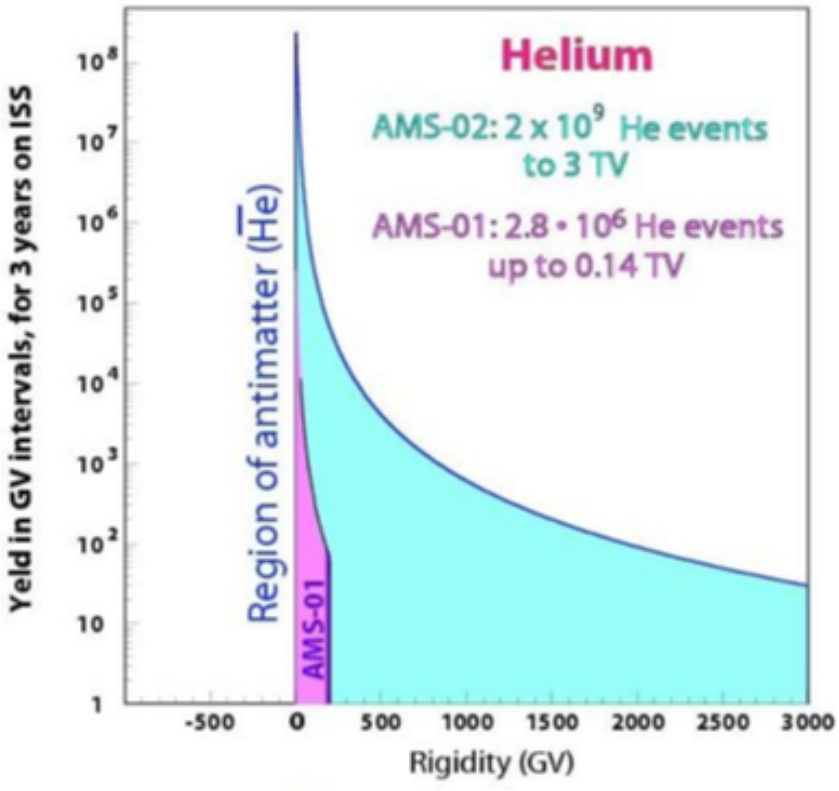

Figure 3.27: The expected Helium spectrum with AMS-02 after 3 years on the ISS compared to the AMS-01 measurements.

3.3 The AMS-02 yields

Helium - AntiHelium

AMS-01 during the 10 days precursor flight on the Shuttle, has pushed the limit on the anti-^4He at a level of less than about one part in a million; AMS-02 will eventually reach a sensitivity a thousand times better: in three years on the ISS, AMS will collect approximately 2×10^9 Helium events up to 3 TV (Fig. 3.27).

Protons, anti-protons, electrons, positrons

In three years on the ISS the estimated collected data include:

$\sim 10^6$ proton events above 1 TeV;

$\sim 10^6$ anti-proton events above 5 GeV;

$\sim 10^7$ electrons above 10 GeV up to 1.4 TeV;

$\sim 2 \times 10^6$ positrons above 5 GeV;

Gamma ray sources

EGRET [197] has detected more than 60 blazar AGNs with a mean red-shift near $z = 1$ and more than 10 unidentified, likely blazar γ-rays sources. AMS will detect about one thousand such objects in three years [198, 199]. Further details on AMS capability to perform gamma ray sources detection will be presented in Chap 8.

Gamma ray spectra

Precise measurement of diffuse gamma ray fluxes may also reveal the origin of dark matter, while gamma rays originating from different sources such as active galactic nuclei (AGN) and gamma ray bursts may provide information about possible quantum gravity effects.
AMS-02 will be able to measure the galactic and extragalactic diffuse gamma ray spectra up to 1 TeV [198]. In addition, up to 10 gamma ray bursts and about 500 AGN per year will be recorded. The main backgrounds to gamma ray signals are the proton and electron (positron) events. Two distinct gamma ray signatures were exploited to estimate the capability of AMS-02 to detect gamma rays: *low energy mode* (or *conversion mode*) and *high energy mode* (or *electromagnetic mode*). In *low energy mode*, the photon is converted in top of AMS and an electron-positron pair is detected in the AMS TRACKER. From the measurement of the production angles and energies of the e^+, e^- pair, QED provides excellent information on the initial direction of ray. In this mode photons may be detected from 1 to 200 GeV with excellent pointing accuracy.
In *high energy mode*, the photon is detected by its characteristic shower in the electromagnetic calorimeter and an absence of charged tracks in the rest of the detector. In this mode photons may be detected from a few GeV up to TeV with an energy resolution of a few per cent and a typical angular resolution of 1 degree.

Isotopes

Regarding the stable light isotopes, AMS will be able to identify ^2H from ^1H and ^3He from ^4He up to ~ 10 GeV/n and, after 3 years of data taking. AMS will collect $\sim 10^8$ ^2H and ^3He. Among all β-radioactive secondary nuclei in cosmic rays, ^{10}Be is the lightest isotope having a half-life comparable with the confinement time of cosmic rays in the galaxy. AMS will be able to separate ^{10}Be from the stable ^9Be [200, 201, 202, 203].
These measurements can provide a detailed description of the cosmic ray propagation history for individual elements. Moreover, the ratio of selected unstable isotopes of the same origin is directly related to the cosmic ray confinement time in the galaxy.

Chapter 4

The AMS-02 Silicon Tracker

4.1 Introduction

The AMS-01 Silicon Tracker [204, 205, 185] was the first application in space of the high precision silicon technology developed for position measurements in accelerator experiments [206, 207]. The high modularity, low voltage levels (< 100 V) and gas-free operation of the device are well suited to operation in space. The AMS Silicon Tracker is the largest silicon tracking detector built for a space application with what would be an excellent precision for a ground based array. The 1998 shuttle test flight demonstrated both the successful adaptation of the technology to the space environment and the feasibility of large area detectors. The AMS-02 Silicon Tracker design and construction is under the responsibility of INFN-Perugia with the strong participation of the University of Geneva and RWTH-Aachen groups. The assembly of the silicon ladders, which represents a substantial part of the construction effort, is performed at INFN-Perugia, University of Geneva and at an Italian industrial research facility operating under an ASI contract. The Tracker mechanical support as well as the Tracker laser alignment system are designed and built in Aachen. The DAQ electronics and power systems were developed at the University of Geneva and INFN-Perugia in collaboration with MIT [208] and fabricated at CSIST [209]. The online data reduction software is developed at Montpellier. The Tracker Thermal Control System is designed and built by NLR in collaboration with the University of Geneva, Sun Yat-sen University, Guangzhou, NIKHEF and INFN-Perugia.
Silicon micro-strip sensors were originally developed for vertex detectors in colliding-beam experiments in order to provide a few high precision position measurements near the interaction point. The AMS application differs considerably. The tracking information is provided uniquely by the silicon sensors, which implies a large surface area. The major challenges were to maintain the required mechanical precision and low-noise performance in this large scale application.

The Silicon Tracker is composed of eight layers of double-sided silicon microstrip detectors as shown in Fig. 4.1. The mechanical structure is made of five aluminum honeycomb support structures, called planes, previously used in the AMS-01 tracker. The new silicon sensor configuration enables a better track reconstruction, intro-

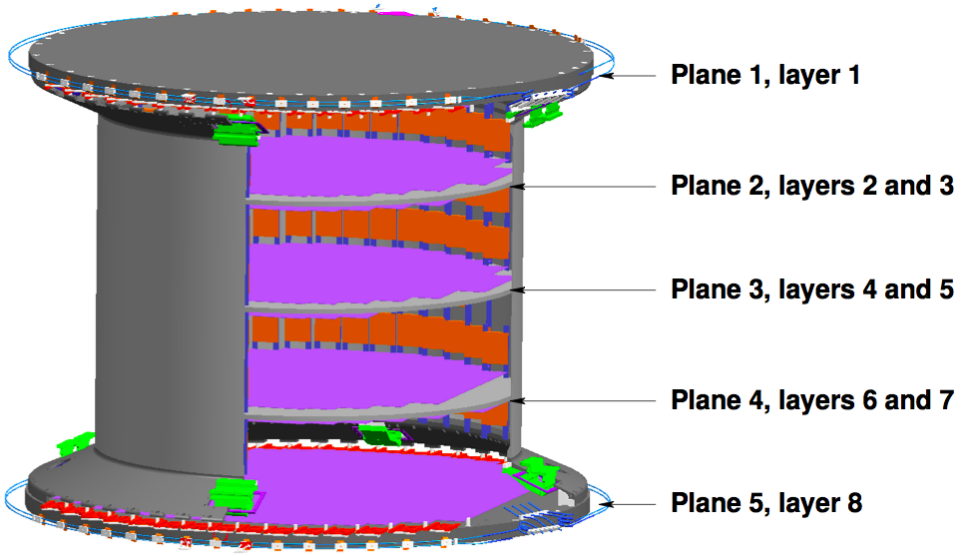

Figure 4.1: The silicon tracker of AMS-02. The internal planes (2 to 4) are equipped with silicon microstrip detectors on both sides, while the external planes (1 and 5) are equipped on one side only. The total detection surface is 6.39 m^2.

ducing redundancy for each internal plane. The number of measurements in the magnetic field volume is increased to better evaluate the track sagitta. Finally, this configuration allows to better compare tracks separately reconstructed with the upper and the lower layers.

The spectrometer is able to measure rigidities up to a few TV. The measurement of specific energy loss, dE/dx $\sim Z^2$, in the silicon serves to identify nuclei. The tracker also measures the direction and energy of photons, converted in the material above the first tracker layer, with excellent directional resolution and good energy resolution.

The sensitive area, composed of 192 ladders provides 196608 channels for a total detection surface of 6.39 m^2. The module mechanical concept is based on the Silicon Microvertex detector (SMD) of the L3 experiment at CERN [206]. The spatial resolution is 10 μm on the bending plane (p-side, here and in the following denoted as S-side) and 30 μm on the non-bending plane (n-side, here and in the following denoted as K-side) [210].
The magnet design has important implications for the cooling. While the AMS-01 permanent magnet played the role of heat exchanger, the new one must be isolated from the heat produced by the ladder front-end electronics. For this purpose, a cooling system composed of mechanically pumped two-phased CO_2 loop is used. The tracker power consumption is foreseen to be of the order 640 W and its weight is 198.5 kg taking into account of the alignment system ($\sim$ 3 kg) and the cooling loop ($\sim$ 2 kg) but without the external mechanical structure and cables.

The ladder front-end electronics is connected, via flat cables, to the Tracker Data Reduction boards (TDR). The TDR design consists of a Common Digital Part, a circuit structure common to each AMS-02 subdetector readout and the analog-to-digital front-end. The CDP (Common Digital Part) is connected to the analog-to-digital frontend, reading out the sub-detector. The CDP is composed of a gate array, a DSP, a buffer memory for input and output data and a flash memory for the ROM Monitor and the DAQ programs.
In the TDR, the analog-to-digital front-end is composed of three 12-bits ADCs and a 3-bit DAC. The ADCs are used to read out the signals coming from the ladders: 2 ADCs are dedicated to the S-side, the remaining ADC to the K-side. As AMS is a space experiment, with no possibility to recover a defunct part, it is necessary to implement redundancy. The TDR's present no redundancy in contrast to other subsystems in AMS. The redundancy is materialized by the silicon modules themselves, with 8 silicon layers, each having two detection sides. The data are transmitted from the ISS to Earth via two connections. The High Rate Data Link enables a peak transmission rate of 10 Mbps, with a mean orbit rate of 2 Mbps. The Low Rate Data Link, offers a constant 10 kbps (out) and 1 kbps (in) transmission and is used to transmit the status information and also the control signals.

4.2 Silicon sensors

The silicon tracker is composed of close to 2500 of $41.360 \times 72.045 \times 0.300\ mm^3$ double-sided silicon micro-strip sensors (Tab. 4.1). The n-type, high resistivity (> 6 kΩ) sensors are biased with the punch-through technique and p^+ blocking strips, implanted on the K-side, are used to minimize the influence of surface charge on the position measurement obtained from the ohmic side [211]. The sensor design uses capacitive charge coupling [212] with implantation (readout) strip pitches of 27.5 (110) μm for the S-side and 104 (208) μm for the K-side. The finer pitch S-side strips are used to measure the bending, or y, coordinate while the orthogonal K-side strips measure the non-bending, or x, coordinate. Fig. 4.2 shows the sensor layout.
The ionization loss of singly charged particles traversing the fully depleted, reverse-biased 300 ± 10 μm thick sensor is described by a Landau distribution [214]. The peak energy loss of a singly-charged, minimum ionizing particle at normal incidence produces 22,000 electron-hole pairs. The opposite sign +/- charge carriers drift rapidly ($10 \div 25$ ns) in the electric field to the two surfaces (p/n) where the accumulated charge on the metalized strips (p+/n+) is fed to the front-end electronics. The position of the particle is determined by the relative signal levels observed at the readout strip positions. At the single sensor level, the position resolution depends on the readout pitch and the signal-to-noise performance.
The sensors have been produced at silicon foundries located in Switzerland [215] and Italy [216] using identical geometries and procedures. More than 4000 sensors have been produced to select the 2500 highest quality sensors required to assemble the Silicon Tracker. The sensors were cut with a mechanical accuracy of 5 μm (rms) at a facility in Finland [217]. All the sensors were tested twice, once at the foundry

	AMS-01	AMS-02
Dimensions	$72.045 \times 41.360 mm^2$	$72.045 \times 41.360 mm^2$
Thickness	$\sim 300 \mu m$	$\sim 300 \mu m$
Active width, S-side	$70.595 mm$	$70.595 mm$
Strip pitch, S-side	$27.5 \mu m$	$27.5 \mu m$
no. of p-strips	2568	2568
no. of metal strips, S-side	1284	1284
no.of S-side readout strips	640	640
readout pitch, S-side	$110 \mu m$	$110 \mu m$
Active width, K-side	$39.832 mm$	$39.832 mm$
Strip pitch, K-side	$52 \mu m$	$104 \mu m$
no. of n-strips	767	384
no. of metal strips, K-side	767	384
no.of K-side readout strips	192	192
readout pitch, K-side	$208 \mu m$	$208 \mu m$

Table 4.1: AMS microstrip detectors geometries.

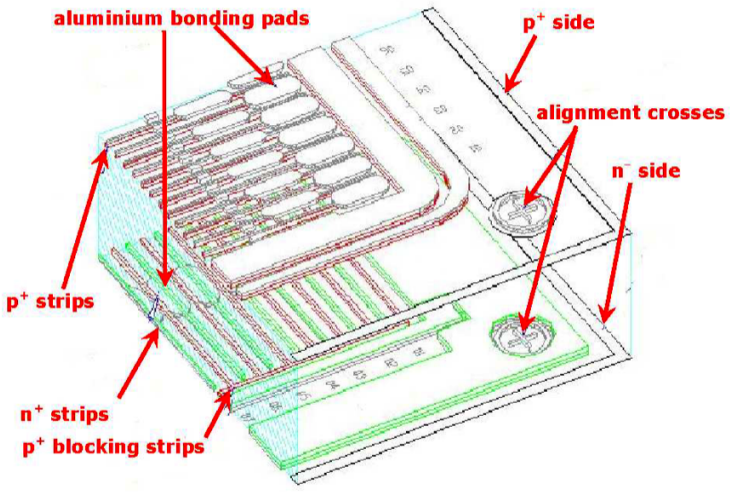

Figure 4.2: Layout of the double-sided silicon microstrip sensor.

and a second time, after cutting, at INFN-Perugia and the Italian industrial facility, to ensure that electrical parameters and performance meet the space qualification requirements, for example that the number of noisy strips was less than 0.6% per sensor. Over 2×10^7 electrical measurements have been performed using four automatic test stations. The data were stored in a database and used to select the silicon detectors to be used in assembling the Tracker.

For AMS-02, the silicon design was upgraded to decrease as much as possible the noise transmitted to the readout channel. It is important to note that long silicon modules (up to 15 double-sided silicon sensors) are not common in particle physics experiments, due to noise and occupancy limitations, e.g. in high multiplicity collider environment. The noise issued from a silicon ladder is due to:

- the strip leakage current;
- the polarization resistance, i.e. the resistance between the strips and the guard ring to which is applied the biasing voltage;
- the strip metalization resistance;
- the preamplifier noise, which depends on the input capacitance;

All these parameters depend on the channel length, i.e. the number of sensors in a ladder. An intense collaboration between the tracker group and the manufacturer resulted in the modification of the sensor design and fabrication, to:

- decrease the silicon dark current ("Lowleak" process);
- decrease the strip metalization resistance, in increasing the metalization thickness;
- increase, on the K-side, the polarization resistance, using the surface through method.

In addition to these points, other modifications are:

- the n-strips are wider and their number is reduced by half, to increase the K-side charge collection [210];
- the sensors have a 1 μm SiO_2 passivation layer to protect the silicon surface against degradation during manipulations and surface contacts. This enables safer assembly procedures;
- new metrology patterns have been designed, to take a better advantage of the optical pattern recognition system of the metrology machine;
- the cutting line has dashed metalized lines, to make the cutting procedure easier;

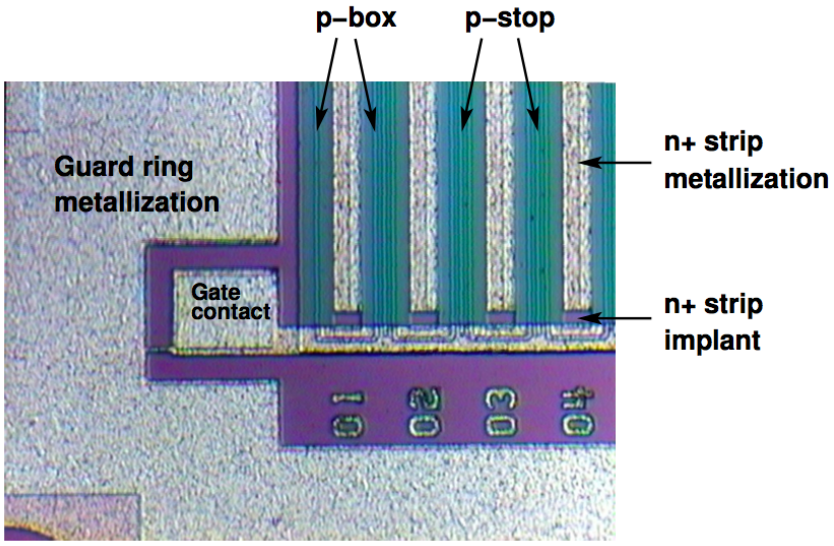

Figure 4.3: K-side of the AMS-02 detector: closeup view.

- the bonding pad length has been increased to 300 μm.

The maximum allowed depletion voltage is 50 V (thus corresponding to a bulk resistivity of minimum 6 k$\Omega\cdot$ cm), and the chosen operating voltage is 80 V.

The K-side strip insulation is different from the solution retained in AMS-01. The strips are surrounded by n-boxes, themselves separated with n-stops, as depicted in Fig. 4.3. We also recognize a FOXFET-like structure, with a 0 V gate voltage, as the gate metalization is connected to the guard ring metalization.

Anti-reflective sensors

In the tracker, an infrared laser alignment system has been implemented to survey the tracker alignment (see Chap.3). For this purpose, openings are designed on the corresponding K-side Upilex cables and on the Upilex shielding. Moreover, the silicon surface has to be treated in a circular patch and the strip metalization is narrowed (from 12 μm to 10 μm for the S-side) to improve the infrared beam passage through the detectors. Fig. 4.4 shows the silicon anti-reflecting patch design. Note that thanks to the anti-reflective treatment, the strip implantations are optically observable as shown in Fig. 4.5.

4.3 Ladders

The silicon modules, the ladders, composed of 7 to 15 (except 8) microstrip detectors, have a length ranging from 29 to 62 cm (Tab. 4.2). Each ladder provides 1024

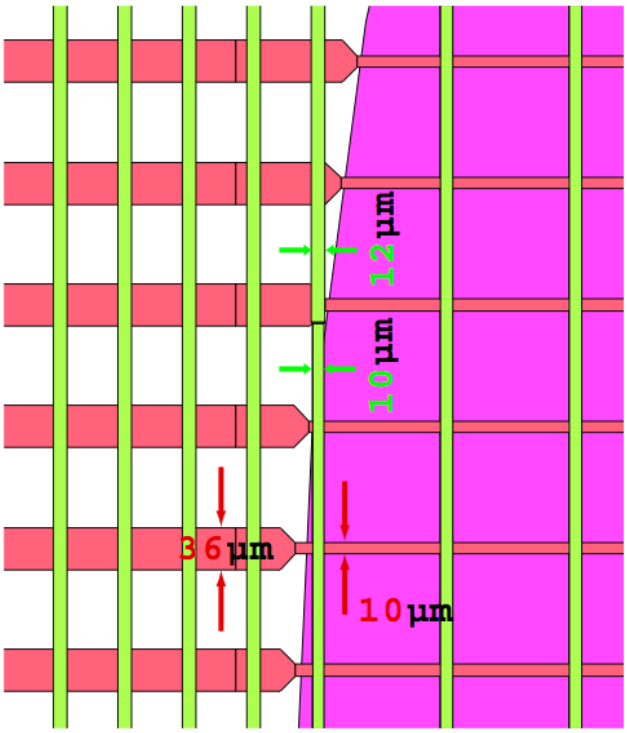

Figure 4.4: Anti-reflective patch design, detail.

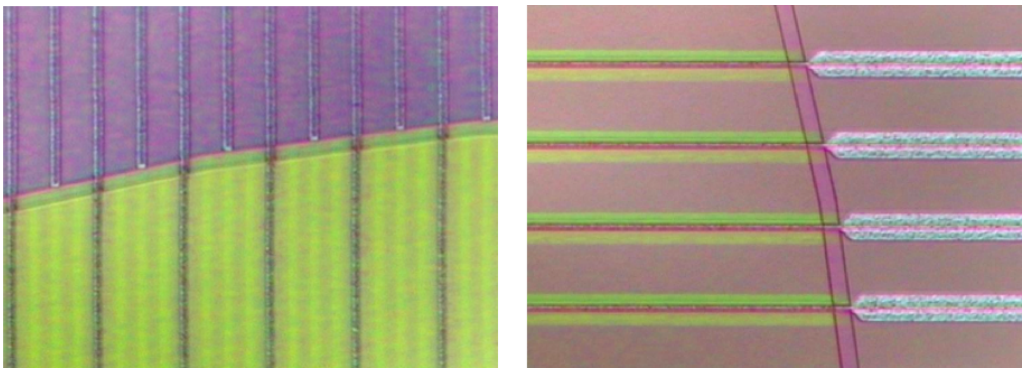

Figure 4.5: Anti-reflective patch, S-side (left) and K-side (right). Note that thanks to the special surface treatment, the strip implantations are optically observable.

Length	Type	L1	L2	L3	L4	L5	L6	L7	L8	Ladders	Sensors
7	I(K5)		2					2		4	28
9	I(K5)		4	4	4	4	4	4		24	216
10	I(K5)		2	2	2	2	2	2		12	120
10	O(K7)	4							4	8	80
11	I(K5)		4	4	4	4	4	4		24	264
11	O(K7)	2							2	4	44
12	I(K5)		5	5	5	5	5	5		30	360
12	H(K5l)		3	2	3	2	3	2		15	180
12	J(K5u)		2	3	2	3	2	3		15	180
12	O(K7)	2							2	4	48
13	O(K7)	4							4	8	104
14	I(K5)		2	2			2	2		8	112
14	O(K7)	6							6	12	168
15	N(K7l)	3							2	5	75
15	P(K7u)	2							3	5	75
15	O	7							7	14	210
	Total:	30	24	22	20	20	22	24	30	192	2264

Table 4.2: Ladders composing the AMS-02 tracker. There is a total of 192 modules, corresponding to a total of 2264 silicon detectors, i.e. a total detection surface of 6.39 m^2.

readout channels.

Fig. 4.6 shows the main elements of the silicon ladder and the components of the readout hybrids. The S-side is facing up and is known as the ladder S-side. The reverse side, corresponding to the silicon K-side, is called K-side. On the S-side, the strips are daisy chained with micro-wire bonds, to redirect the signals to the electronics. The final routing is achieved through a short Upilex cable, connecting the first sensor strips to the S front-end electronics ("S-hybrid"). On the K-side, a long Upilex cable is glued to redirect the signals to the K front-end electronic ("K-hybrid"), as the strips are transverse. In total, a ladder provides 1024 readout channels, 640 for the S-side, 384 for the K-side. In order to ensuring a sufficient flexibility to sustain the strong vibrations during the shuttle flight, yet maintaining sensor positions to the required accuracy, a reinforcement, made of 5 mm Airex [218] foam and carbon fiber, is glued on the K-side Upilex.

The exposed surface of the foam is covered with a 100 μm thick layer of carbon fiber. Small $5 \times 5 \times 5$ mm^3 aluminum support feet are glued to the carbon fiber surface; the exact number depends on the ladder length. The feet contain screw fixation holes which are used to attach the ladder to its tracker plane.

The principal goals of the ladder fabrication are to guarantee the required preci-

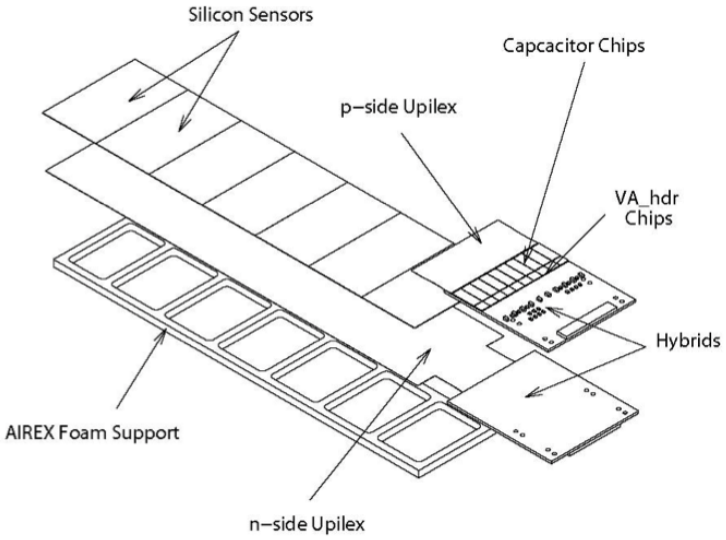

Figure 4.6: The main components of the silicon ladder.

sion for the relative alignment of the silicon sensors (< 5 μm), and minimize the degradation of the electrical performance due to handling and ultra-sonic bonding.

Ladder fabrication was organized between three centers operating with identical procedures derived AMS-01 [219] and located at INFN-Perugia, the University of Geneva, and the Italian industrial center operating under an ASI contract. These centers used state of the art facilities in class 10,000 clean rooms and follow strict quality control procedures. The alignment precision is provided by the mechanical precision of the jigs (1-2 μm) and the precision of the sensor cut. During fabrication the sensor positions on a ladder are recorded with a 3D semi-automatic measuring machine. The results for the sensor alignment for 125 over 192 AMS-02 ladders are shown in Fig. 4.7. A particular effort has been made to lower the noise by passivation of the silicon and by optimization of the ladder assembly procedure.

4.4 The Ladder Front-End Electronics

An overview of the front-end electronics of the AMS-02 tracker is given in the following. More details are available in Ref. [220].

4.4.1 The Hybrids

The silicon sensors are grouped together, for readout and biasing, in ladders of different lengths to match the cylindrical geometry of the AMS magnet. The maximum combined strip length in the silicon for a single readout channel is about 60 cm. The relatively large input capacitance (30 to 180 pF), as well as the need for a high dy-

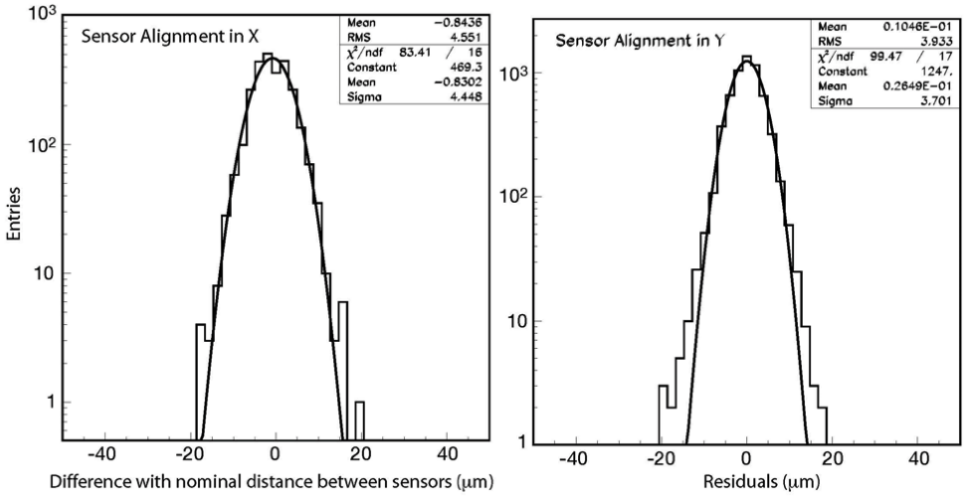

Figure 4.7: Assembly precision of 125 AMS-02 ladders: distribution of the measured differences of the distance between adjacent sensors and the nominal distance (left), and the residual distribution of the sensor positions about the line fits defining the ladder axis parallel to the magnetic field (right). As a reminder, the distance between to adjacent sensors is given by the sum between twice the distance of the sensor border from the metrology cercle ($2 \times 300\ \mu m$) and the gap between the border of the two sensors themselves ($40\ \mu m$).

namic range (up to 100 MIPs), led to the development of a new front-end readout chip based on the low-noise Viking design [221], the VA_hdr9a [222]. As for the ladders and support structure, the tracker electronics is an upgraded and updated version of the circuits developed for AMS-01 [223].
The most important improvements with respect to previous version of this board that flew on the STS-91 mission are:

- the modification of the coupling capacitor chips with the removal of the protection diodes;
- the choice of a new version of the front-end chip, the VA_hdr9, with a gain increase by a factor of 1.6 with respect to the AMS-01 chip;
- the introduction of a custom made chip, called HCC (Hybrid Control Circuit), developed to steer control signals to the VA_hdr9. This chip minimizes the effect of malfunctioning of any front-end chip and reduces also the number of control lines, essential in order to have the cabling satisfy the tight mechanical constraints;
- the inclusion of an amplifier in the hybrid, based on the chip AD8052 from Analog Devices to drive the analog signals through the cables.

Two separate boards are used to readout the ladder, one for each side. The S-side board reads 640 channels, while the K-side reads 384 channels. The main hybrid

structure is the same on both sides: the first stage is composed of decoupling capacitor chips (RCAMS), the second stage is composed of the preamplifier/shaper, the VA64_hdr9a. The VA control sequences are driven by the HCC chip, and the output signals are amplified by AD8052 operational amplifiers. Additionally, K-hybrid is equipped with a DS1820 temperature sensor, with a unique serial number, which identifies the ladder.

Each of the 64 channels of the VA_hdr9 chip consists of a charge sensitive amplifier, a CR-RC semi-Gaussian shaper, and a sample-and-hold stage. An analog multiplexer, shift register and buffer are incorporated in the chip for sequential data output at a maximum clock frequency of 10 MHz. The equivalent noise charge as a function of capacitance load C_{det} has been measured to be (350+4C_{det}/pF) electrons at a 6 μs peaking time and nominal bias currents. The VA_hdr chips are operated at a lower bias current resulting in a peaking time of 3 to 4 μs and average power consumption of 0.7 mW per channel. The single channel response of the VA_hdr chip has been measured to be linear up to $\sim$75 MIPs. The strips of the silicon sensors are AC-coupled to the VA_hdr via 700 pF capacitor chips [224]. Both the VA_hdr chips and the capacitor chips are housed on the Tracker Front End board (TFE) that also contains a resistor network to furnish the VA_hdr operating currents, a receiver chip for digital control signals and a low power analog amplifier for the current-to-voltage conversion.

In total 192 flight hybrids per type are needed. Including spares and prototypes, 250 pairs have been assembled.

The RCAMS

The RCAMS is composed of 64 capacitors, each with a typical capacitance of 700 pF. An additional line, the bias, is available to transmit the bias voltage to the silicon detector. The designs for AMS-01 and AMS-02 present differences. The AMS-01 capacitor chip was based on the models used for the ALEPH [225] and L3 [206] experiments at LEP. The schematic design is presented in Fig. 4.8. Double Zener diodes have been included in order to protect the capacitor from heavy charge release which might occur in case of beam loss [206]. The diodes become conductive, thus avoiding that the charge accumulates on the capacitors and eventually damages them.

In AMS-02 the RCAMS design has been simplified: as the detector is not exposed to an intense particle beam, it was decided to suppress the protection diodes. The motivation to simplify the design was to decrease the risk of having defective capacitor channels, due to a too low diode conductive threshold voltage, thus hindering the signal to reach the VA input.

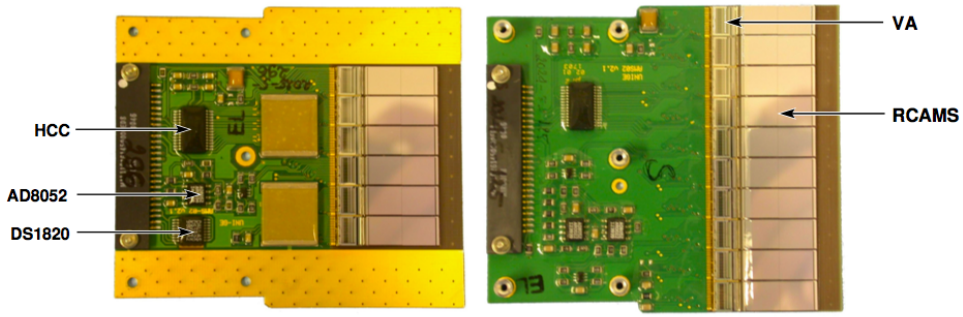

Figure 4.8: AMS-02 hybrids: K-side on the left, S-side on the right.

The VA preamplifier

The VA family of analogue front-end chips exists in versions with different number of input channels and various gains [221, 226]. The motivation for developing such a device was the necessity to have a low noise amplifier, particularly adapted to silicon microstrip and photomultiplier detectors. Indeed, the signal produced by a minimum ionizing particle (about 22000 electron-hole pairs) needs to be amplified and thus all noise sources need to be reduced. The VIKING design is based on the AMPLEX chip, described in detail in [227].

The AMPLEX processor

This chip was used for the readout of the UA2 silicon detectors [228]. It had to fulfill two main constraints: a low power consumption (less than 1 mW per channel), and a signal processing time between 600 ns and 800 ns. An important aspect of the AMPLEX design is that it allows for a DC coupling with the detector: the readout channel is biased through the amplifier. Also, it is constantly sensitive to the input signal: no trigger is needed to start the readout. The AMPLEX design relies on two operating transconductance amplifiers (OTA). Fig. 4.9 shows the schematic of one AMPLEX channel.

The VA64_hdr9a

The VA64_hdr9a is a high dynamic range charge sensitive amplifier-shaper circuit, with simultaneous sample and hold. It has a multiplexed analog readout and has a gain calibration mode. Initially, for AMS-02, three versions of this VA were developed, “a” and “b” versions had different fixed gains, while the “c” version offered 4 different gains. The VA architecture is presented in Fig. 4.10. The VA is operated with 3 voltage levels: -2V (V_{ss} and back contact), 0V (gnd) and +2V (V_{dd}). The analog input pads are at -1V.
As mentioned earlier, a calibration mode is available. In this mode, the clock is used to select the channel to be examined and the output signal of the selected channel

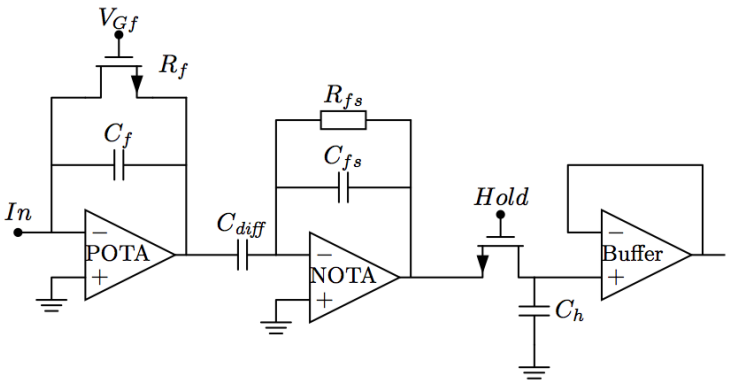

Figure 4.9: Amplifier and shaper stages of one AMPLEX channel.

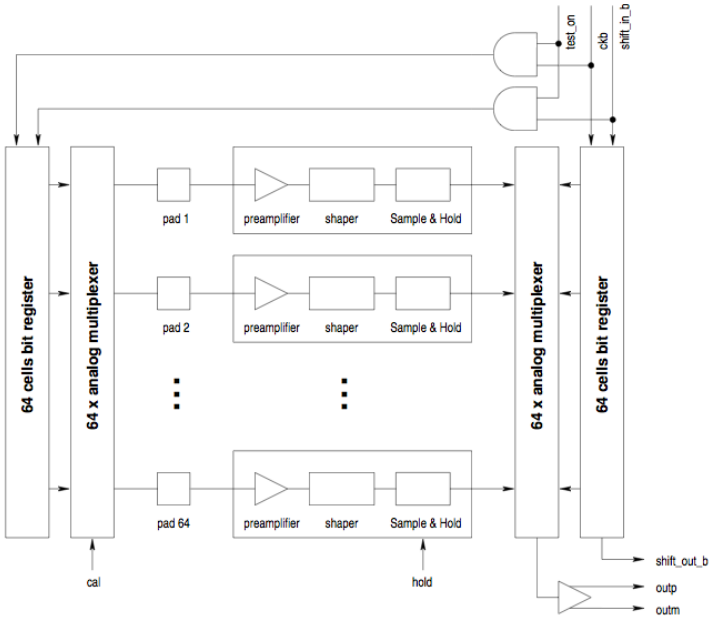

Figure 4.10: VA64_hrd9a architecture [229].

can be constantly monitored.

4.5 AMS-02 ladder production

Before the assembly starts, the silicon sensors composing the future ladder are tested a last time in a probe station. The total leakage current of each sensor is measured, for biases going from 0 to 100 V. Figure 4.11 shows the measurements for the sensors of an 11-long ladder. The sensors show a limited leakage current up to a given break-down voltage. Sensors are accepted if their leakage current is below 1000 nA at 80V.

If a non-standard, unexpected behavior is observed, the ladder assembly is suspended, and a replacement sensor is selected. After this test, the sensors are visually examined and if necessary, dust particles are removed from the sensor surface. The sensors are then stored, and usually assembled the day after. Once the sensors are positioned on the ladder assembly jig, a metrology measurement is performed of the position of optical fiducial marks on the sensors. Their residuals with respect to their nominal position should not exceed ± 10 microns. The precision is obtained thanks to the jig, which gives the alignment, but also depends on the sensor cut quality and reproducibility. This is shown for example in Figure 4.12. All sensors composing a mechanical prototype ladder (M11GT004) come from the same batch, which means the sensors were cut with exactly the same parameters. The sensors composing the ladder shown for comparison (L09GI002) come from various batches and were cut with slightly different cutting parameters: the residual variation is larger, though still within the acceptance criteria.

The hybrids are also visually inspected, in particular, the bias connections, the capacitor positioning and the capacitor bonding pads cleanliness are examined. The hybrids are electrically tested before assembly.
When the hybrids are glued, the ladder is tested. It is then possible to compare the ladder current with the expected values, estimated from the sum of individual sensor measurements as shown in Figure 4.13. The agreement is generally good indicating that no additional degradation is caused by the bonding process.

Before starting the real production, five mechanical prototype ladders were produced until January 2001. The sensors used were 300 μm thick with the AMS-02 metalization scheme, but with no implantation. The main goal of this assembly was to qualify the assembly procedures at University of Geneva and at CERN.
The official production of ladders started in February 2001 and ended until September 2005. At the end of 2005 ladders integration onto tracker inner planes was completed. Outer planes integration lasted until the end of 2006.
A total of 212 ladders were assembled from which the best 192 were used to be installed on AMS-02 Tracker.

The overall quality of the production is high, as shown in the following sections. The amount of ladders where a sensor or a hybrid had to be replaced due to damage during assembly is low.

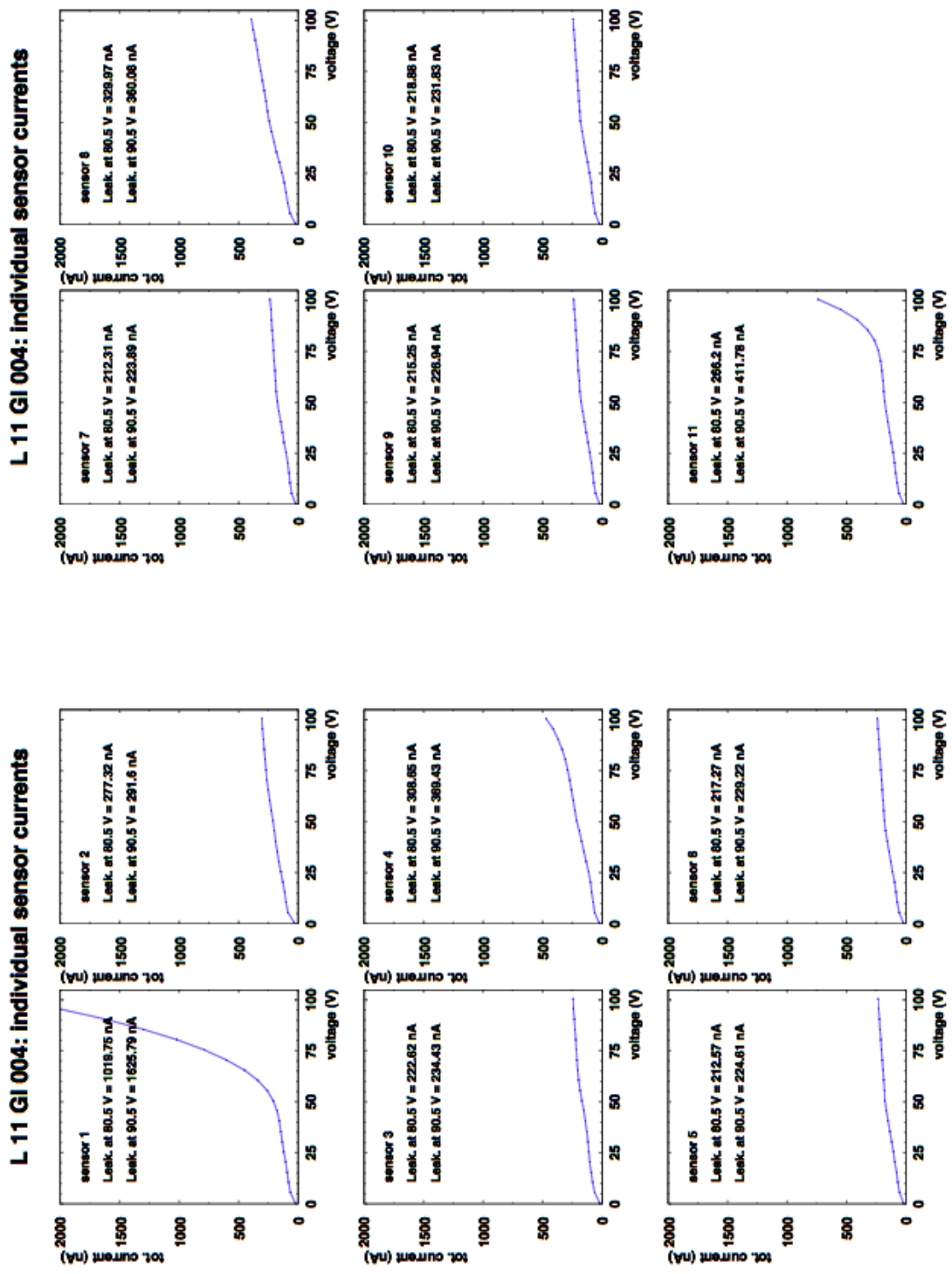

Figure 4.11: Individual sensor current measurements as a function of bias voltage for an 11-long ladder. The leakage current of sensor 1 is marginal but inside cuts.

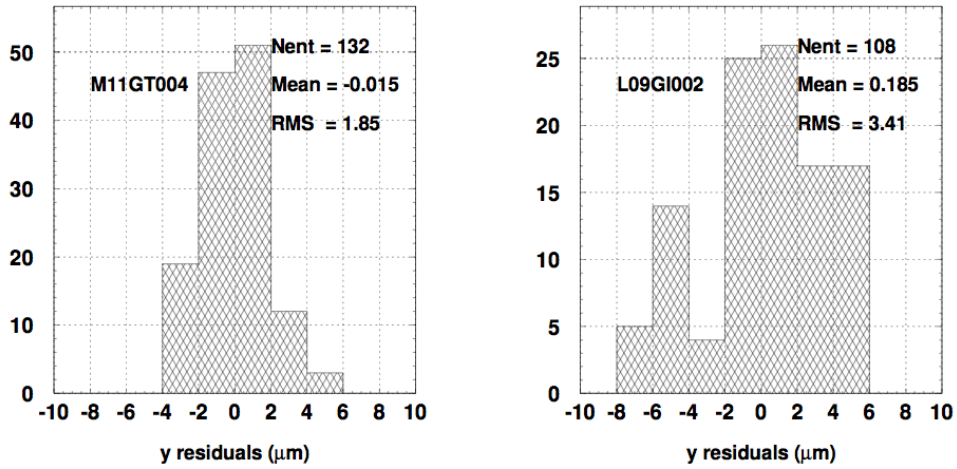

Figure 4.12: Distributions of residuals between nominal and measured sensor positions on an electrical (left) and a mechanical prototype (right). The sensor positioning is better for the ladder M11GT004 for which all sensors were cut with the same parameters.

Global performance

Fig. 4.14 shows the residuals of the metrology crosses (AMS-01) or circles (AMS-02) with respect to their nominal positions. The geometrical AMS-02 ladder quality is similar to the one observed for AMS-01. In Fig. 4.15 the channel noise of all the AMS-02 ladders located at University of Geneva is shown. The channel noise is much lower than for AMS-01 ladders as shows a comparison to Fig. 4.16.

4.5.1 The ladder assembly and the University of Geneva assembly line

As already mentioned, the ladder assembly involved three sites: the University of Geneva (in collaboration with an ETHZ team at CERN), the University of Perugia, and an Italian industry, G&A Engineering.
The assembly sequence and quality control criteria are identical for the three sites. We distinguish three assembly steps:

- silicon detectors final qualification;
- assembly Phase 1;
- assembly Phase 2.

Phase 1 corresponds to the silicon sensor gluing, the hybrid gluing and the microwire bonding. Phase 2 corresponds to the hybrid final operation, feet gluing and metalized foil wrapping. Once the assembly Phase 2 is completed, the ladder is ready to be installed on a tracker plane (integration). G & A [213] had in charge

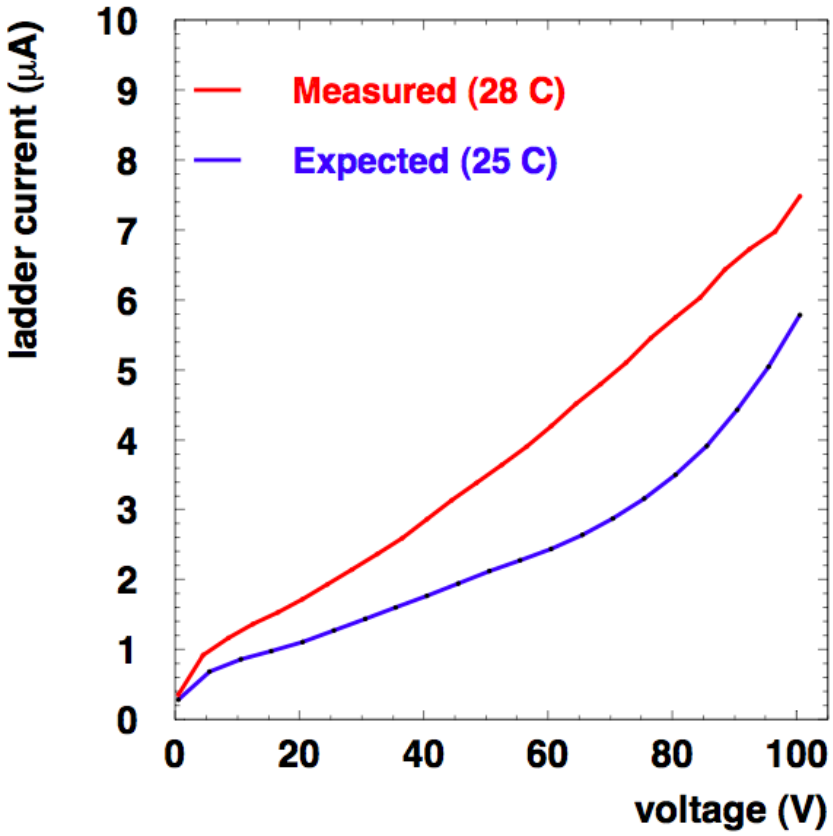

Figure 4.13: The current of ladder L11GI004 as a function of the bias voltage, compared to the sum of all sensor currents. The measured total current is compatible with the expected values, taking into account the temperature conditions.

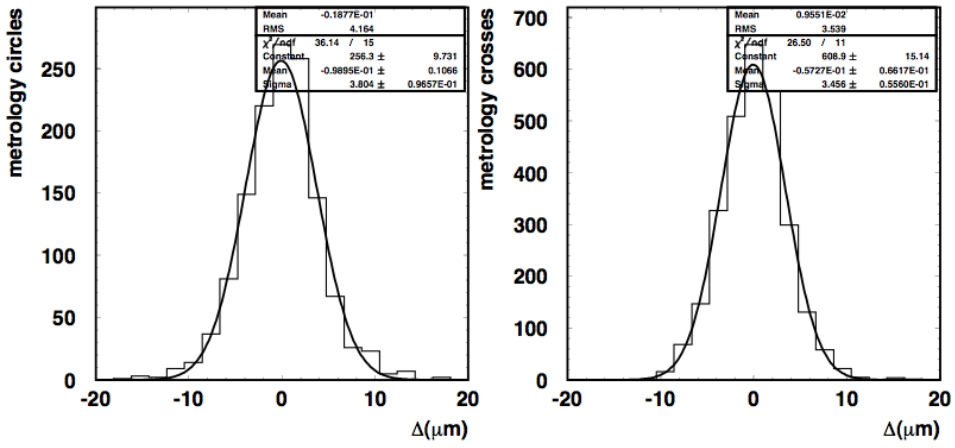

Figure 4.14: The residual distribution of metrology reference circles (AMS-02, left) and crosses (AMS-01, right). The sensor positioning accuracies are similar.

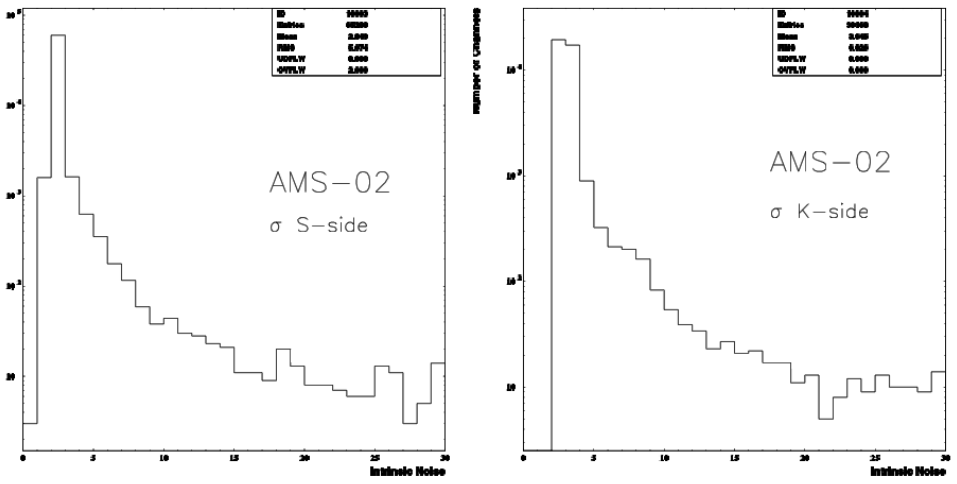

Figure 4.15: Channel noise distribution of the AMS-02 ladders (left: S-side, right: K-side).

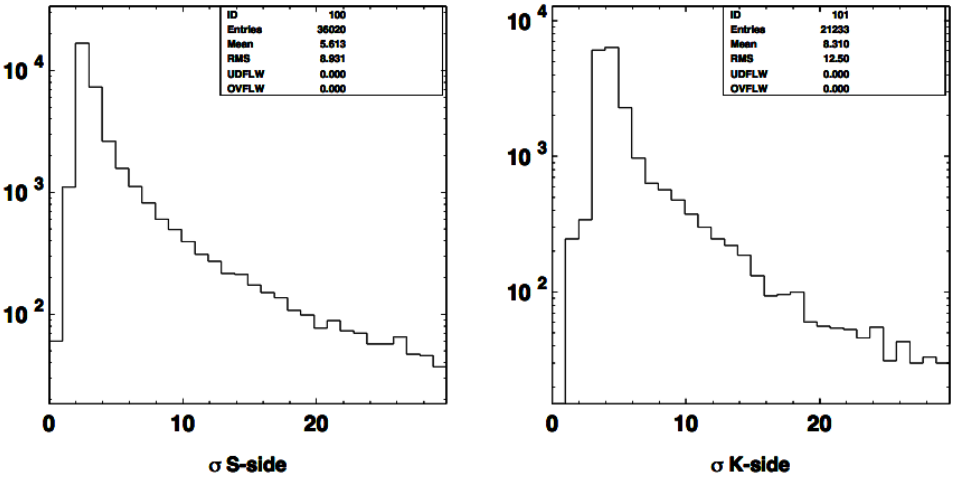

Figure 4.16: Channel noise distribution of the AMS-01 ladders (left:S-side, right: K-side).

site	Silicon tests	Phase 1	Phase 2	Integration
Geneva/ETHZ		X	X	X
Perugia	X	X		
G & A	X	X		

Table 4.3: The three production lines and their activities.

most of the Phase 1 production, while University of Geneva is the only site performing Phase 2. Furthermore the ladders are installed on planes at University of Geneva. Tab. 4.3 sums up the production activities of the three assembly lines.
Silicon microstrip detectors are sensitive devices: producing ladders is thus not an easy task and cannot be performed in a standard laboratory. It is mandatory to work in a clean room environment to avoid dust particle contamination, which could degrade the silicon quality (mechanically and/or electrically). As the detector spatial resolution is of the order of microns, precise alignment and survey tools are needed. The assembly conditions must minimize the impacts on the silicon sensor qualities. Furthermore, the reproducibility of the ladder properties, in terms of mechanical and electrical parameters is mandatory.
University of Geneva clean room has a Mitutoyo metrology machine (equipped with a touch probe and an optical pattern recognition system) to check the precise alignment. To perform efficient, precise and yet fast gluing procedure, a CAM/ALOT gluing machine with a volumetric glue dispenser is used. Two binocular microscopes are also available for all precise handling or inspections. Finally, a vacuum network is needed, to ensure the stability of the silicon detectors once they are precisely aligned.
A grey room is available to perform electrical verifications on the ladders during the multiple assembly tests. Also, visual inspections were realized with a binocular microscope equipped with a video camera connected to a computer. In the same room, the last assembly steps are completed, before the ladders are installed on the tracker plane.
An exploded view of the ladder assembly is shown in fig 4.17

4.5.2 Assembly Phase 1

The assembly Phase 1 defines the operations starting from silicon positioning, and ending with wire bonding. University of Geneva discontinued this task in March 2003, to allow a full involvement in the Phase 2 activities. In the following some phase 1 assembly details are described:

- Preparation:
  before starting the ladder assembly, the total current of each sensor is measured a last time, to check the quality before assembly. If a sensor presents an unsatisfactory behavior, it is replaced. The detectors are then visually inspected on both sides with a microscope and all dust particles are removed using vacuum. The assembly jig surface is then cleaned with isopropyl alcohol

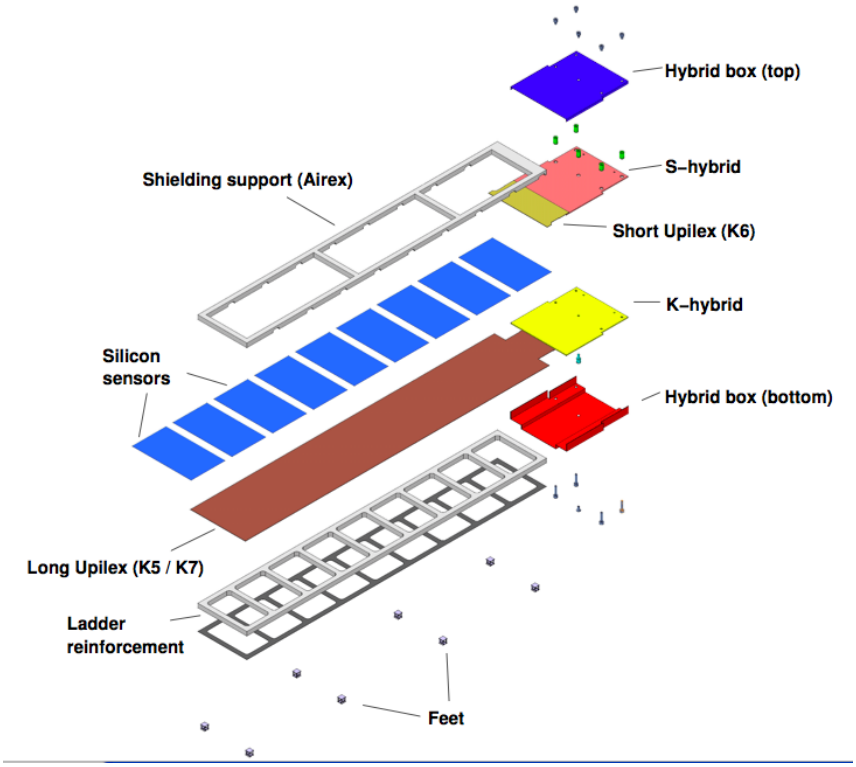

Figure 4.17: AMS-02 ladder exploded view: structure of silicon ladder, the electromagnetic shield is not shown here.

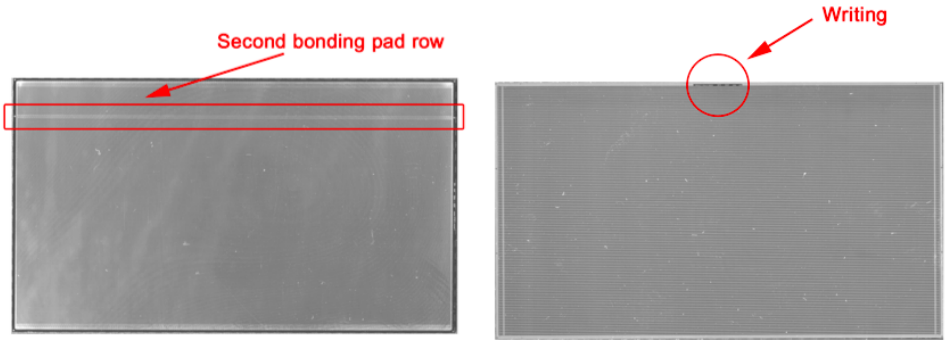

Figure 4.18: AMS microstrip detector: S-side (left) and K-side (right).

and the jig is connected to ground.

- Silicon positioning:
  Fig. 4.18 shows how to differentiate the S- and K-sides of the AMS microstrip detector. The S-side is easily recognizable thanks to the second bonding pad row. On the K-side, a pattern, corresponding to a lack of metalization, is located at the same edge of the second S-side bonding pads raw.
  A metrology program assists the operator during the detector positioning procedure.
  In fact, this operation is handmade (Fig. 4.19). The silicon is gently slid against the teflon pins inserted in the metrology holes of a mechanical jig. Once the sensor is placed, the metrology program moves the camera above the silicon alignment pins to check if the silicon edges touch the alignment pins. If there is no contact with one pin, the detector is removed and the procedure is started again. When the detector is correctly aligned, the pins are removed the procedure is repeted for the next detector. Once all sensors are positioned the final metrology program is executed.

- Long Upilex (K5/K7) gluing:
  for this manipulation, two jigs are needed: the Upilex alignment jig is used to prepare the Upilex cable for the transfer to the Upilex transfer jig, used for the glue deposition on the Upilex surface and for the Upilex gluing on the silicon detectors.

- Reinforcement gluing:
  the reinforcement is inspected and possible foam burrs are removed. The glue is dispensed on a glass plate and expanded with a spatula to obtain an uniform surface. Then the reinforcement is laid on it (carbon fiber up). When ready it is disposed on the Upilex slightly pushing against an alignment bar. A pressure is applied on the reinforcement using glass plates and lead blocks.

- S and K-hybrid gluing:

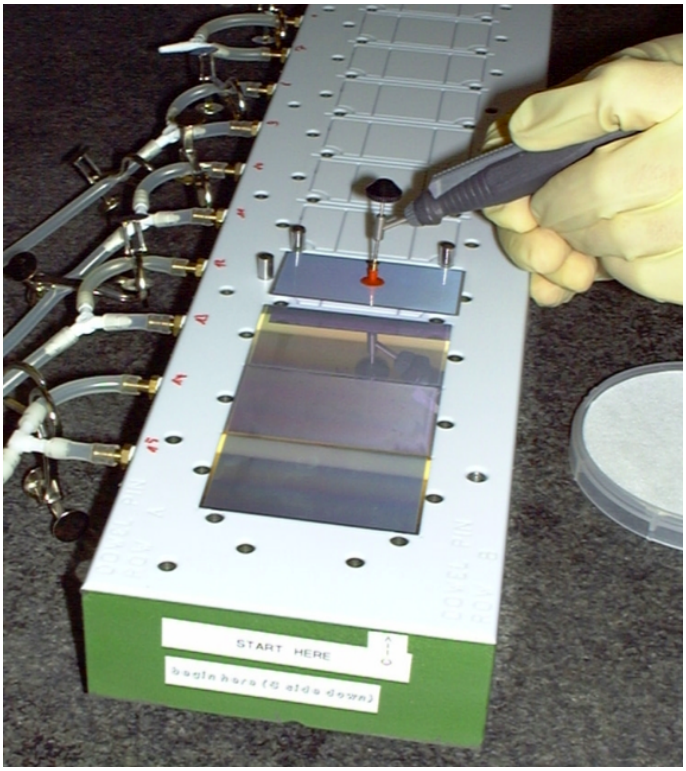

Figure 4.19: Sensor positioning. The detectors are longitudinally aligned with two pins, and transversely with one pin.

S and K hybrid gluing requires two different set of tools (bonding jigs, extensions, etc.) specifics for each side. The alignment between the ladder and the hybrid is crucial and for that reason the whole manipulation is checked continuously under microscope. When the mechanical precision is reached, the Araldit 2011 is dispensed on the hybrid (K-side) or the K6 Upilex (S-side).

- Sensor and hybrid bonding:
  bonding is the most complicated and time-consuming process. To semplify the process the bonding pad dimensions were increased and aligned to optimize the bonding geometry. For the AMS ladder bonding the flat wedge technique was adopted using a 25 μm diameter wire. A thicker wire requires higher bonding power which could damage the silicon sensors in case of bond failures, while too thin wires with low breaking load are dangerous in a space experiment where it will undergo significant vibration [230].

4.5.3 Assembly Phase 2

After a careful ladder visual inspection and electrical test, its hybrid needs some additional manipulations before the feet are glued. A detailed procedure helps the operator to check the numerous control and assembly steps.

All ladders with hybrids glued and bonded are sent from Italy and CERN to University of Geneva, where the so-called assembly Phase 2 is performed. It consists of the following steps:

1. Visual and electrical tests;
2. Hybrid preparation:
   - Bias bonds are protected with Araldit.
   - Spacers are glued on each hybrid.
   - Thermal grease is dispensed between hybrids S and K.
   - Column, used to fix together hybrids, is screwed and secured on K-side.
   - Thermal grease is dispensed on K-box.
   - K-box is installed.
   - S-box is installed;
3. Legs gluing. At maximum, legs can be glued on four ladders at a time;
4. As a final step, an electro-magnetic shielding foil made of 50 μm Kapton coated on both sides with a 3 μm thick Cu/Au pattern is wrapped around the ladder without mechanical contact with the silicon. The design of these foils is responsibility of University of Geneva as well as the electric quality control. Eleven different lengths and configurations are needed.

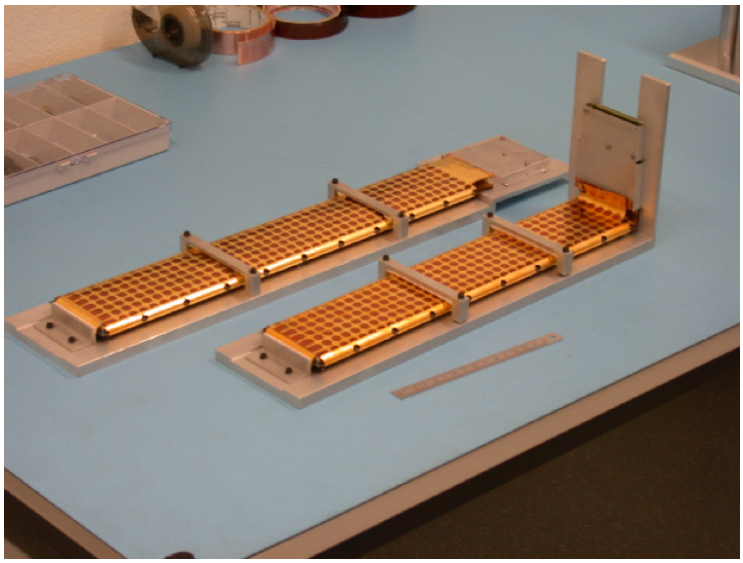

Figure 4.20: Two AMS-02 ladders ready to be mounted onto the support plane.

Fig. 4.20 shows two ladders at the end of this operation, ready to be installed on a support plane.

An more extensive description of Phase 1 and Phase 2 procedures is available in [220].

AMS-01 Ladder Refurbishing

The best AMS-01 ladders have been refurbished to be used as AMS-02 spare ladders. The refurbishing operations have been examined with two low quality ladders. It involves the following operations: the shielding is removed, then the AMS-01 hybrids are unglued, while the Upilex cables need to be left undamaged, as they will be glued again on new AMS-02 hybrids. The ladders with no hybrids are sent to CERN to add bonds on the K-side: this increases the strip charge collection. The ladders are then sent back to University of Geneva, where they are thoroughly cleaned and prepared for the AMS-02 hybrid gluing. After gluing the ladders are sent back to CERN to bond the hybrids. A total of 9 ladders have been refurbished successfully.

4.6 Ladder bias

To better control the strip voltages with respect to the VA input channel voltage, the bias voltage is split into three stages, as shown in Fig. 4.21. The voltage between the S and K local grounds (respectively $lgnd_s$ and $lgnd_k$) is (improperly) called *bias voltage*. To adjust the readout strip with the VA input voltage ($lgnd$ - 1 V), it is possible to correct the voltage between the local ground and the guard ring.

Knowing the mean voltage drop between the strips and the guard ring allows to choose a value minimizing the voltage difference between the capacitor terminals:

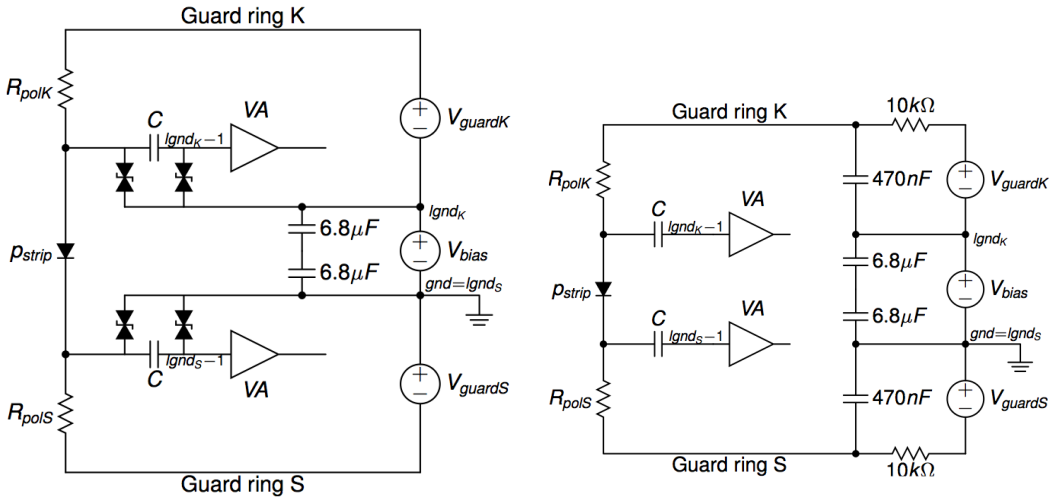

Figure 4.21: Biasing of an AMS-01 ladder (left). Biasing of an AMS-02 ladder (right).

if a decoupling capacitor is damaged, the current flowing into the amplifier will be minimized to limit the amplifier saturation [231]. Due to the design evolution between AMS-01 and AMS-02 both cases will be treated.

4.6.1 AMS-01 case

Fig. 4.21 (left) describes the bias scheme:

- V_{bias} is the voltage between the local ground S ($lgnd_S$) and the local ground K ($lgnd_K$);
- the local ground S corresponds to the system ground;
- V_{guardS} is the voltage applied between the guard ring S and $lgnd_S$;
- V_{guardK} is the voltage applied between the guard ring K and $lgnd_K$;
- R_{polS} is the mean polarization resistance between the guard ring S and a p-strip;
- R_{polK} is the mean polarization resistance between the guard ring K and a n-strip;
- p_{strip} symbolizes a p-n junction, an individual strip on the S-side.

The schematic of Fig. 4.21 is symbolic: a p-strip is not individually connected to the n-guard ring. Actually, it is resistively and capacitively connected to all the n-strips. The schematic allows a simplified representation of the biasing. The silicon is operated at reverse bias; thus a positive voltage is applied on the K-side, i.e. the K-side, while the negative voltage is applied on the S-side, i.e. the S-side. In

the case of AMS-01 detectors, the voltage drop U_{pol} between the guard ring and the strips was of some hundreds millivolts for the K-side, and around 3 V for the S-side at operating bias voltage. Neglecting the voltage drop at R_{polK} leads to $V_{guardK} = -1V$. For the S-side, we need:

$$-V_{guardS} + lgnd_S = -U_{polS} + lgnd_S - 1 \tag{4.1}$$

i.e. $V_{guardS} = U_{polS} + 1$. Finally, if we consider to apply a voltage V_0 between guard ring S and guard ring K, the voltage applied between both local grounds will be:

$$V_{bias} = V_0 - V_{guardK} - V_{guardS} \tag{4.2}$$

For example, if $V_0 = 50V$ then $V_{bias} \sim 50 - 3 - (-1) = 48V$. To achieve better comparisons between single sensor current measurements and ladder measurements, one should take into account this difference. When measuring single detectors, V_{bias} is the voltage between n- and p- guard rings, while on a ladder V_{bias} usually corresponds to the voltage difference between the local grounds.
Two 6.8 μF capacitors, located on the K-hybrid are connected in series between the two local grounds. They ensure a bias voltage stability in case of load fluctuation. Moreover, they act as a filter from the power supply. The capacitors are in series for redundancy: if one capacitor is damaged, a short between the local grounds is avoided thanks to the second capacitor.

4.6.2 AMS-02 case

The biasing method is similar to the one described in the previous paragraph (Fig. 4.21 (right)). In addition to the AMS-01 design there is the low-pass filters (the 10 $k\Omega$ resistors and the 470 nF capacitors) between the guard ring and the local grounds. The average voltage drop between n-strips and n-guard is of the order of 4 V, much larger than for AMS-01. This means that $lgnd_K - 1 + 4 = lgnd_K + V_{guardK}$ leads to $V_{guardK} = 3V$. In the case of AMS-02, $V_0 = 80V$. Thus $V_{bias} = V_0 - V_{guardK} - V_{guardS}$ and the difference between V_0 and V_{bias} is larger than for AMS-01. Note also the simplification of the schematics due to the absence of the protection diodes. It points out a weakness of the hybrid design: if a bias line (S or K) is broken, the ladder will be biased through the VA channels, once at least one capacitor channel is shorted due to an over-voltage on the terminals. In such a case, the corresponding amplifier may be saturated, hindering then signal transmission. The protection diodes would have prevented the hybrids from this circumstance, even though they were initially not designed for this purpose.

4.7 Tracker Support Structure

The tracker support structure, developed by RWTH-Aachen, is divided into three sections: a carbon fiber cylindrical shell which supports the planes 2 to 4 located inside the magnet, and two carbon fiber flanges which support the exterior planes

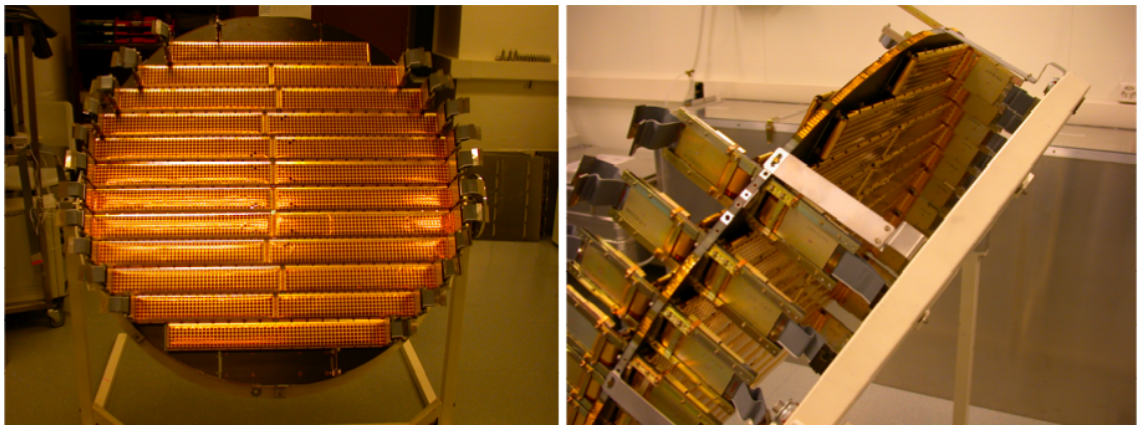

Figure 4.22: Plane 4 equipped with silicon ladders on both sides during the completion in September 05. The support jig is visible as a white structure.

1 and 5. With respect to the AMS-01 configuration, the number of silicon layers has been increased from 6 to 8 by suppressing one internal plane and equipping both sides of the remaining three internal planes with silicon ladders. The tracker planes located inside (outside) the magnet are the same as those used for AMS-01. They have a composite structure with two 220 (700) μm thick layers of carbon fiber surrounding a 12 (40) mm thick, low density aluminum honeycomb interior, ρ= 16.02 (32.0) kg/m^3. The diameter of the interior (exterior) planes is 1.0 (1.4) m. The AMS-01 interior planes have been modified to accommodate the second layer of ladders; the latter increases the material thickness of an interior plane to 1% of a radiation length at normal incidence. In view of the marginal increase of the plane hermeticity, and the very significant complication of the mechanical design, there is no overlap between the ladders in the planes of the tracker.

4.8 Tracker assembly and cabling preparation

Operations start by mounting ladders onto the support planes. The bare honeycomb plane is first installed on an assembly jig already used for AMS-01 which allows rotation of the plane and easy access to both sides (Fig. 4.22). The thermal bar assemblies are then installed. Their mechanical compatibility with the cooling loop interface is tested. The first side can then be equipped with ladders. Installation of the second layer on the other side is more delicate since one has access from only one side for fixation. A strict sequence of assembly and tests must therefore be followed. The assembled plane is finally stored in a tight container under dry Nitrogen.

Cabling of the inner part of the tracker has to be interleaved with this operation, since cables must pass through the planes by openings in the thermal bars. External cabling (384 flat cables) and piping is studied in detail with RWTH Aachen and the AMS integration team. A detail of the cable passage through a plane is shown in Fig. 4.23.

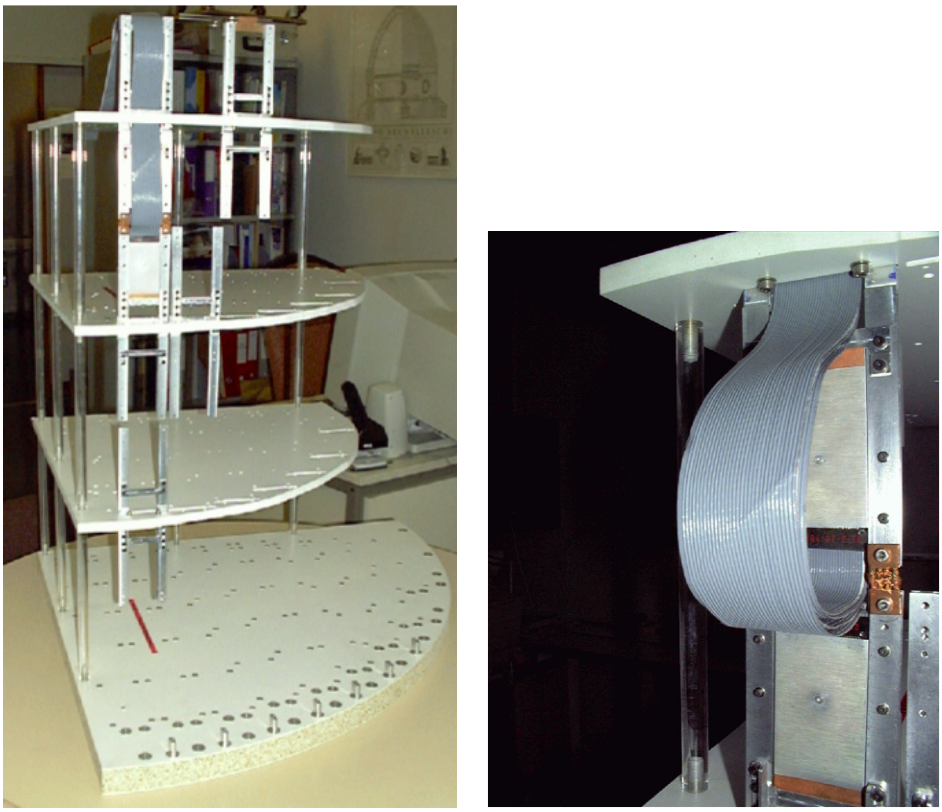

Figure 4.23: Left: Overview of the tracker assembly mock-up. Right: Detail of the thermal bar and cable passage through a tracker plane as well as elements of the thermal interconnect.

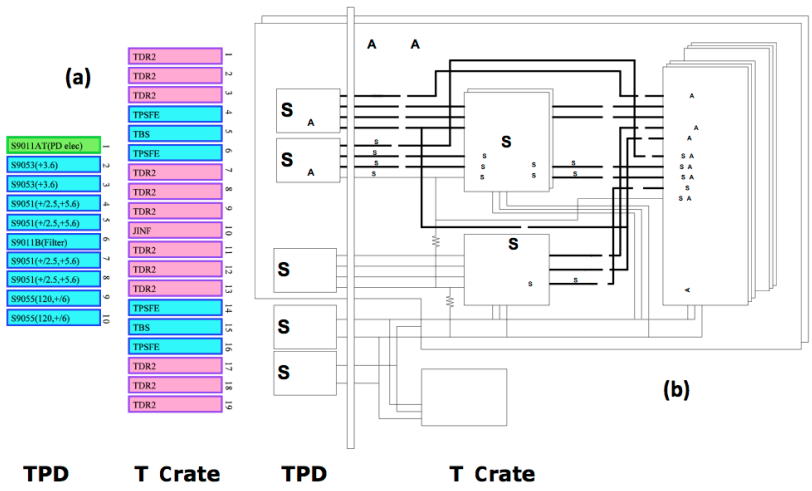

Figure 4.24: Layout of boards in TPD and Tracker Crates (a), Tracker power scheme (b).

4.9 Tracker Electronics

The readout and power distribution system of the Tracker detector is composed of a total of 232 boards divided into 8 sections. Each section takes its power from an independent 28 V line coming from the Power Distribution System (PDS) and provides the readout, data compression and power supplies for 24 silicon sensor ladders. As shown in Fig. 4.24, each section is composed of readout crate (T-Crate) and a power distributor. The T-Crate hosts the 12 readout and data reduction boards (TDR2, each containing two TDR circuits), 4 power supply front-end (TPSFE), 2 bias supply (TBS) and the interface to the slow control and the higher level of the DAQ chain (JINF). The TPD contains an input filter, a slow control interface and 8 dual DC-DC converters for the generation of the different voltages needed to operate the detector system. The high performance DC-DC converters were custom developed after an extensive investigation and provide high efficiency and very low noise to meet the system requirements.
One half of a TDR2 board is pictured in Fig. 4.25. Each S-side (K-side) TFE is connected to a TDR through a 21 (19) line quasi-coaxial cable with a mean length of 2.5 meters. Digitization is performed on the TDR with a 12-bit, 5 MHz analog-to-digital converter (ADC) that is coupled through a set of digital isolators to a Common Digital Part (CDP), composed by a data buffer, a programmable gate array chip, which controls the VA_hdr chips and the data buffer, and a Digital Signal Processor (DSP) for calibration and data reduction.
The reduction algorithm is based on the one used in AMS-01 and achieves the required average compression ratio of 600 at rates above 3 kHz.

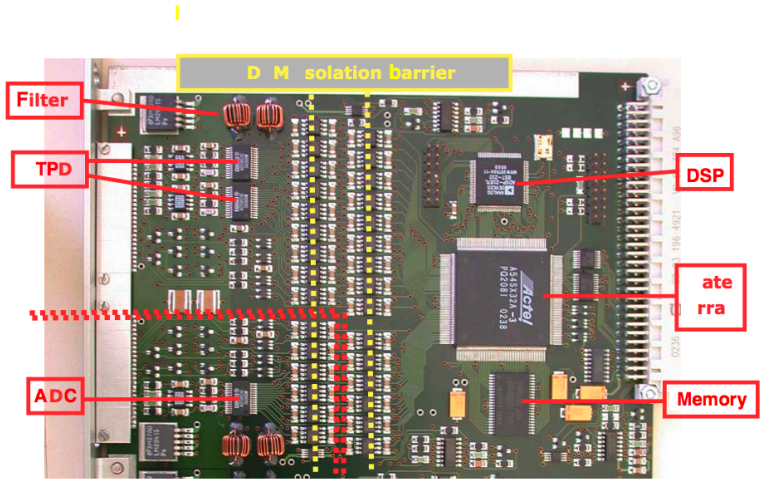

Figure 4.25: One half of a flight quality TDR2 board.

4.9.1 Tracker Electronics Production and Qualification

University of Geneva is responsible for part of the readout electronics of the tracker, mainly the TDR2 boards, its design, its programming, as well as the quality assurance during production. Qualification and flight boards themselves are produced and financed by CSIST. The full electronics consisting of T-Crate and TPD have been space qualified at CSIST during a three week test campaign. The crates have undergone an environmental stress screening (ESS), which consists of the following subtests:

- Thermal cycling:
  the electronics has undergone thermal cycling between -45^0 and +85^0 C non-operational temperatures, with functional tests at -25^0 and +55^0 C operational temperatures. A dedicated readout system and test procedures have been developed for this purpose. No failure of the system during the tests has been observed.

- Vibration tests:
  both crates have been tested during 10 minutes vibration in x, y and z direction each according to the test spectrum shown in Fig. 4.26. Functional tests have been performed during the vibration, no failure has been observed

- EMI/EMC tests:

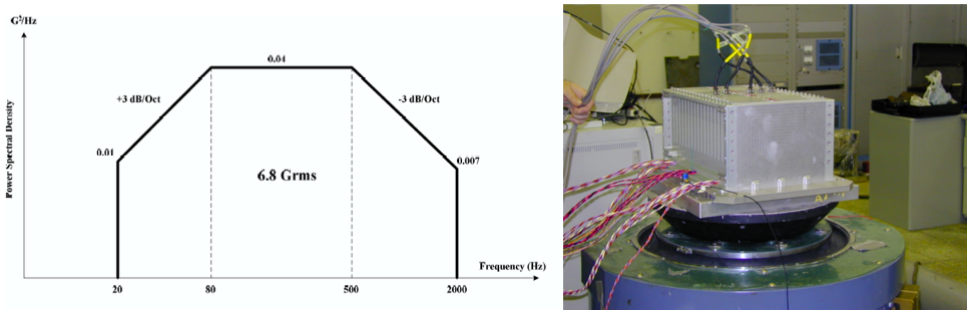

Figure 4.26: ESS random vibration spectrum (left); T-crate on the vibration support (right)

the electronics has been tested for electromagnetic interference and emittence according to NASA specifications at CSIST. Some problems have been discovered concerning emittence, which was slightly above the NASA limits as well as functional failures during immittence of a high field. Further tests have been performed at a laboratory in Terni, Italy. After discussion with experts, the problems have been traced back to an insufficient grounding scheme and shielding issues. A full requalification of the electronics has been successfully performed in October 2006 in Terni.

- Thermal vacuum test (TVT):
  for the final qualification, the full electronics has been successfully tested in a vacuum chamber in Terni, Italy in May 2006: the thermal profile is shown in Fig. 4.27. All hardware/software for the test has been prepared during 2005.

The production of 120 flight models of the TDR2-board started at CSIST by the end of 2005 and has been tested between July 2006 and July 2007, using the same test setup, as for the qualification models. At the end of the production and qualification phase, the tracker electronics will move to CERN and be integrated together with the rest of the tracker and the other subdetector-components. An early integration test, using qualification models has taken place in spring 2007.
The on-board software for all this electronics is developed under University of Geneva responsibility, in collaboration with colleagues from MIT, Montpellier and Perugia. The calibration, readout sequence, data flow and data reduction are controlled by this software. During the test beam in September 2004, a first milestone version for the online data reduction has been implemented and tested. In 2005, the results have been analyzed and further improvements to the code in terms of performance and stability have been added (see Chap.5).

4.10 Tracker Thermal Control System

The AMS-Tracker Thermal Control System (TTCS) consists of a mechanically pumped two-phase loop with carbon dioxide (CO_2) as working fluid. CO_2 was

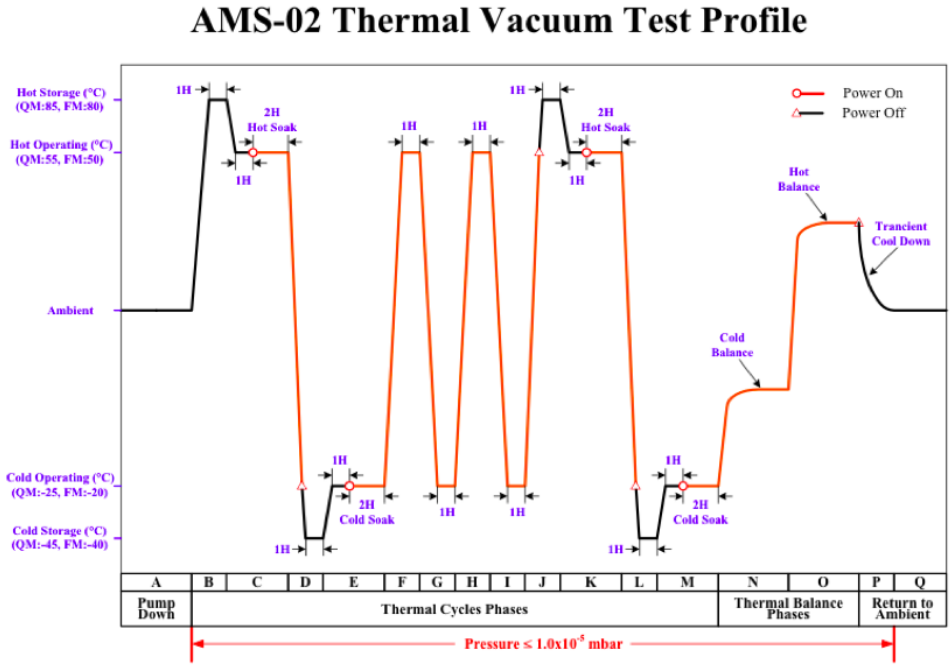

Figure 4.27: The thermal profile used for the TVT in Terni.

proposed as refrigerant because of its very good thermodynamical properties and the possibility of using small diameter evaporators. This small amount of thermal control system hardware inside the AMS tracker makes integration possible with the existing tracker hardware. The tracker support structure from the AMS-01 Tracker can therefore be reused for AMS-02, while no major modifications have to be made to accommodate this thermal control system. The initial studies for this system, the model calculations and the flight hardware construction came out from the collaboration of University of Geneva with NLR Amsterdam and partially subcontracted to NIKHEF Amsterdam.

4.10.1 TTCS conceptual design and testing

In the year 2000 a CO_2 system was proven to work in a test set-up within the thermal specifications of the AMS-Tracker. Due to this successful test, CO_2 as refrigerant appeared to be the most promising solution. After the feasibility test the TTCS design was developed to a preliminary design status in November 2001. The principle of operation of the system is schematically shown in Fig. 4.28.
During 2002, important steps have been made for the establishment of the most critical components of the TTCS. The TTCS pump is a modified Mars Pathfinder pump. This pump worked successfully during the long mission to Mars, and it is the record holder for a long duration mission in space. The pump impeller is modified for the TTCS, but the rest of the concept is unchanged, so the TTCS pump can rely on the experiences of the Mars Pathfinder pump. This saves a long period of

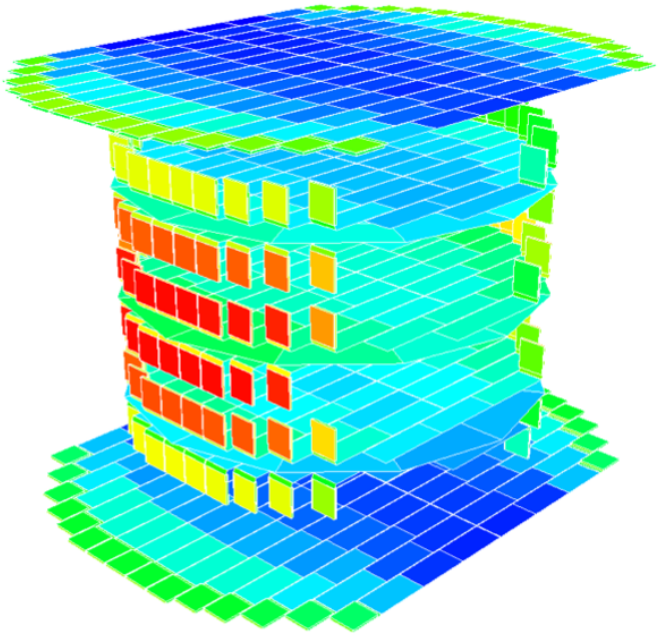

Figure 4.28: Principles of operation of the Tracker Thermal Control System

testing and space qualification. Another important component is the evaporator. The evaporator is fully integrated in the AMS tracker. It has an interface to every hybrid circuit and must therefore be integrated in the tracker in an early stage. The evaporator assembly consists of 132 conductive structures called thermal bars and 2 fluid loops where the heat is absorbed into the carbon dioxide by evaporation. They are also the support structures for hybrids circuits and cables. This structure is made of the highly conductive TPG embedded in an aluminum housing. The inner plane thermal bars are mounted in strings of three thermal bars, connected to each other with flexible copper connectors. Each string is connected to both fluid loops. The outer plane thermal bars are connecting directly to one fluid loop. The two fluid loops are operated in parallel, one on the top of the tracker and one on its bottom. One evaporator loop has a length of 10 m and an inner diameter of 2.6 mm. The thermal bars underwent thermal vacuum testing. The thermal bar design was verified and approved. The next step was a performance test of a full scale evaporator loop, where pressure drop, heat transfer coefficients and flow regime have been tested.

An important part of the TTCS design is the optimization of the transient behavior of the complete system. The temperature of the evaporator needs to be stable over orbit while the radiator temperature varies mainly due to the changing solar input. The TTCS is able to damp the temperature variations due to a heat exchanger. However the range of a heat exchanger is limited. When it exceeds its limits, electrical power is needed to get the evaporator temperature stable. The amount of extra power is a function of several design choices, such as radiator mass, radiator efficiency etc. To study the complicated transient behavior and to minimize the

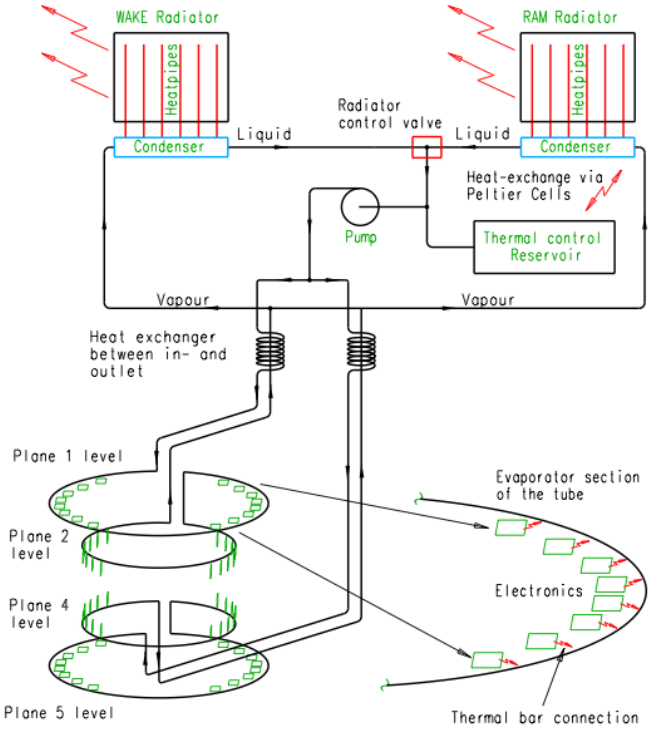

Figure 4.29: Example of a temperature distribution inside the tracker volume as predicted by the tracker thermal model.

electrical power needed, a complicated network of thermal models at different institutes has been created. NIKHEF/UNIGE is responsible for the tracker thermal model, which is shown in Fig. 4.29. This model is connected to the TTCS fluid model and the AMS overall model with fixed thermal interfaces.

4.11 Performance tests

An extensive series of tests has been performed to verify the performance of the AMS-02 silicon tracker. These include bench tests at the ladder by ladder level and beam tests with minimum ionizing particles, light ions and heavy ions. An important modification with respect to the original design was the increase by a factor of two in the implantation pitch on the K-side of the silicon sensors. The presence of four p+ blocking strips in the 208 μm readout gap of the AMS-01 sensors resulted in a 35% lower signal level at normal incidence for tracks passing in the middle of the readout gap [205], and consequently on average, a 20% lower signal level for the singly-charged particles compared to the S-side performance. Moreover, the silicon manufacturing process has been improved and it should lead to a significant reduction in the noise level on both silicon readout sides.
A detailed description of all the beam tests performed with AMS-02 ladders will be given in the next chapter.

In conclusion, if compared to the precursor AMS-01 mission, the performance of the tracker in terms of signal to noise, position resolution and charge resolution has been greatly enhanced. The increase of silicon layers from 6 to 8, together with the more powerful AMS-02 cryomagnet, has significantly increased the physics reach of the AMS-02 detector, making a wide range of physical phenomena accessible during the AMS-02 mission.

Chapter 5

Test Beam Setup @ CERN

5.1 Test Beam at CERN

In this Chapter the setup of a test beam performed at CERN on September 2004 will be described. A simplified tracker design, realized with 11 AMS-02 flight ladders, was tested together with an AMS-02 ECAL prototype using an electron beam. The aim of this test was to validate the Montecarlo predictions of gamma detection with AMS-02, in particular the energy and angular resolution. As by-product, ladder spatial resolution and momentum resolution for electrons was also tested. Before the detailed description of 2004 test beam, a review of previous test beams with protons and heavy ions will be given together with the preparatory tests on the magnet and the Čerenkov's detectors needed for the 2004 setting up.

5.1.1 Location and Beam Features

The site where the test was performed is located in the *East Area* of *Proton Synchrotron* (PS [232]) and the *T7 beam line* was used (Fig. 5.1).
The *East Area* is an experimental area at the PS. It contains five beam lines: T7, T8, T9, T10 and T11. A schematic view of the beam line geometry is available in Fig. 5.2.
The beam lines are derived from the 24 GeV/c primary beam from the PS, which provides 2.4 second cycles with a flat top of about 400 ms. Some cycles serve the North target (for T9, T10, and T11 beams), some the South target (for T7 and T8). The number of East Area cycles per super-cycles depends on schedule constraints.

The T7 Beam

The T7 line (Tab. 5.1) is a secondary beam that delivers secondary particles up to 10 GeV/c at a production angle of 0 degrees (Fig. 5.3).
It is mainly dedicated to test of LHC-B experiment and only occasionally available for external users.
The design should guarantee good and reproducible beam quality at the experimental focus, within its expected usable range. The optical design is an adaptation of

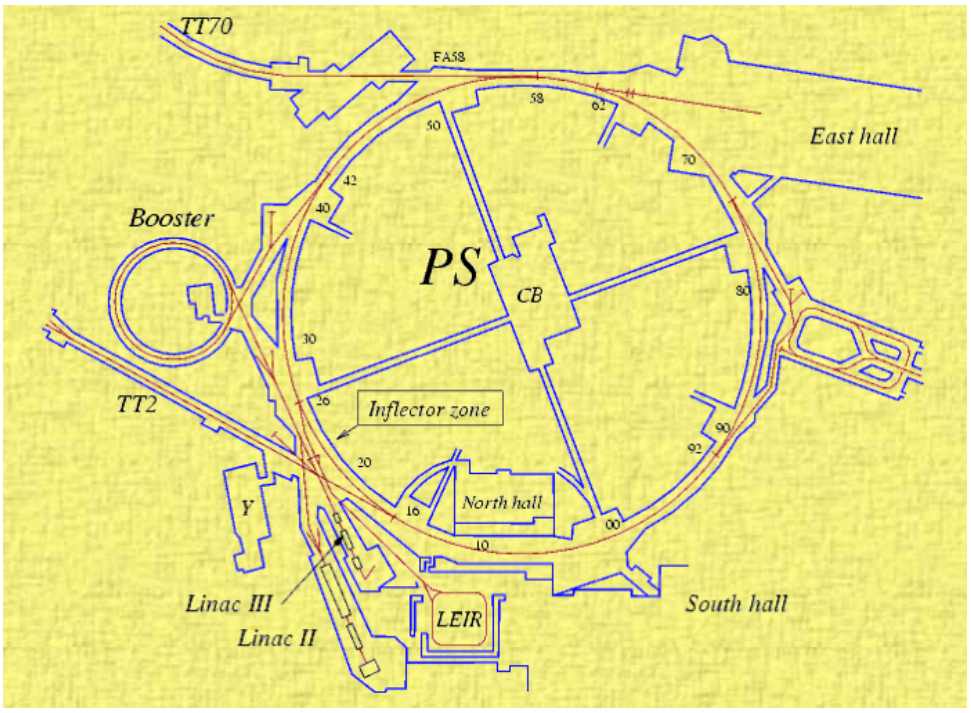

Figure 5.1: The PS East Area in the PS Complex.

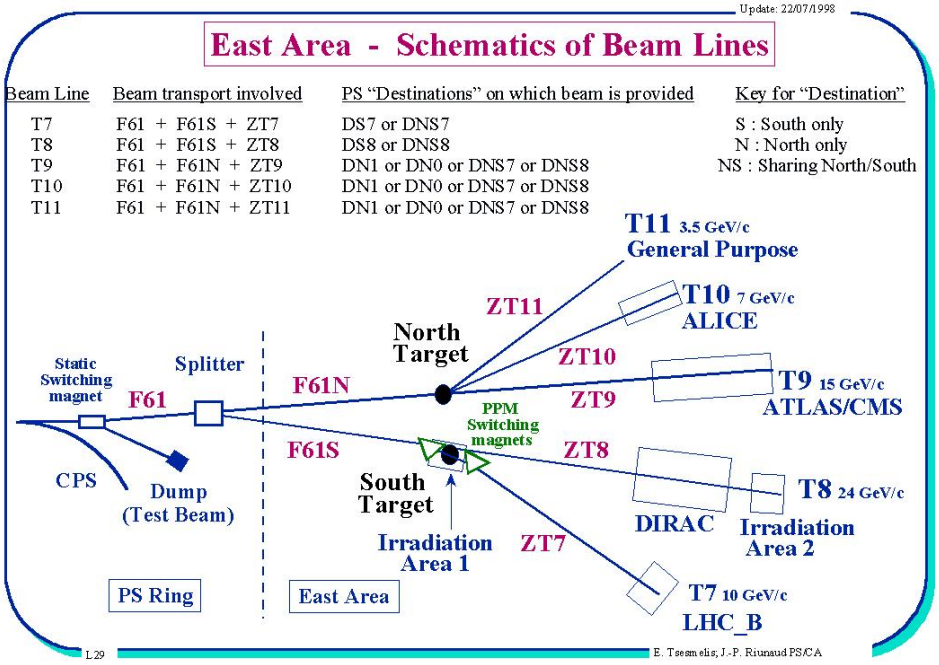

Figure 5.2: A schematic view of the beam line geometry of the *East Area* experimental area at the PS. The five beam lines are visible: T7, T8, T9, T10 and T11.

Max momentum	10 GeV/c
Target distance-focal point	37.45 m
Beam height	1.28 m
δp/p	$<$1 %
Beam section (line end)	50 mm
Beam divergence (max intensity)	$\sim$ 5 mrad
Beam intensity	$10^4 \rightarrow 10^6$ particles/spill

Table 5.1: Main features of beam *T7* in the PS East Hall at CERN

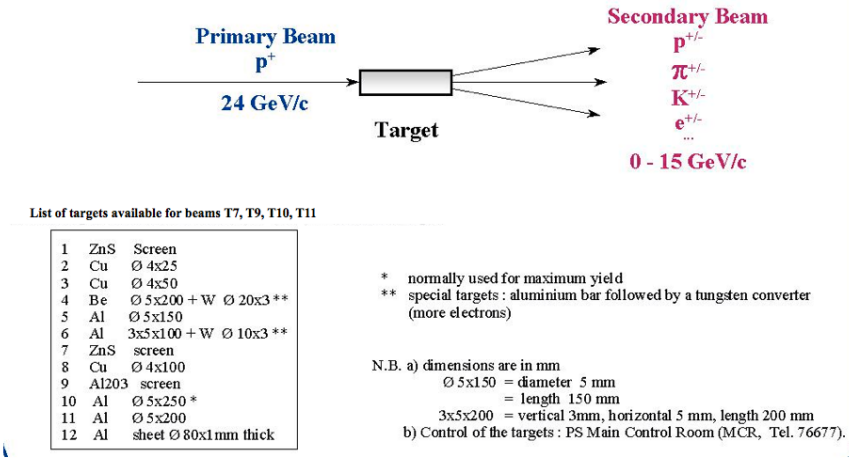

Figure 5.3: Schematic view of the PS primary and secondary beams [233].

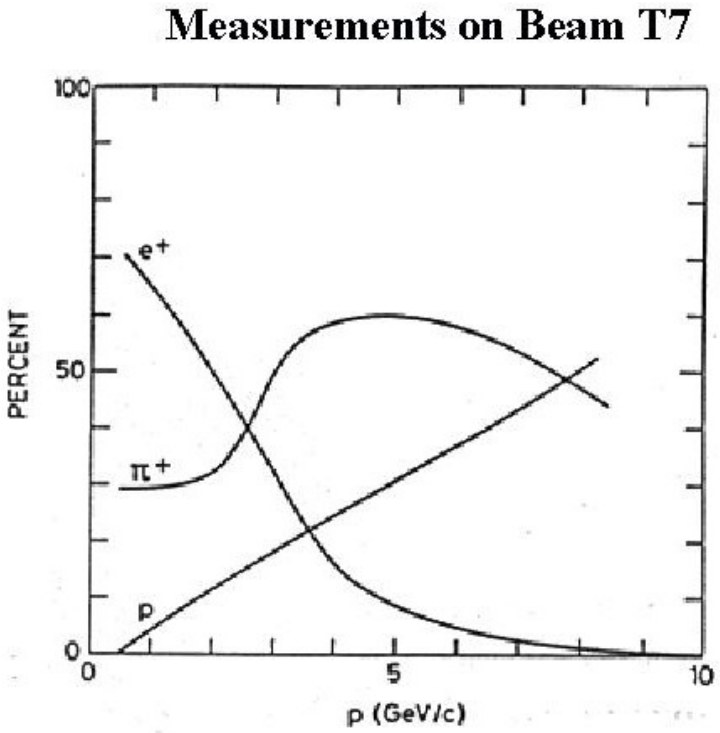

Figure 5.4: Measured particle flux of the beam in PS *T7* line [234].

the classical monochromator scheme.
The switching element, for the physical separation of T7 and T8 lines, is a laminated magnet of molded circuit board (MCB) type. This magnet deflects the beam by 39 mrad to the right when feeding the T7 target and let it pass directly for the T8 line. The optics itself, in particular a full set of quadrupoles had also to be changed in a quasi pulse position modulation (PPM) mode in order to give the proper set of optical parameters for each mode of beam operation.
The nominal beam height is 1.28 m above ground; a vertical correction magnet is included which will allow for a small vertical steering in the experimental area.
This line has the dispersion magnets embedded in the optics, this couples focusing and dispersion control. Thereafter the last focus is modified using only the last doublet. It has been verified that the residual dispersion in doing so is small enough to be safely neglected. Monitoring devices are also installed:

- a position detector, with a resolution of the order of 3 mm, at line end and at the vicinity of experimental focus.
- an intensity measurement device in order to detect the delivered intensity to the experiment and a possible beam degradation.

The line is under vacuum (< 10 Pa); this ensure minimal multiple scattering in air and vacuum windows. Intensity of various particle species is almost identical as the source itself is unmodified (Fig. 5.4). The standard beam on target comes

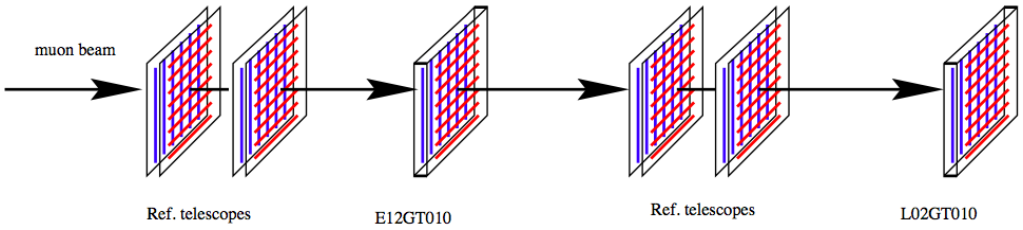

Figure 5.5: Setup of the CERN test-beam for evaluation of the first AMS-02 electrical prototype with serial number E12GT010.

from the slow extraction of a PS coasting beam with a spill time around 350 ms. The target and the line are transparent to the impinging time structure down to the nanosecond level.

5.2 Previous Test Beams on AMS-02 Ladders

Prior to September 2004 campaign, an extensive series of tests have been performed to verify the performance of the AMS-02 silicon tracker. Here some of those tests will be briefly described together with the related information on the tracker ladder performances.

Test Results in a Muon Beam

At the beginning of September 2000, an AMS-02 electrical prototype ladder was exposed to a test-beam at CERN. Test particles were 120 GeV/c muons at the SPS [235] X5 facility in the West Area. The main goals of this test were the validation of the new silicon and the new VA front-end chip. Results about improved resolution, charge collection efficiency and increased signal-to-noise ratio (S/N), using minimum ionizing particles, were obtained. The experimental setup was quite simple and it is shown schematically in Fig. 5.5. Two scintillators and four pairs of reference position measuring detectors (single-sided silicon sensors with 50 μm pitch readout), were used to determine the track parameters. About 200000 events were collected during 3 days of data acquisition. Results have shown an improved performance compared to the AMS-01 sensors.
After event selection, a fit to the distribution of the residuals yields a resolution of 8.5 μm and 30 μm on the S and on the K side, respectively, which are described by a Gaussian function and flat background (Fig. 5.6). The most probable values of the signal-to-noise ratio distribution of matched clusters, S/N, are 12.0 and 7.6. The charge correlation between S and K side is 23%, with an average charge loss on the K side of 3.6%. Both results are shown in Fig. 5.7. Requesting the extrapolated track to hit a region of the detector without defects, an intrinsic efficiency of 99%

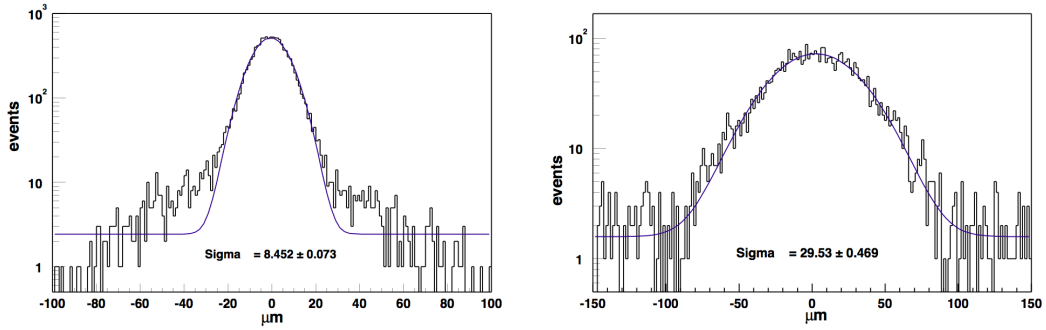

Figure 5.6: Residuals distribution of hits on the prototype ladder with respect to the position expected from the beam telescope. The resolution is 8.5 μm on the S-side and 30 μm on the K-side.

is obtained. The signal asymmetry η, defined as the fractional distance between readout strips of the center of gravity of the cluster energy, between neighboring strips reflects the position of the intermediate floating strips. S and K sides are compared in Fig. 5.8. In contrast to the AMS-01 design, on the new AMS-02 K-side the strips are increased in width to 40 μm, while two of the three intermediate strips are suppressed. This gives a better charge collection efficiency, as shown in Fig. 5.9, while preserving the same position measurement accuracy. The new strip layout and design of the AMS-02 sensor is thus proven to lead to better performance than its predecessor had.

Test Results in a Proton Beam

In June 2003, four AMS-02 ladders were exposed to a 10 GeV/c proton beam at CERN to determine the optimal shaping time for the front-end VA_hdr9a chip. Fig. 5.10 shows the performance of the two sides of the AMS-02 silicon sensors for minimum ionizing protons, for the optimal shaping time of 3.5 μs. The data are described by a Landau distribution convoluted with a Gaussian noise distribution. The fitted widths for the latter are 2.0 and 1.8 ADC counts for the S- and K-sides respectively. In Fig. 5.11, the fitted Landau peak values as a function of the shaping time are shown.

Test Results in a Heavy Ion Beam

A test was done in October 2002 at CERN (SPS) using a lead ion beam with 20 GeV/c momentum. The main goal of this test was to access the performance of AMS-02 ladders for the measurement of the specific energy loss dE/dx. The incoming lead beam was steered onto a target and the outcoming fragments analyzed in a spectrometer, selecting a fixed Z/A ratio. In this beam, test set-ups of the AMS time-of-flight counters, the RICH counter and the tracker were situated as well (Fig. 5.12). As far as the tracker was concerned, the set-up included six ladders from all three production chains, read out by three engineering models of the Tracker

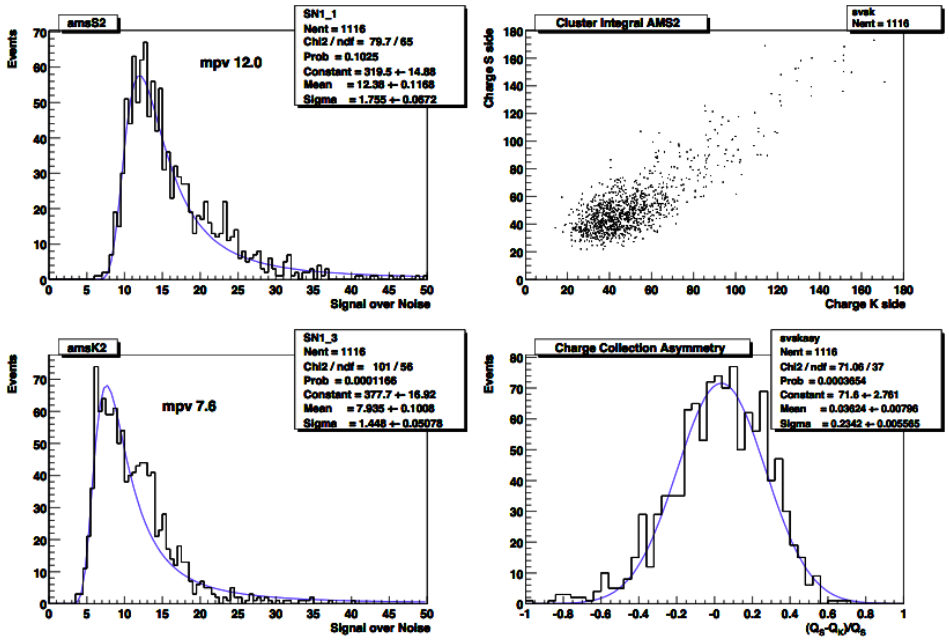

Figure 5.7: Signal-to-noise ratio (left), the charge correlation between S- and K-side hits and its asymmetry (right) for the prototype ladder.

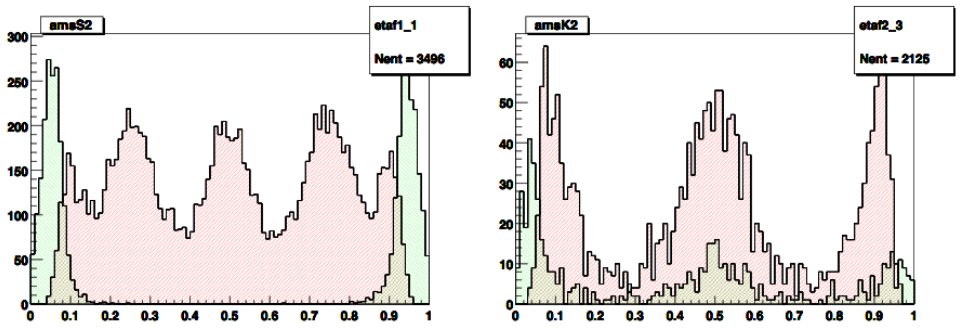

Figure 5.8: Distribution of the η value on the S-side (left) and the K-side (right), corresponding to the strip arrangement on the two sides. The red histogram shows the distribution for clusters with two significant strips, the green one is for clusters with one significant strip, when the highest neighbor is included.

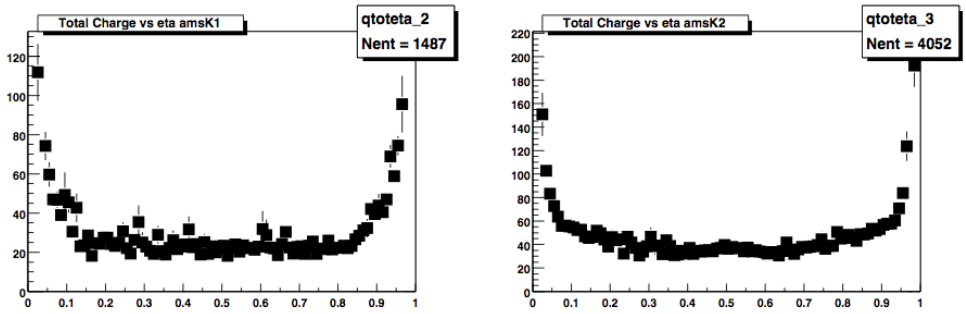

Figure 5.9: Total cluster charge as a function of η, i.e. as a function of the hit position relative to the metalization. The charge collection is rather uniform and the charge collection efficiency is good.

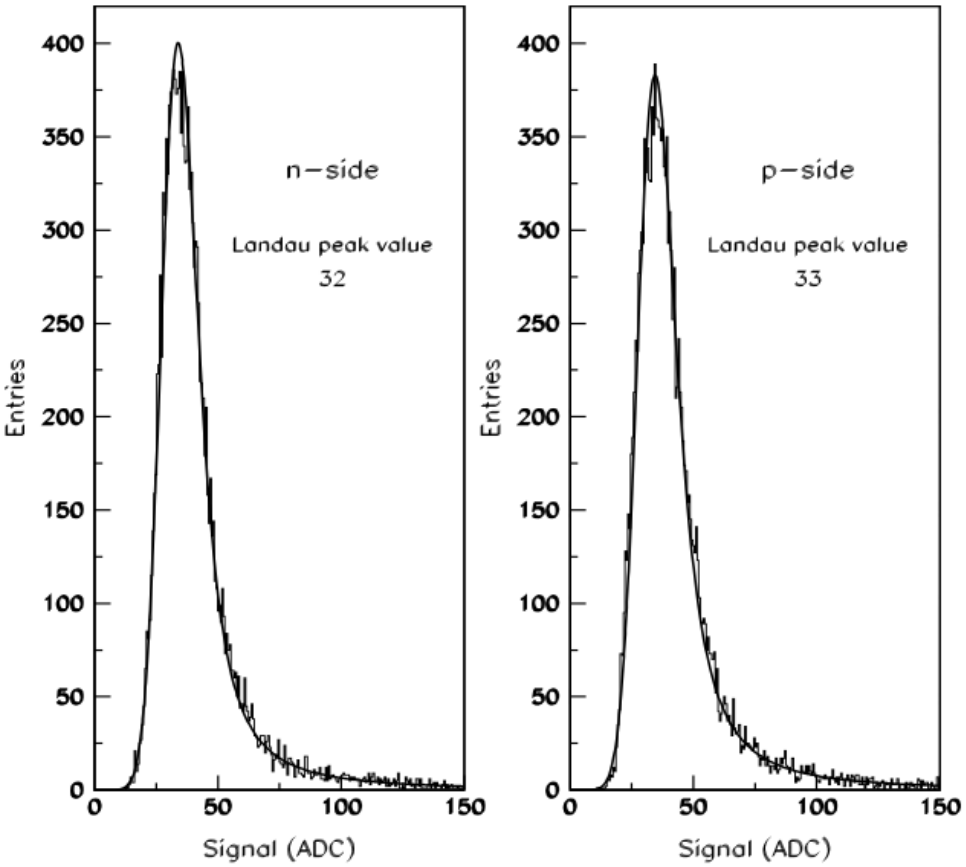

Figure 5.10: AMS-02 silicon tracker performance: signal levels for minimum ionizing protons.

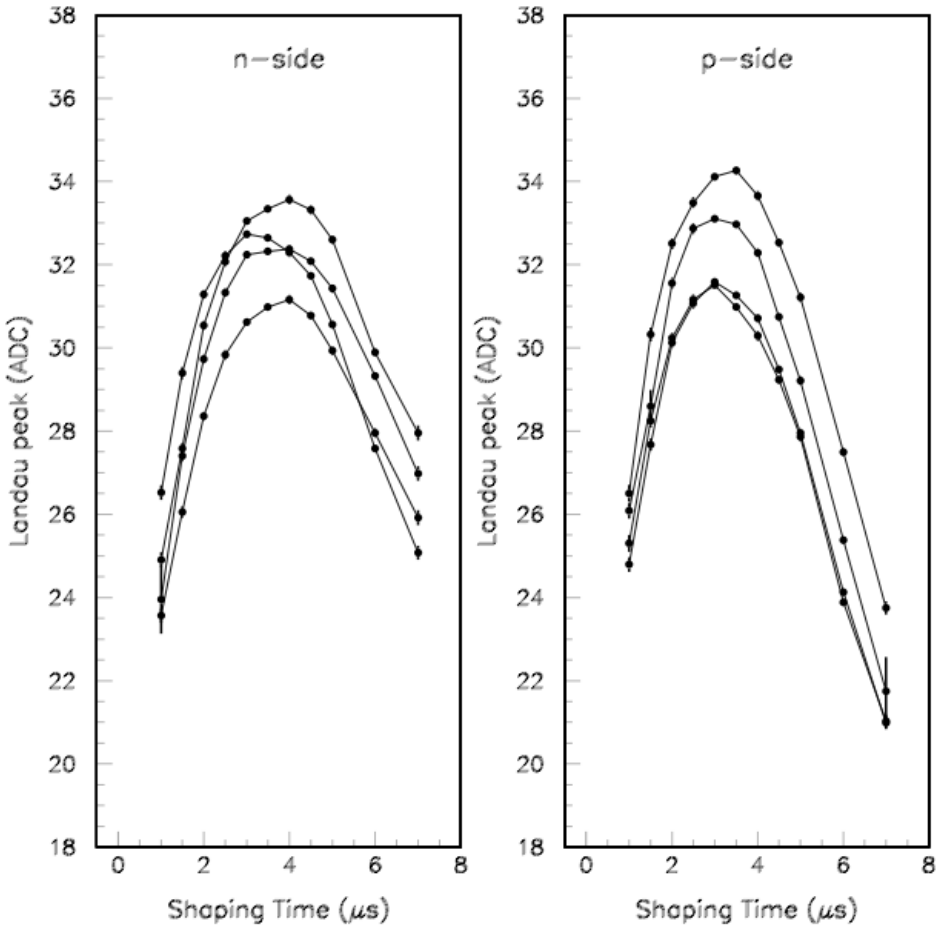

Figure 5.11: Landau peak position for minimum ionizing protons as a function of the VA_hdr9a shaping time for four AMS-02 silicon ladders.

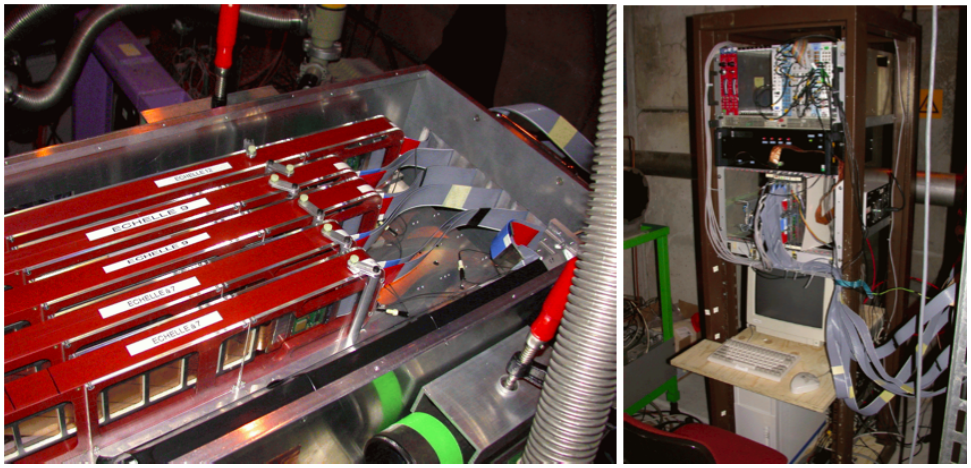

Figure 5.12: Left: Aluminum box containing six AMS-02 ladders in the heavy ion beam test. One of the ladders is inclined to study the response as a function of angle. Right: Electronics rack in the beam test. The black crate contains the power supply engineering model, the crate below three engineering models of the Tracker Data Reduction (TDR) board.

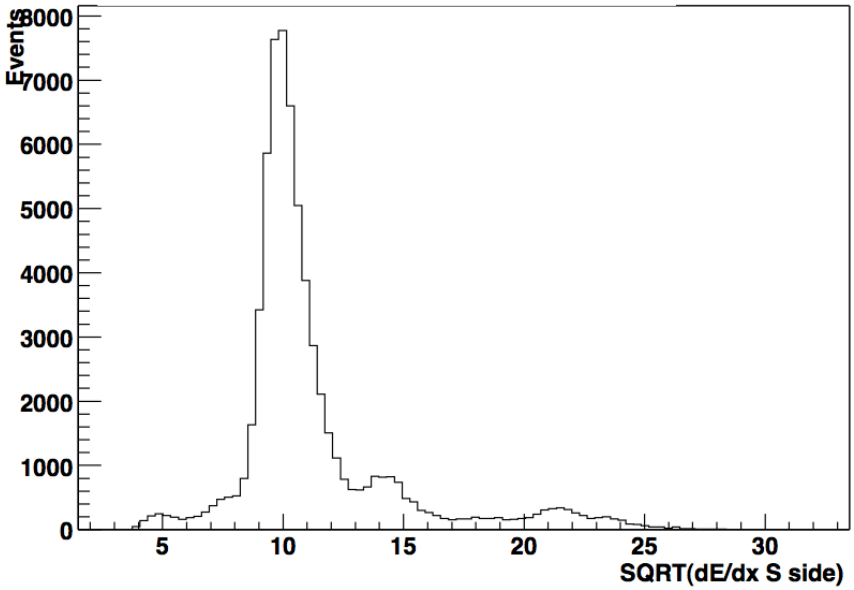

Figure 5.13: S-side distribution of $\sqrt{dE/dx} \sim Z$ (in arbitrary units), for a typical run where $A/Z = 2$ was selected to enhance helium contents of the beam. Besides the high helium peak, smaller ones from D, Li, Be and B nuclei are observed from the single side signals of a single ladder, without further cuts.

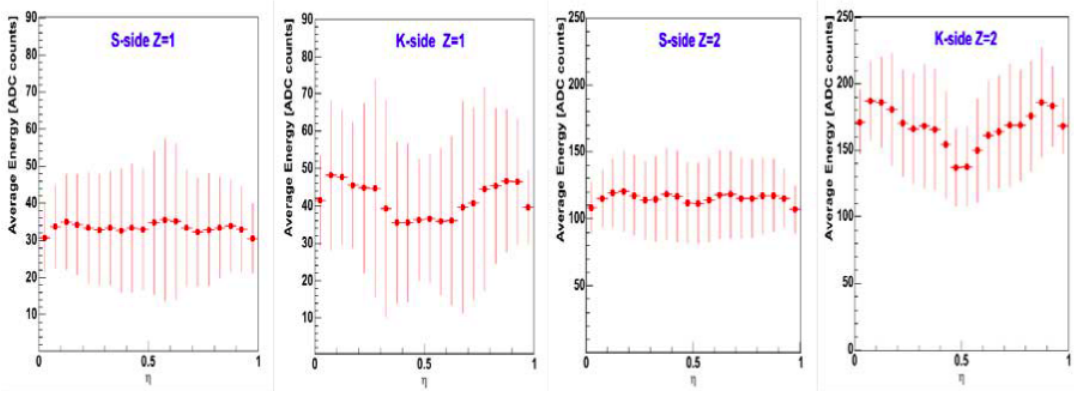

Figure 5.14: Average cluster energy as a function of center-of-gravity of the cluster energy, η, on the S and K sides of a ladder, for protons and helium nuclei.

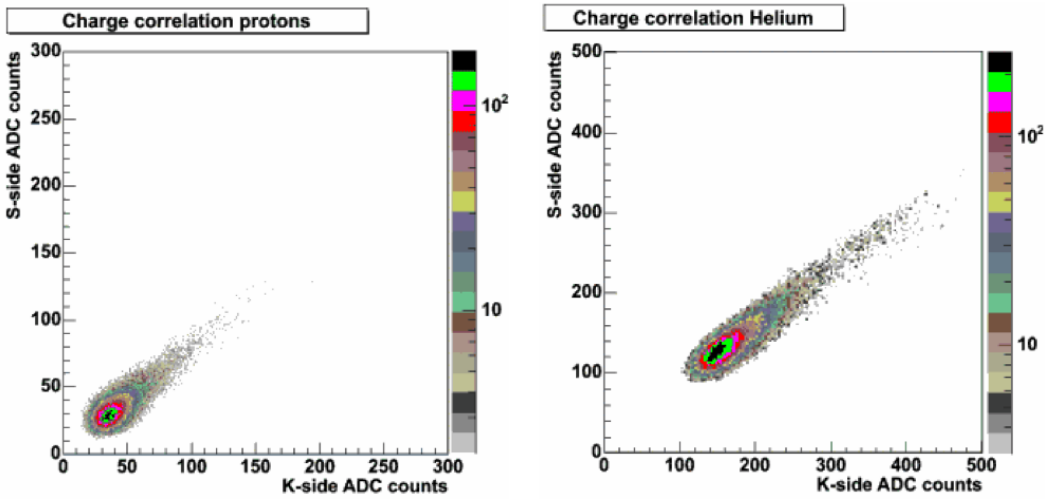

Figure 5.15: Cluster energy as measured on the S and K sides of the same ladder for protons and helium nuclei.

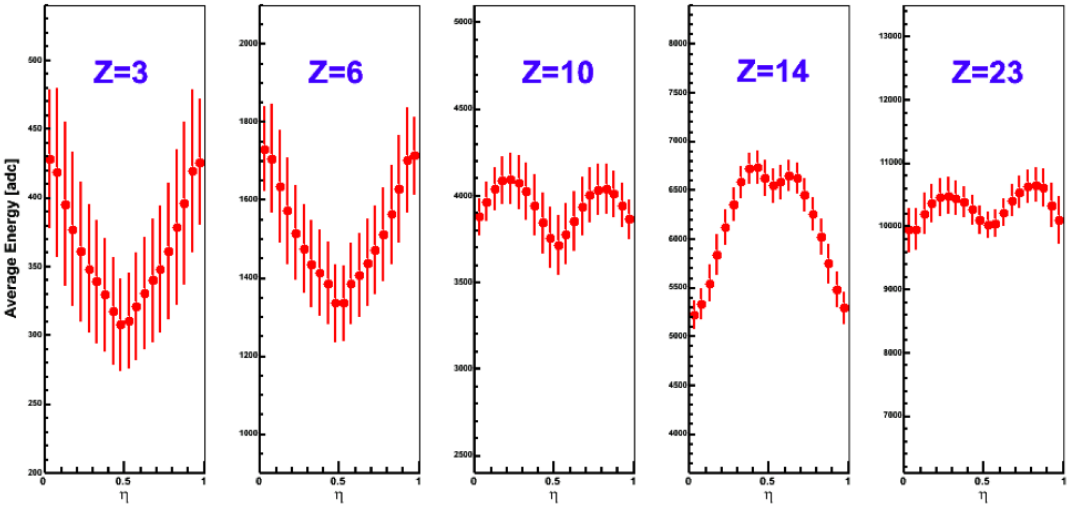

Figure 5.16: Average cluster energy as a function of center-of-gravity of the cluster energy, η, in different ion types in the K side of a ladder.

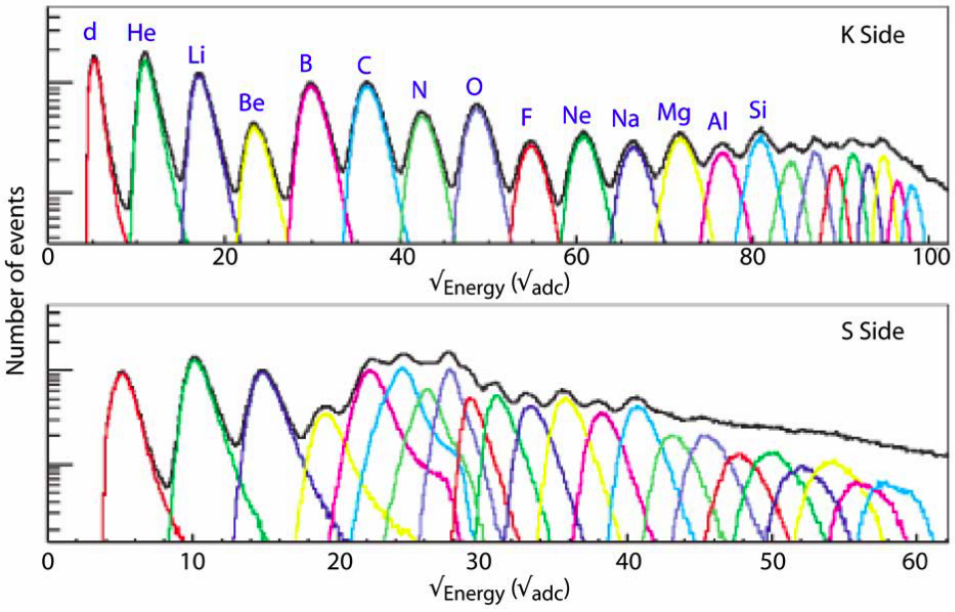

Figure 5.17: Corrected cluster energy spectrum measured in the K and S side of one ladder.

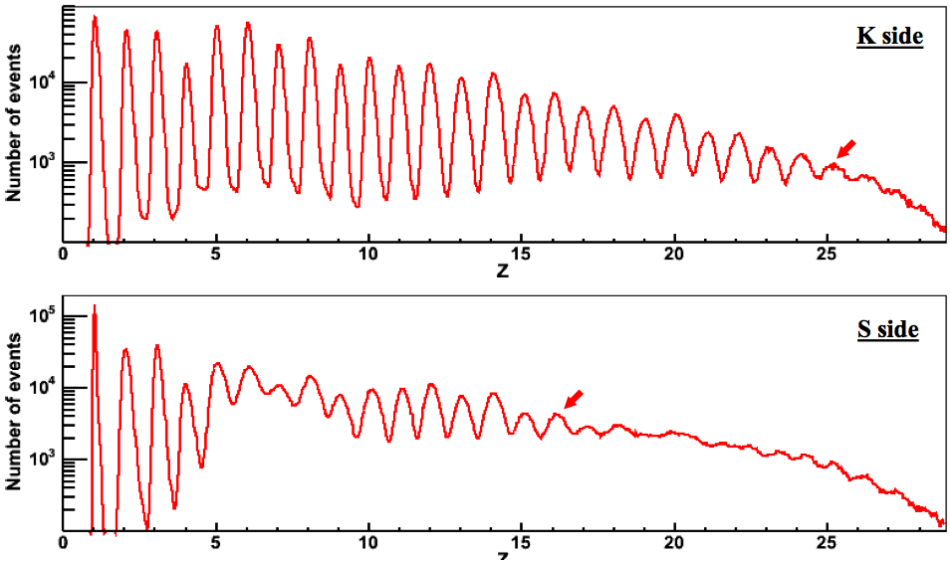

Figure 5.18: Combined Z measurements for 4 or more ladders on the K and S sides.

Data Reduction board. Power was supplied to the ladders by an engineering model prototype of the power supply system developed in Perugia. From October 14 to 19, 2002, data with proton and ion beams were taken, resulting in about ten million events for analysis. Spatial resolution was studied up to Z=6 giving resolutions as 7.1 μm (S-side) and 22.1 μm (K-side), very close to what obtained with MIPs. The tracker capability to identify ions was obtained by energy loss measurements (one for each traversed layer) which go proportionally with Z^2. Using data from both S and K side, an identification up to Z=13 was possible.
Fig. 5.13 shows a distribution of pulse height as observed with a beam selected for $A/Z = 2$. This setting enhances the helium content of the beam while suppressing protons and beryllium. Clear peaks for nuclei up to boron are observed. Note that this distribution is obtained from a single side of a single ladder. Details of the dE/dx measurement including the saturation behavior for high Z particles have also been studied. Another test beam to study the AMS-02 ladder response to light and heavy ions was performed at CERN in October 2003: again six ladders were exposed to an ion beam . A fragmentation beam was produced with primary Indium ions impinging with an energy of 135 GeV/A on a beryllium target. The fragmentation ions could be selected according to their A/Z ratio, and different data samples corresponding to A/Z = 1, A/Z = 2 and A/Z = 2.25, were collected. An independent measurement of the ion charge was also performed by the prototype AMS-02 RICH detector.
A representative set of two 12-sensor long ladders from each of the three assembly lines was selected from the final AMS-02 production and mounted in a light tight aluminum box orthogonal to the beam. Engineering models of the power supplies were used to supply bias voltage to the silicon sensors as well as low voltages to the front-end hybrids. Three data reduction boards (TDR2) read out two ladders

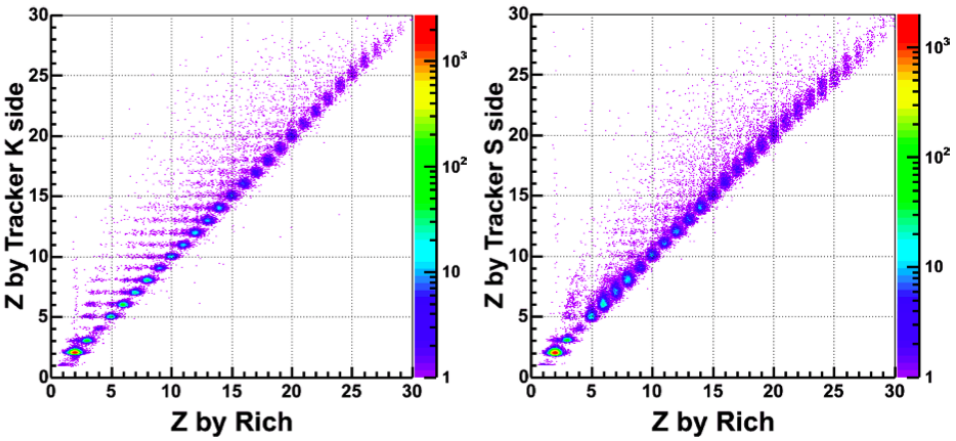

Figure 5.19: Correlation of charge (Z) measurements by the tracker and the RICH.

each and transmitted the acquired data to a PC computer running under a Linux operating system. A trigger was provided using a scintillator beam telescope.
The standard data acquisition mode for the tests was in uncompressed mode, to allow the test of different algorithms of common mode noise subtraction, signal finding and clustering.
In Fig. 5.14 the average cluster energy as a function of the particle's impact position in the readout gap is shown for protons and He, on the S and K sides of a ladder. The impact position is represented by the η parameter. On the K side, an energy loss of 30% is still present in the central part of the readout gap, for both proton and helium nuclei, however the signal is well above the noise level, insuring a good efficiency for the selection of the proton signal.
In Fig. 5.15 the cluster energy collected on the two sides of a ladder is shown for protons and helium nuclei. For both protons and helium, a Landau distribution convoluted with a Gaussian noise distribution describes the cluster energy distribution and can be used to define a probability density function for proton and helium signals as a function of the cluster energy. The η dependence of the cluster energy observed for protons and He has also been observed for heavier nuclei. In Fig. 5.16 the average cluster energy measured on the K side of a ladder as a function of η is reported for different ion charges. The η dependence of the cluster energy varies with ion charge (deposited energy) and the variation is different between the K side and the S side. To improve the charge measurement, an energy and η dependent correction factor is applied to the measured cluster energy and the corrected cluster energy spectrum of a ladder is shown in Fig. 5.17 together with the contribution from individual ions. The K side shows a better ion identification capability than the S side. Up to Z = 14, the ion species can be distinguished by a single tracker layer. The ion species can be distinguished up to Z = 25 with the K side and to Z = 16 with the S side. These measurements are compared to those of prototype RICH detector in Fig. 5.19. An excellent correlation to the RICH Z measurement is seen for both the K side and the S side.

5.3 2004 Test Beam

5.3.1 Goals

The main goals expected from this test beam are summarized here:

- test tracker flight ladder response to electrons and positrons of different energies;
- test the feasibility to detect e^+e^- pairs coming from the conversion of photons;
- measure the tracker electron momentum resolution, the photon energy and angular resolution to be compared with simulation predictions;
- validate the calibration and data reduction algorithm;
- test a prototype of the flight electronics.

The ECAL group participated to this test beam with only one calorimeter superlayer because of the non-availability of the electronics needed for the readout of the complete calorimeter.
This test beam was the first one using a setup approaching the final design.

5.3.2 2004 Test Beam Setup

Environment

The test had place at CERN in the East Hall using the T7 beam line. A scanning in momentum was done using beams of 3, 5 and 7 GeV/c. Moreover, in order to improve the percentage of electron in the secondary beam, a primary beam of anti-protons was used together with an enriched electron target. A set of additional instrument were already present in the experimental zone:

- the dipolar magnet able to supply more than 1 T magnetic field; a mapping of this field was performed before the test beam;
- two Čerenkov detectors: the first, 2m-long, was placed inside the experimental zone between the beam exit and the first telescope; the latter, 4m-long, was placed immediately before the beam exit (before the concrete shielding).

Set-up

In Fig. 5.20 a scheme of the test beam setup is presented together with the adopted reference system: the z axis is parallel to the beam direction, the y axis goes along the vertical and the x axis is oriented in order to have a left-handed reference system. Different elements are shown:

- Čerenkov detectors **C1** and **C2** needed for the electron selection from the beam;

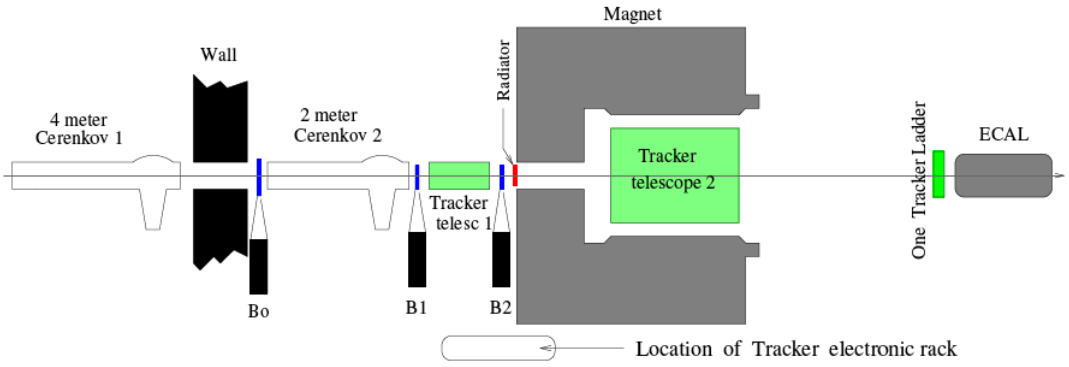

Figure 5.20: Experimental setup of 2004 test beam.

- three scintillator counters **B0**, **B1**, **B2** used for the trigger.
- the dipolar magnet **M**;
- a tungsten converter **R** necessary to generate photons by bremsstrahlung and convert them in e^+e^--pairs;
- telescope **T1**: it was composed of four 12-sensors long flight ladders installed inside an aluminum box. These modules have 5cm distance between them along the z axis and their S-side strips were parallel to the y axis direction. It was used to monitor the beam position and orientation.
- telescope **T2** also referred as the "minitracker": it was the central element of the test beam. It was composed of 11 AMS-02 flight ladders, 9-sensors long arranged in 8 layers (3 of them having two ladders) inside an aluminum box. These modules mimic the AMS-02 Tracker structure both for distances between ladders and for the strips orientation with respect to the magnetic field direction. The last two planes were equipped with 2 ladders per layer (instead of 1 ladder as for the upstream layers) to improve the downstream particle collection. In fact, as the main component of the magnetic field was along the vertical direction, the beam particles were deflected into the horizontal plane.
- telescope **T3**: it was composed by a single tracker flight ladder, 14 sensors long, oriented as **T1** telescope.
  It was used to detect the track impact point on the electromagnetic calorimeter.
- One super-layer of the electromagnetic calorimeter (**ECAL**) was placed downstream the tracker.

A set of pictures of all above elements is reported in Fig. 5.21 and Fig. 5.22. The detailed lists of ladders used in the 2004 test beam with their properties migh be found in Tab. 5.2.

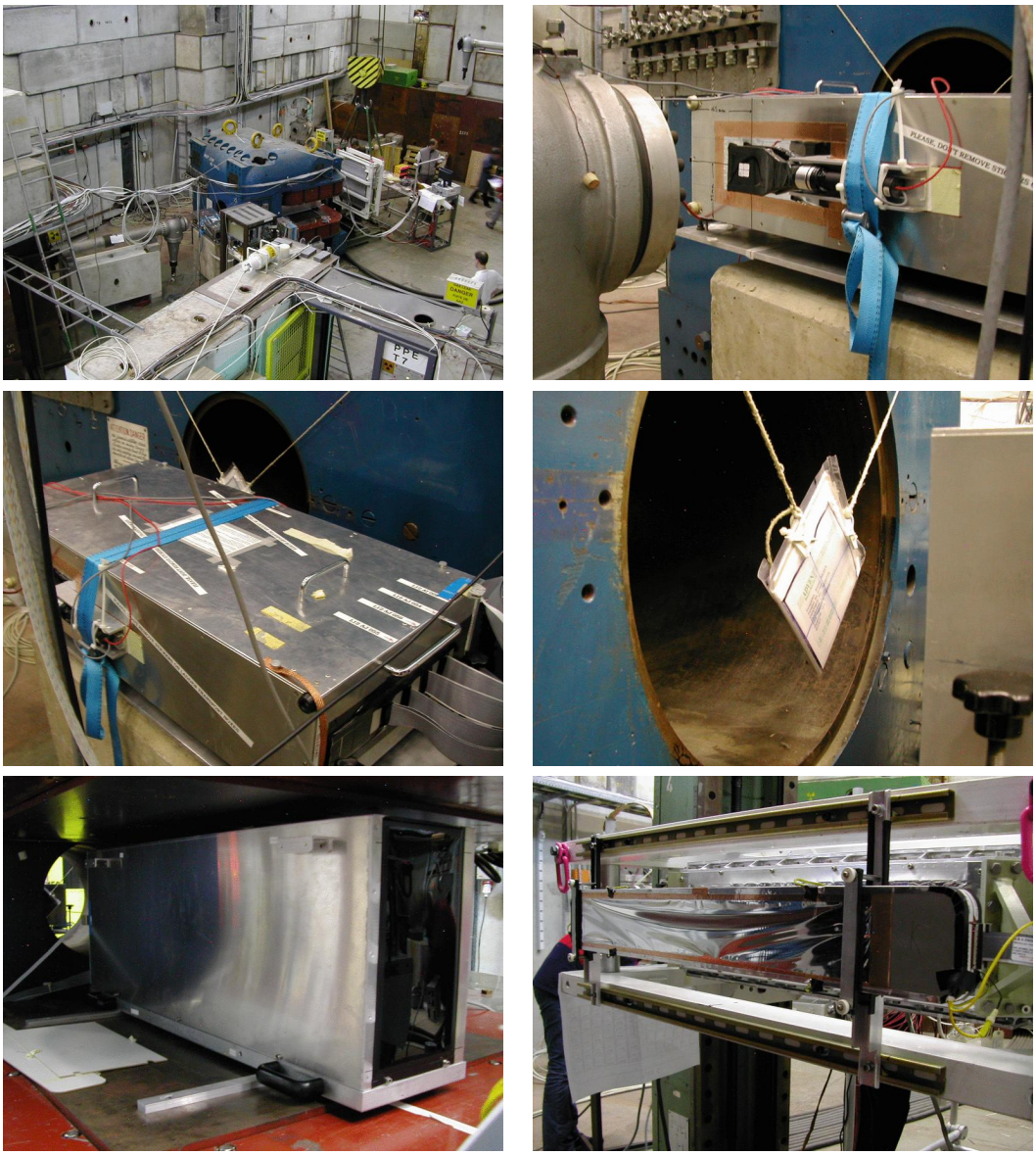

Figure 5.21: Selected photos from the experimetal zone: experimental zone (top-left), **C2-B1-T1** (top-right), **T1** (middle-left), converter **R** (middle-right), **T2** (bottom-left), **T3**(bottom-right).

Figure 5.22: Selected photos from the experimetal zone: **ECAL-T3** (top-left), **T2** closed box (top-right), **T2** open box (middle-left), **T2** ladders with their support structure (middle-right), electronics inside the experimental zone (bottom-left), electronics in the control room (bottom-right).

Ladder	Ladder position in beam	TDR	Current (μA)	Δped-S ADC counts	σped-S ADC counts	Flagged-S channels(%)	Δped-K ADC counts	σped-K ADC counts	Flagged-K channels(%)
L12 AJ 055	T1-00	10	3.7	1.9	2.85	2.0	2.0	3.85	2.6
L12 AJ 056	T1-01	6	3.9	5.6	2.82	1.1	7.3	3.84	2.3
L12 AJ 054	T1-02	2	10.6	5.8	3.00	2.2	5.6	3.78	4.2
L12 AI 002	T1-03	3	2.3	3.5	2.62	1.4	9.6	3.92	2.3
L09 AI 090	T2-04	1	2.5	5.7	2.65	4.8	8.7	3.66	4.2
L09 GI 012	T2-05	0	5.1	7.7	2.87	9.4	3.0	3.32	9.6
L09 AI 089	T2-06	5	3.6	3.7	2.42	2.0	9.4	3.69	2.6
L09 AI 091	T2-07	4	3.9	6.2	2.72	1.7	2.3	3.57	2.1
L09 AI 138	T2-08	9	3.2	0.9	2.37	0.6	1.3	3.51	2.6
L09 AI 102	T2-09	12	3.9	1.6	2.72	3.0	2.2	3.87	2.3
L09 AI 103	T2-10	8	2.6	4.7	2.82	4.1	10.2	3.66	4.9
L09 AI 136	T2-11	21	2.4	5.1	2.56	1.4	15.3	4.06	2.9
L09 AI 135	T2-12	17	4.6	4.0	2.63	2.7	9.4	4.07	3.6
L09 AI 092	T2-13	20	1.9	6.1	2.85	2.3	8.2	3.96	1.8
L09 PI 010	T2-14	16	6.5	4.7	2.82	2.2	11.9	3.88	1.8
L14 AI 044	ECAL-15	7	5.8	5.0	2.89	2.7	9.5	5.10	3.9

Table 5.2: Summary of the S-side calibration results over a *355 h* operation period (runs *712-1508*): Δped, the standard deviation of the pedestals; σped, the average channel noise; $\Delta\sigma$ped, the standard deviation of the noise; and *flag*, the fraction of flagged channels (noisy or dead) in the reference calibration (first calibration of the first run of the period).

5.3.3 Operation Mode

The aluminium boxes hosting the T1,T2 and T3 telescopes had a mylar window to minimize the material to be traversed by the beam. The windows were situated at the level of the last two sensors of ladders for T1 and T3, while in T2 it was opened along the whole length.

The Tracker Data Reduction (TDR) boards controlled the ladder data acquisition: they pilot the hybrid readout sequence and digitize the analog signals issued by each hybrid. Every TDR circuit was connected to one ladder and, after reset, calibrated the ladder to compute each channel pedestal, raw noise and common noise. The standard data acquisition consisted in reading out the 1024 channels, subtracting the pedestal for each channel, computing and subtracting the common noise for each VA. Finally, a cluster identification was done. In real conditions, the communication bandwidth was limited to 2Mbps and only the cluster information was transmitted. Nevertheless the TDR could transfer raw data alone or combined with the reduced data. This latter mode was used for debugging purposes only. During beam tests, the mixed mode was preferred to evaluate the performance and reliability of the data reduction algorithm, provided sufficient data storage is available. In September 2004, only compressed data were recorded, apart few runs taken in raw data mode. The data acquired by the TDRs were transmitted to a PC-computer run under Linux, using the AMSWire [60] protocol. AMSWire is based on the SpaceWire [61] protocol, specifying full-duplex, point-to-point, serial data communication links. SpaceWire is used in space applications, and allows transmission rates from 2Mbps up to more than 100Mbps. An other AMS sub-detector participated to the beamtest: ECAL.
A common trigger was setup and a common event number was available, to compare beam test data.

5.3.4 DAQ System

The coincidence of signals both from the three scintillator counters and the two Čerenkov detectors inside a window of 10 ns constituted the main trigger [248]. At the same time, the system had to be able to accept a new event (NOT BUSY): this meant that telescopes T1, T2, T3 and ECAL had to have completely processed the previous event.
The trigger signal was emitted by a NIM system located in the control room. This signal was sent to the three DAQ subsystems:

- the 15 microstrip silicon ladders;
- the ECAL prototype;
- the CAMAC system giving general information on the event.

Concerning the silicon ladders, the trigger signal was sent to an intemediate board, the JINF, which stood in between the acquisition and the readout. This board was

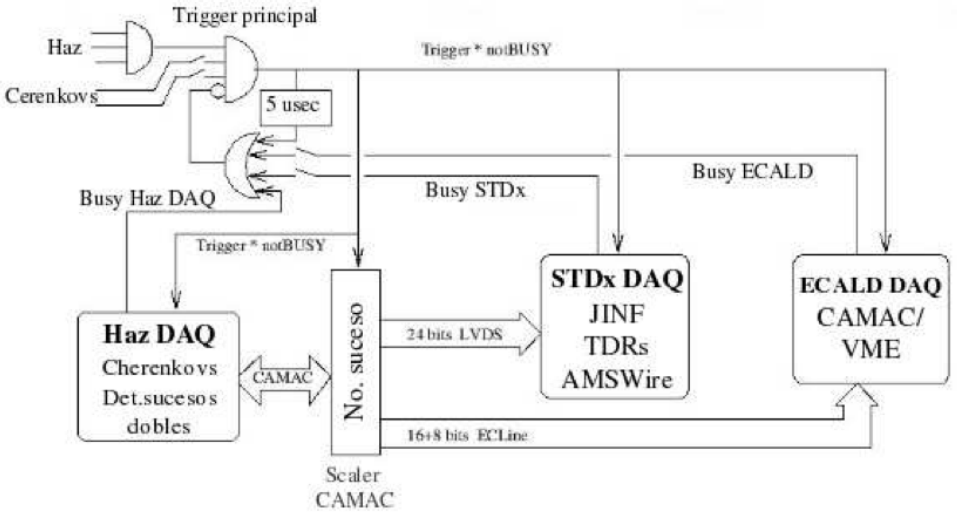

Figure 5.23: A simplified scheme of the DAQ system adopted during the test beam.

in charge to decide when the front-end board (TDR) had to send their data. The digitalization of the signal from each channel of each module and the data reduction took place inside the TDR board. This reduced information was then sent back to the main DAQ system via the JINF board. Another system which received the trigger signal was the CAMAC counter. It had the specific task of numbering events detected in each detectors to make possible the global association of the information from T1, T2, T3 and ECAL. In addition, this device stored the ADC counts from the Čerenkov detectors and carried out the detection of double events, that is those events which contain more than an electron. Eventually, the CAMAC system managed to open a window of $4 \div 7\ \mu s$ inside the scintillator counter B_0 to allow the detection of the subsequent particle.

5.4 Mapping of the Magnetic Field

In order to study the performance of the AMS-02 tracker ladders (via the **T2** telescope), the capability of a precise particle trajectory reconstruction was necessary. These tracks were extrapolated both towards the upstream telescope **T1** and the **ECAL** in order to determine respectively the photon angular resolution (comparison between **T1** and **T2**) and the momentum resolution (curvature in **T2** and energy in **ECAL**). Therefore a very good knowledge of the magnetic field, by its mapping, is crucial for both of these measurements.

5.4.1 MNP22/A Dipolar Magnet Features

A dipolar magnet able to supply a magnetic induction B up to 1.4 T was used. One of the main reason which led to the choice of this magnet was the wide air-gap

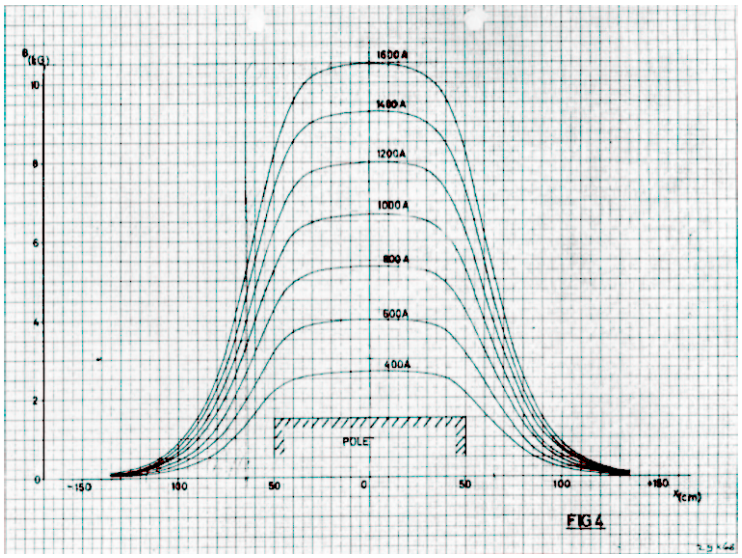

Figure 5.24: Magnetic intensity versus induction characteristics of MNP22/A magnet placed on *T7* beam line as it was measured before the mapping described in this Chapter [236].

height (50 cm). The pole surface was 1 m × 1 m. These dimensions allowed to place the **T2** telescope reproducing the same configuration of the AMS-02 tracker with respect to the magnetic field.
Plot of magnetic induction B versus magnetic intensity H is shown in Fig. 5.24.
Two series of measurements have been taken with 0.4T and 0.8T field value at the center of the magnet which correspond to currents of 600A and 1200A respectively. The current value was fixed using a NMR probe It was put at the center of the gap and it made possible to measure the magnetic field value with a precision of the order of tens of Gauss (10^{-3}T).

5.4.2 Method of Measurement

The magnetic field mapping was realized using a probe able to sweep the whole gap volume. This sweeping was done thanks to a measuring bench able to exploit a 3D orthogonal motion. The reference system was chosen to have the z-axis oriented along the outgoing beam direction and the y-axis was the up-going vertical direction. The origin of the reference system was chosen at the center of the air-gap.
The mapping was done for the air-gap volume and in finer steps where the **T2** telescope had to be placed. Also the value of the fringe field was investigated, in particular in the zone between the **T2** telescope and **ECAL** in order to verify that the latter would not be perturbed by the presence of a residual magnetic field.
The measuring bench alignment and the probe positioning were done by a specialized technical staff with a precision of the order of 0.5 mm in each direction. The probe movement was authomatized.
For a fixed (x,y) position the probe swept the horizontal $\pm z$-axis with a 1.0 cm/s

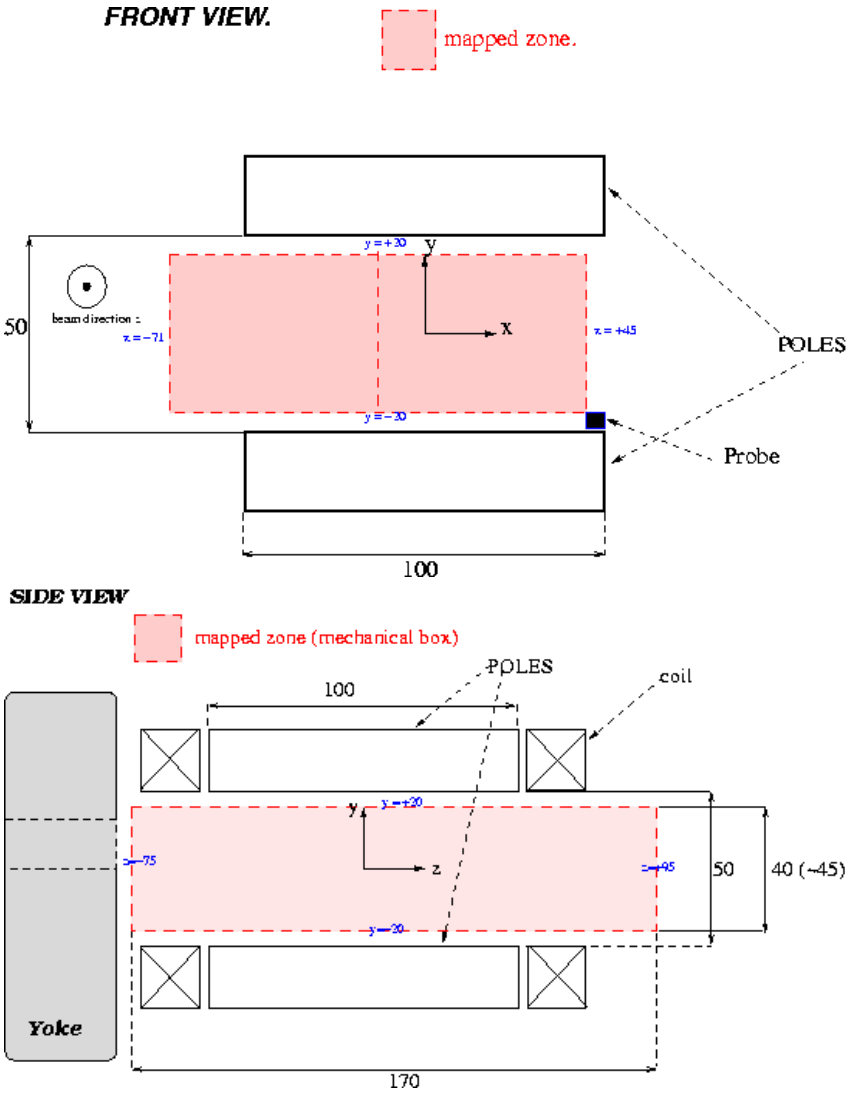

Figure 5.25: Details of different MNP22/A magnetic field mapping zones. Upper: front view. Lower: side view. All units are in cm.

constant velocity.
Given that the probe was not able to cover completely the zone to be studied, a set of "measuring zones" (boxes) was defined with overlapping edges (Fig. 5.25). The measuring method relays on Hall effect. The measuring probe was composed of three independent Hall probes orthogonally placed with respect to each other.
Each probe is composed by a InAs parallelepipedic crystal with a very thin section. If a magnetic field is present, a Hall's voltage is established between the two edges and a current is present. Each of these voltages was measured by a digital voltmeter with a precision of the order of 10^{-3}mV. So three independent voltmeters were used and connected to an acquisition system which recorded each measurement on files (ASCII format).
For each fixed position there was a correspondant voltage measurement performed

by each voltmeter as a Hall probe reached the position one wishes to measure. Measurements were taken each centimeter in the z-axis direction. The (x,y) grid was finer as a compromise between the total measuring time and the precision of the mapping.

5.4.3 Magnetic Field Determination

The raw data files contain the three Hall Voltages, measured by each of the three probes, for each point (x,y,z) of the chosen grid. In order to determine the correspondent magnetic field value, the calibrations for each probe had to be taken into account. In Fig. 5.26 the magnetic induction for each probe is shown. The corresponding mathematical relations have the following form:

$$B_i = a \cdot V_i \tag{5.1}$$

where the index i stays for one of the three coordinate x,y or z.

The error on the magnetic field measurements comes essentially from the calibration. Eventually the relative error on the induction measurements turns out to be under 0.5%. The three probes should work in a constant temperature environment. Both temperature and current have been measured showing no significant variations to justify a data correction.

5.4.4 Field Characteristics

The main component of the magnetic field was the vertical component B_y. Fig. 5.27 shows the variation of this component along the z-axis (for different x values) and x-axis (for different z values) as y is equal to zero. It had a 2.5% maximal variation for $|z| < 300$ mm in the center of the magnet along the beam line (y=0 and x=0). This variation reaches 23% for $|z| < 500$ mm, i.e. the zone where the **T2** telescope is placed. So, it is crucial to have a finer mapping in that zone in order to reconstruct the particle trajectory as precisely as possible. The variation is comparable along the x-axis. The main component is quite homogeneous (less than 100 Gauss variation) along the ladder width (few centimeters for the last plane).

Fig. 5.28 shows the 3D-representation of the field in the central part of the air-gap, again for y=0. The sharp field decrement outside the air-gap is also evident. The main field component B_y is less than 600 Gauss at 1.0 m from the magnet center and falls to 100 Gauss at 1.4 m. This small value is acceptable for the **ECAL** positioning.

For what concern the B_x and B_z components, Fig. 5.29 shows that their modules are less than few hundreds of Gauss.

5.4.5 Magnetic Field Mapping Summary

More than 60000 measurements of the B field were conducted in different positions for the two magnetic field values (0.4 and 0.8 T).

The obtained mapping shows a strong homogeneity of the field in the central part

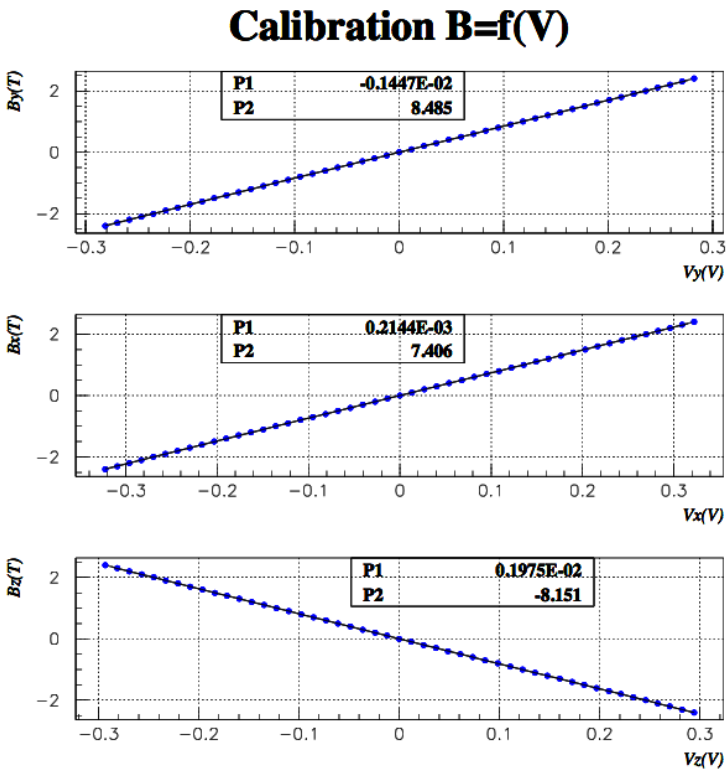

Coordinate	Coefficient a (T/mV)	Relative error on a
X	7.41	0.03
Y	8.48	0.04
Z	-8.15	0.05

Figure 5.26: Calibration characteristics (voltage V - magnetic induction B) for each Hall probe.

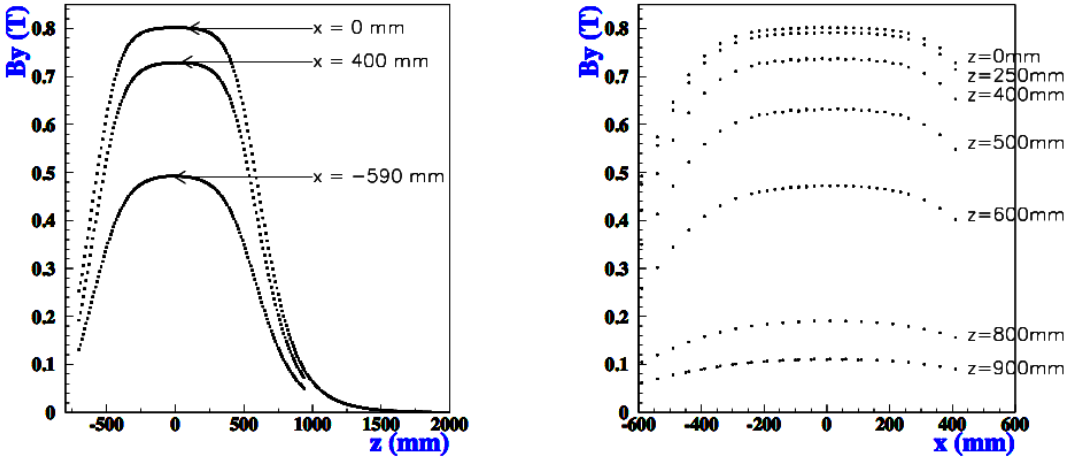

Figure 5.27: B_y variation as a function of z (left) and as a function of x (right), for $y = 0$.

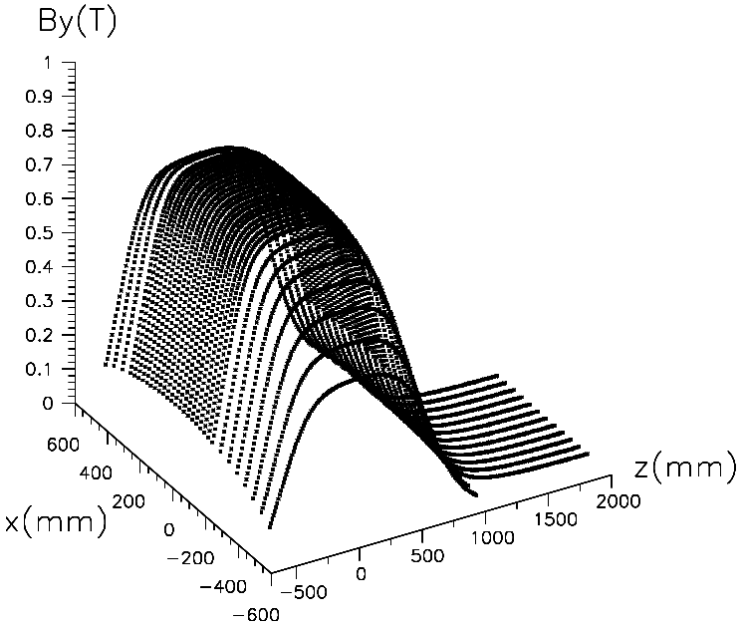

Figure 5.28: B_y variation as a function of x and z for $y = 0$.

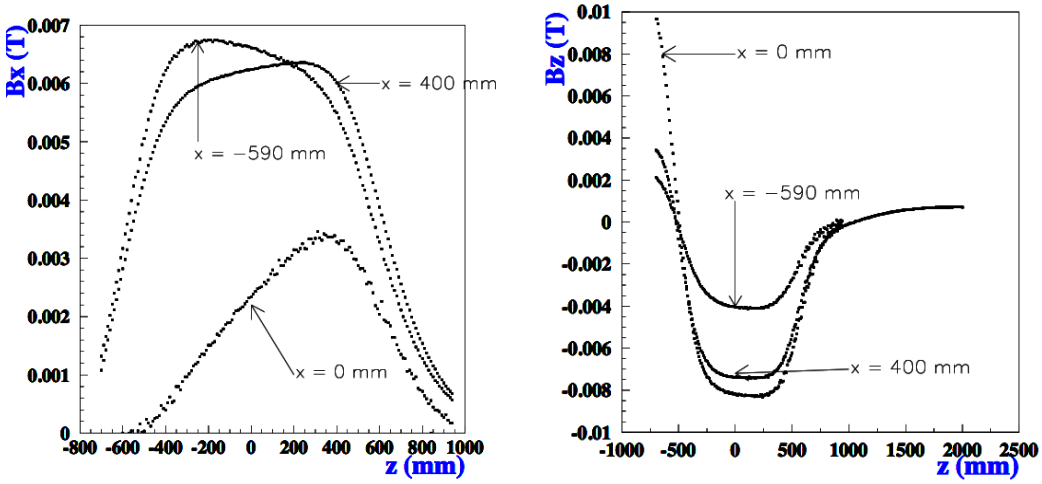

Figure 5.29: -B_x variation as a function of z (left) and B_z as a function of z (right), for $y = 0$.

of the air-gap of the magnet. This is very important in particular at the edge of the magnet poles where the first and last two ladders would be placed.
The field topology for a magnetic field of 0.4 T (in the center of the air-gap) is the same as the one already described (which uses a correspondent value of 0.8T).
These data have been stored in files giving the three field components corresponding to each grid position. So two files exist for a field of 0.4 T and 0.8 T in the center of the magnet air-gap. Those data have been used as an input for the test beam simulation code. Further details are presented in [236].

5.5 Electron Identification

As already mentioned, the main aim of this test beam was to test the AMS-02 flight ladder performances in detecting electrons (or positrons) using an assembling configuration as close as possible to the AMS-02 tracker.
Only a fraction of beam particles were electrons so it was crucial to efficiently identify them. This identification have been done using two threshold Čerenkov detectors.
In order to verify the performances of these two Čerenkov detectors, some preliminary tests had to be done.

5.5.1 Threshold Čerenkov Detector

A threshold Čerenkov detector has two distinct parts. The first one is a cylindrical tube of length L in which the radiator (a gas of refraction index n) is located. It is here that the Čerenkov effect can take place and the produced photons are propagated till the opposite end. A mirror is placed with an inclination of 45^o with respect of the beam direction (the tube axis). Photons are then reflected towards a photomultiplier where the signal can be detected.

The Čerenkov effect appears as a charged particle move inside a medium (liquid or gas with refraction index n) having a velocity v (and $p = \gamma mv$) greater than the speed of light in the same medium (c/n). If the particle velocity is lower than c/n, the Čerenkov effect does not take place.
Over this threshold, atoms closer to the particle trajectory are polarized and the emission of a coherent radiation is observed. This radiation is characterized by an angle θ_c (Čerenkov angle) defined as:

$$\cos\theta_c = \frac{1}{n \cdot \beta} \tag{5.2}$$

where the velocity β has to be greater than $1/n$.
The number of photons per unit path length inside the radiator of a particle with charge Z ($e = 1$) and per energy interval dE of the photons is:

$$\frac{d^2N}{dxdE} = (\frac{2\pi\alpha}{hc})Z^2 \sin^2\theta_c \tag{5.3}$$

where α is the fine structure constant, h is the Planck constant and c is the speed of light ($2\pi\alpha/hc$= 370 eV^{-1} cm^{-1}).

One of the Čerenkov features is the weak emission of photons (with respect to a scintillator, for example) and, consequently, also the number of photo-electrons is very low. In order to improve the PM output signal, the length L and the angle θ_c can be modified. However the length is fixed (L_1=4m and L_2=2m) so one can only act on the angle θ_c. As the main goal was to select electrons, it was chosen to work below the pions, kaons, etc. detection threshold, which means to work with very low signals.
The only way to change the detection threshold of fixed momentum particles is to modify the refraction index n.
The following relation is valid:

$$\sin^2\theta_c = 1 - \frac{1}{\beta^2 n^2} \tag{5.4}$$

The refraction index depends on the used gas and on its pressure. From Lorentz-Lorentz law one gets the following equation:

$$\frac{n^2-1}{n^2+1}\frac{M}{\rho} = R' \tag{5.5}$$

R' being the molecular refraction index.
If a gas is used, n is close to 1 (for example, at P=1 bar, $n(CO_2) - 1 = 4.50 \times 10^{-4}$ et $n(N_2) - 1 = 2.97 \times 10^{-4}$). The previous equation can then be modified as follows:

$$n - 1 \sim \frac{3}{2}\frac{R'}{M}\rho \tag{5.6}$$

Finally, considering the perfect gas law:

$$P = \rho RT/M \tag{5.7}$$

one obtains:

$$n - 1 = (n_0 - 1)\frac{P}{P_0} \tag{5.8}$$

where the index "0" means that the measurement has to be done at atmospheric pressure.

Modifying the pressure (for a fixed momentum beam) the refraction index changes, consequently the detection threshold and the signal intensity from the Čerenkov counter:

$$\sin^2\theta_c = 2(n_0 - 1)\frac{P}{P_0} - \frac{m^2c^4}{p^2c^2} \tag{5.9}$$

For electrons (m_e = 511 keV/c^2) with 1GeV/c momentum, the second term can be neglected. This means that the Čerenkov signal intensity will depend only on the refraction index, so on the gas pressure. This is not true for the other particles

Gas	CO_2	CO_2
Momentum	3 GeV/c	5 GeV/c
electrons	$\sim$ -0.9	$\sim$ -0.9
muons	0.4	-0.5
pions	1.4	-0.1
kaons	> 3	> 3

Table 5.3: Relative pressure threshold (bar) for different particles and momentum in CO_2.

Gas	N_2	N_2
Momentum	3 GeV/c	5 GeV/c
electrons	$\sim$ -0.9	$\sim$ -0.9
muons	1.1	-0.25
pions	2.7	0.3
kaons	> 3	> 3

Table 5.4: Relative pressure threshold (bar) for different particles and momentum in N_2.

present in the beam (m_π = 140 MeV/c^2, m_K = 495 MeV/c^2): there is a strong dependence of the threshold from the particle momentum. The maximum pressure authorized for the counters usage, 3 bar (relative), makes impossible to detect kaons and in general all particles with larger mass (as protons) when their momentum is less than 9 GeV/c (CO_2) and 11 GeV/c (N_2).

5.5.2 Čerenkov Test Setup

The first Čerenkov counter had a length of 4 m and it was placed at the end of the T7 line just before the experimental area. The second one, 2 m long, was placed inside the experimental zone and, for these tests, it was placed downstream the magnet for practical reasons.
Fig. 5.30 shows the setup where C1 and C2 are the two Čerenkov detectors while B1 and B2 are two scintillator counters. The data acquisition was realized via a NIM/CAMAC chain. Some counters connected with B1 (C1) and B2 (C2) gave the number of counts in the scintillators (Čerenkov detectors) during the spill time T. Also the coincidences (B) between B1 and B2 were recorded defining the trigger. Finally the following coincidences were also recorded:

- B1C1 and B2C1
- B1C2 and B2C2

The analog signals coming from the Čerenkov detectors were then converted via an ADC chain.

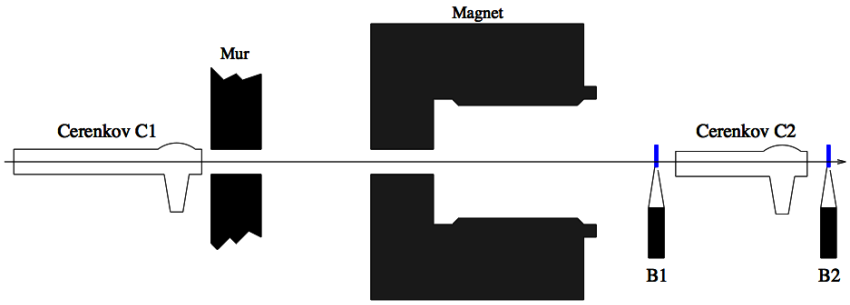

Figure 5.30: Test beam setup with the two Čerenkov detectors placed in.

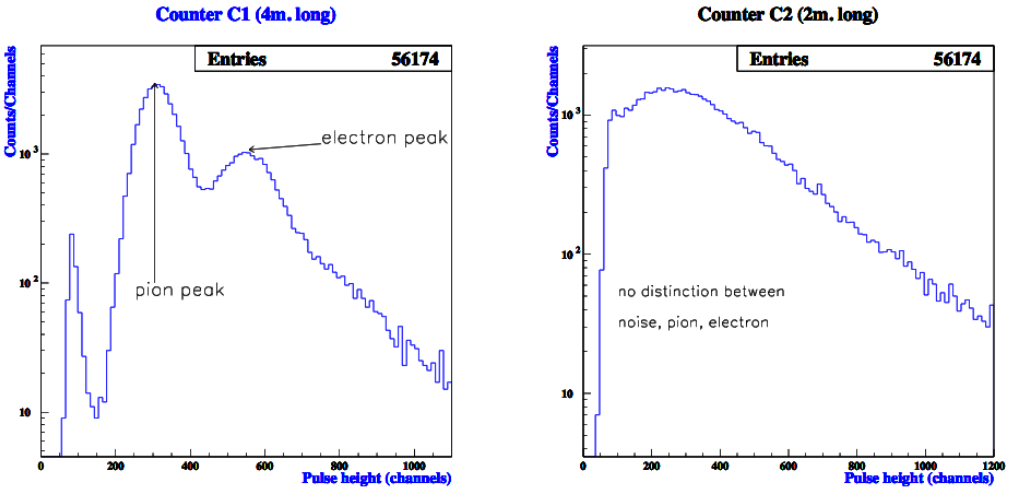

Figure 5.31: ADC signal from counter C1 (left) and counter C2 (right).

There were 3 days of tests where a set of measurements for a fixed beam momentum were performed varying the gas pressure inside the Čerenkov detectors. Two gas were used, Carbon Dioxide (CO_2) and Nitrogen (N_2), performing a manual pressure scanning from 3 bar to -0.9 bar (relative to the atmospheric pressure). All changes concerning the beam property were done by the PS Control Room operator, following user needs.

5.5.3 Performances of the two Detectors

A preliminary test consisted to investigate the performances of the two Čerenkov detectors. The working conditions were chosen in order to be clearly able to distinguish between electrons and pions. CO_2 at 3 bar pressure was used. The momentum of the secondary beam was chosen to be -5 GeV/c (negative sign means that negative charged particles are used).
In Fig. 5.31 the signals (ADC counts) from C1 and C2 are shown. A strong differ-

Setup	a	b
CO_2, 3.0 bar, 3 GeV/c	2.6 ± 0.2	2.5
CO_2, 2.5 bar, 3 GeV/c	3.1 ± 0.2	3.2
CO_2, 2.0 bar, 3 GeV/c	5.3 ± 0.5	5.0
CO_2, 1.8 bar, 3 GeV/c	7.5 ± 0.5	8.2

Table 5.5: Comparison of coefficients a and b for different gases, pressures and momenta.

ence between the C1 and C2 behavior is observed. In fact, the expected three peaks structure is evident for C1: pedestals, pions and electrons. Concerning C2, a rather poor resolution has been found.
This limited the usage of the C2 counter during the test beam.

The correspondence of the electrons and pions peaks is confirmed by comparing:

$$a = \frac{Electron\ peak\ channel}{Pion\ peak\ channel} \tag{5.10}$$

$$b = \frac{(\sin^2\theta_c)_{electron}}{(\sin^2\theta_c)_{pion}} \tag{5.11}$$

These quantities were computed for the four runs where the electron and pion peaks were visible, and the results are summarized in Tab. 5.5.

5.5.4 Particle Selection

In the previous paragraph the capability of C1 counter to identify electrons against pions was shown. A scanning in pressure (Tab. 5.6) was then performed. Results are shown in Fig. 5.32(a, b) and Fig. 5.33(c, d):

Case	Gas	p(GeV/c)	P_{min} rel. (bar)	P_{max} rel. (bar)	Target
A	CO_2	-3GeV/c	-0.9	3	Al
B	CO_2	+5GeV/c	-0.3	1	Al
C	N_2	+5GeV/c	0.0	3	Al
D	N_2	-5GeV/c	-0.7	3	W

Table 5.6: Scanning in pressure for CO_2 and N_2 with different targets and momenta.

Case A)

Under high pressure, signals from electrons and pions can be clearly distinguished. The smaller the pressure the smaller the signals from electron and pions are detected.

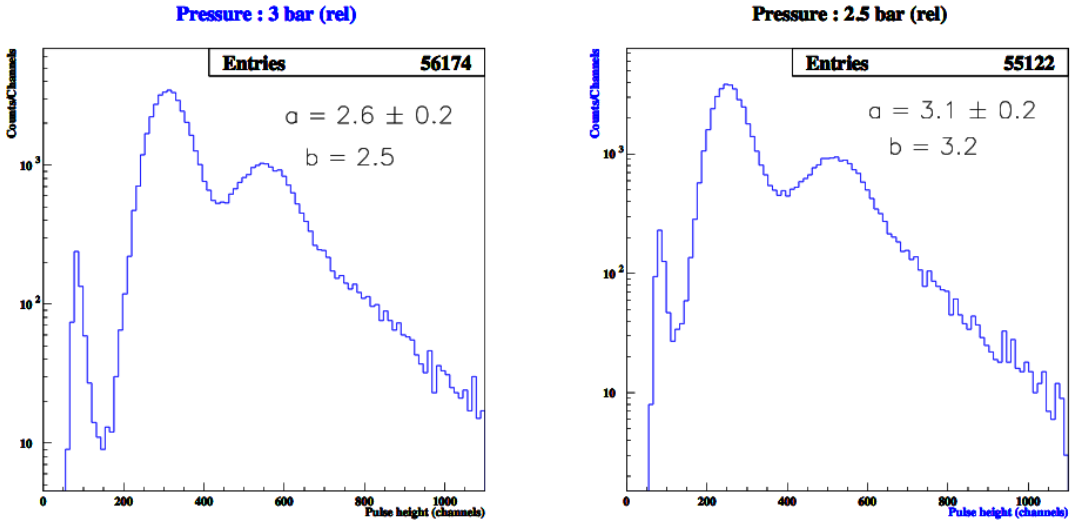

Figure 5.32: Pressure scanning: case A (left), case B (right) (see Tab. 5.6).

Between 1.0 bar and 2.5 bar, the signal from pions disappear. The pion detection threshold is 1.4 bar. The second peak corresponds to 1.25 bar and could be related to the presence of muons. Finally when the pressure is very low the signal from electrons disappears as well.

Case B)

As above but the threshold now is between 0.1 bar and -0.3 bar. Given that CO_2 was used during the test beam, for beam momentum greater than 5 GeV/c, we had to work below the atmospheric pressure.

Case C) and D)

With Nitrogen it is more difficult to distinguish between electrons and pions. However, using this gas the detection threshold of pions is higher than with CO_2. This threshold is found between 0.5 bar and 0.0 bar for a beam momentum of +3 GeV/c and between 0.0 bar and -0.7 bar for a beam momentum of -5 GeV/c.

In order to study the counting rate of coincidence, random coincidences were taken into account. Some set of data has been taken introducing an interval of 100 ns among the coincidence circuits. Consequently, BC1 and BC2 countings correspond to random coincidences.
The counting rate of accidentals between B and C1 is given by:

$$R_1 = R_B \cdot R_{C1} \cdot w \tag{5.12}$$

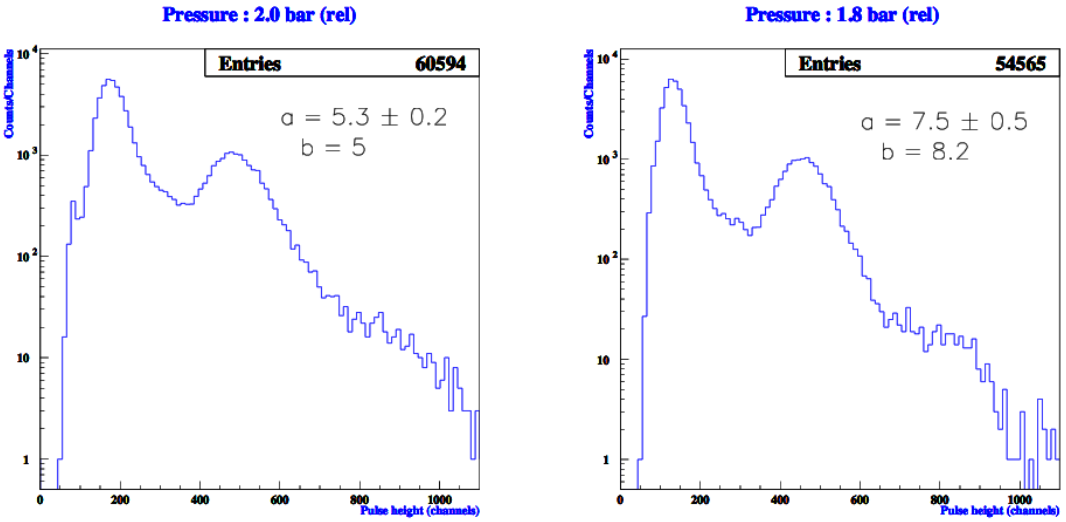

Figure 5.33: Pressure scanning: case C (left), case D (right) (see Tab. 5.6).

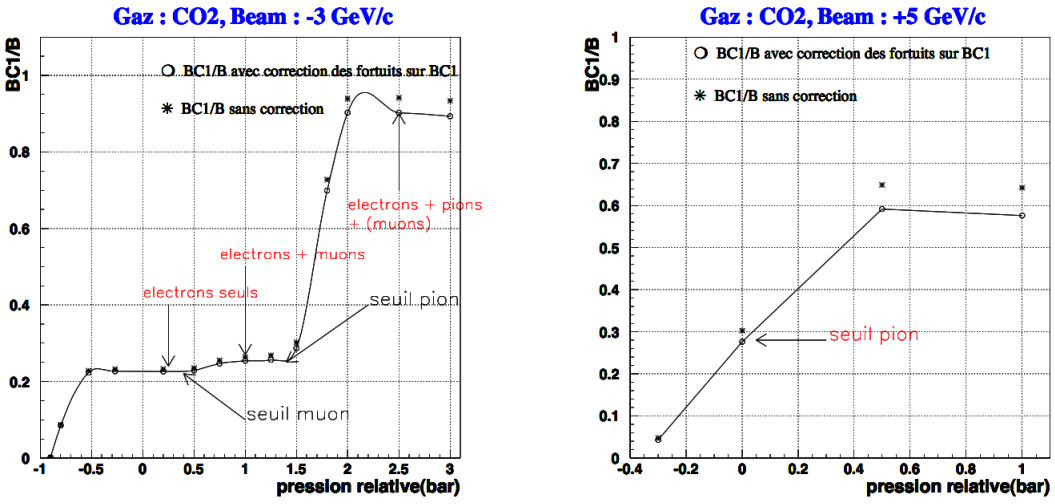

Figure 5.34: BC1 over B counting ratio: case A) (left) and case B) (right).

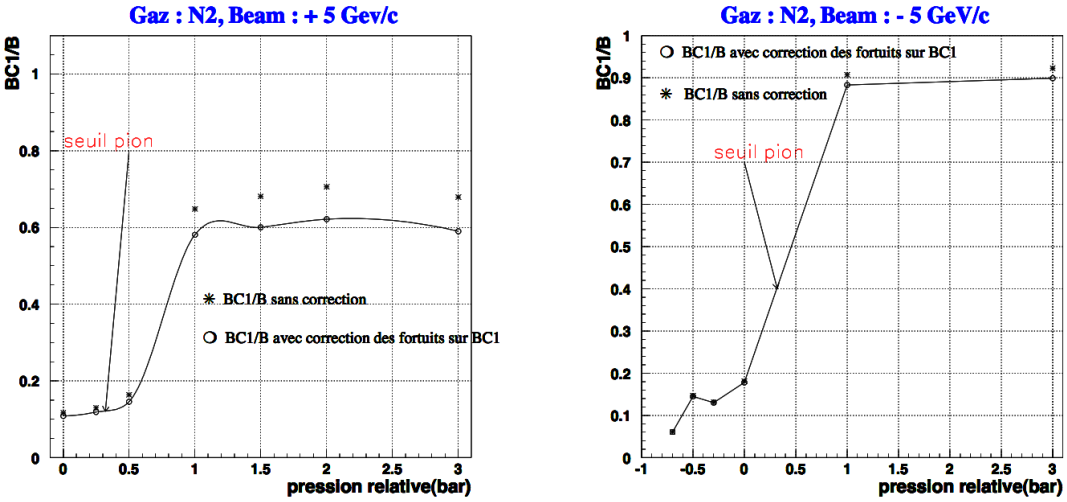

Figure 5.35: BC1 over B counting ratio: case C) (left) and case D) (right).

where w is given by $w = T_B + T_{C1} \sim 30$ns, sum of the coincidence intervals T_B and T_{C1} and where R_i is the counting rate of the counter i.
The number of accidentals can be found multiplying this rate by the spill duration time T (800 ms for case A) and 500 ms for cases B), C), D)). Data and predictions agree very well (relative error $\sim 15\%$). When this correction is done the quantity BC1/B can be plotted as function of the pressure. Fig. 5.34 shows results for case A).
From this picture previous ADC results have been confirmed. The pion detection threshold is evident. This is also true for muons. The presence of a "*plateau* electrons+muons" is a confirmation of the muon peak in Fig 5.32 (for 1.25 bar of pressure). Cases B), C), D) are shown in Fig. 5.34 and Fig 5.35.

5.5.5 Counter C2 Usage

As shown before, C2 counter performances were not optimal. However, it was used to improve the purity of the signal from C1, as shown in Fig. 5.36.
It was also used to estimate the efficiency and the purity of counter C1. A condition where electrons can be detected was chosen: case D (N_2, +5GeV/c) with a pressure of 0.0 bar (Fig. 5.36).

Efficiency ε and purity π are defined as follow:

$$\varepsilon = \frac{\text{Number of triggered electrons}}{\text{Number of total electrons}} \tag{5.13}$$

$$\pi = \frac{\text{Number of total triggered electrons}}{\text{Number of total triggers}} \tag{5.14}$$

In order to find the optimal cut on C2 a plot of the efficiency ε as function of the cut on C2 is done. Fig. 5.37 shows that a suitable cut on C2 ($C2 > 200$), gives an

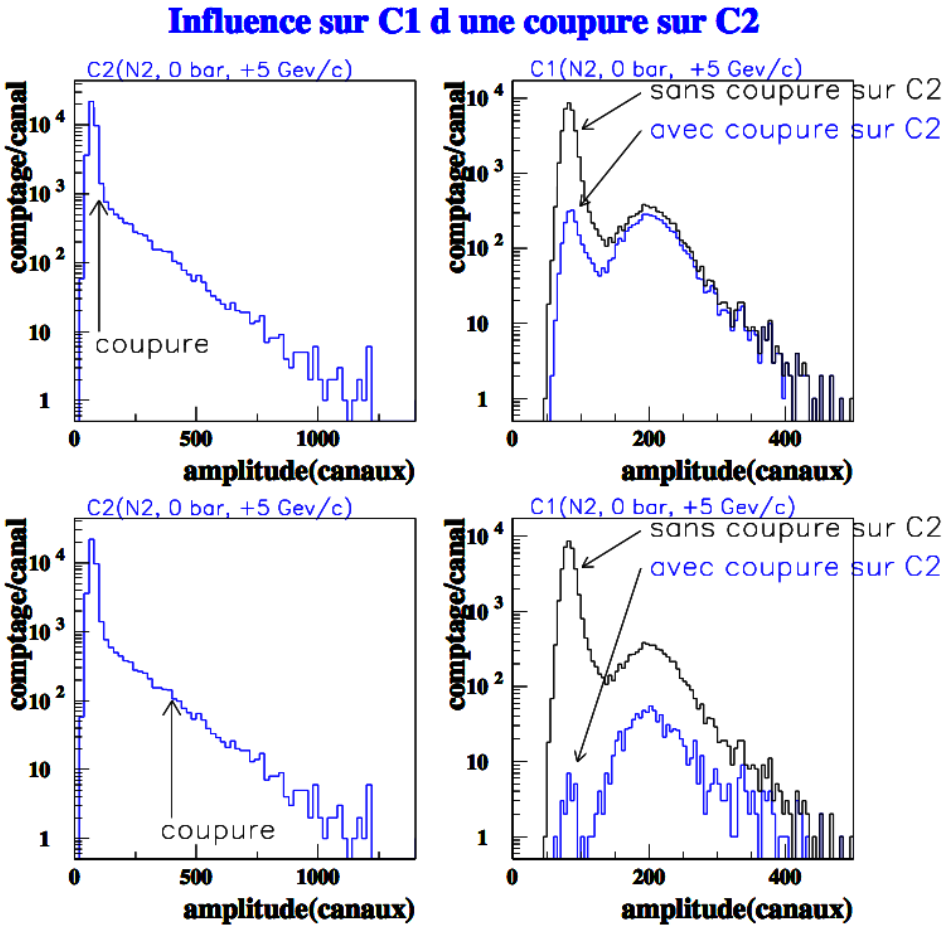

Figure 5.36: C1 behavior when applying a cut on C2.

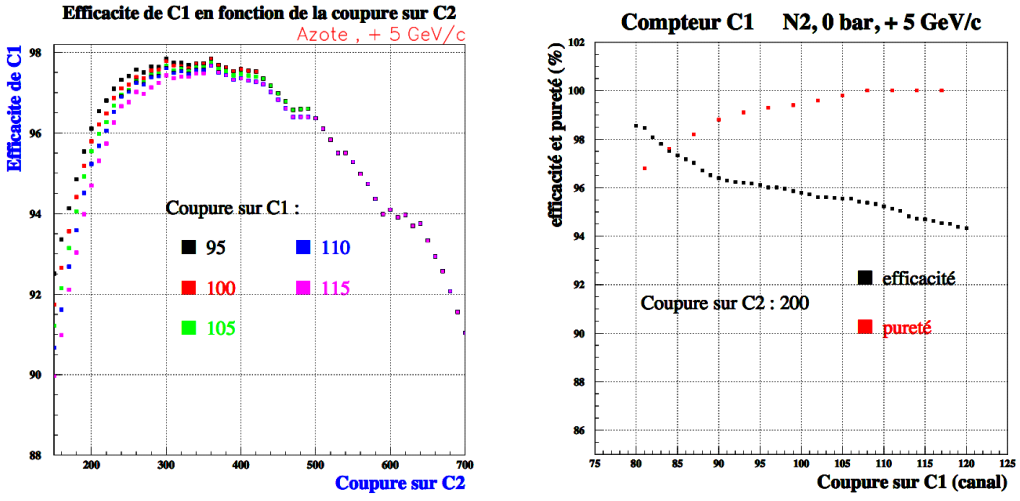

Figure 5.37: C1 efficiency as a function of cuts on C2 (left); efficiency and purity as a function of cuts on C1 (right).

efficiency for C1 greater than 94%.
For a fixed cut on C2 at 200, the efficiency and purity can be plotted as function of the cut on C1. Results are shown in Fig. 5.37 and allowed to fix the cut on C1 between 80 and 85, in order to obtain the best compromise between efficiency and purity.

5.6 Electron Identification Summary

This study confirmed the good performance of C1 Čerenkov detector: both good resolution and detection efficiency. Concerning C2 Čerenkov detector, even if with worse performances with respect C1, it improves the electron selection performed by C1.
Further details are presented in [237].

Chapter 6

The Monte Carlo Simulation

6.1 Introduction

The expected AMS-02 detector response to the passage of cosmic rays and gamma rays is evaluated by means of a simulation program, based on the GEANT package [238]. Mechanical drawings and measurements during the assembly are used to describe in detail the detector geometry. The GEANT package is used to simulate the energy deposit and interactions of incident particles within the different detectors. Physical signals are converted in the equivalent experimental signals and the event reconstruction proceeds as it would for real data. The final output of the full simulation is a compressed data file, using the ROOT framework [239]. It contains the original Monte Carlo record of the generated particle, the kinematical parameters of the particle reconstructed in the different sub-detectors, as well as the relevant sub-detector signals registered in the event [240].
In this chapter, the topics of the AMS Monte Carlo simulation, which are relevant for our study, will be described.
Large samples of Monte Carlo events are needed for an accurate estimate of the AMS acceptance. However, due to the isotropic distribution of cosmic rays and the steep decrease of their flux with energy, an efficient generation strategy and an early suppression of uninteresting events is mandatory to keep manageable the sample to analyze.

After a short description of the event generation and trigger system of AMS-02, the main emphasis in the following is given to the simulation and reconstruction of electron and photons.

6.2 The Event Generation

The first step in the simulation consists in the random generation of the particle momentum according to the expected energy and spatial distribution for the physics channel under study.
However to sample with significant statistics the full energy spectrum observable with AMS, the generation process has to be carefully planned in order to prevent

the total number of events to grow beyond a manageable size. The possible optimizations are connected with the choice of the spectrum to be generated and of the generation volume.

6.2.1 Probe Spectrum and Energy Range

The CR differential energy spectra are generally described by a power law with spectral index < -2.5. This would imply that to generate a significant statistics at energies above O(100 GeV), according to its natural shape, the corresponding number of events generated in the low energy part should be almost three orders of magnitude larger. With this approach the total number of generated events can easily grow out of scale. However the detector response may be studied with a probe spectrum and the results for a different input spectrum obtained just weighting the events accordingly. The chosen probe spectrum follows a less steep power law: $dN/dE \propto E^{-1}$. This provides an enhancement in the event production at high energies, while keeping a larger statistical weight for the low energy part of the spectrum. As a further optimization of the process, the generation range was split into three sub-ranges, namely 0.5 to 10 GeV, 10 to 200 GeV and 200 to 1789 GeV, where the Montecarlo production took place separately.

6.2.2 The Generation Volume

Along with the energy spectrum, it is also necessary to simulate the homogeneous and isotropic spatial distribution of the CR fluxes. This is easily obtained enclosing AMS in a volume V and choosing a random point on the surface of V. From that point, representing a surface element $d\hat{\sigma}$, particles are generated with an energy according to the probe spectrum and direction isotropically distributed towards the interior of the generation volume, i.e. covering a 2π solid angle. The choice of the volume is arbitrary, so a cube both concentric and coaxial with AMS was used. The acceptance of one face of the cube is:

$$A_0(P) = \frac{N(P)}{\Delta t \;\; \Phi(P)} = \int_{S,\Omega} d\hat{\sigma} \cdot d\hat{\Omega} = \ell^2 \int_{\Omega} \sin\theta \cos\theta d\theta d\Phi = \pi \ell^2 \qquad (6.1)$$

where $N(P)$ is the number of particles with momentum P that enter the square in the time interval Δt due to the generated flux Φ, ℓ is the cube edge length and θ is the particle incident angle with respect to a plane normal to the surface. $A_0(P)$ contains a dependence from the trajectory inclination that goes like $\sin\theta\cos\theta$, so the particle directions must be generated according to that distribution. The acceptance of AMS is obtained multiplying the cube acceptance by the detection efficiency $\varepsilon = N_{AMS}/N_{gen}$, estimated as the ratio between detected and generated particles. AMS has a field of view (FoV) of about 45^o around the zenith direction. Particles that are out of the FoV would hit the sides of the detector, either stopping in the large amount of material to traverse (magnet, He vessel etc.) or hitting the ACC system; these particles do not trigger AMS and can be safely ignored. As particles that enter AMS from the bottom must traverse the structure of the ISS, they do

not contain any interesting signal and are therefore rejected a priori, so they do not contribute to the detector acceptance too. The cube edge can be set in such a way that its top plane covers the entire FoV of AMS; in this case only a fraction $\eta_{top}\ \varepsilon_{top}$ of particles generated in the top plane of the cube will be accepted by the detector. It follows that the simulation can be further optimized by generating particles at the top plane of the cube only and obtaining the AMS acceptance as:

$$A_{AMS}(P) = A_0(P) \times \frac{N_{AMS}(P)}{N_{gen}(P)} = \pi\ell^2 \times \frac{N_{AMS}}{N_{top}(P)} = \pi\ell^2\varepsilon_{top} \tag{6.2}$$

The cube edge was set to $\ell = 3.9$ m, , which is the dimension required to have the top plane FoV matching the one of AMS, thus achieving the maximum generation efficiency. From now on the cube top plane acceptance $A_0 = \pi\ell^2 = 47.78$ m^2 sr will be used as the base for the subsequent calculations.

6.2.3 Trigger Simulation

In the previous section the number of detected particles (N_{AMS}) has been defined. This notion relies on the Monte Carlo ability to determine whether a particle crossed the detector or not, however the criterion cannot be simply a geometrical one, but to to reproduce as closely as possible the response of the detector. In real operation the decision to store data depends on pre-set trigger conditions, that can only take into account the signals produced in the various subsystems by the impinging particle. In order to correctly interpret the Montecarlo data the trigger logic must be simulated too.

Only events which satisfied certain criteria will be stored on disk. This can be considered as the simulation of a very loose trigger, called unbiased trigger, which requires that at least three TOF planes out of four carry signals compatible with a charged particle (also referred to as fast trigger or TOFZ1 in the following discussion); in addition, events with a significant energy deposition signal in the ECAL are also stored.

The application of this loose criterion restricts data storage to just 2.6 to 5.8% of the total generated sample depending on the range and the particle species. This corresponds on average to a detector acceptance of 1.2 to 1.8 m^2 sr (0.5-10 GeV), 2.2 to 2.4 m^2 sr (10-200 GeV) and 2.6 to 2.8 m^2 sr (200-1789 GeV) respectively for protons and electrons.

The unbiased trigger acceptance is almost equal to the geometric one and operating the detector with such a trigger would allow to collect a maximum of statistics. Although during the mission a fraction of the events will be acquired with such a trigger for efficiency studies, the unbiased trigger would accept plenty of events marginally measured in the detector therefore of negligible interest for physics studies which would saturate the Data Acquisition (DAQ) of the experiment.

The average event size and the bandwidth for data retransmission to Earth limit the average DAQ rate for AMS to about 2 kHz, with a maximum peak rate of 2.5 kHz. A thorough simulation of flux levels during the AMS mission and the study of the corresponding acquisition rates for different trigger configurations [241, 242]

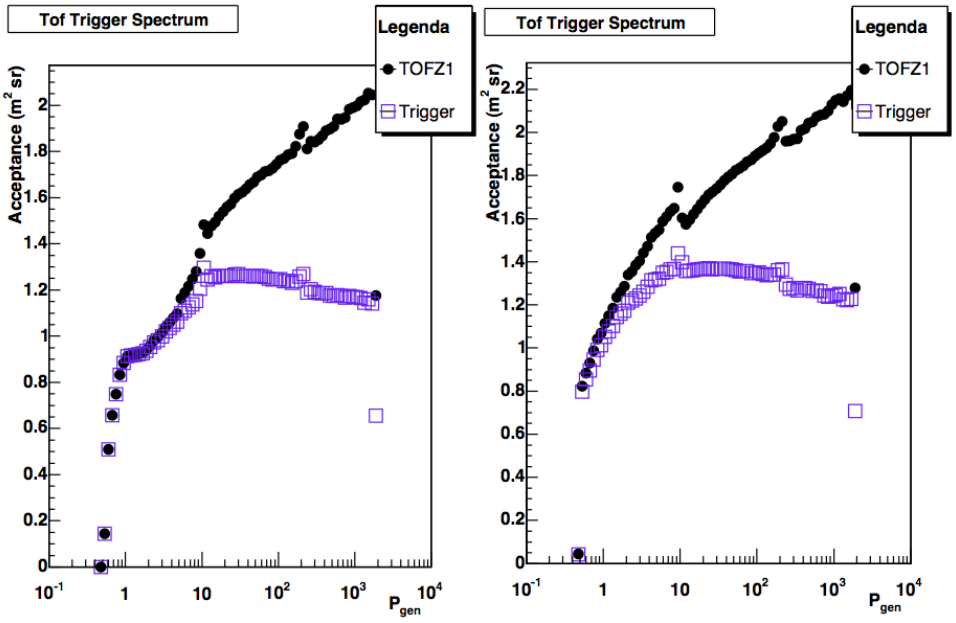

Figure 6.1: Geometric acceptance of the detector after the simulation of different trigger logics, both for p (left) and e (right). The dots refer to the TOF Z1 condition, the squares refer to the full requirements.

have shown that the TOFZ1 condition is likely to exceed peak values of 3 kHz. In order to allow a proper operation of the experiment, the hardware implementation of the trigger logic will be required to:

a) keep the acquisition rate below 2.5 kHz, corresponding to about 75% of live time,

b) feature an almost uniform selection efficiency for properly reconstructed events of 95% or better over the whole measurable rigidity range,

c) be efficient with respect to all the partcile species AMS will study.

The acceptance after the requirement of TOF Z1 is displayed in Fig. 6.1 as a function of generated momentum by the black circles, both for protons (on the left) and electrons (on the right). The decrease of acceptance below about 10 GeV is a common feature for both protons and electrons, though for the former it is steeper towards 1 GeV. The presence of this cut-off is due to the spectrometer magnetic field, which bends the trajectories of low momentum particles to the extent that they do not reach the lower TOF.

6.3 Electrons and Photons Simulation

The GEANT package describes the propagation of the particles impinging on AMS, taking into account the geometry and the material composition of the whole detec-

tor.
This implies, in each small step of the particle trajectory, the evaluation of the probability of each possible physical process and the determination of the final state. When the process takes place its differential cross-section is used to describe the final state.

In the case of photons and electrons/positrons, the following processes have been included:

- pair conversion e^+e^-;
- Compton effect;
- photoelectric effect;
- Coulomb scattering;
- ionization and δ-rays production;
- bremsstrahlung;
- positron annihilation inside the material;
- Cherenkov effect.

The simulation includes the AMS-02 geometrical elements and the materials together with all the attached structures. The simulation software of the test beam also incorporates the components of the experimental setup, including:

- the ladders constituting the T2 telescope (main tracker) and the T3 downstream telescope, with a 300 μm silicon thick sensors; the metallic protection layers (shielding) together with all the support structures;
- the electromagnetic calorimeter super-layer with one photomultiplier readout;
- the 1 mm tungsten converter;
- a magnetic field based on the mapping described on Chap. 5;
- the scintillator counter placed between T2 and T3;
- other setup elements as the aluminum transportation box of the detectors and the mylar layer used to close the box windows (T1 and T2 telescope).

The distribution of the charge between the tracks in digization is simulated introducing an effective uncertainty in the position, according to the measured spatial resolution.
This uncertainty can be represented by one or two Gaussian distributions of variable width. In this effective position uncertainty, effects are included such as the channel noise, the uncertainty derived from diffusive process of propagation of electrons in silicon, fluctuations in the ionization process or the coefficients of charge transfer

(dispersion) to non-adjacent strips.
The relocated impact point determines the strips which constitute the simulated signal. Subsequently, cuts on the seed, used on data to build clusters will be applied. The conversion of deposited energy in silicon in ADC counts is done using an empirical table as function of the interstrip point, obtained in a previous test on such modules and similar readout electronics.
Finally a set of simulated events containing "raw" clusters for each ladder is available, as for data. Both types can be provided as entries to the reconstruction program.

6.4 Electrons and Photons Reconstruction

6.4.1 ECAL Reconstruction

In electromagnetic calorimeters the discrimination between electromagnetic and hadronic showers is based on the difference in the shower profiles [23]. The e/h discrimination in the AMS-02 ECAL derives from its imaging capability. Taking advantage of its fine granularity with alternate planes of fibers oriented along orthogonal directions, the calorimeter can image the longitudinal and lateral development of electromagnetic and hadronic showers, providing two orthogonal views for each event. An example is shown in Fig 6.2. An ECAL event is analyzed in the following way.
The code first checks if the energy deposit and the 3D image of the event are compatible with the ones of a minimum ionizing particle. If the output of this "mip hunting" routine is negative, then the code performs a cluster searching algorithm (separately in x and y views) among those cells of the calorimeter which have been hit. Then, the identified clusters x and y coordinates are paired together using the criteria of proximity and of the least difference in energy. For each shower, if the number of fired layers is ≥ 4 in both views and the lateral leakage is estimated to be negligible, the axis direction is reconstructed via a truncated centre-of-gravity (COG) fit. This procedure considers the COG of the energy deposit in each layer which is plotted as a function of the layer z-position. The separate plots for x and y views are fitted with a straight line. The θ angle of the shower axis with respect to the normal direction to the ECAL surface is inferred from the combined fits. In order to improve the angle reconstruction, the COG in each layer is calculated using only the cells within one Molière Radius from the cell where the maximum energy was released. This truncated COG is more accurate, since the energy deposited in more distant cells from the shower axis is due to particles suffering multiple scattering and hence degrading the shower collimation.

The particle impact point on the ECAL surface is then extrapolated from the COG fit and the longitudinal profile of the shower is fitted using the following parametrization for electromagnetic showers:

$$\frac{dE}{dt} = E_0 \frac{b^{\alpha+1}}{\Gamma(\alpha+1)} t^{\alpha} e^{-bt} \tag{6.3}$$

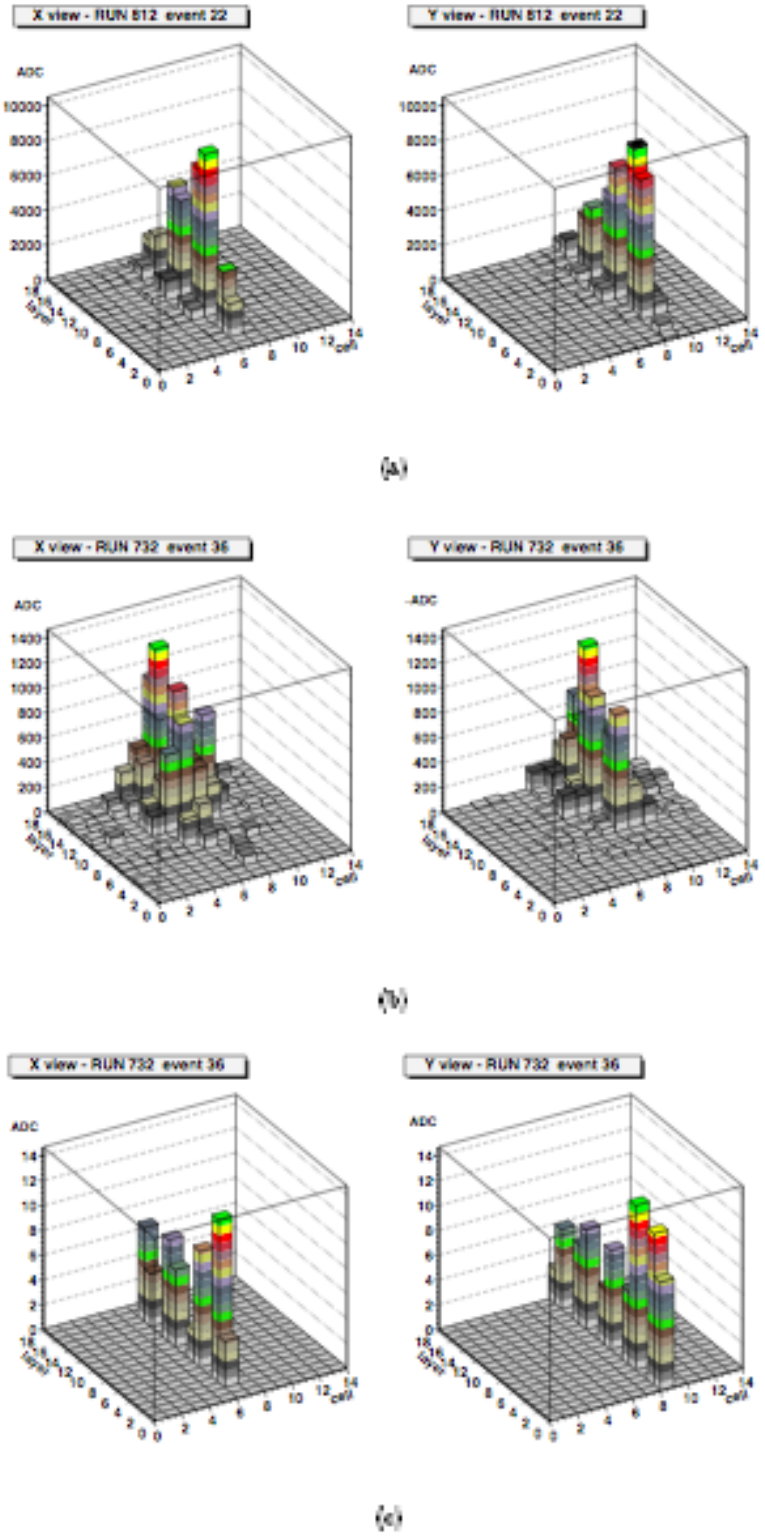

Figure 6.2: AMS-02 ECAL images of: (a) an electromagnetic shower generated by an electron at 120 GeV; (b) a hadronic shower generated by a proton ar 120 GeV; (c) a minimum ionizing proton.

where $t = z/X_0$ is the longitudinal depth in units of radiation length X_0, E_0 is the energy of the incident electron or photon, and $b \approx 0.5$ with a weak dependence on Z. The parameter α is determined by the fitting procedure.
The maximum of the shower t_{max} is also obtained from the fit:

$$t_{max} = \frac{\alpha}{b} = log(\frac{E_0}{E_c}) + C_j \qquad\qquad C_j = e, \gamma \tag{6.4}$$

where $C_e = -0.5$ for electron-induced cascades and $C_\gamma = +0.5$ for photon-induced cascades, E_c is the critical energy defined as the energy at which the bremsstrahlung loss rate equals the ionization loss rate.

At this point, for each reconstructed event, four estimators are evaluated:

1) the ratio E_{1MR}/E_{tot} between the energy deposited within a cilynder with 1 Molière radius and the total energy of the shower;

2) the thrust value, defined as:

$$T = \frac{\Sigma_i |\vec{n} \cdot \vec{p}_i|}{\Sigma_i |\vec{p}_i|} \tag{6.5}$$

where $\vec{p}_i$'s are the momenta of the shower particles and $\vec{n}$ is the unitary vector whose direction maximizes T. The thrust is an event shape variable widely used in accelerator physics experiments to determine jets direction and collimation, but it has also been applied successfully in Cerenkov Telescopes for air shower reconstruction. This method relies on shower symmetry properties assuming that the momenta of particles in the shower are distributed with axial symmetry around the primary particle direction.

3) the determinant M_{COG} of the center of gravity covariance matrix.
This estimator gives a measure of the area of the surface covered by the shower "footprint"in ECAL. It is defined as:

$$M_{COG} = M_{xz} + M_{yz} \tag{6.6}$$

where M_{xz} and M_{yz} are the determinants of the covariance matrices calculated in the two ECAL orthogonal views:

$$M_{xz} = \sqrt{\begin{vmatrix} \sigma_x^2 & \sigma_{xz} \\ \sigma_{xz} & \sigma_z^2 \end{vmatrix}} \tag{6.7}$$

and analogously for M_{yz} while σ_x^2 and σ_{xz} are calculated as follows:

$$\sigma_x^2 = \frac{\Sigma_i (x_i - < x >)^2 E_i}{\Sigma_i E_i} \qquad \sigma_{xz} = \frac{\Sigma_i (x_i - < x >)(z_i - < z >) E_i}{\Sigma_i E_i} \tag{6.8}$$

where $< x >$ and $< z >$ are the center of gravity respectively in the x and z coordinates;

4) the z-position T_{max} corresponding to the shower maximum.

For gamma ray physics the reconstruction of tracks and vertices is also of the utmost importance. In the following, a very detailed description of the tracking reconstruction will be given.

6.4.2 Tracker Clusters

Multiple maxima in strip pulse height, as coming from the DAQ, are separated into *Raw Clusters*, creating as many reconstructed clusters as the detected maxima. A strip which belongs to two reconstructed clusters shares its charge respecting the ratio between the two seed strips of clusters (maxima).
In the software used for the test beam, two sets of quality criteria have been used:

A) *Raw Clusters* are required to have a maximum of six strips. The electrons are not expected to give a signal on more than two or three strips. At least one channel to the left and one to the right of the maximum is always kept even if they are below the fixed 3 σ threshold (this is to take advantage of weak signals in case of noise problems).

B) *Raw Clusters* coming from DAQ are grouped into two samples:

   - 6 strips at maximum, corresponding to the expected signal from minimum ionising particles;
   - more than 6 strips, which have to be corrected because of a failure in the DAQ reduction software. A detailed description of this study will be given in the Chap.7.

   Only strips whose signal-to-noise ratio is $\geq 1\sigma$, where σ is the specific noise, is retained. The minimum threshold to start the clusterization algorithm is fixed to a signal of 4 σ. A Cluster is then formed around this *seed* adding the two closest channels (right and left): this means that a Cluster has three channels at maximum.

A comparison between the two clusterization is shown in Fig. 6.3. In the following the clusterization of type (A) will be referred to as the "old" reconstruction algorithm, while (B) will be referred to as the "new" algorithm.

The stored information for these reconstructed clusters include:

- number of channels;
- charge and the noise value for each channel (in ADC counts);
- total cluster charge and cluster center of gravity;
- the quantity $\eta = Q_R/(Q_R + Q_L)$ where $Q_{R,L}$ is the charge associated to the channel immediately to the right and to the left of the maximum (seed);

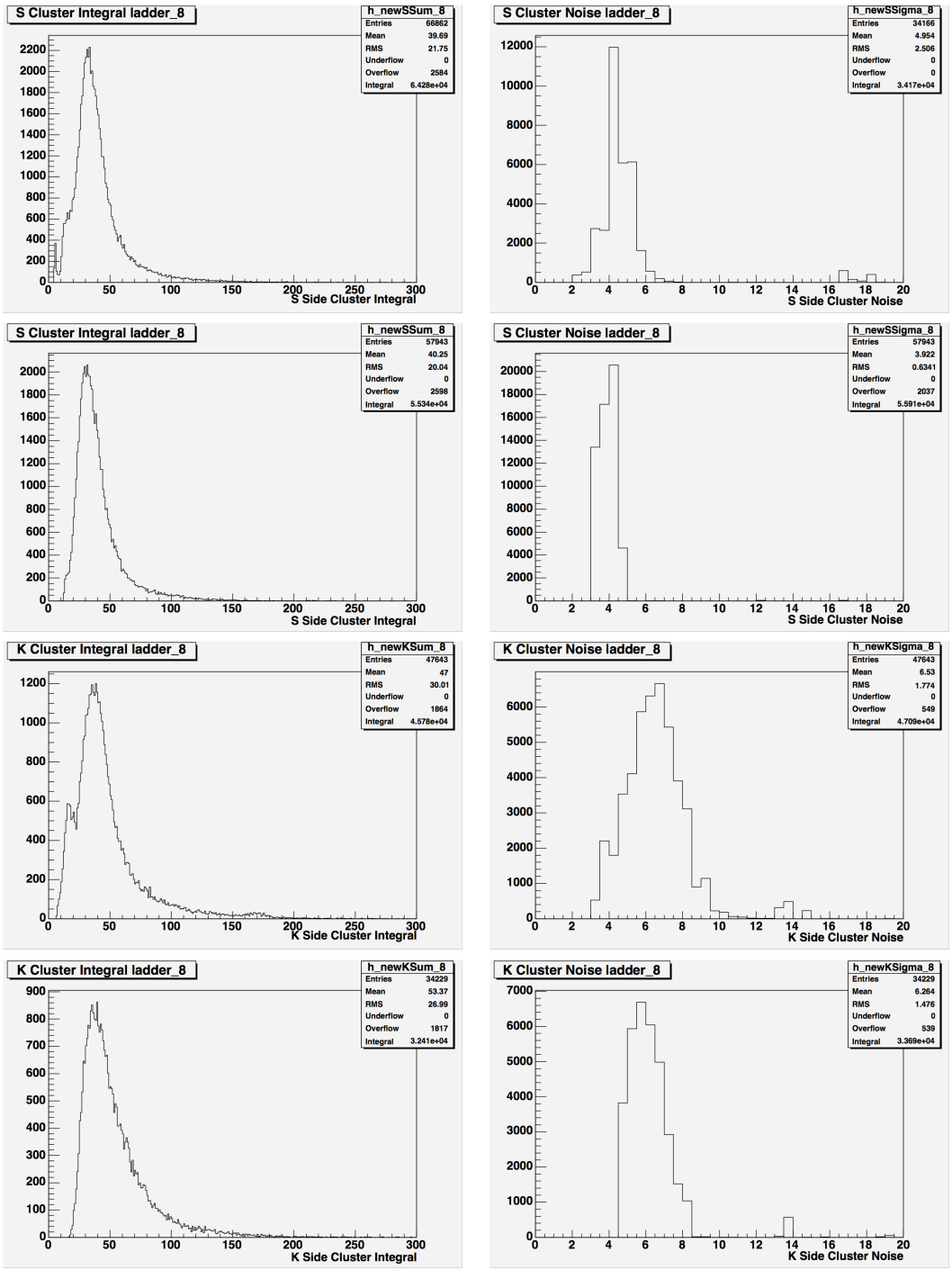

Figure 6.3:
First row: S-side cluster signal(left) and noise (right) using the old reconstruction.
Second row: S-side cluster signal(left) and noise (right) using the new reconstruction.
Third row: K-side cluster signal(left) and noise (right) using the old reconstruction.
Fourth row: K-side cluster signal(left) and noise (right) using the new reconstruction.

- the noise associated to the cluster as $\sqrt{\Sigma_{i=1}^{n}\sigma_i^2}$, i being the number of channels of the cluster.

6.4.3 Hits

The next step is to build hits by an association between S-side and K-side clusters of the same ladder. The K-side readout is multiplexed giving rise to an ambiguity in associating clusters. This ambiguity results in a larger number hits with respect to the reconstructed cluster pairs due to the possible combinations (see Sec. 6.4.4). Concerning the 2004 test beam, this ambiguity is resolved because the height of the beam is known (external constraint). A detailed description of the hit reconstruction will be given in Chap. 7. The hit information, as stored by the software, also includes the position and the strength of the magnetic field in that point. Both of them are fundamental for the determination of the track parameters.

6.4.4 Tracks

The starting point of track reconstruction is the identification in the ladder of clusters of adjacent strips whose signal to noise ratio (S/N) exceeds a threshold value. Since the two sides of a ladder are characterized by different values of the noise, the S/N thresholds depend necessarily on the scanned side. The spatial information carried by clusters is bi-dimensional as S-side cluster measure the bending coordinate (y in AMS coordinate system) and K-side clusters the non bending one (x), while the third coordinate is given by the z position of the layer to which the ladder belongs. In principle clusters from different sides of the same ladder may be matched according to their signal amplitude, however at the start of the Montecarlo production, this was not implemented and all possible combinations were considered [243]. Due to the ladders layout, the position of K-side clusters has an intrinsic ambiguity along the x coordinate, so for each pair of clusters from six to eight hits are created with the same y position and equally spaced x (~ 8 cm).
In AMS-02, in order to determine which hits form a track efficiently, the track finding algorithm will use information from the TOF. The impact positions on the TOF planes are known with accuracy of $\mathcal{O}$(cm) so, combining the upper and lower TOF planes impact coordinates, it is possible to evaluate a rough straight line estimate of the particle trajectory in the (x,z) plane and define a *road* around it. In this way only hits that lie within the road need to be considered by the track finding algorithm. There are actually three methods to evaluate the particle rigidity $R = p/q$:

- the 5×5 matrix inversion method, used for track identification because of its speed of execution, considered the standard algorithm and often referred to as the *Fast Fit*;

- a method based on the use of the GEANE [244] package, integrated with GEANT and accessing directly the simulation geometry and material definition;

- an alternative fitting method called *Path Integral* [245] method, based on the propagation of a particle in the magnetic field from a tracker plane to the next one: the trajectory parameters are evaluated by a χ^2 fit of the observed positions to the ones evaluated in the propagation.

The last two methods, with different approaches, take into account the effect of the interaction of the particles with the material of the detector to improve the accuracy of the particle rigidity measurement.
In Fig. 6.4 and 6.5 are shown the results of a test performed applying the three fitting algorithms on a sample of MonteCarlo data in correspondence to three reference rigidities: 1 GeV, 10 GeV and 100 GeV. The GEANE algorithm performance tends to be worse than the other two at both high and low momenta. On the other hand the *Path Integral* algorithm achieves a better performance at higher momenta, while at low ones it does not seem to improve on the results of the *Fast Fit*.

6.4.5 Vertices

The vertex reconstruction is a key point in the photon analysis given that photons will be reconstructed in the tracker through their conversion in the material in front of the tracker. Vertices are built from two or three tracks. In the AMS-02 standard reconstruction, a vertex is identified by the following conditions:

- at least two tracks having defined reconstructed velocity $\beta = v/c$ are required;
- one track should contains at least 5 hits. This requirement is relaxed to 4 hits for the other tracks;

Concerning the test beam software and the results shown in this thesis, a new algorithm has been implemented and used. It will be described in detail in Chap. 7. The reconstructed variables for any vertex are:

- the momentum defined as the sum over all momenta of the tracks participating in the vertex reconstruction. In AMS-02 this corresponds to the photon momentum, while in the test beam setup the momentum of the recoiling beam particle is included;
- the charge, i.e. the sum of the signs of all track rigidities. In AMS-02, photons generate vertices with zero charge (e^+e^- pairs). In this test beam analysis, vertices with total charge zero and -1 (2 e^- and 1 e^+) will be analyzed;
- the invariant mass;
- the position, defined as the average over all closest points for each couple of tracks. Alternatively, it is also determined as the track intersection point with planes xz and yz;
- the direction, defined as the unit vector parallel to its momentum.

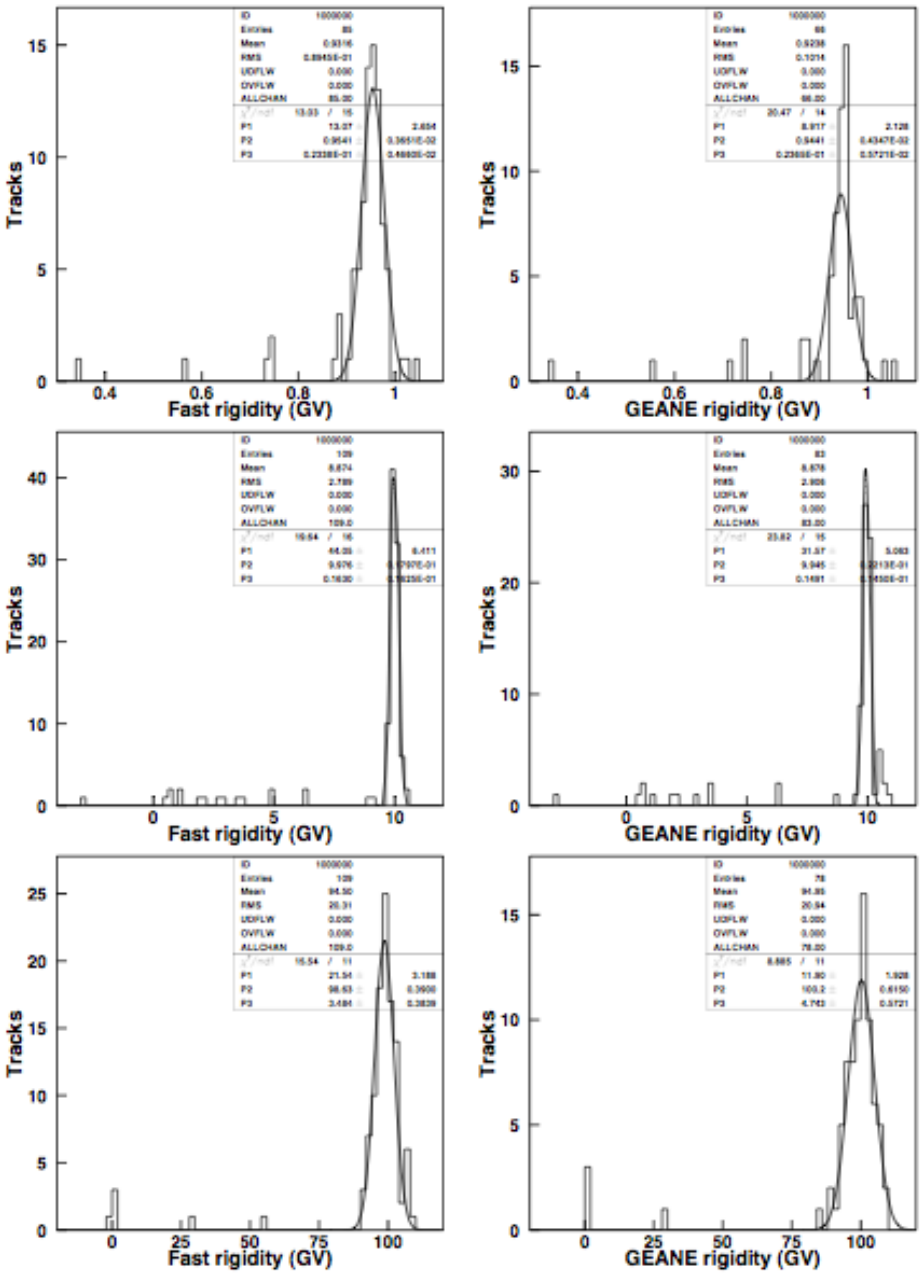

Figure 6.4: Comparison between the rigidities measured by use of Fast Fit (on the left column) and GEANE Fit (right column). The generated rigidities are from top to bottom 1 GeV,10 GeV and 100 GeV.

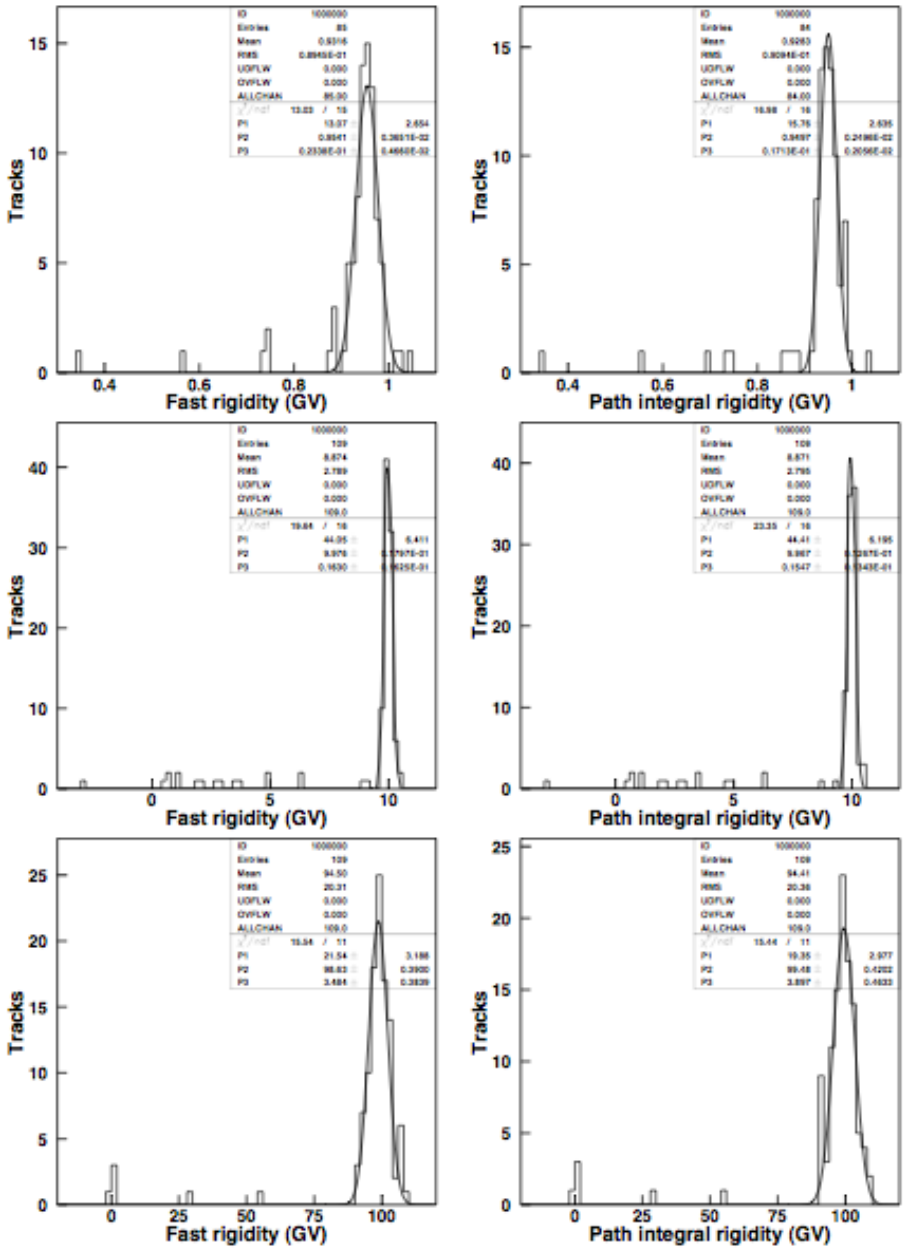

Figure 6.5: Comparison between the rigidities measured by use of Fast Fit (on the left column) and Path Integral Fit (right column). The generated rigidities are from top to bottom 1 GeV,10 GeV and 100 GeV.

Chapter 7

Detector Performance for Electrons and Photons

7.1 Introduction

In September 2004 a slice of the AMS-02 Silicon Tracker was tested at CERN PS T7 line using a beam of electrons with energy ranging from 3 to 7 GeV.
A detailed description of the experimental setup and the main goals to achieve have already been given in Chap. 5.

7.2 Pulse Height Detection and Calibration

This topic is closely related with spatial resolution and signal collection efficiency. Let us consider a microstrip detector with a strip pitch p, crossed by a minimum ionizing particle impinging perpendicular to the detector surface and assume that only one strip collects the charge released by the particle passage. For a homogeneous energy deposit, the spatial resolution is then expressed as:

$$\sigma^2 = \frac{1}{p}\int_{-p/2}^{p/2} x^2 \cdot dx = \frac{p^2}{12} \tag{7.1}$$

In this case, the resolution does not depend on the readout method, digital or analog. The resolution is improved if the readout pitch decreases to the order of the charge diffusion width, which in case of a MIP is about 20 μm. In such a case, the charge is shared between two strips, and calculating the center of gravity of the total signal will improve the spatial resolution.
The limitation of the readout electronics imposes an increase of the readout pitch. This does not necessarily imply a degradation of the spatial resolution, if the capacitive coupling between adjacent strips is taken into account. Indeed this method enables to get a very good resolution with a readout pitch larger than the implant pitch. In the best case, it has been shown that a resolution of 10 μm could be achieved with up to 200 μm readout pitch, but electronics with a high signal-to-noise ratio is required [220].

The signal collected by a readout strip is amplified and digitized. The digital values corresponding to each readout channel need then to be correctly interpreted to extract the deposited charge or specific energy loss as measured by the channel pulse height.

Pulse height reconstruction

Let us denote by x_k^{ij} the pulse height issued by channel i located on preamplifier chip j for event k:

$$x_k^{ij} = p^{ij} + cn_k^j + s_k^{ij} + q_k^{ij} \tag{7.2}$$

where:

- p^{ij}, the pedestal, is the channel mean value in the absence of a particle passage, a constant proper to each readout channel;
- cn_k^j is the preamplifier chip *common mode* noise value at the time of the measurement;
- s_k^{ij}, the random channel fluctuation, follows a Gaussian distribution $N(0, \sigma^{ij})$; σ^{ij} is commonly named the channel *noise*;
- q_k^{ij}, the real signal, follows a Landau distribution around a mean proportional to dE/dx.

The residual r_k^{ij} is defined as:

$$r_k^{ij} = x_k^{ij} - p^{ij} - cn_k^j \tag{7.3}$$

Note that the mean value of r_k^{ij}, in the absence of signal, is 0 as the channel noise is random. A cluster is defined as a group of contiguous channels such that r_k^{ij} is larger than a given threshold. The cluster selection criteria are the following:

$$\frac{r_k^{ij}}{\sigma^{ij}} > C, \tag{7.4}$$

where $C = c_1$ for the maximum signal channel and $C = c_2$ for the boundary channels with $c_1 > c_2$.
The cluster integral, proportional to the deposited energy, is defined as:

$$\mathrm{int}_k = \Sigma_{i=i_0}^{i_0+\ell-1} r_k^{ij} \tag{7.5}$$

where ℓ is the cluster length, i.e. the number of channels composing the cluster, and i_0 the first channel index.

Calibration

To evaluate the residual r_k^{ij}, the parameters p^{ij} and σ^{ij} must be computed from a calibration procedure. The channel pedestal p^{ij} is calculated with N_{ev} events:

$$p^{ij} = \frac{1}{N_{ev}} \Sigma_{k=1}^{N_{ev}} x_k^{ij}. \tag{7.6}$$

This assumes a low occupancy and a mean common mode noise close to zero.
To characterize the channel stability, the width of the distribution of $x^{ij} - p^{ij}$ for $N_{\sigma 0}$ events is calculated:

$$\sigma_0^{ij} = \sqrt{\frac{1}{N_{\sigma 0}} \Sigma_{k=1}^{N_{\sigma 0}} (x_k^{ij} - p^{ij})^2} \tag{7.7}$$

σ_0^{ij} is called the channel *raw noise*. It is possible to separate the fluctuation into two components: a common mode fluctuation of a whole preamplifier chip, and an individual channel fluctuation. The common mode noise cn_k^j is calculated for each readout event k and each preamplifier j:

$$cn_k^j = \frac{1}{N_{CN}} \Sigma_i (x_k^{ij} - p^{ij}) \cdot s^{ij} \tag{7.8}$$

with

$$N_{CN} = \Sigma_{i=(j-1)N_a+1}^{jN_a} s^{ij} \tag{7.9}$$

where N_a is the number of channels per chip.
The channel noise σ^{ij} is defined as the width of the distribution of r^{ij} for N_σ events:

$$\sigma^{ij} = \sqrt{\frac{1}{N_\sigma} \Sigma_{k=1}^{N_\sigma} (r_k^{ij})^2} \tag{7.10}$$

The noise parameters allow to interpret the channel behavior, directly related to the silicon quality. Furthermore, the width of the distribution of cn^j contains information about the electromagnetic insulation of the setup.

7.3 Data and Montecarlo samples

Data have been acquired in three different configurations:

1) Without magnetic field and without converter (BoffWoff), used for alignment studies.

2) With magnetic field and without converter (BonWoff), used for the electron momentum resolution studies.

3) With magnetic field and with converter (BonWon), used for the photon energy and angular resolution studies.

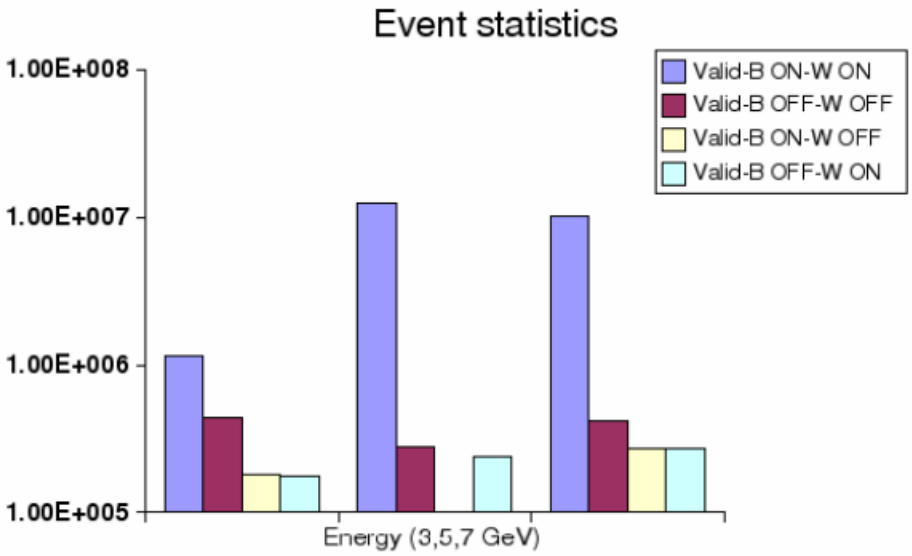

Figure 7.1: Statistics collected for the three beam momentum condition. Different colours correspond to the different combined conditions of data taking with or without both magnetic field $\vec{B}$ and tungsten converter.

In addition, a scanning in energy was also done using a beam with momentum respectively of 3, 5, and 7 GeV/c.The total collected statistics is shown in Fig. 7.1. More than 2.5×10^7 triggered events were collected.

Each run lasts about 30 minutes and four ladder calibrations, each associated to a run, are performed every 8 minutes. In particular a calibration considers the following quantities for each channel: pedestals, channel noise ($\sigma^{i,j}$), status of the channel and the standard deviation of the collected ADC counts (σ_{raw}).

The Montecarlo simulated events for the three beam and converter configuration and for the three choices of beam momentum contains ten times more statistics than the corresponding data sample.

7.4 Preliminary analysis

Before starting the physics analysis a check on the collected data was done. One of the aim of this test beam was testing the data reduction algorithm that was the prototype of the official flight code for AMS-02. The data reduction algorithm involves the channel pedestals analysis as well as the VA chip Common Noise subtraction from the signal.

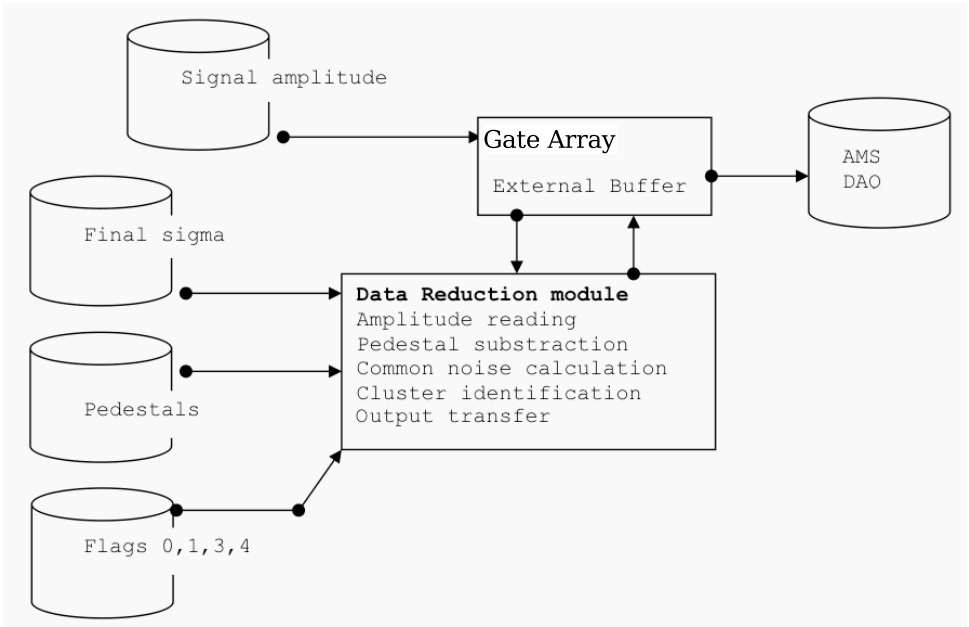

Figure 7.2: Block diagram describing the different functions of the Data Reduction Module.

7.4.1 Pre-handling of data

The reduction algorithm is executed by the Data Reduction Module (Digital Signal Processor) inside the TDR board. Almost the whole data collected during the test beam was collected using this software apart a small sample from a single ladder and for a very limited data taking period.
In order to test the algorithm, parameters (as the *seed* to start the clusterization) were systematically modified resulting in different set of collected data. Studies were done varying the *seed* between 3 and 5 $\sigma^{i,j}$. Finally it was fixed to 4 σ as a compromise between the statistics collection and the accepted background hits.
The issue of the reduction module is to provide the complete list of event clusters from the 1024 channels treated by each TDR [246].
The Data Reduction Module, as shown by the scheme in Fig. 7.2, consists of the following steps:

1) reading and reordering of the amplitudes (1024 channels);

2) common noise calculation, excluding bad channels and those with noise greater than a fixed threshold; in case of a channel with a signal above the seed cut, it will be memorized in a table as "candidate" for a cluster seed;

3) cluster analysis, exploiting the table of candidates from the second step, after subtraction of the common noise: the address and the length of such clusters are memorized in a table and sent to the next step; clusters are then written to be used by the analysis.

In a first version of the Data Reduction Module code [247], the result of the subtraction of the pedestals from the ADC output values was compared to a threshold. If the values exceeded that threshold, the corresponding channels were excluded from the common noise calculation. The consequence of such an algorithm is that, in case of high common noise fluctuations, a large number of channels were excluded and the final common noise was smaller than the actual value. At the clusterization level, the reduction algorithm found fake clusters containing a large number of channels. This software failure required offline correction on affected clusters which will be described later (see Sec. 7.5.3).

7.5 Detector performance

7.5.1 Alignment

To study the alignment of ladders several runs with straight tracks have been used; this configuration was obtained switching off the magnetic field and removing the converter (runs BoffWoff of data sample). This alignment process has been carried out in several iterations:

1) Ladders of the T2 telescope have been internally aligned using three free parameters: x, y and a rotation around the z-axis, assuming the tracks having a perpendicular incidence angle and fixing the position of the first ladder.

2) Ladders of the T1 telescope have been aligned using the same method as in point 1).

3) The relative alignment between T1 and T2 has been performed using tracks traversing the two detectors and fixing the position of T2.

4) The internal alignment of T1 and T2 is then completed including rotations around the x and y axes.

5) Eventually, the T3 telescope has been aligned using tracks traversing both the T2 and the T3 telescope.

Residuals are defined as the difference between the reconstructed hit on a specific ladder and the predicted impact point of a track built using the remaining hits from the rest of ladders.

After the alignment, the distributions of the residuals of each layer had width values less than 25 μm, 0.8 ± 0.1 μm being the mean on x coordinate and -0.02 ± 0.10 μ m on y coordinate.
The output of the alignment procedure is a new geometry file with corrected positions for each ladder. The new recalculated positions are used in reconstruction to determine the positions of the hits.

7.5.2 Calibration

Calibration runs were regularly taken during data taking. The calibration procedure, as described in Sec. 7.2, has been used for each run to derive pedestals, channel noise and their widths. In Tab. 5.2 of Chap. 5, a summary of calibration results for the studied period of data taking is shown. The fraction of channels marked as *noisy* or *dead*[220] lies in the range between 2 and 4% except for ladder 5 which reach a value of 10%.
Calibrations indicate a small percentage of channels identified as "*bad*", ($\sim 3\%$) as well as a stable behavior of the noise. This is fundamental for the identification of clusters and determination of the particle impact point.

7.5.3 Cluster Reconstruction

Two different cluster algorithms are compared in this analysis. The first algorithm (A) is limited to a maximum of 6 strips for each raw cluster while the second one (B) recovers large raw cluster recomputing the common noise which was wrongly computed by the Data Reduction Module. The common noise is calculated over 64 channels (VA width) trying to suppress the signal channels which sometimes leads to an underestimation of the noise and artifically long clusters.
Reconstruction (B) re-runs offline the correct algorithm for noise suppression on long raw cluster, recomputing the noise and producing a new set of seed clusters to be used in reconstruction.
The effect of the wrong computation of common noise is visible in Fig. 7.3. The integrated charge of clusters reconstructed using both algorithms is shown in Fig. 7.4 as well as their associated noise. The large raw clusters after the proper common noise appears as it is expected from an electron hit (Fig. 7.5). In addition, a certain K-side clusterization inefficiency of the level of 5 to 10% has been observed.

As a consequence a deficit in the number of reconstructed hits and tracks was present. This affected the three tracks event statistics, which is the most interesting sample for the photon study.

A subsequent laboratory test detected an ondulatory pattern superimposed to the K-side VA signal throughout all the 64 channels. It was identified as a problem of insulation solved for the final implementation. For this reason it was decided to use a technique by which K virtual clusters are created and used together with the corresponding real S clusters to build hits. These K clusters are characterized to have a fixed value of their position, but the correspondent hit, which participates to the track fit, has a very large error in order to weaken the corresponding bias. In that way, a great amount of events with five hits (minimum threshold to start the track fit) were recovered. In Fig. 7.6 the increase in the number of reconstructed hits using this procedure is shown. No significant effect on reconstructed tracks is observed.

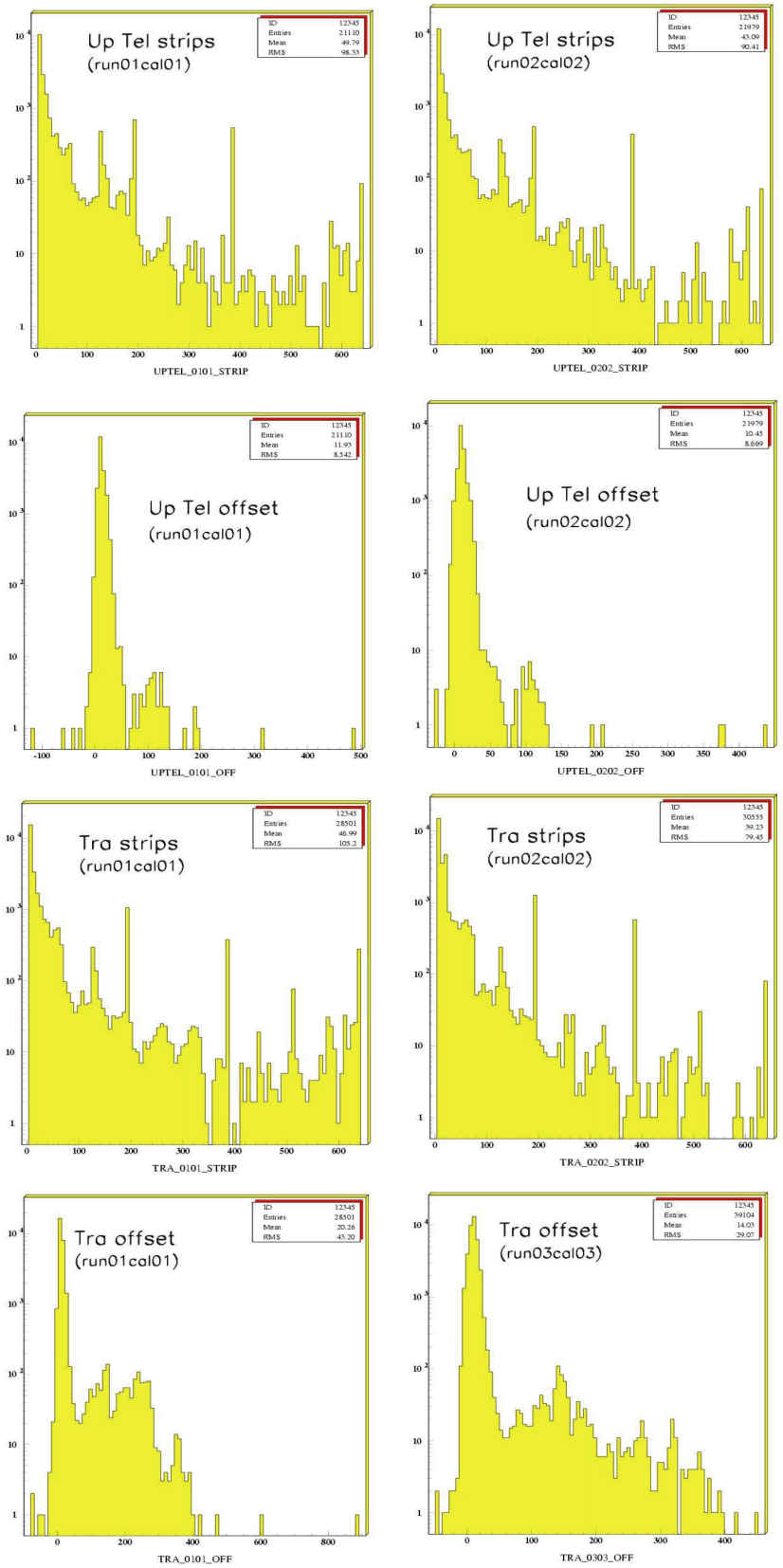

Figure 7.3: Number of strips and offsets for T1 telescope (top two rows) and T2 telescope (bottom two rows). For correctly built raw clusters the offset should be around zero and the size of cluster should be of few strips.

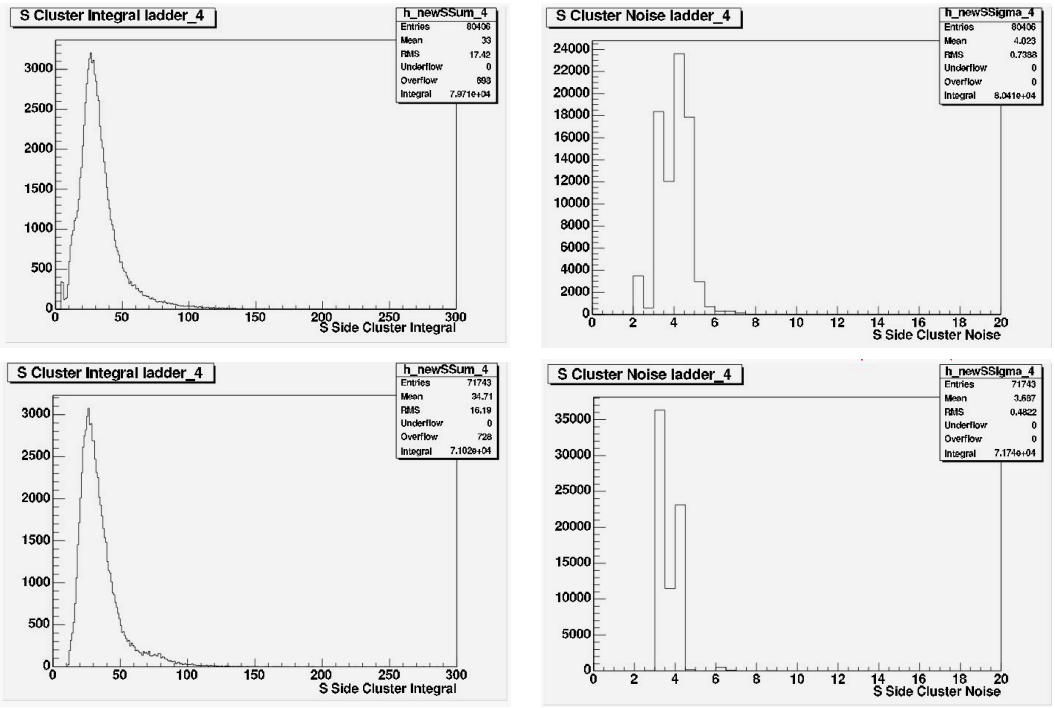

Figure 7.4: Distributions of integrated charge of clusters and their noise using the old (top) and the new (bottom) reconstruction.

7.5.4 Track Mirroring

The mirroring effect comes from an incorrect deconvolution of the K-side channel multiplexed read-out. The effect is evident in Fig. 7.7 where the double peak structure in the data is due to the multiplexing. The mirroring effect is corrected extrapolating the track from the T1 telescope to the first ladder of the tracker (T2) and accepting the hit in a window $2\text{cm} \times 2\text{cm}$ around the extrapolated impact point.

For each layer inside T1 and T2 telescopes both x and y hit coordinates have been studied. The scatter plot of the coordinates before and after the correction of *mirroring effect* are shown in Fig. 7.8. The recovering of the mirrored hits in the y coordinate is evident.

In Fig. 7.9 the distribution of the difference between the Montecarlo prediction of the hit position coordinate extrapolated from T1 telescope to the first layer of T2 telescope and corresponding coordinate before the correction of the *mirroring effect* are shown: it confirms the necessity to introduce such a correction.

7.5.5 Hit and Track Efficiency

The single hit and the track efficiency are defined, respectively, as:

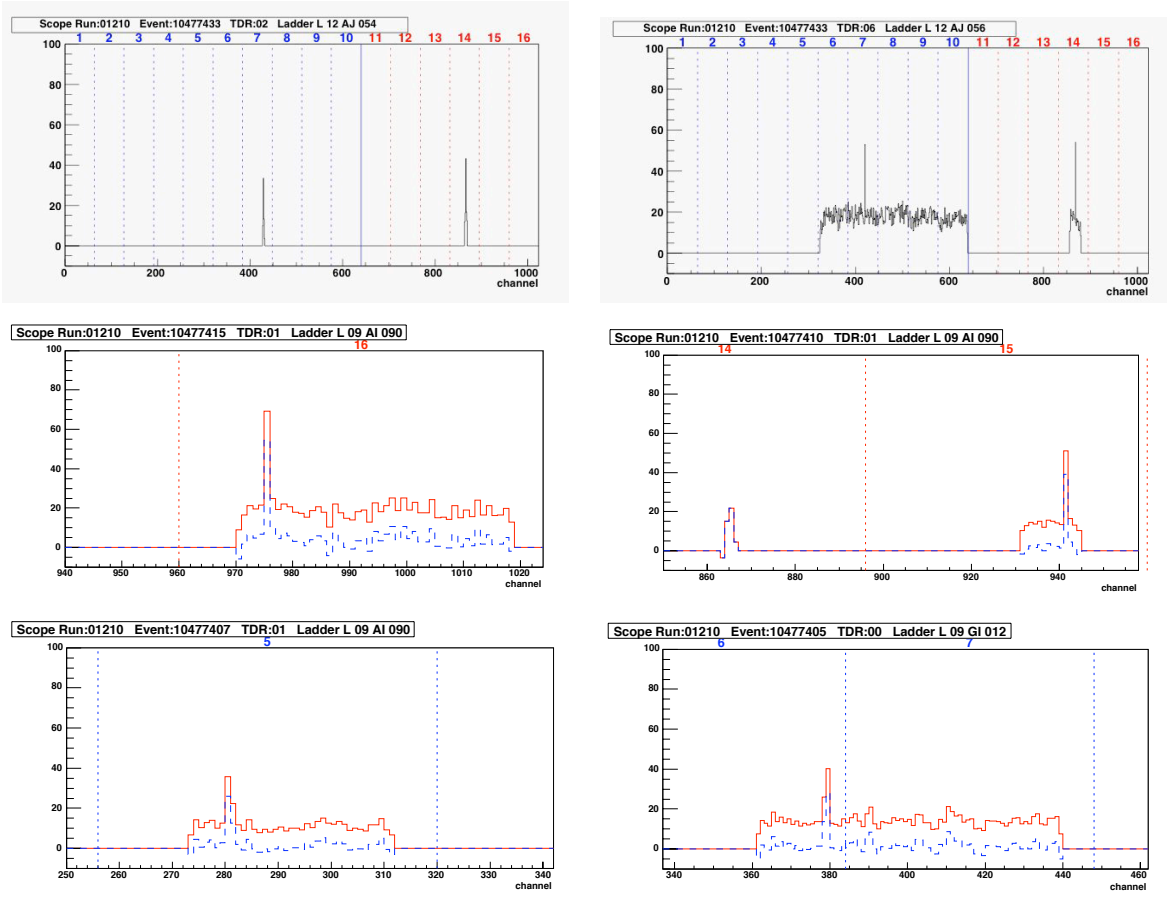

Figure 7.5: Original good (top left), not good (top right) and corrected (others) raw clusters.

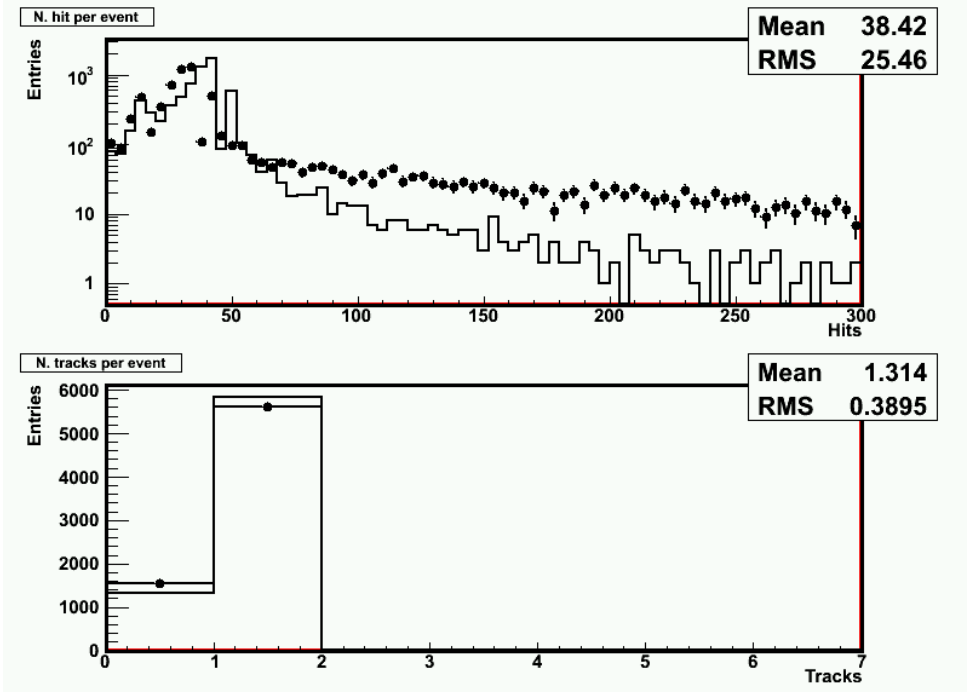

Figure 7.6: Number of reconstructed hits and tracks with (dots) and without (line) using the virtual K-side clusters.

- *Hit efficiency*:

$$\varepsilon_{hit} = \frac{\text{Number of } \textit{hits} \text{ detected on layer}}{\text{Number of } \textit{hits} \text{ predicted using all but the current layer}} \tag{7.11}$$

- *Track efficiency*:

$$\varepsilon_{track} = \frac{\text{Number of hit belonging to a track detected on layer}}{\text{Number of hit predicted from tracks on all but the current layer}} \tag{7.12}$$

where for both equations the denominator means that all ladders are included except the one whose efficiency is being computed.
The hit and track efficiencies have been computed using both cluster reconstruction algorithms. The results are shown in Fig. 7.10 and Fig. 7.11 and listed in Tab. 7.1 for each layer and compared to Montecarlo simulations. The efficiency improvements range from 1 to 10% between the reconstruction algoritms (A) and (B).

7.5.6 Spatial Resolution

In the test beam environment the position of the beam is not known with enough precision to determine the spatial resolution. The residuals of the hit positions are used instead, via a calibration method based on Montecarlo studies. Detectors of systematically varying intrinsic resolutions are simulated and the corresponding

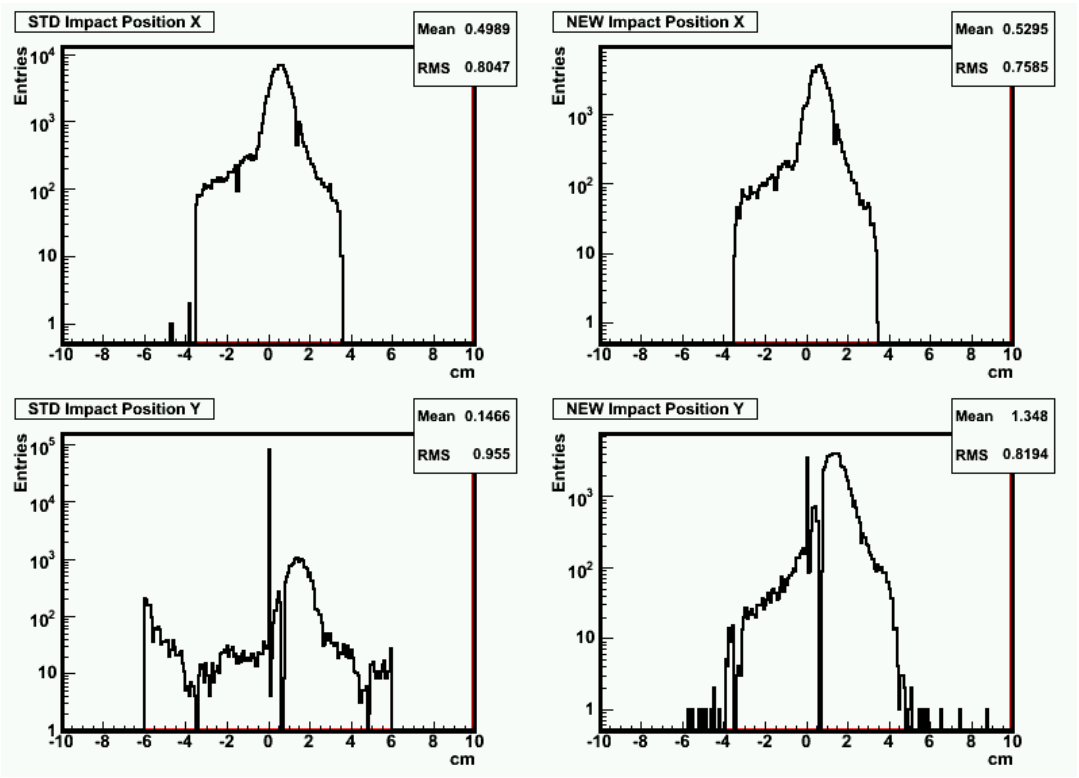

Figure 7.7: Impact positions of hit reconstructed on the first layer of T2 telescope before mirroring correction (left) and after correction (right). Both X and Y coordinates are given.

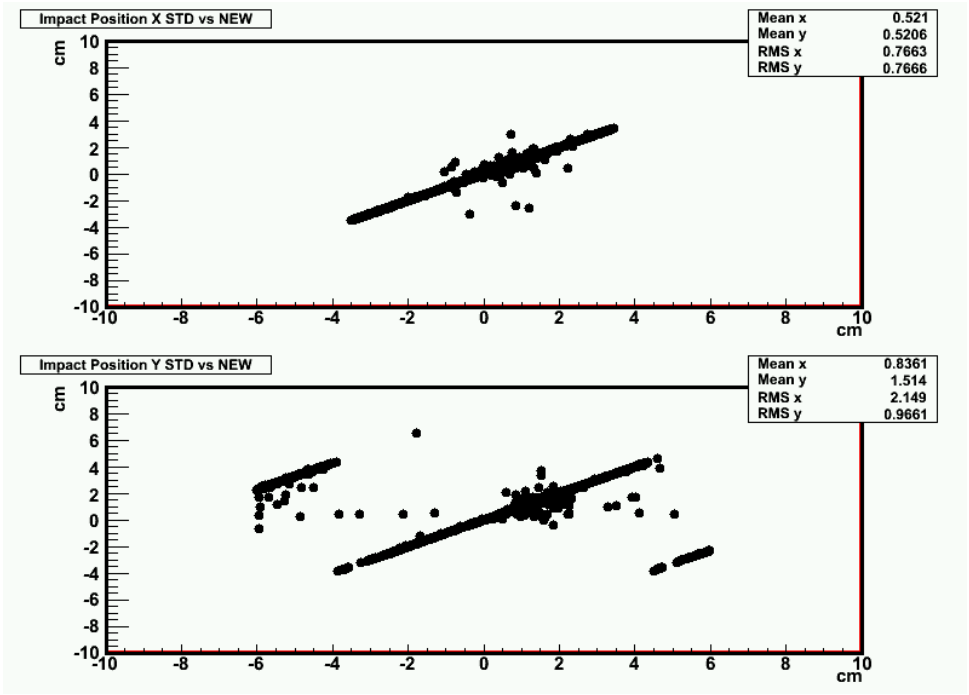

Figure 7.8: Scatter plot of coordinates (X and Y) before vs after mirroring correction.

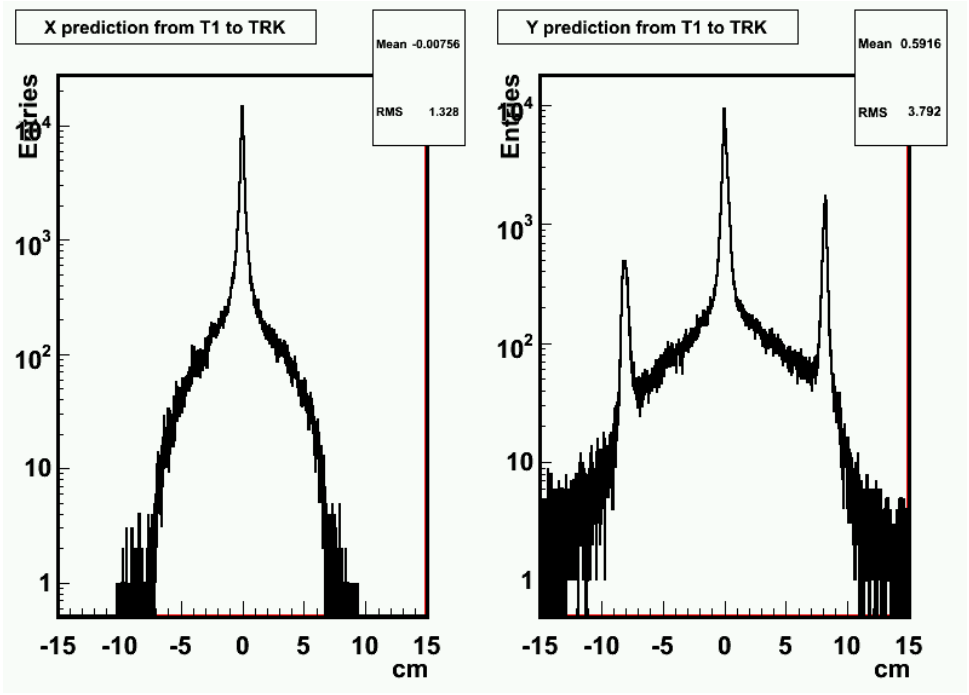

Figure 7.9: The distribution of the difference between the Montecarlo prediction of the hit position coordinate extrapolated from the T1 telescope to the first layer of the T2 telescope.

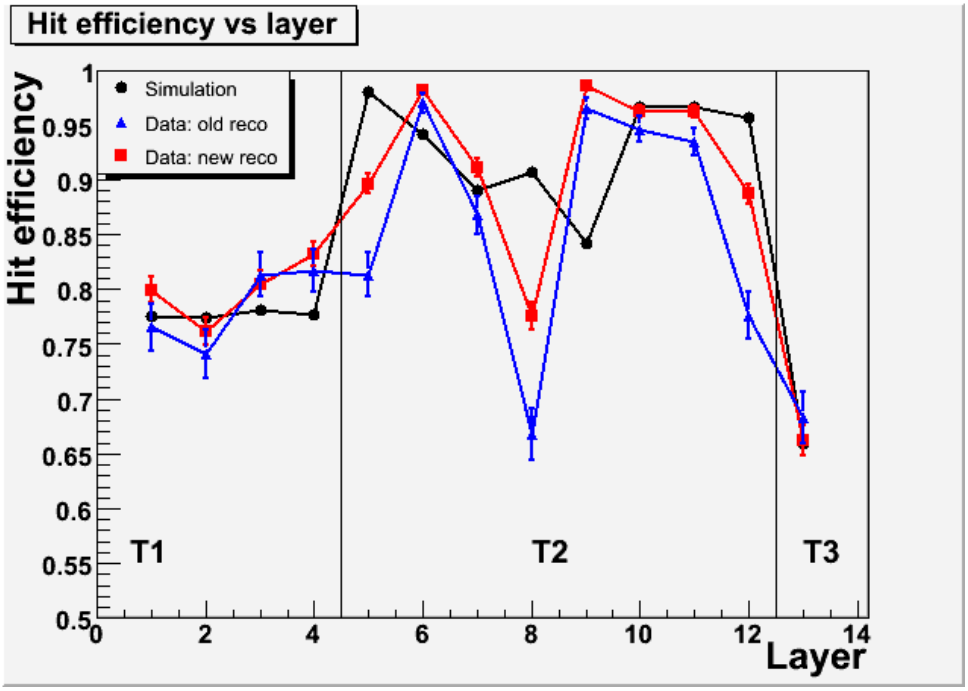

Figure 7.10: Efficiency of hit reconstruction vs layer. Layers from T1, T2 and T3 are shown.

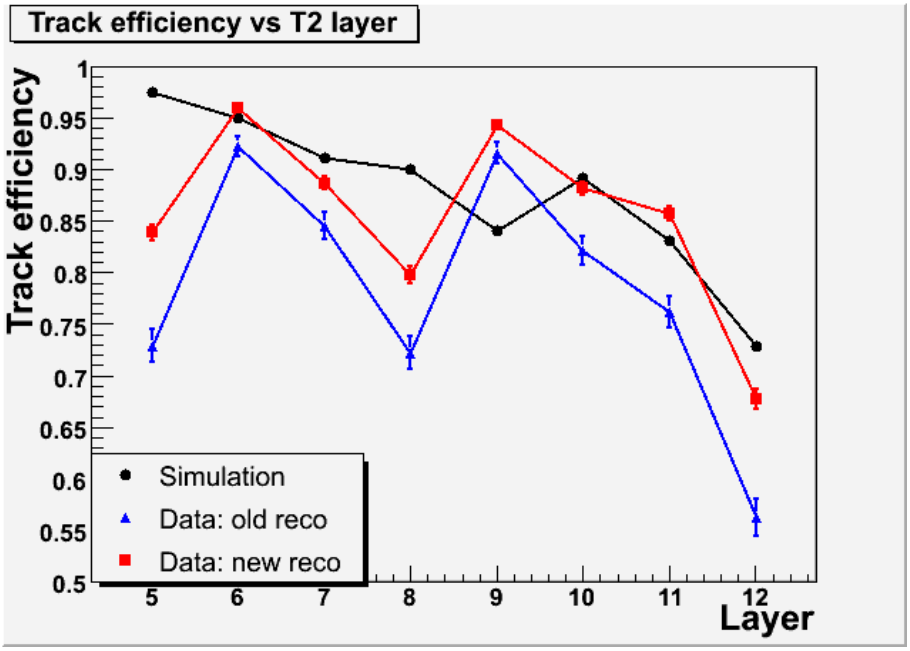

Figure 7.11: Efficiency of track reconstruction vs layer. Layers from T2 are shown.

LAYER	Hit efficiency (%) standard reco	Hit efficiency (%) new reco
0	76.53	79.93
1	74.05	76.19
2	81.34	80.49
3	81.68	83.21
4	81.34	89.60
5	97.00	98.21
6	86.80	91.09
7	66.78	77.52
8	96.52	98.64
9	94.63	96.25
10	93.49	96.25
11	77.60	88.71
12	68.31	66.23
	Track efficiency (%) standard reco	Track efficiency (%) new reco
0	72.91	83.85
1	92.22	95.90
2	84.52	88.66
3	72.22	79.74
4	91.56	94.32
5	82.14	88.16
6	76.20	85.75
7	56.31	67.73

Table 7.1: Comparison between efficiency for data reconstructed using the two clusterization methods. The first series of results is for the *hit* efficiency while the second one is for the *track* efficiency. The typical error on these values are of the order of 1 to 2 permille.

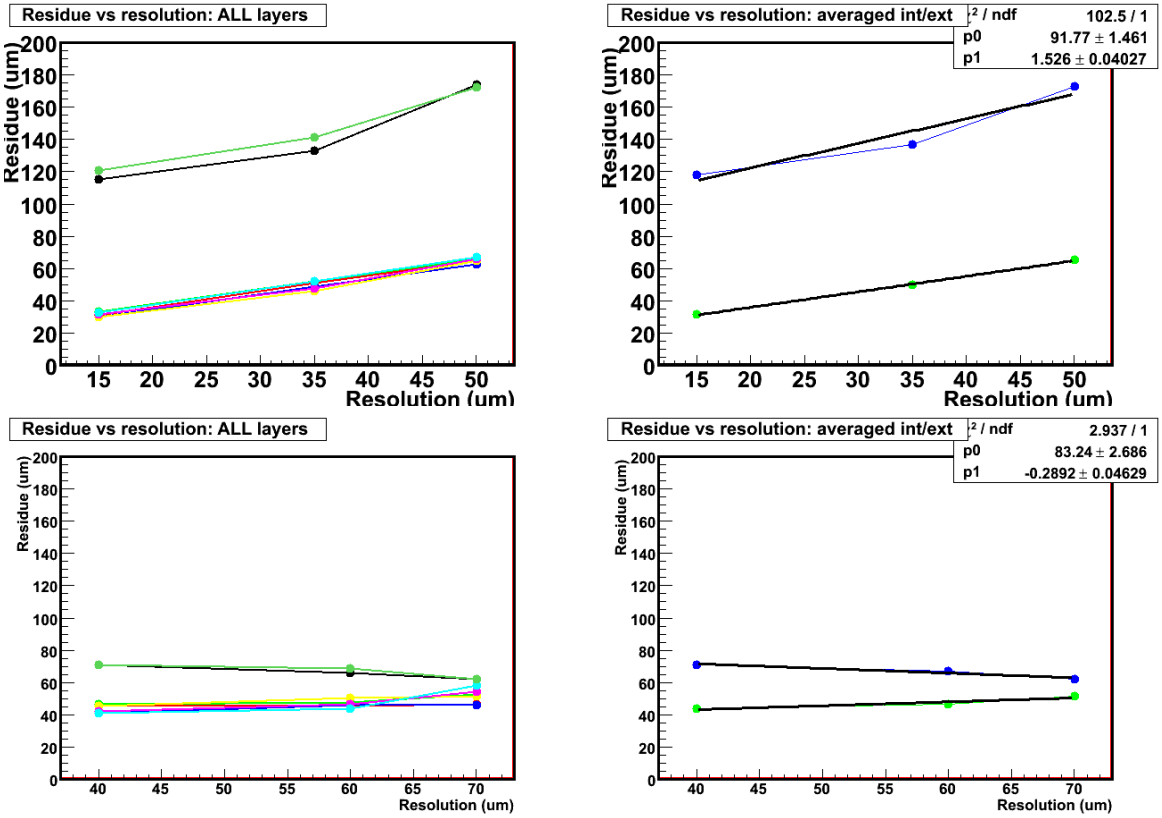

Figure 7.12: Residual vs true resolution in Montecarlo studies. Upper: S-side, lower: K-side. The left plots show the correlations for all layers while the right plots give the averages for internal and external layers.

residuals are studied. The observed real residuals in data are compared with these results.
For this study the following quality cuts have been applied to tracks:

- At least four hits per track in T2;
- A χ^2 per degree of freedom < 20 for the track fit.

The method consists in varying the S-side simulated intrinsic resolution from 15 to 50 μm and the K-side one from 40 to 70 μm, assuming them to be the same for all modules.

The widths of the residuals from a double Gaussian fit are linearly related to the resolutions as it can be observed in Fig. 7.12. The linear fit to these points has been done separately for S and K sides and for each modules. The parameters of this fit appear in Tab. 7.2. The residuals of the external layers are affected by edge effects where the tracks are unconstrained on one end.

This study was carried out for T1 telescope in another work [248]. Here, for completeness, ladders belonging to the T2 telescope are taken into account. A slight worsening, confirmed by this analysis, is expected due to the Coulomb scattering

	Constant term	Slope
S-side (internal)	$16.8 \pm 1.5 \mu$m	0.96 ± 0.04
K-side (internal)	$33.5 \pm 2.7 \mu$m	0.24 ± 0.05

Table 7.2: Parameters relating the residual and the true resolution in Montecarlo simulation (internal layers).

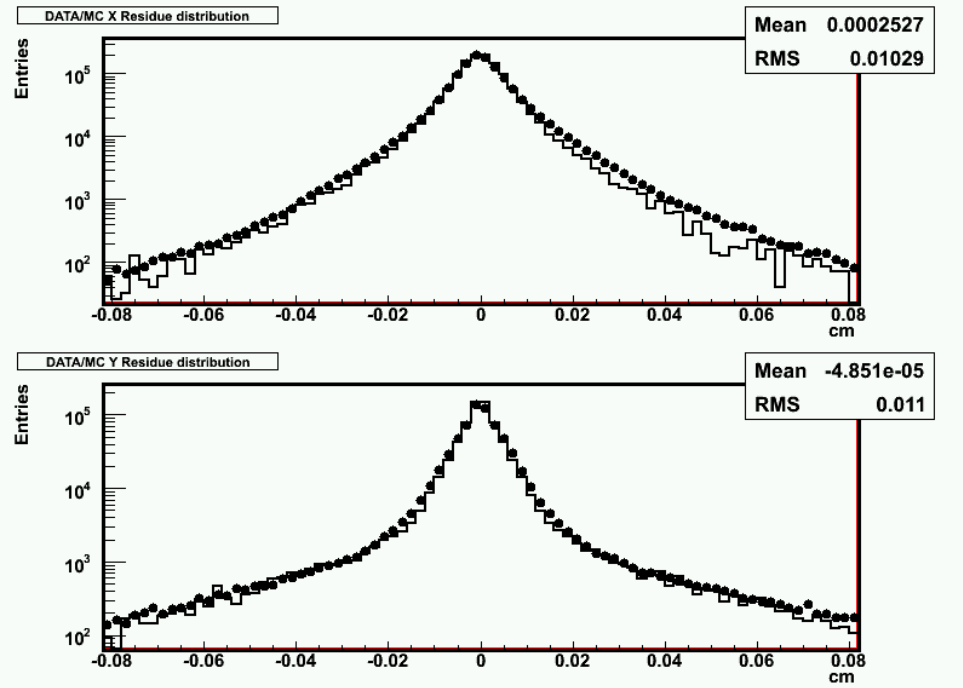

Figure 7.13: Comparison of residuals for S-side (left) and K-side (right). Both Montecarlo (lines) and data (dots) distributions are shown.

dispersion. Fig. 7.13 shows the agreement between the distribution of S- and K-side residuals for Montecarlo and data. The resolution obtained from Montecarlo studies for selected T2 ladders is shown in Fig.7.14 while the residuals obtained from data using the new reconstruction algorithm are presented in Fig. 7.15. In both cases the distributions are fitted with a double Gaussian function hypothesis where the parameters p_2 and p_5 represent the standard deviations.
The obtained spatial resolution for the tested ladders of the tracker is compatible with the predicted one by the AMS-02 simulation: 10 μm for the S-side of the silicon detector and 30 μm for K-side. However an important contribution (up to $\sim 30\%$ for S-side) of a second Gaussian exists in the distributions of residuals.

7.5.7 Momentum resolution

In order to estimate the momentum resolution of the apparatus with an electron beam, the BonWoff data-taking configuration. The cuts applied on the selected

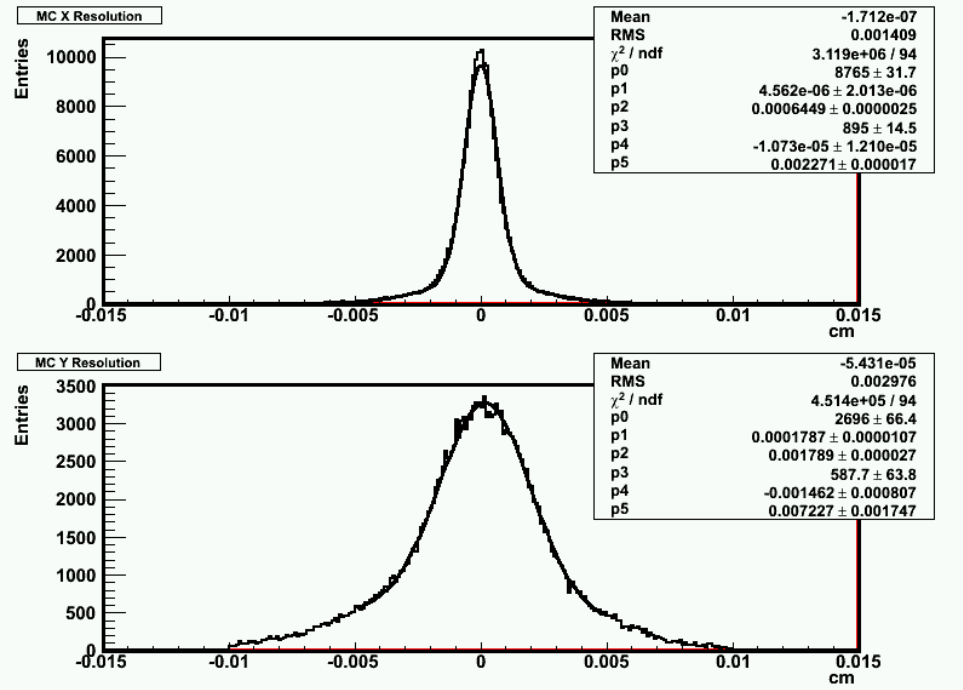

Figure 7.14: The expected resolutions as obtained from Montecarlo studies on T2 ladders.

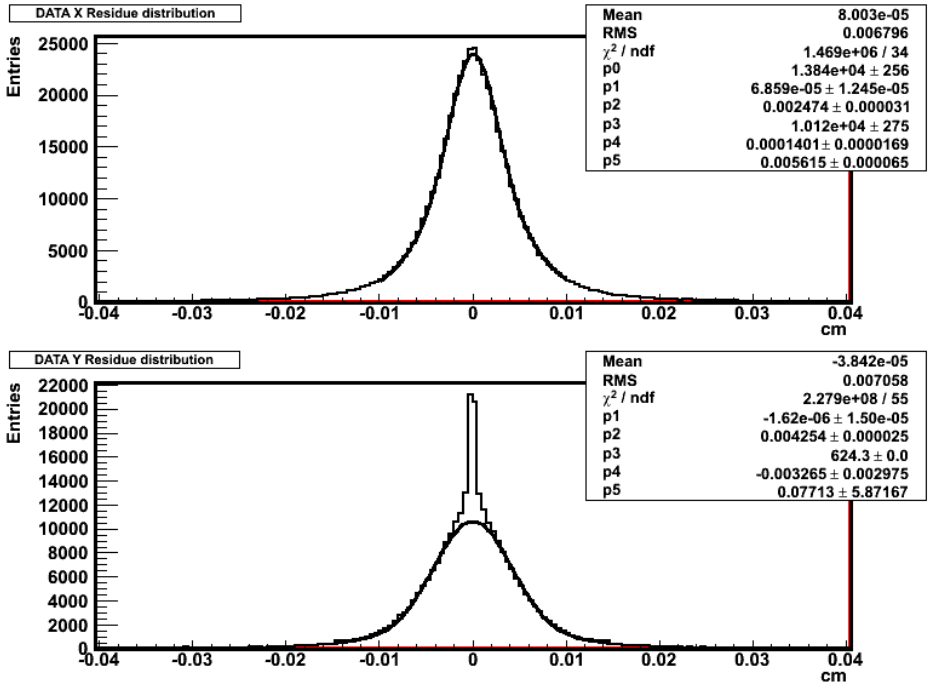

Figure 7.15: Residuals as obtained from data using the new recontruction algorithm. The non-gaussian peak near 0 for the Y coordinate is due to the K-side virtual clusters.

sample are:

- only one track per event;
- more than 6 hits used in the track reconstruction fit;
- a geometrical cut to select electrons inside a restricted zone of the beam (main zone): polar angle < 5 mrad, track starting point inside a 3 cm radius with respect to the measured beam axis;
- a χ^2 per degree of freedom < 20, in order to avoid events suffering from inelastic scattering inside the T2 telescope;
- hit residuals on downstream layer less than 0.25 mm;
- an energy deposit inside the ECAL > 4 GeV;

The generic relation for the momentum resolution of a tracker is:

$$\frac{\Delta p}{p} = A \cdot p \oplus B \tag{7.13}$$

where the $\oplus$ symbol represents the sum in quadrature. This relation is valid only if the energy loss of the particle is small.
The first contribution $A \cdot p$ is the intrinsic resolution of a detector with a fixed spatial resolution which measures the momentum of a particle through the curvature of its trajectory. The second contribution B comes from the effect of Coulomb dispersion on the beam momentum.

The analysis was performed both on simulated and data events; for this second sample, events corresponding to 5 GeV/c beam momentum are missing due to problems in the calibration procedure. In Fig. 7.16 the momentum resolution for all available energies are shown both for Montecarlo and data. The resolution dependence on the beam momentum is shown in Fig. 7.17 giving as A and B parameters:

$$\begin{array}{cc} \text{MC} & A = (2.82 \pm 0.69) \times 10^{-3}; B = (3.09 \pm 0.18) \times 10^{-2}; \\ \text{Data} & A = (2.00 \pm 0.54) \times 10^{-3}; B = (3.45 \pm 0.08) \times 10^{-2}. \end{array}$$

As expected from the multiple scattering, the agreement between data and Montecarlo simulations improves with the energy of the electron.
The momentum resolution on the track *span*, the *span* being defined as the distance between the first and the last hit, is shown in Fig. 7.18 for different span intervals. Its dependence is shown in Fig. 7.19.
A similar study was performed to infer the effect of the number of hits used in the tracking on the momentum resolution. The resolutions obtained for different ranges of required hits are shown in Fig. 7.20. The dependence of the resolution on the hits is shown in Fig. 7.21.
In both cases, as expected, the resolutions are improving with the increasing lever

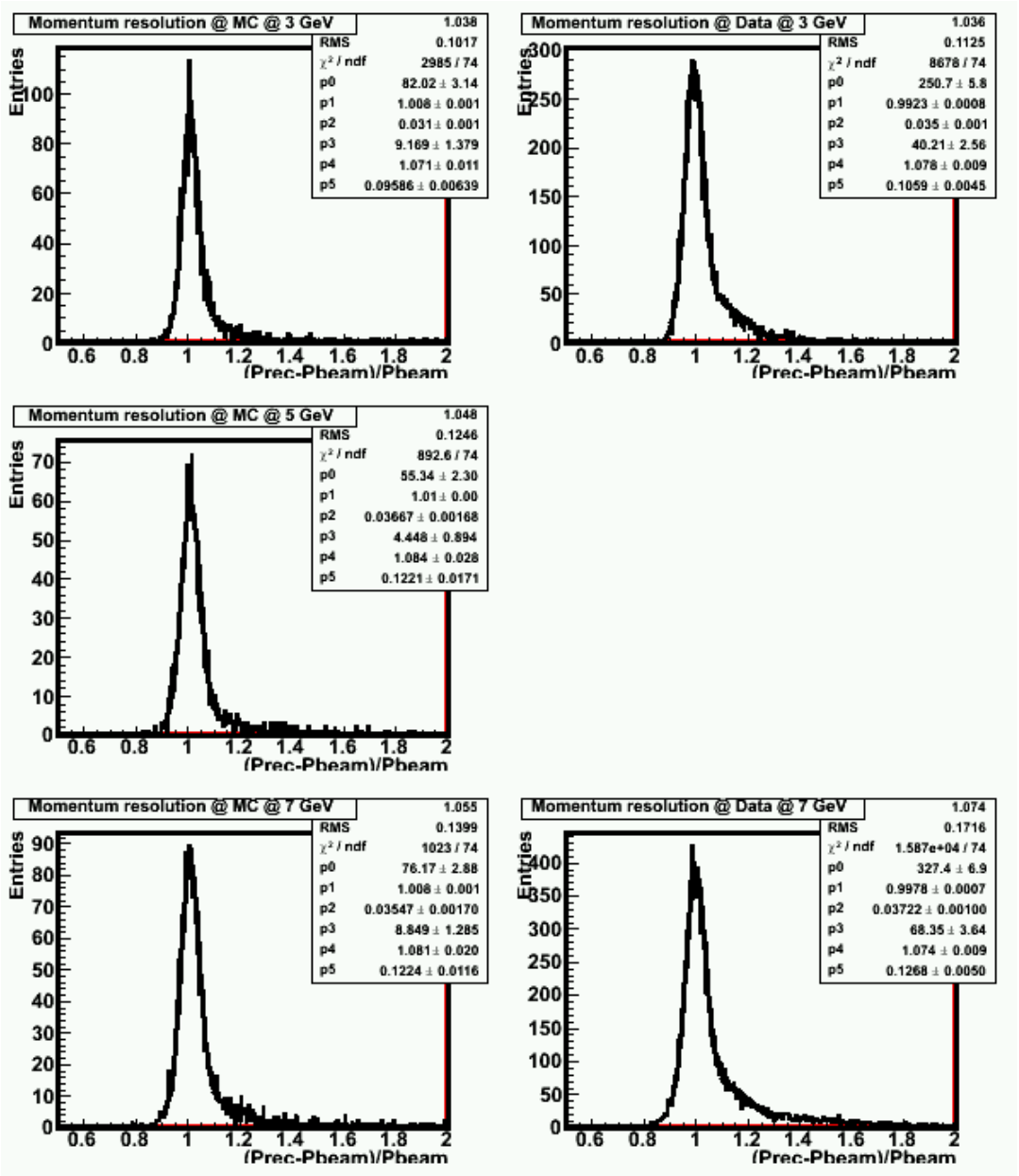

Figure 7.16: Comparison of Montecarlo and data resolutions for the three momenta considered here.

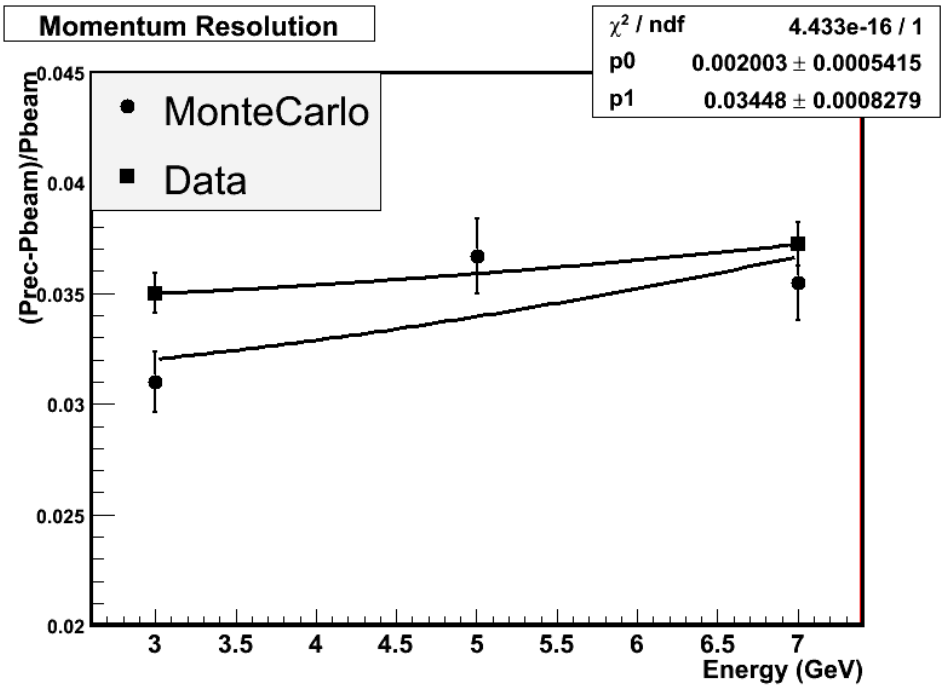

Figure 7.17: Momentum resolution as a function of beam momentum.

arm of the track (either "span" or total number of hits).
The χ^2 probability distribution of the track fit is shown in Fig. 7.22 where the presence of the "virtual" K-side hits explains the increase at high probabilities.

As a cross-check, the momentum error as obtained from the fit to the track distribution is shown in Fig. 7.23. The mean values obtained at different energies, ranging from 2 to 3%, are compatible with the results from the above resolution studies. The double peak structure is due to the different intrinsic precision with respect to the number of hits used to reconstruct the track.

The uncertainty on the beam momentum is of the order of 0.5% and gives a negligible contribution to the constant term when summed in quadrature.
The $\delta p/p$ resolution determined in the test beam, $\sim$ 3.5%, is in good agreement with the simulation prediction in this energy range.
The statistical error dominates this measurement because of the limited number of runs with the useful configuration (BonWoff) and the fact that coincidences between the tracker system and the ECAL were not 100% efficient for this set of data.
The extrapolation of this result to the flight configuration gives a momentum resolution around $\sim$ 1.7 %, in rather good agreement with the AMS-02 simulation prediction. The difference comes mainly from the fact that during the test beam the magnetic field intensity was lower than the one which will be used inside the final detector. In fact the resolution is inversely proportional to the magnetic field:

$$\Delta(1/p) = \frac{\Delta p}{p^2} = \frac{\Delta C}{0.3 \cdot qB} \sim 1/B \tag{7.14}$$

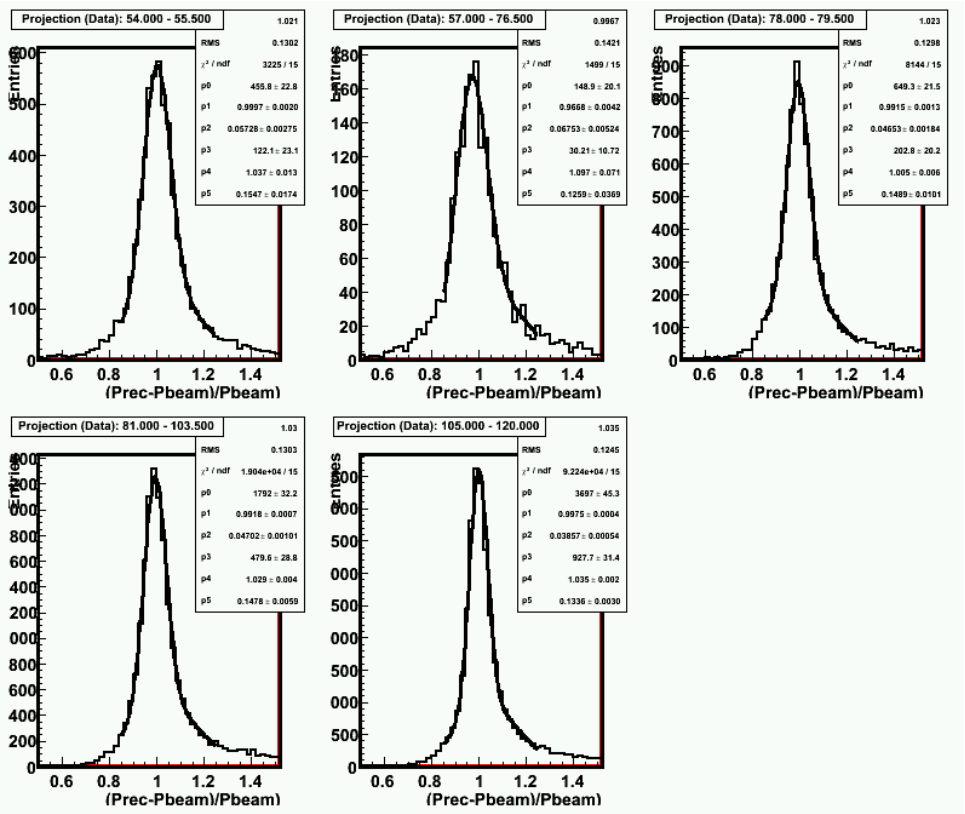

Figure 7.18: Momentum resolution distributions as a function of the "span" of the track. The "span" variable is described in the text.

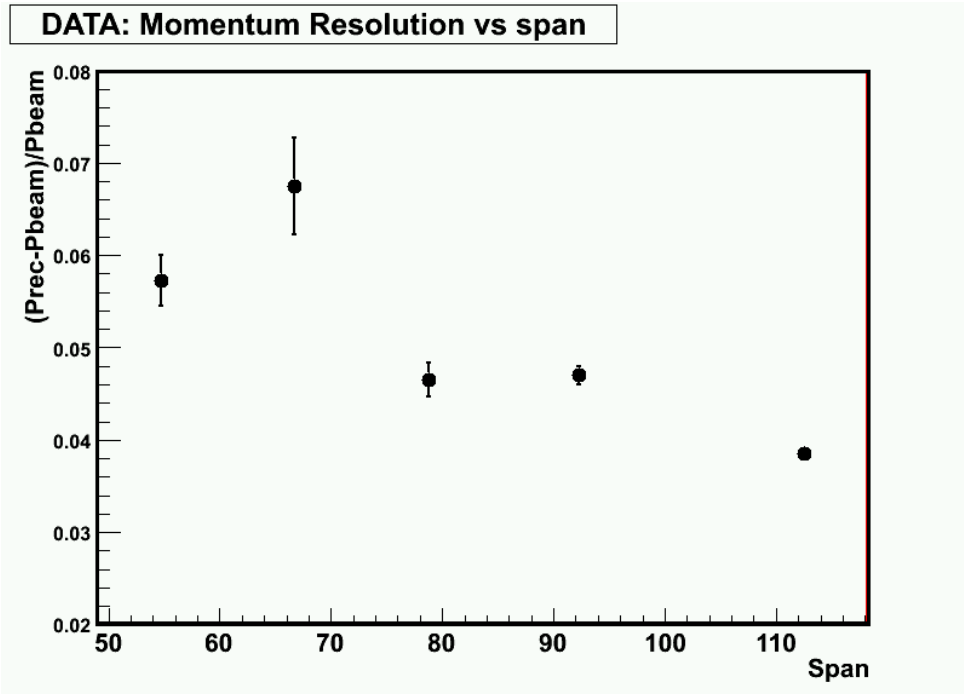

Figure 7.19: Dependence of the momentum resolution as a function of the "span" of the track (in cm).

where C is the track trajectory curvature, q is the particle charge and B the magnetic field.
The beam test results confirm the simulation findings at high energies.

7.5.8 Photon Analysis

One of the most relevant goals of the 2004 test beam has been the study of the photon detection and measurement capabilities of the AMS tracker via conversion processes. A tungsten converter, 1mm thick, has been placed between T1 and T2 telescopes outside the magnet region. An electron traversing the converter thickness ($\sim 0.3X_0$) has a probability of $\sim 85\%$ to emit a photon of more than 500 MeV. This photon has a certain probability P to convert depending on the remaining path:

$$P(x) = 1 - \exp(-\frac{7}{9}x/X_0) \tag{7.15}$$

where X_0 is the radiation length of tungsten and x the remaining path (thickness) to be traversed by the photon. For a converter of the actual thickness this probability is $\sim 20\%$. In Fig. 7.24, the radiation probability is plotted as a function of the energy of the most energetic photon in the event. If the photon produced by bremsstrahlung converts in an electron-positron pair, it will give a 3-track configuration inside the T2 telescope, where also the electron from the beam, with low transverse momentum, will be visible (*golden events*). It should be noted that a

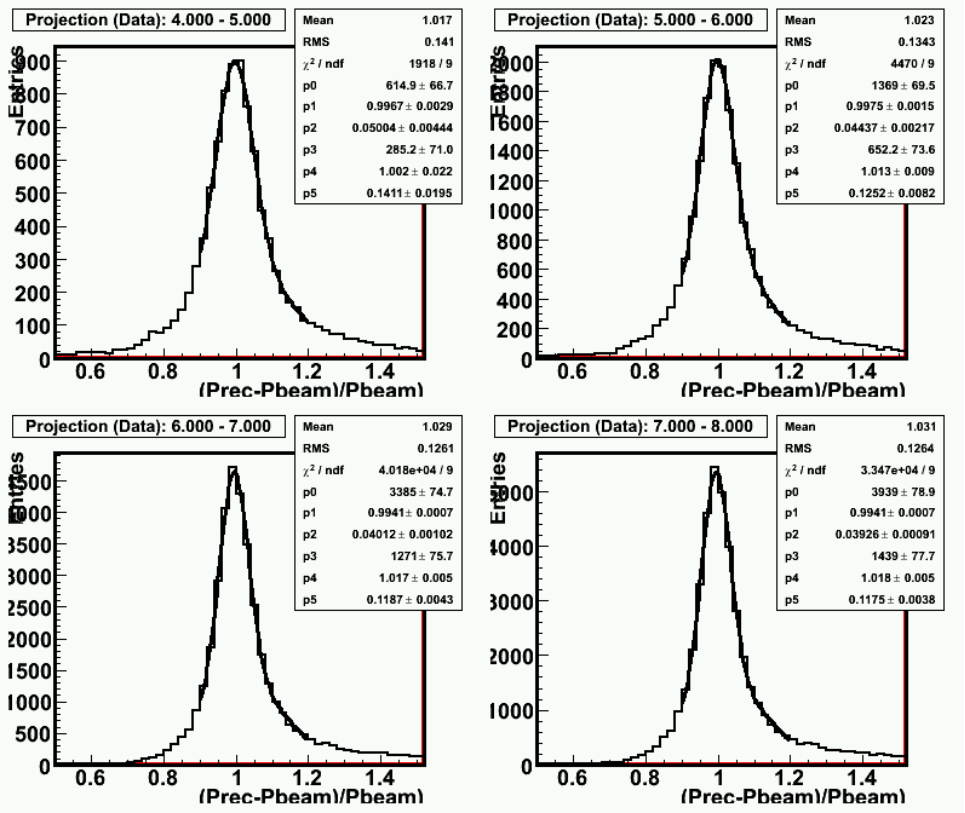

Figure 7.20: Momentum resolution distributions as a function of the number of hits in the track.

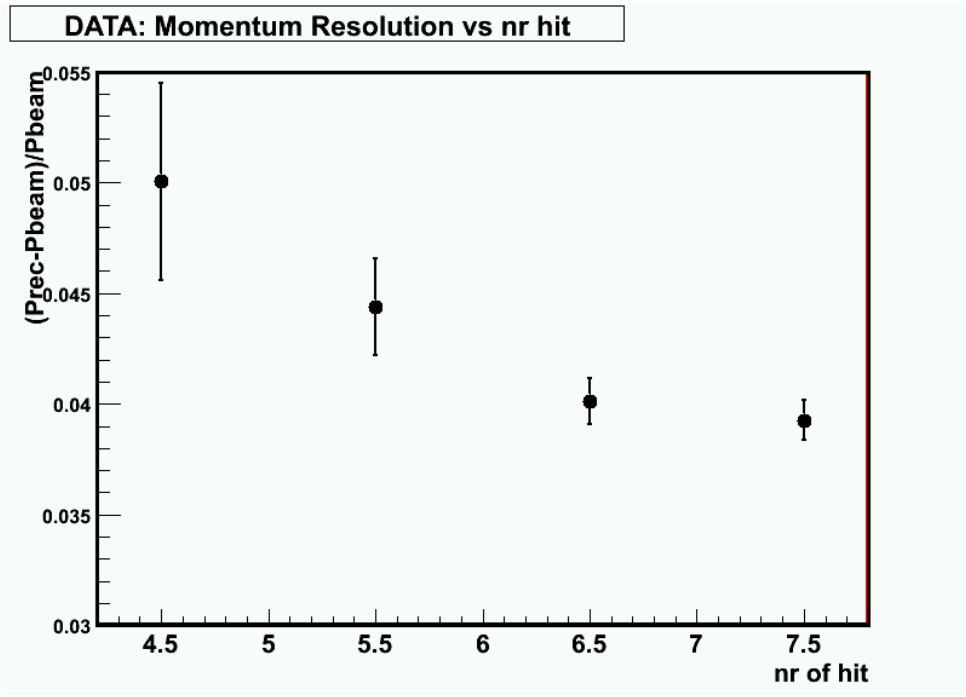

Figure 7.21: Dependence of the momentum resolution as a function of the number of hits of the track.

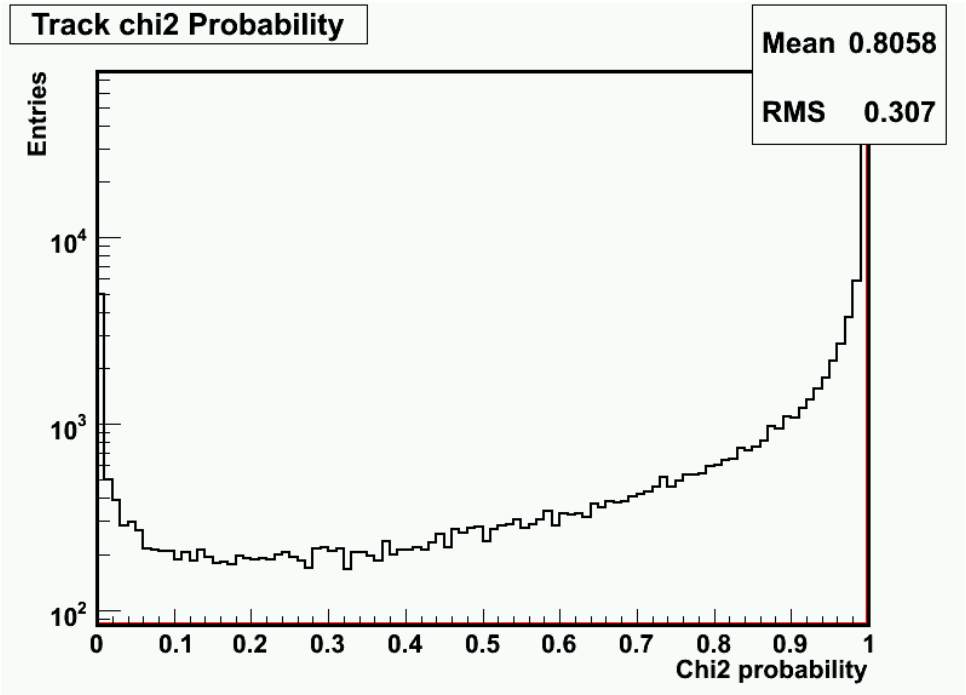

Figure 7.22: Distribution of χ^2 probability from the track fitting procedure.

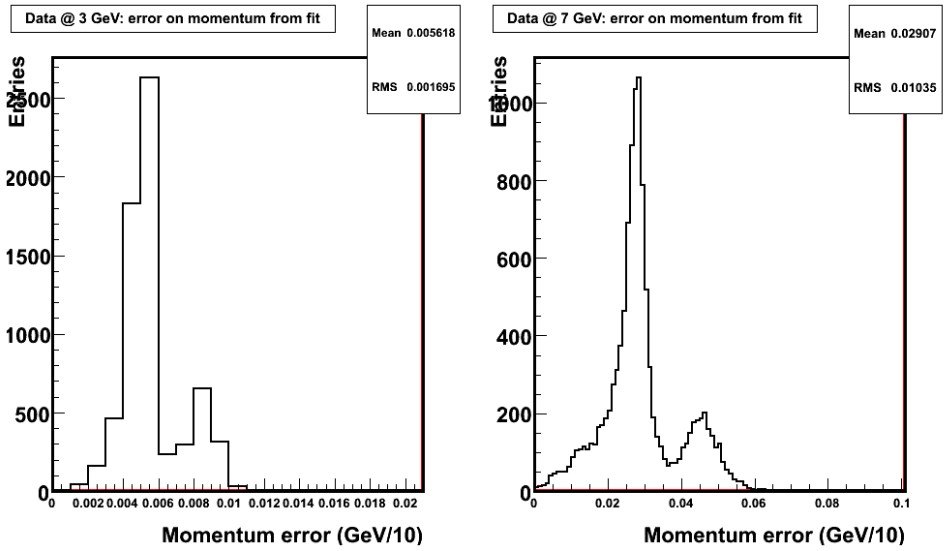

Figure 7.23: Momentum resolution error from the track fitting procedure.

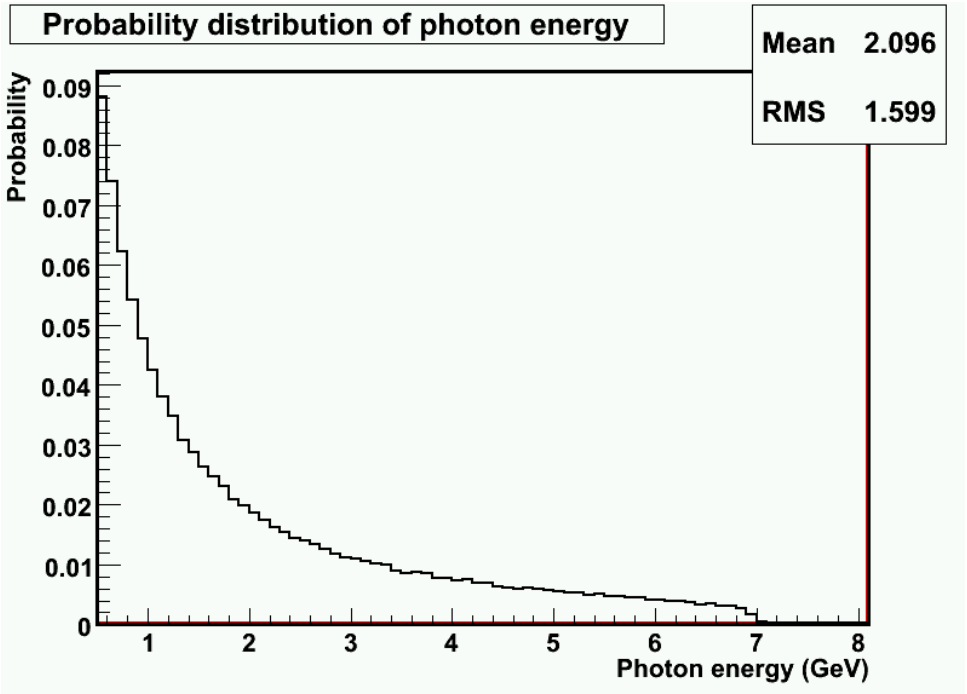

Figure 7.24: Photon emission probability in the test beam converter, from Monte-carlo simulation, as a function of the most energetic photon in the event.

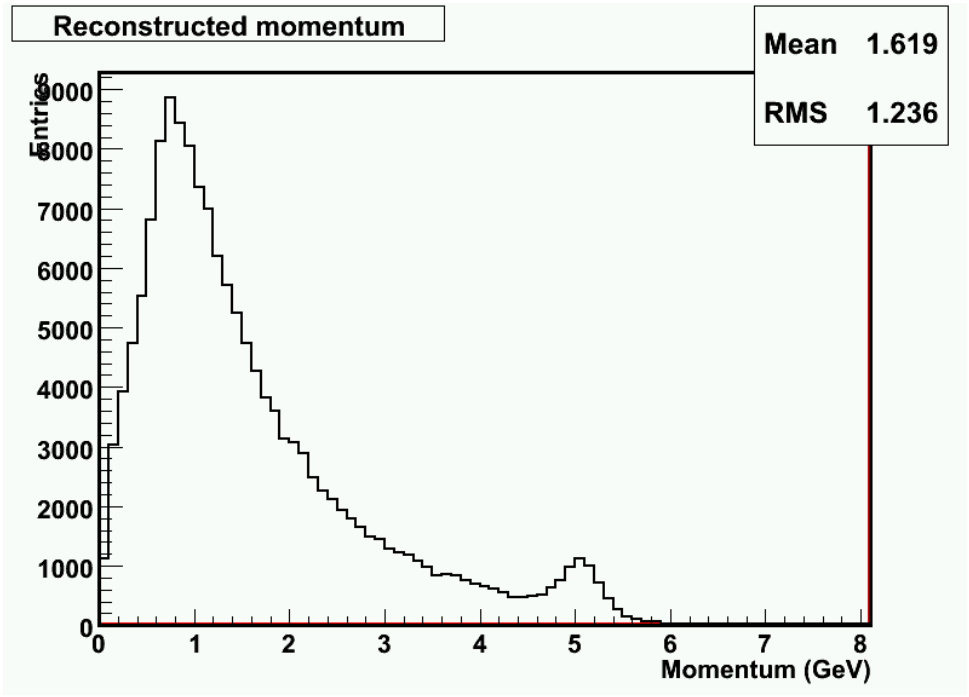

Figure 7.25: Distribution of reconstructed momenta for all reconstructed track in the data (5 GeV beam momentum). The threshold at $\sim$ 700 MeV is due to the geometrical acceptance.

geometrical threshold is present and that particles with less than 700 MeV cannot be detected by the apparatus due to their bending in the magnetic field (Fig. 7.25). This reduces the efficiency of detecting all tracks. To improve the statistics, a sample of 2-tracks topologies was also considered assuming that they are genuine photon events for which one track has not been detected (*silver event*).

In Table 7.3 the percentage of photon events, in a Montecarlo simulation of 4×10^4events, with two or three reconstructed tracks is reported with the additional requirement that the track should have a momentum of more than 700 MeV. This condition is equivalent to the requirement of having at least 5 hits in the track, as can be seen in Fig. 7.26.

Vertex Reconstruction

In this study an alternative vertexing algorithm with respect to the standard one used in the AMS-02 reconstruction [248] has been adopted. A detailed description of this new algorithm and a comparison with the standard one, is presented in the following.

After having selected i-tracks events with $i = 2, 3$ (*silver and golden events*, respectively), the vertex is computed minimizing the distances d_i between the tracks

Event features	2-tracks	3-tracks
Total reconstructed (%)	5.3	0.7
With a converted γ(%)	53.3	72.4
Charge 0 (2-tracks), -1 (3-tracks) (%)	50.0	95.0
Electron from γ matched with MC (%)	58.0	49.7
Electron from beam matched with MC (%)	42.0	50.2

Table 7.3: Probability for an event to produce 2 or 3 reconstructed tracks from converted photons (total). The cascade probability of a good matching with Montecarlo information is also reported.

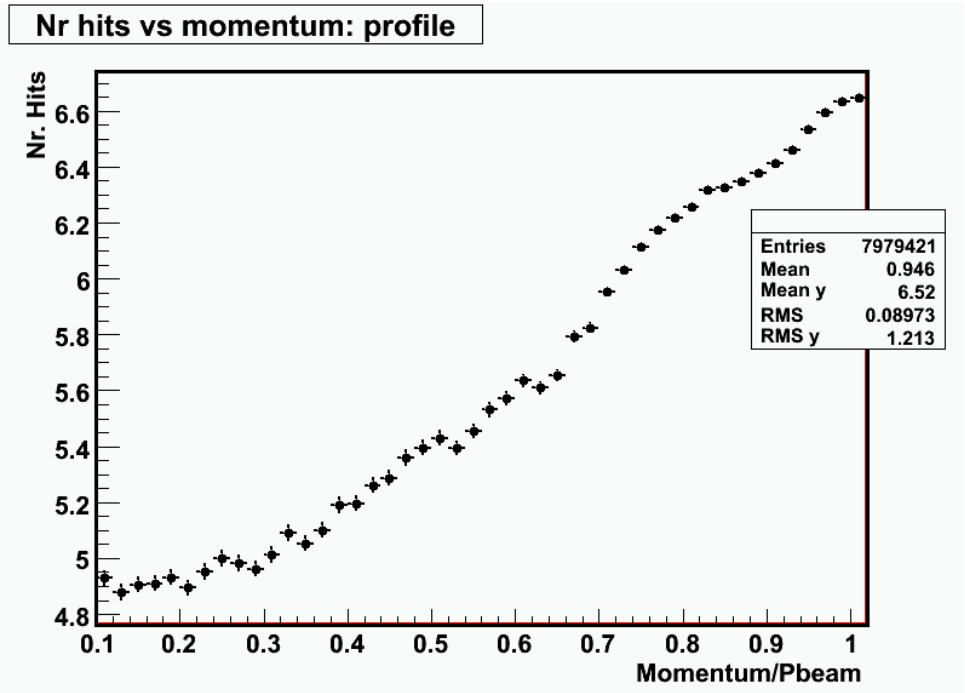

Figure 7.26: Profile distribution of the number of hits in the reconstructed tracks vs momentum of the tracks.

and a generic point P(x,y,z) (Fig. 7.27).

The distances d_i are calculated in the following way:

$$\vec{d_i} = \vec{P_V P_i} \ \wedge \ \hat{u_i} \tag{7.16}$$

where P_i is a generic point belonging to the track i and u_i is its unit direction vector, with $i = 1, 2, 3$. A characteristic function of this distance is then minimized with the aim of finding the point of closest approach.
Three different functions were tested:

$$f_1 = \Sigma_i |d_i| \tag{7.17}$$

$$f_2 = \Sigma_i (d_i)^2 \tag{7.18}$$

$$f_3 = \Sigma_i (d_i/\sigma_i)^2 \tag{7.19}$$

where σ_i are the calculated errors of each distance d_i.
The best performance has been obtained using the function f_3, which corresponds to the $\chi 2$ for the vertex point, and in the following all the results are referred to this specific choice.

In order to validate the algorithm, generated and reconstructed verteces variables using simulated events were compared.

This test was done only for 3-tracks simulated verteces (*golden events*) and the efficiency, defined as:

$$\varepsilon_{3vtx} = \frac{\text{Number of Montecarlo reconstructed verteces}}{\text{Number of Montecarlo generated verteces}} \tag{7.20}$$

was found to be 61.6% considering only generated verteces giving rise to tracks with more than 700 MeV momentum.
The usage of the new cluster reconstruction and of the mirroring correction in the track definition allow to increase this efficiency by 50%. Compared to the standard vertex reconstruction, the new vertexing algorithm keeps the same high efficiency, slightly improving the photon energy resolution as shown in Fig. 7.28.

In order to carefully study the performance of the vertex reconstruction algorithm and to compare them with Montecarlo simulation, a good particle association must be designed.

Particle Association

Several tests have been performed in order to check in detail the *particle association* concerning 3-tracks verteces. The positron e^+ association is straightforward from a test on the charge of the particle. Concerning the two electrons e^-_γ and e^-_{beam}, they can be discriminated using:

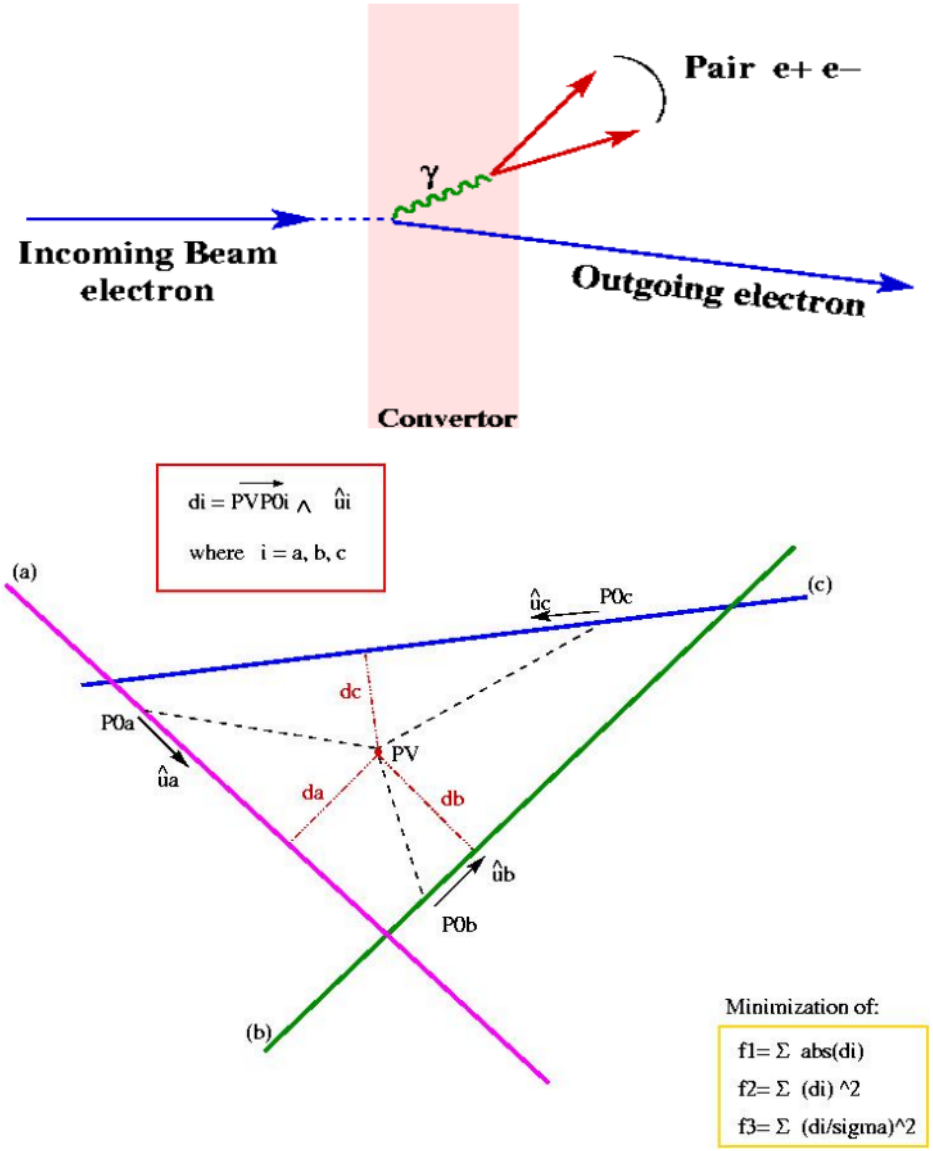

Figure 7.27: Schematic of the vertex definition (top) and the used vertex algorithm projected in a plane for simplicity (bottom).

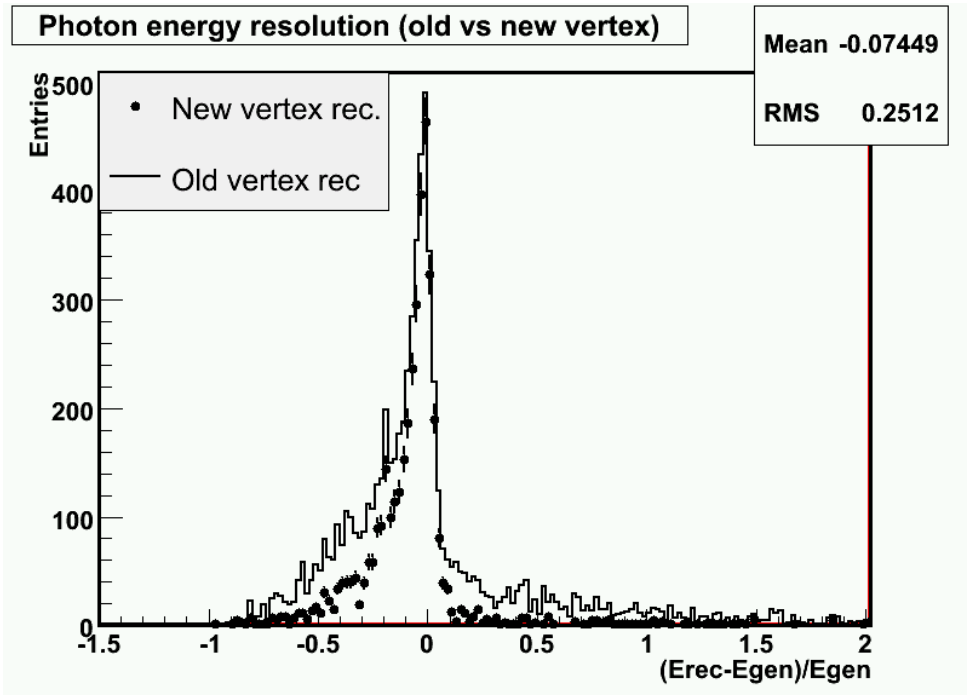

Figure 7.28: Comparison of photon energy resolutions using the standard (line) and the new (dots) vertex reconstruction.

1) at generation level (exact association), the minimum angular difference $\Delta\alpha$ between the generated and the reconstructed particle direction:

$$\min(\Delta\alpha) = \min\left(\arccos(\frac{\vec{p}_{gen}\cdot\vec{p}_{rec}}{p_{gen}p_{rec}})\right) \tag{7.21}$$

and the minimum energy difference;

2a) at reconstruction level, using the minimum invariant mass between the two possible positron-electron pairs:

$$\min(\mathrm{M}(\mathrm{e}^+,\mathrm{e}_1^-),\mathrm{M}(\mathrm{e}^+,\mathrm{e}_2^-)) \tag{7.22}$$

with e_1^- and e_2^- being the two electron candidates. The electron candidate with the minimum associated mass is retained as the e_γ^- candidate.

2b) or, the most(least) energy association criterium:

$$min(E(e_1^-,e_2^-)) \tag{7.23}$$

where the lowest energy electron is retained as the e_γ^- candidate.

The points 2a) and 2b) are used to discriminate between electrons coming from beam or from the γ conversion, to be compared with the generator level information obtained in point 1). Fig. 7.29 shows the energy of the reconstructed electron and the invariant mass of the candidate photon in the case of correct and wrong association. The criterium 2b), based on the least energy, shows a better discriminating power and will be used in the following.

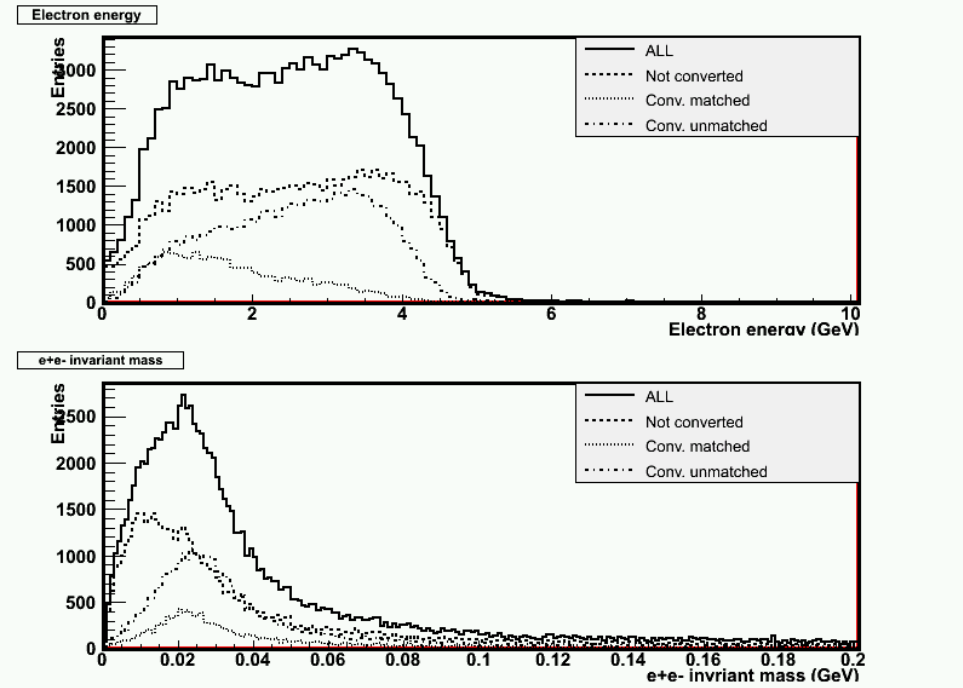

Figure 7.29: Energy of the reconstructed electron and the invariant mass of the candidate photon in the case of correct and wrong association.

7.5.9 Photon Energy and Angular Resolution

For what concerns the photon, two reconstruction definitions are possible when considering 3-tracks events:

A) **Direct:**
from the positron-electron pair as shown in Fig. 7.30;

B) **Indirect:**
from the recoil of the incoming beam electron as shown in Fig. 7.31.

Several tests using Montecarlo simulated events have been performed using the *direct* photon reconstruction.

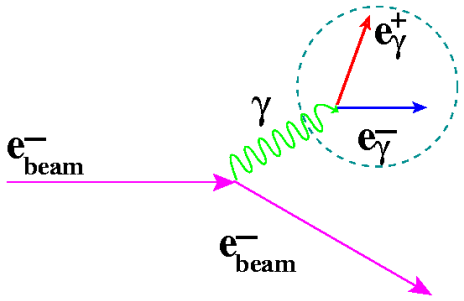

Figure 7.30: Schematics of direct photon reconstruction.

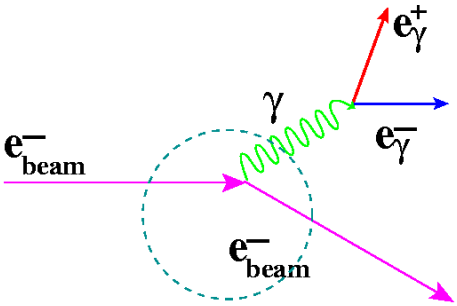

Figure 7.31: Schematics of indirect photon reconstruction.

Fig. 7.32 shows both generated and reconstructed photon energy distributions using both the good and the bad generated/reconstructed association for electrons. In Montecarlo simulation the *true* photon energy and angular resolutions, respectively σ_E^{true} and σ_α^{true}, are defined as:

$$\sigma_E^{true} = \frac{E_\gamma^{rec} - E_\gamma^{gen}}{E_\gamma^{gen}} \tag{7.24}$$

$$\sigma_\alpha^{true} = \frac{\vec{p}_{gen} \cdot \vec{p}_{rec}}{|p_{gen} p_{rec}|} \tag{7.25}$$

where $\vec{p}$ is the total momentum vector of the vertex. Fig. 7.33 shows the obtained distribution for σ_E^{true} and σ_α^{true}. The σ_{68} line represents the effective σ defined as the value where 68% of the events are contained integrating from $\cos(\Delta\theta) = 1$. A double gaussian one-sided fit is also superimposed. The obtained resolutions amount to: $\sigma_{68} = 0.8°$ and $\sigma_{gauss} = 0.60°$, respectively.
In order to estimate the agreement between the photon energy and angular resolution obtained from *data* and the ones obtained from Montecarlo simulation, new variables based on reconstructed quantities need to replace the ones used at generator level. The less precise indirect photon reconstruction will be used.

Fig. 7.34 shows the correlation between the photon energy estimated using both the indirect and the direct reconstruction in Montecarlo simulation. A strong correlation between the two is evident with a large bias towards higher values in the indirect reconstruction due the resolution on the recoiling of the electron beam.
The angular and energy "resolutions" from data, using the above definitions, are shown in Fig. 7.35. The superimposed fit, in the energy resolution distribution, takes into account only the positive tail of the distribution where the main effect is believed to come from resolution. The angular resolutions obtained from data are: $\sigma_{68} = 0.9°$ and $\sigma_{gauss} = 0.61°$, respectively.

Two Tracks Events

To improve the vertex statistics, several investigations have been performed in the sample of 2-track "vertex" topology (*silver event*) assuming that they are genuine photon events for which one track has not been detected.

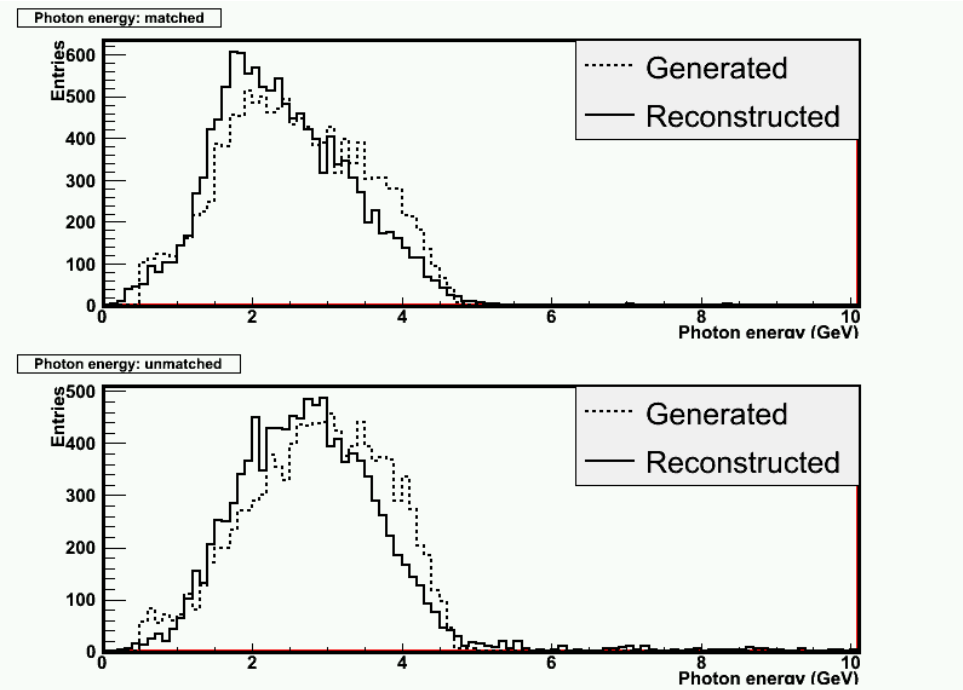

Figure 7.32: Direct photon reconstruction: generated and reconstructed energy distributions for good (top) and bad (bottom) association of the electron to the converted photon.

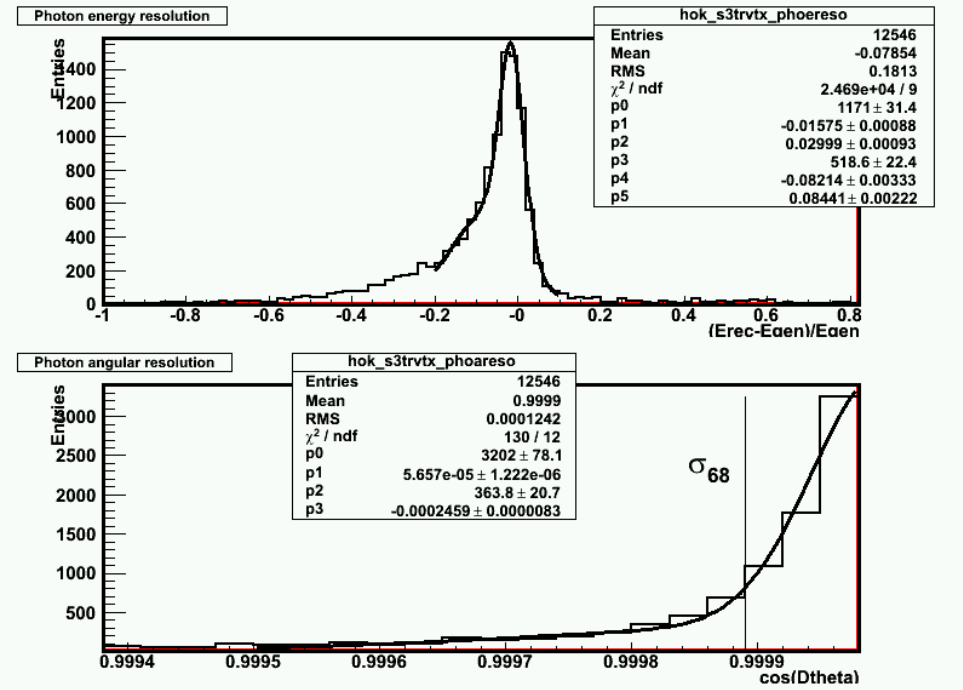

Figure 7.33: Photon energy and angular resolutions in Montecarlo for direct reconstruction.

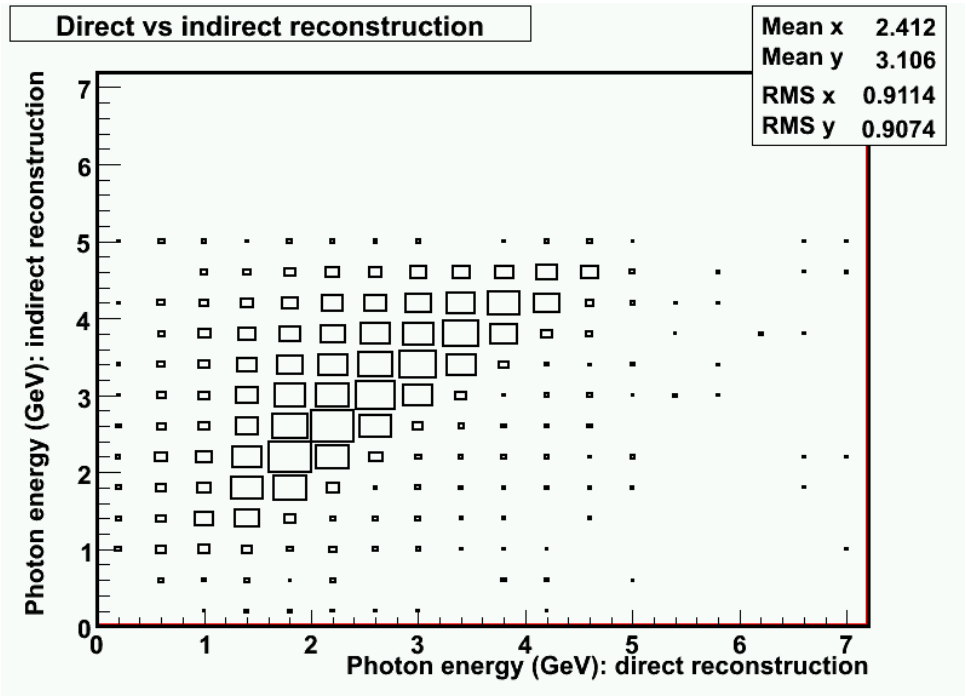

Figure 7.34: Photon energy using "direct" reconstruction vs "indirect" (recoil) reconstruction.

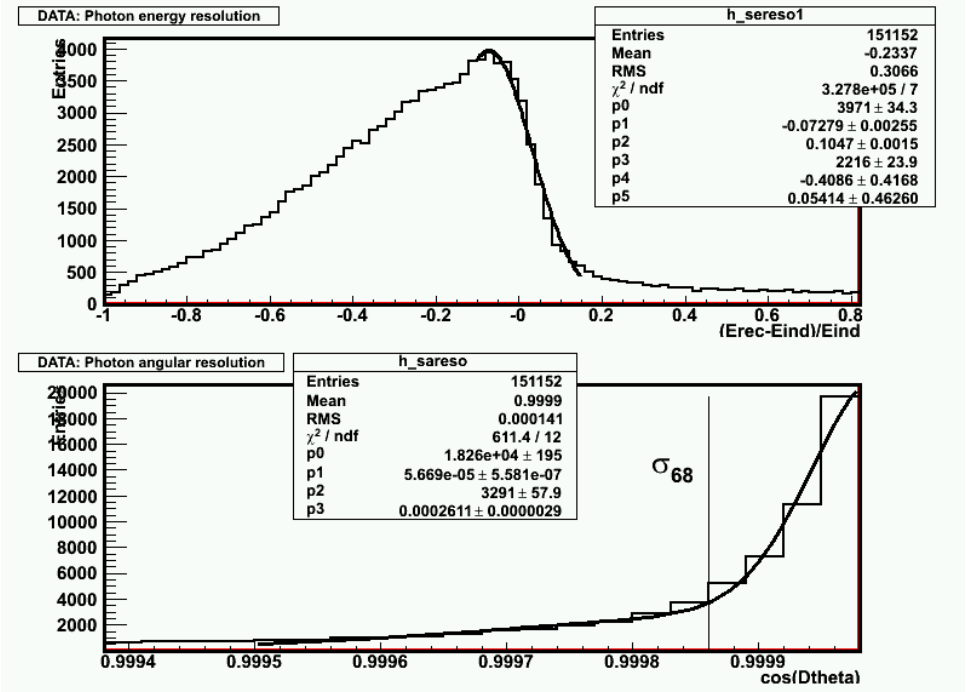

Figure 7.35: Photon energy and angular resolutions as obtained from data.

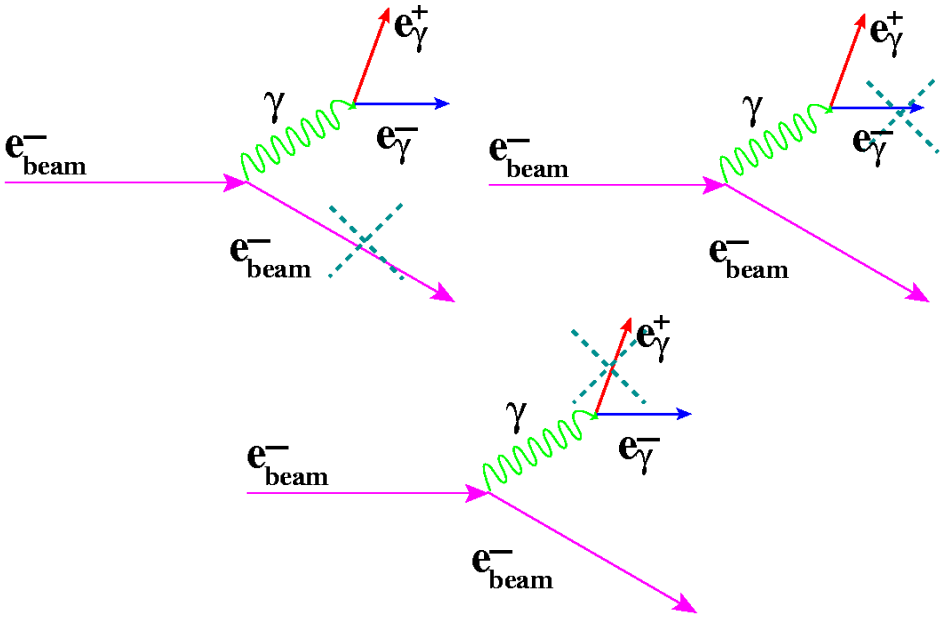

Figure 7.36: Schematics of the different topologies of two-tracks events. Upper (from left to right): topologies 1a) and 1b). Lower: topology 2).

Three specific topologies can be distinguished:

1a) the beam electron is not detected: the event contains only the positron-electron pair from the γ conversion. In this case the photon can be reconstructed using the *direct reconstruction*. The vertex charge, defined as the sum of the charges of tracks associated to it, is 0.

1b) the electron from the γ conversion pair is not detected: the event contains only a positron from the γ conversion and an electron from the incoming beam. In this case the photon can be reconstructed using the *indirect reconstruction*. Also in this case the vertex charge is 0.

2) the positron is lost: the event contains an electron from the γ conversion and another one from the incoming beam. In this case the photon can be reconstructed using the *indirect reconstruction* and assuming that the most energetic electron is the one coming from the beam. In this case the vertex charge is -2.

The three topologies are schematically sketched in Fig. 7.36.
It was verified that the case 1a) occurs only in a small percentage of cases with respect to the second one due to the low momentum electron and geometrical acceptance as can be seen in Fig. 7.37. For this reason only the 1b) and 2) topologies were taken into account in the following.
The generated/reconstructed energy criterium is used for the association.

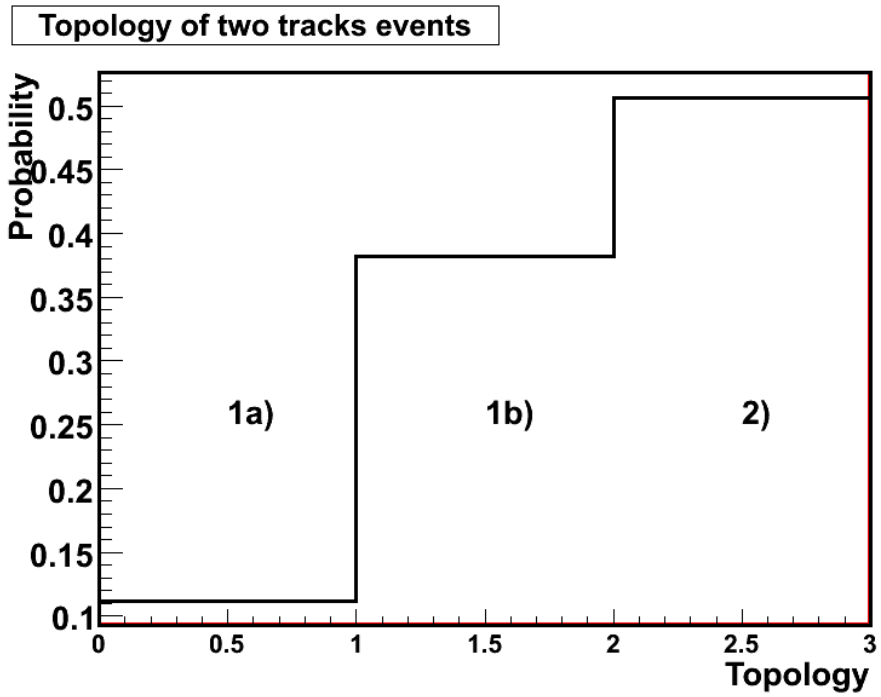

Figure 7.37: Occurences of the three topologies for two-tracks events.

Considering only cases 1b) and 2), the photon energy is estimated from the indirect reconstruction and the resulting photon energy and angular resolutions, defined as:

$$\sigma_E^{true} = \frac{E_\gamma^{ind\ rec} - E_\gamma^{gen}}{E_\gamma^{gen}} \tag{7.26}$$

$$\sigma_\alpha^{true} = \frac{\vec{p}_{gen} \cdot \vec{p}_{ind\ rec}}{|p_{gen} p_{ind\ rec}|} \tag{7.27}$$

are shown in Fig. 7.38. The large tails observed on the positive side is due to the unprecise photon energy measurement using the indirect reconstruction as discussed in the previous section and observed already in Fig. 7.34.

The distributions can be compared to the ones obtained with 3-tracks vertex events (Fig. 7.39). Due to the indirect reconstruction the agreement is largely worsened on the positive tail of the energy resolution distribution, as already pointed out. The negative tails, dominated by the real resolution, is anyhow comparable. No significant difference is observed on the angular resolution.

Summary

In summary, two topologies of vertex have been considered:

- verteces with 3-tracks and referred to as *golden events*;
- verteces with 2-tracks, where a track has been lost for acceptance reasons and referred to as *silver events*;

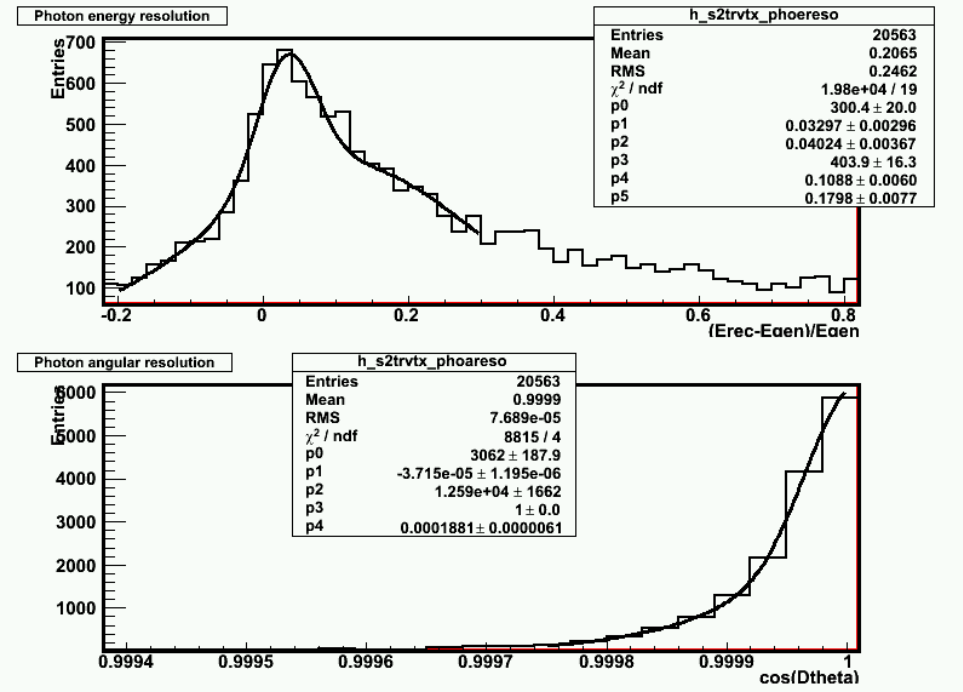

Figure 7.38: Photon energy and angular resolution in two-tracks events from Montecarlo simulation.

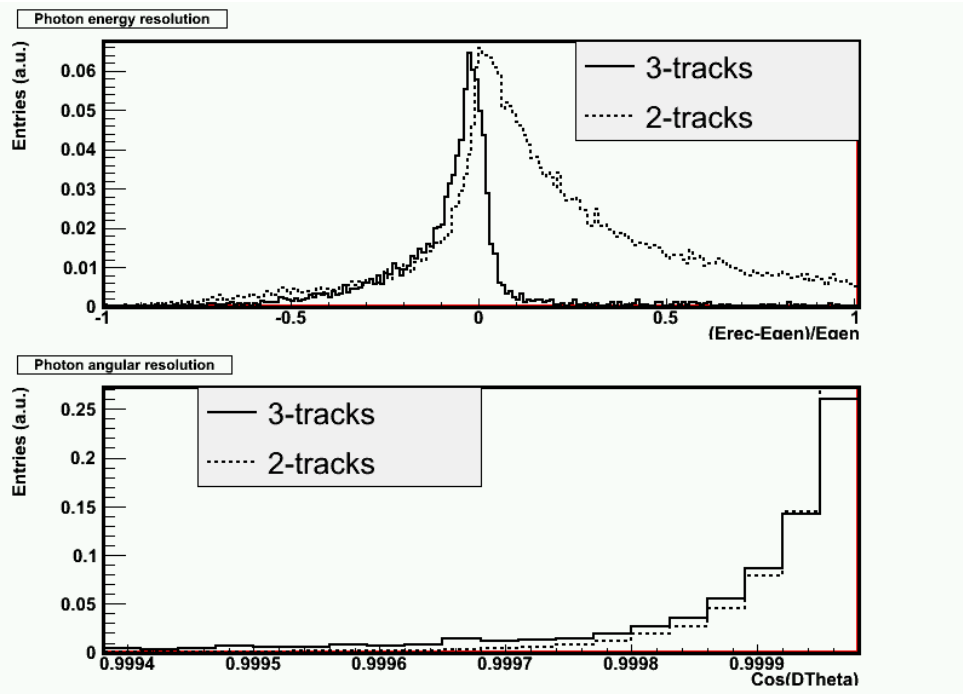

Figure 7.39: Comparison of angular and energy resolutions for photons using three-tracks and two-tracks events from Montecarlo simulation.

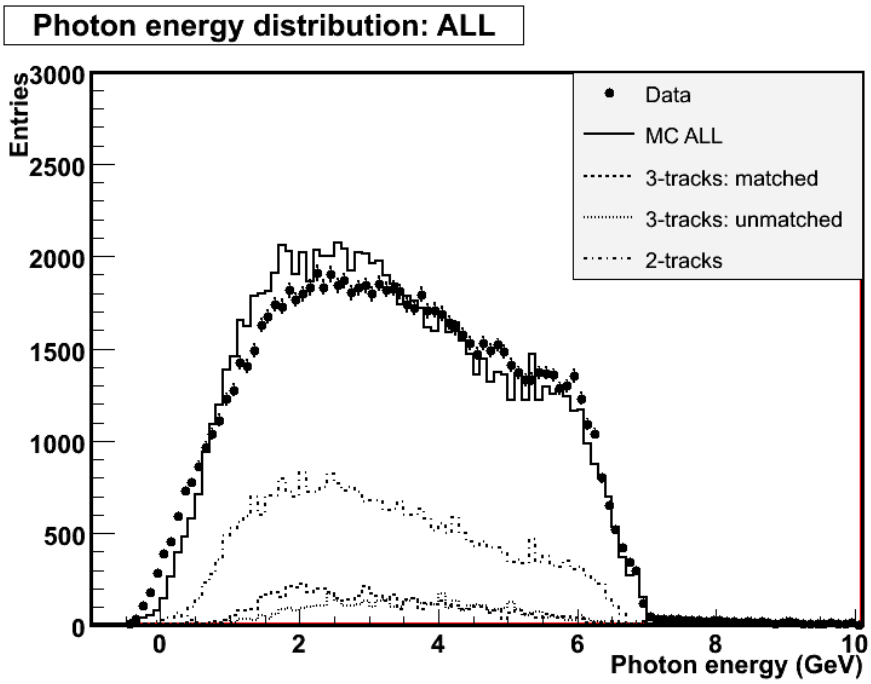

Figure 7.40: Photon energy distribution as obtained from data in the testbeam 2004. Montecarlo expectations are also shown.

The photon detection efficiency, energy and angular resolution have been estimated for the following two samples of events:

- *golden events*;
- *golden events* + *silver events* .

For *golden events*, the distribution of the energies of the direct and indirect reconstructed photons are shown in Fig. 7.40. The energy and angular resolutions for photons, using the indirect reconstruction as a reference, are also shown in Fig. 7.41 compared with the Montecarlo expectations.
The usage of *silver events* in the test beam increases by roughly a factor of 7 the yields of reconstructed photons.

The comparison of these results with the ones obtained from the AMS-02 Montecarlo simulation shows a good agreement (Fig. 8.3). As for the track momentum resolution, the photon energy resolution has to be divided by roughly a factor of two to be compared with AMS-02 due to the higher magnetic field. In this case the dominant error comes from the statistical uncertainty in the determination of the track momentum resolution.

These results experimentally verify the excellent angular and energy resolutions predicted by the AMS-02 Montecarlo simulation.

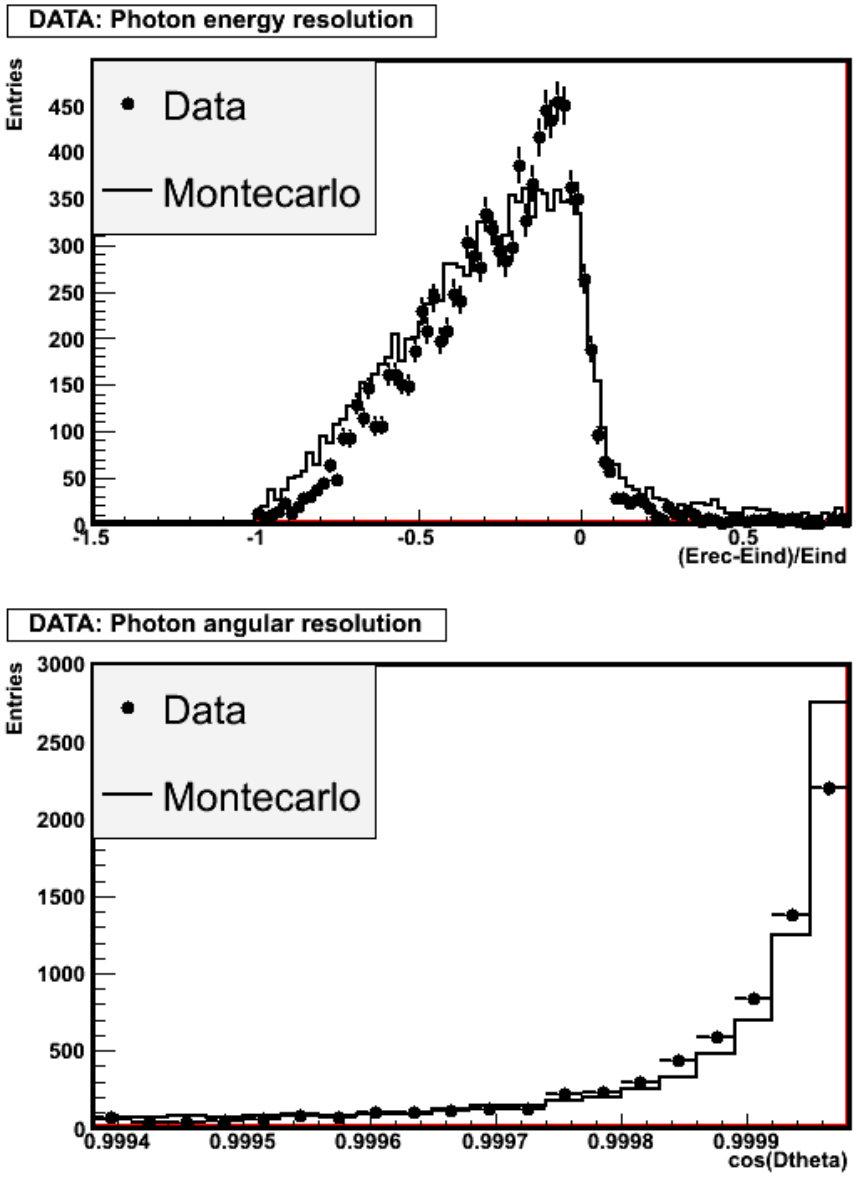

Figure 7.41: Photon energy and angular "resolution" distributions as obtained from data in the testbeam 2004 using the indirect reconstruction. Montecarlo expectations are also shown.

Chapter 8

Physics of High Energy Photons with AMS-02

8.1 Introduction

AMS-02 can contribute to the study of cosmic photons with sensitivity in the energy interval from 1 GeV to 1 TeV during its three-year mission on board the ISS. The lower bound is due to the curvature of the charged tracks in the strong magnetic field; below this value an event would no longer be entirely contained in the tracker. Reconstruction of the two tracks becomes increasingly difficult above 400 GeV because hits are not enough spatially separated.
The electromagnetic calorimeter, measuring electromagnetic showers due to photons which have not converted, will extend the energy reach. This subdetector will be sensitive in the energy region between 10 GeV and 1 TeV. For calorimetrically detected photons the relative energy resolution will be about 5% at 10 GeV and better than 3% at high energies above 100 GeV. The angular resolution for these photons is modest, about 1.5° at 10 GeV, reaching 0.5° at high energies. This way of detecting high energy photons will be referred to as the *calorimetric mode*.
Conversely, for converted photons the energy resolution is modest because of bremsstrahlung losses, a constant 15% below 100 GeV and slowly increasing above. The angular resolution is however excellent going down like a power law from about 10.5 mrad at 1 GeV to below 0.12 mrad at high energies. It is the angular resolution which is crucial for the detection of photons from point-like sources and their association to astronomically detected objects. In the following we will therefore concentrate the discussion on photon detection by conversion, referred to as the *conversion mode*. An analysis has previously been made on the AMS-01 data [210]. It should be noted that the AMS-01 mission was not specifically designed for such a measurement, but was optimized for the precise measurement of charged particle cosmic ray spectra and for antimatter search. Nevertheless a small amount of e^+e^- pair candidates was found thus proving the validity of the *conversion method* (Fig 8.1). One sees a clear signal of e^+e^- pairs. The excess coming from photons is seen in opposite sign pairs only, not observed in like-sign pairs which are well explained by the background calculation.

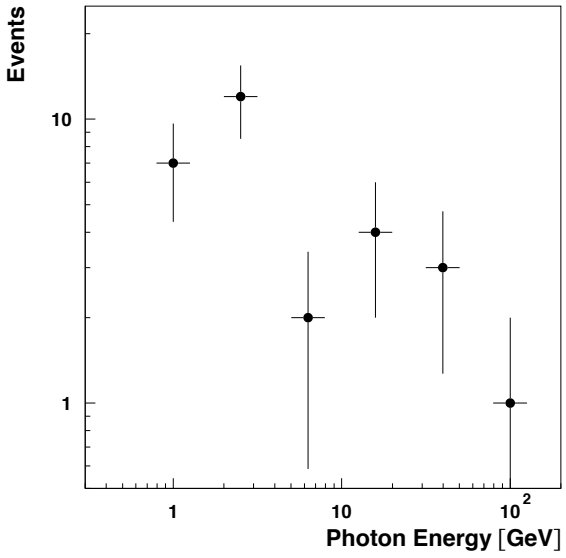

Figure 8.1: Energy distribution of selected photons, as observed during the AMS-01 mission.

8.2 AMS-02 Monte Carlo Simulation for Photon Detection

Detecting photons inside the dominant flux of charged cosmic rays is a complex task. The full GEANT Monte Carlo has been used to determine the AMS-02 performance for gamma rays. An exact geometry was incorporated with mechanical structures around AMS-02 included. The detector was then isotropically irradiated by incident protons, He nuclei and photons at different energies. In particular, for the photons, conversions were allowed from the top of the apparatus down to the second TOF plane. For those γ-rays which converted, the charged particles were tracked through the inhomogeneous magnetic field of the magnet. The hit positions in the silicon tracker planes were assigned Gaussian errors with $\sigma = 10\mu$m and 30μm in the bending and non-bending plane, respectively, as measured in beam tests. The tracker noise was also simulated. A signal-to-noise ratio 20% better than for AMS-01 was assumed, as observed for the AMS-02 production, but the noise and common noise spectra were taken from AMS-01. Two million photon events were generated at energies of 1, 2, 4, 8, 16, 32, 64, 128 and 256 GeV within a maximum zenith angle of $\pm 45°$. The conversion was required to take place in the material upstream of the second TOF plane so that the event would be triggered by the time-of-flight system. The corresponding material in AMS-02 amounts to 0.25 radiation lengths, providing a 17% probability of conversion (compared to $0.08X_0$ for AMS-01). The momentum of each electron and positron is measured in the spectrometer and the primary

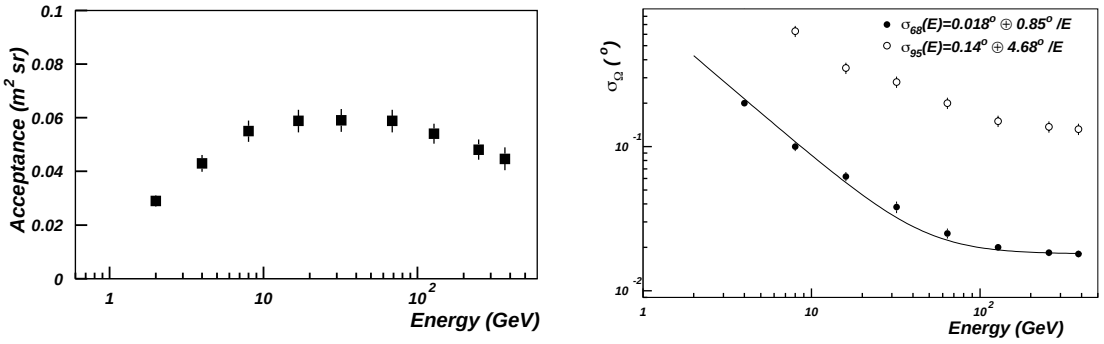

Figure 8.2: Left: Acceptance of the AMS-02 tracker for photon in *conversion mode* as a function of energy. Right: Angular resolution *in conversion mode* as a function of primary energy.

photon energy and incident direction are determined by adding the fitted momenta vectors of all secondaries, evaluated at the entrance to the magnetic field. A Star Tracker will be used to give the angular orientation of AMS-02 with respect to the celestial sphere to an accuracy of better than 1.5×10^{-4} radians. This additional device is required because the Space Station cannot provide attitude information to better than $\sim 2^\circ$ while the AMS-02 angular resolution for photons in the *conversion mode* is better than 0.1° for $E_\gamma \geq 10$ GeV (Fig. 8.2).
The following criteria were applied to reconstruct genuine γ events:

- a minimum of three out of four TOF scintillator planes fired;
- a minimum of 4 reconstructed hits over a minimum lever arm larger than 3/4 the height of the tracker for each of the e^- and e^+ candidate tracks;
- charge measurements from both TOF and tracker compatible with $|Z| = 1$ particles;
- reconstruction of a track pair of opposite charge and low invariant mass.

The main sources of background for the *conversion mode* option are protons and e^- which interact with the AMS material, producing delta rays within the spectrometer. A small fraction of those will be reconstructed as double-track events mimicking e^+e^- pairs from γ conversion. A rejection factor $> 0.8 \times 10^6$ was found for the protons and $> 0.5 \times 10^5$ for e^- using the above criteria. The *conversion mode* acceptance which is dominated (~ 40 %) by the reconstruction efficiency, was found to be constant at a value of 0.058 m^2sr for photon energies between 7 and 200 GeV as shown in Fig. 8.2. The energy resolution is dominated by bremsstrahlung losses throughout the material traversed by the electron-positron pair after conversion. In the reconstructed energy distribution for 32 GeV incident photons as shown in Fig. 8.3, one observes an important low-energy tail due to these bremsstrahlung losses. Fig. 8.3 also gives the relative r.m.s. energy resolution and the relative width of the Gaussian peak as a function of primary energy. It is rather constant

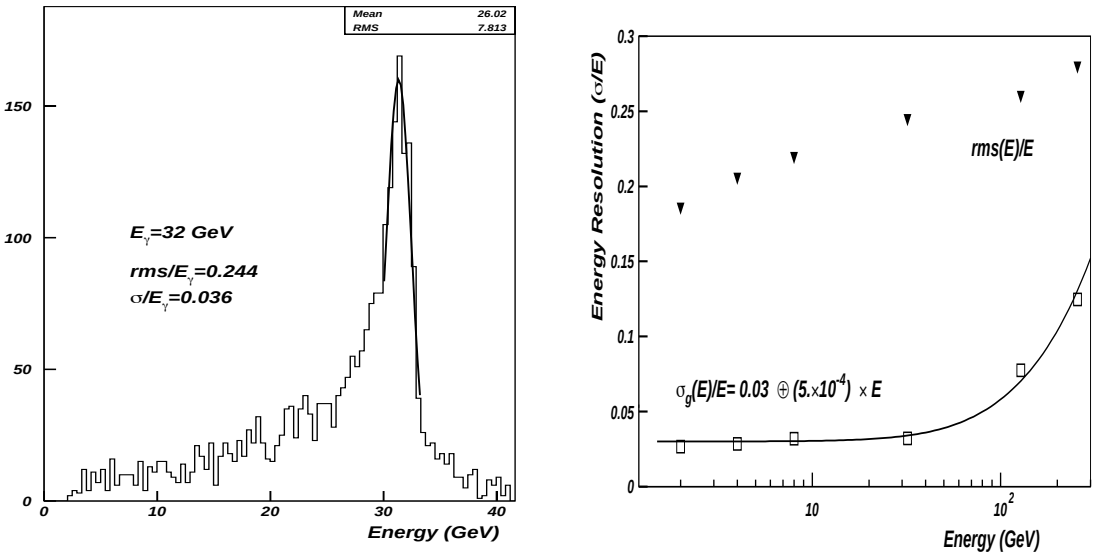

Figure 8.3: Left: reconstructed energy distribution for 32 GeV incident γ-rays. Right: relative r.m.s. energy resolution (triangles), and the relative width of the Gaussian peak of the distribution (open squares) as a function of primary γ-ray energy.

between 3 GeV and 100 GeV, but rises above 100 GeV. Eventually a fit to the relative energy resolution gives:

$$\sigma(E_\gamma)/E_\gamma = 0.03 \oplus (5 \times 10^{-4})E_\gamma \tag{8.1}$$

where E_γ is the photon energy in GeV.
The *conversion mode* angular resolution, as shown in Fig. 8.2, can be parametrized as:

$$\sigma_{68}(\Delta\theta) = 0.14^\circ \oplus 4.68^\circ/E_\gamma \tag{8.2}$$

where $\Delta\theta$ is the difference between the true and the reconstructed angle. The subscript "68" indicates that, being the distribution not gaussian, the equivalent σ is chosen such to contain 68% of the events.

The increase at high energies is due mainly to multiple Coulomb scattering. For detection of point-like sources, this parameter is crucial as it enters when calculating the number of background photons within the source area.

8.3 AMS Gamma Fast Simulator

The full simulation, described so far, is very CPU-time consuming and there is a need for faster, efficient and still precise tool to estimate the detector sensitivity to gamma sources (in particular the variable sources like pulsars that will be considered later).
The fast simulation tool, called AMSFS (AMS Fast Simulator) [260] is devoted

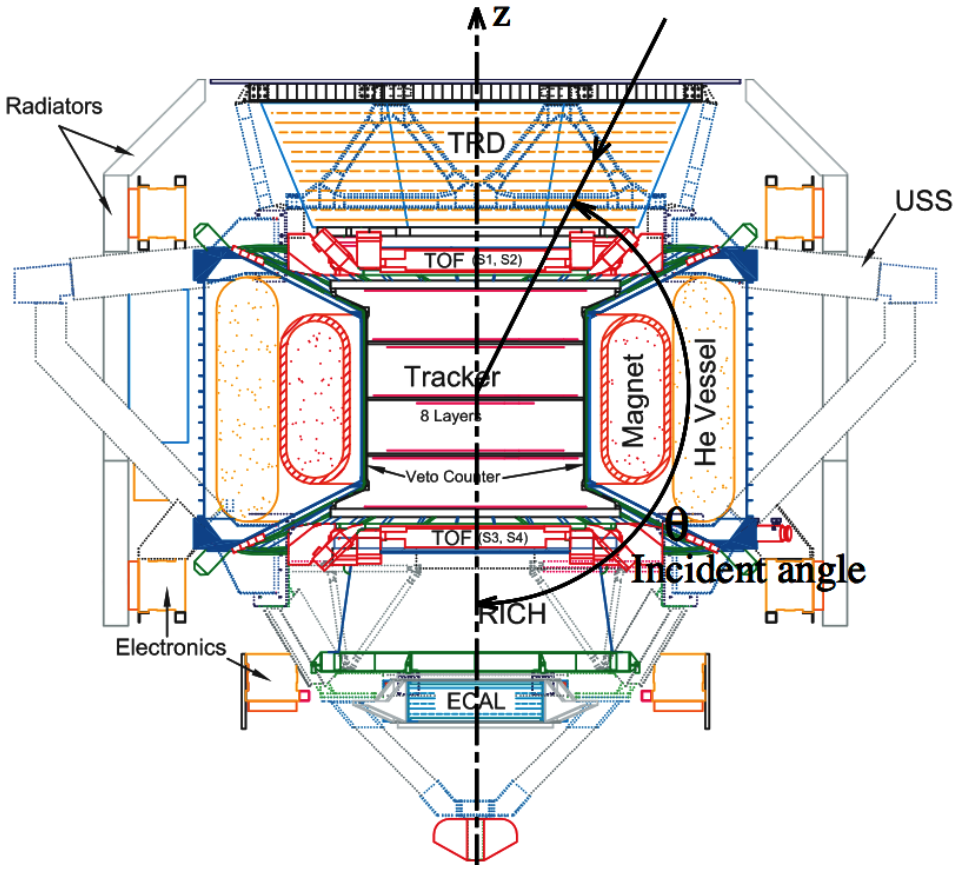

Figure 8.4: Definition of the incident angle for AMS-02 detector.

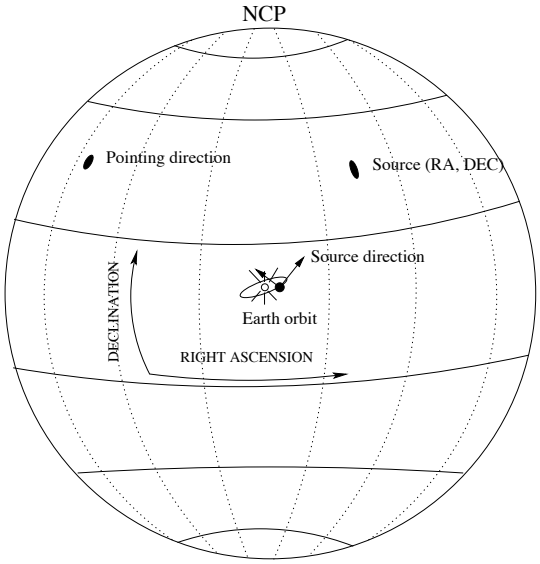

Figure 8.5: The celestial sphere as an inertial reference system. Positions in the sphere are independent of the actual geographical coordinates of the observer, so that given a position on the orbit different sky directions depending on the time of the year can be seen.

to study the detection of photons from sources or background. It is also capable to estimate the background from protons which give a photon-like signal in the detector. In the approach used by the AMSFS the response of the detector for the passing particles is parametrized. The crucial parameters of the detector, eg. the effective area, the angular resolution, the background rejection factors are included in AMSFS as functions of energy and incident angle of particles. This allows to perform much faster estimations than with the full simulation and reconstruction. An important part of the program is the orbit simulation which allows to estimate the exposure time of the AMS sub-detectors for a given location in the sky, and therefore also for a given source and background.

In the AMSFS package, all energies are expressed in GeV and all angles in degrees. However, for convenience, acceptances and angular resolutions are used as a function of variables $x = log_{10}E$ and $\alpha = cos(\theta)$ where θ is the incident angle of particles with respect to the vertical, as shown on Fig. 8.4.

8.3.1 ISS Orbit Simulation

In this paragraph the reference system, orbital elements and algorithms according to which the International Space Station (ISS) position can be determined, are described. The calculation of the AMS pointing direction based on the ISS position is then detailed. The implementation of the orbit simulation in the AMS-γ Fast Simulator and in the full AMS simulation code is addressed.

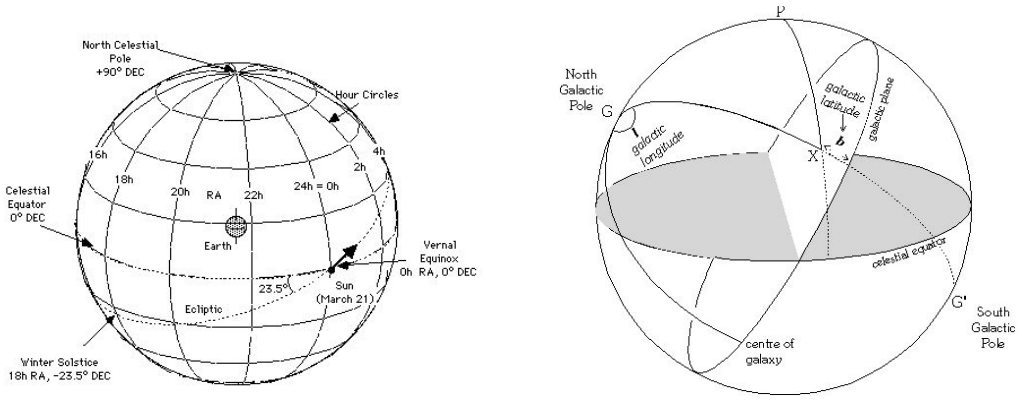

Figure 8.6: The *Equatorial* (left) and the *Galactic* reference systems (right).

The precise determination of the position and pointing vector of AMS during the ISS evolution in its orbit is critical for the investigation of localized, non-isotropic radiation, whether it be point-like or diffuse. For the understanding of the AMS sky coverage during its mission on-board of the ISS, a simulation of its orbit is needed. Here, the standard inertial reference systems to locate sky sources and the detector pointing direction is introduced. Then, the orbital elements which define the station position and evolution are explained. Finally, it is shown how the pointing direction is calculated using this orbital information.

8.3.2 Celestial Coordinates

To study any source or region in the sky an inertial reference frame fixed to the solar system is commonly used. This reference system usually adopts the shape of a sphere (Fig. 8.5) on which one can specify directions towards any point of the universe with spherical coordinates. Using the analogy with the Earth's latitude and longitude, one defines an equator (fundamental plane) and a prime meridian from which to measure the equivalent to latitude and longitude respectively.
The most widespread systems are the **equatorial** and the **galactic coordinates** (Fig. 8.6). For any object in the sky, its coordinates can be specified in a unique way independent of the time of the day/year (given a specified reference epoch which is valid for several decades for our purposes).

These systems are fully explained in Refs. [249, 250].

- **Equatorial coordinates :**
  The Declination angle *Dec* from the equatorial plane of the Earth (in the -90^o to 90^o range).
  The Right Ascension *RA* (24 hours or 360^o range) from the so-called *vernal equinox*, a specific sky direction which serves as reference for this system.

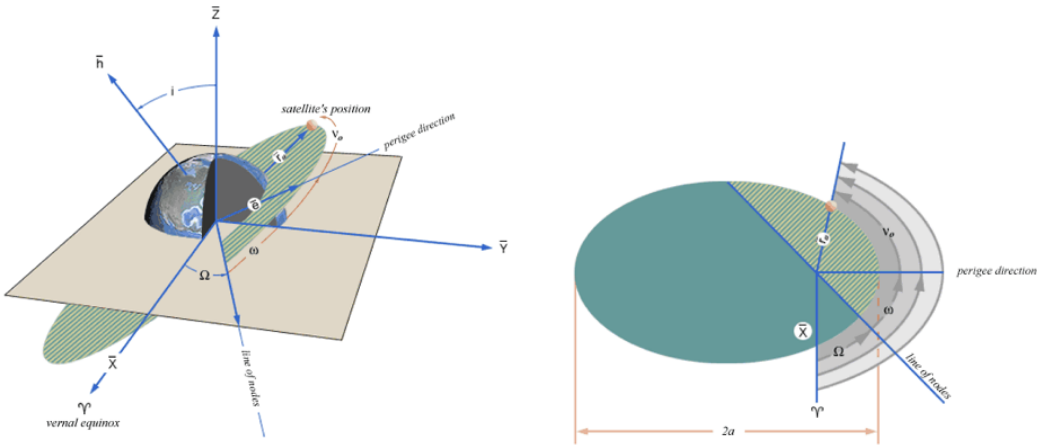

Figure 8.7: The Keplerian orbital elements [251, 252].

- **Galactic coordinates :**
  It is defined by another fundamental plane called *galactic plane*. The new *North Pole* is now the *North Galactic Pole* at RA= 12h49m and Dec= $+27^o24'$. The Galactic Latitude is defined from this plane ($-90°$ to $+90°$ range).
  The origin for longitude is situated at RA: 17h 45m and Dec: $-28^o56'$ (the galactic center) and it defines the Galactic Longitude in a 360 degrees range along the galactic plane.

Both systems are entirely equivalent, the equatorial coordinates are more standard and easier to calculate given the geographical position of the observer or the position in orbit. The galactic coordinates are more useful to visualize the relative position of the source with respect to the Galaxy.

8.3.3 Definition of the Orbit Elements

Any orbit may be specified with a set of six parameters referred to as Keplerian elements [251, 252] which define in a unique way its orientation and shape around the common center of mass of the system (a two-body situation where one mass is much larger than the other one will be considered).
These elements, shown in Fig. 8.7, are:

- The orbital inclination (i) which defines the angle of the orbital plane with respect to the reference plane. In the actual case this is the mean Earth equatorial plane at some reference time (this time is also called epoch).

- The longitude of the ascending node (Ω) indicating the angle along the equator from the x-axis (corresponding to the direction of the vernal equinox) to the line where the orbital plane crosses the equatorial plane (towards the so-called *ascending node*).

Orbit element	Value for ISS
i	51.6331^o
Ω	59.0438^o
T	92.35min
e	$6.55 \cdot 10^{-4}$
ω	230.9298^o
M_ν	129.1131^o
t_0	2003/160.465(yr/UT day)

Table 8.1: International Space Station[253, 254] typical orbit parameters.

- The semi-major axis (a) of the orbit's ellipse. Alternatively one may use the mean motion (n) or the orbit period (T). All three are related by Kepler's third law.
- The eccentricity (e) of the ellipse, $e = \sqrt{1 - b^2/a^2}$, where a and b are the semi-major and semi-minor axes respectively.
- The argument of the perigee (ω), that is, the angle (measured along the orbital plane) from the ascending node to the perigee of the orbit. The perigee is the point where the orbiting body is closest to the center of mass, so this parameter indicates the orientation of the orbit's axis in the orbital plane;
- A reference time (t_0) which may be, for instance, the time of perigee passage of the orbiting body.

Additionally, it is necessary to specify either the mean (M_ν) or the true anomaly (ν), which indicate the actual position of the body in the orbit at time $\boldsymbol{t}$. The mean anomaly is the angle the body would be at if it followed a uniform, circular motion while the true anomaly takes the eccentricity into account. Tab. 8.1 shows some typical values for the International Space Station.

8.3.4 Orbit Elements Dynamics

The potential which describes the gravitational force of the Earth-ISS system may be written in general terms as:

$$V(r, \theta) = -\frac{GM}{r} - U(r, \theta) \tag{8.3}$$

$U(r, \theta)$ being the disturbing function to the central potential, dependent on the orbiting body distance r and its colatitude θ, where θ is the complementary angle of the latitude (i.e. COL=90^o - LAT) in spherical coordinates.
A first approximation due to the non-sphericity of the Earth results in the following expression for this function, arising from the gravitational multipole expansion:

$$U(r, \theta) = -\frac{GMJ_2R_T^2}{r^3}(3\cos^2\theta - 1) \tag{8.4}$$

where:

- G is the gravitational constant;
- M, R_T are the mass and the radius of the Earth, respectively;
- J_2 is the second gravitational moment (for the Earth, J_2=1.08263·10^{-3});

From this perturbative potential the rate of change of the orbit elements can be derived:

$$\frac{da}{dt} = 0 \qquad \frac{de}{dt} = 0 \qquad \frac{di}{dt} = 0 \tag{8.5}$$

$$\begin{aligned} \frac{d\Omega}{dt} &= -\frac{3}{2} n J_2 \left(\frac{R}{a}\right)^2 \frac{\cos i}{(1-e^2)^2} \\ \frac{d\omega}{dt} &= 3 n J_2 \left(\frac{R}{a}\right)^2 \frac{1-(5/4)\sin^2 i}{(1-e^2)^2} \\ \frac{dM}{dt} &= n + \frac{3}{2} n J_2 \left(\frac{R}{a}\right)^2 \frac{1-(3/2)\sin^2 i}{(1-e^2)^{3/2}} \end{aligned}$$

8.3.5 Input Orbit Elements

In order to have the Station's location, and therefore AMS pointing direction, one must keep track of its position within the orbit and the orbit's orientation at time t, with respect to the equatorial reference frame.

- **Station position** $r_{ISS}(t) = (x_{ISS}(t), y_{ISS}(t), z_{ISS}(t))$ in the orbit reference frame at the time t:

$$\vec{x}_{ISS}(t) = a(t) \cdot \cos(\nu(t)) - e(t) \tag{8.6}$$

$$\vec{y}_{ISS}(t) = a(t) \cdot \sqrt{1 - e(t)^2} \cdot \sin(\nu(t)) \tag{8.7}$$

$$\vec{z}_{ISS}(t) = 0 \tag{8.8}$$

where:

$$a(t) = a(t_0) + \frac{da}{dt} \cdot (t - t_0); \qquad e(t) = e(t_0) + \frac{de}{dt} \cdot (t - t_0) \tag{8.9}$$

and the true anomaly $\nu(t)$ is found by solving Kepler's equation in e(t) (the so-called eccentric anomaly):

$$\nu(t) = 2\arctan\left(\sqrt{\frac{1+e}{1-e}} \cdot \tan\frac{e(t)}{2}\right) \tag{8.10}$$

$$M(t) = e(t) - e\sin(e(t)) \tag{8.11}$$

where:

$$M(t) = M(t_0) + \frac{dM}{dt} \cdot (t - t_0) \tag{8.12}$$

and Eq. 8.11 is solved numerically.

- **Orbit orientation at time t:**

$$i(t) = i(t_0) + \frac{di}{dt} \cdot (t - t_0); \qquad \Omega(t) = \Omega(t_0) + \frac{d\Omega}{dt} \cdot (t - t_0); \qquad \omega(t) = \omega(t_0) + \frac{d\omega}{dt} \cdot (t - t_0) \tag{8.13}$$

By rotating $\vec{r}_{ISS}$ using the three angles i, Ω and ω which define the orbit orientation in the equatorial reference system, the ISS position in this reference system is found, which is the same as the ISS (-z) axis pointing direction.

$$\vec{r}_{ISS} = R_Z(-\Omega) \cdot R_X(-i) \cdot R_Z(-\omega) \cdot \vec{r'}_{ISS} = R \cdot \vec{r'}_{ISS} \tag{8.14}$$

where R is:

$$\begin{pmatrix} \cos\Omega\cos\omega - \sin\Omega\cos i\sin\omega & -\cos\Omega\sin\omega - \sin\Omega\cos i\cos\omega & \sin\Omega\sin i \\ \sin\Omega\cos\omega + \cos\Omega\cos i\sin\omega & -\sin\Omega\sin\omega + \cos\Omega\cos i\cos\omega & -\cos\Omega\sin i \\ \sin i\sin\omega & \sin i\cos\omega & \cos i \end{pmatrix}$$

Finally, one can again rotate the pointing direction vector $\vec{r}_{ISS}$ around any specific ISS LVLH1 (Local Vertical Local Horizontal) which is a widely used reference system for the ISS and shuttles. The Z' axis points towards the center of the Earth and the X axis towards the ISS/shuttle movement direction) axis to arrive to the AMS pointing direction $\vec{r}_{AMS}$. This rotation will depend on the final configuration of the AMS payload on the Station.

8.4 AMS Exposure Maps

A straightforward application of these calculations is the derivation of the sky map showing the exposure time of the AMS field of view for each sky region convoluted with the acceptance of the detector. The exposure maps are produced excluding the time spent by AMS-02 in the South Atlantic Anomaly (SAA) (Fig. 8.8). The SAA is a region of the South Atlantic where the belt of radiation surrounding the Earth has a lower altitude (approximately 250 km). In this zone, the high flux of particles (protons, electrons) can saturate the detector electronics so it is preferable to switch it off. To obtain these maps, a simple approach was adopted:

The Orbit Simulation

Inputs to the orbit simulator are:

- ISS orbital parameters

obtained from NASA using the PREDICT [253, 254] software. In Tab. 8.2 a typical Predict software output is shown.
Concerning the outputs, they are given with respect to different reference systems:

- ISS position w.r.t. its orbital plane,

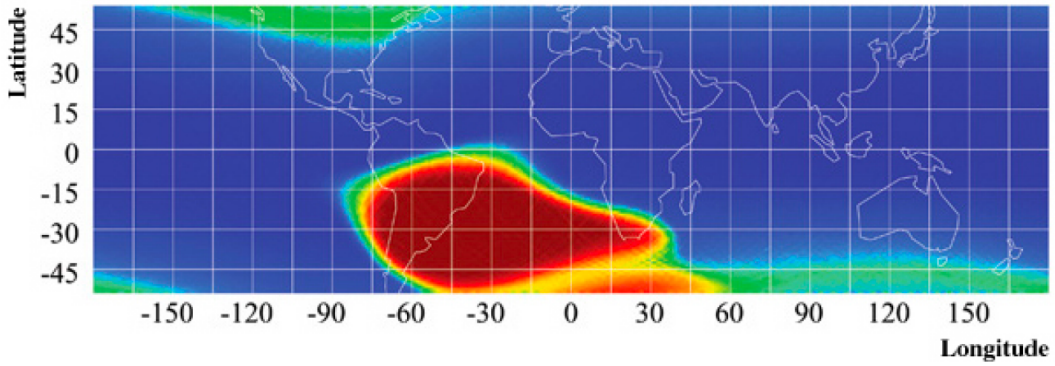

Figure 8.8: Map of the South Atlantic Anomaly.

Orbital Data For ISS / Catalog Number 25544 Issued 46 days ago on Thu 03Jan02 04:36:26 UTC		
Reference Epoch	:	02 3.19196759
Inclination	:	51.6378 deg
RAAN	:	162.2458 deg
Eccentricity	:	0.0002638
Arg of Perigee	:	75.0551 deg
Mean Anomaly	:	276.8259 deg
Mean Motion	:	15.61842842 rev/day
Decay Rate	:	0.00056961 rev/day/day
Orbit Number	:	17828
Semi-Major Axis	:	6760.4042 km
Apogee Altitude	:	384.0526 km
Perigee Altitude	:	380.4858 km
Anomalistic Period	:	92.1988 mins
Nodal Period	:	92.1373 mins

Table 8.2: Format of Predict software output referred to the ISS at Jan. 3^{rd}, 2002.

- ISS position w.r.t. the Geographical reference system,
- ISS position w.r.t. the Equatorial reference system,
- ISS position w.r.t. the Galactic reference system.

The Method

The algorithm starts computing the ISS orbital trajectory. The set of four parameter given by the ISS initial position (x_0,y_0) on its orbit at a fixed time t_0 and the corresponding velocity components (v_{0_x},v_{0_y}). By iteration one can find at $t = t_0+\Delta t$:

$$\begin{aligned} a_{x_0} &= k \cdot \tfrac{x_0}{r_0^3} \\ a_{y_0} &= k \cdot \tfrac{y_0}{r_0^3} \\ \\ v_{x_1} &= v_{x_0} + a_{x_0} \cdot \Delta t \\ v_{y_1} &= v_{y_0} + a_{y_0} \cdot \Delta t \end{aligned} \tag{8.15}$$

where $r_0 = \sqrt{x_0^2 + y_0^2}$ and $k = G \cdot m$. The new position is then:

$$\begin{aligned} x_1 &= x_0 + v_{x_1} \cdot \Delta t \\ y_1 &= y_0 + v_{y_1} \cdot \Delta t \end{aligned} \tag{8.16}$$

Inputs from Predict used for this analysis are:

$$\begin{aligned} t_0 = &\quad 03/01/2002 \qquad 04\text{h:}36\text{m:}26\text{s} \\ \\ x_0 = &\quad 6.67 \times 10^3 \text{ km} \\ y_0 = &\quad 0. \\ \\ v_{x_0} = &\quad 0. \\ v_{y_0} = &\quad 7.68 \times 10^3 \text{ m/s} \\ \\ \Delta t = &\quad 30 \text{ s} \end{aligned} \tag{8.17}$$

From the Orbital to the Equatorial Reference System

Considering the unit vector to be ($\hat{p}$, $\hat{q}$, $\hat{w}$) and ($\hat{i}$, $\hat{j}$, $\hat{k}$) for the Orbital and the Equatorial Reference System respectively, the matrix which performs the transformation between the two systems is:

$$\begin{pmatrix} \hat{p} \\ \hat{q} \\ \hat{w} \end{pmatrix} = \begin{pmatrix} \cos\omega & \sin\omega & 0 \\ -\sin\omega & \cos\omega & 0 \\ 0 & 0 & 1 \end{pmatrix} \begin{pmatrix} 1 & 0 & 0 \\ 0 & \cos i & \sin i \\ 0 & -\sin i & \cos i \end{pmatrix} \begin{pmatrix} \cos\Omega & \sin\Omega & 0 \\ -\sin\Omega & \cos\Omega & 0 \\ 0 & 0 & 1 \end{pmatrix} \begin{pmatrix} \hat{i} \\ \hat{j} \\ \hat{k} \end{pmatrix}$$

with:

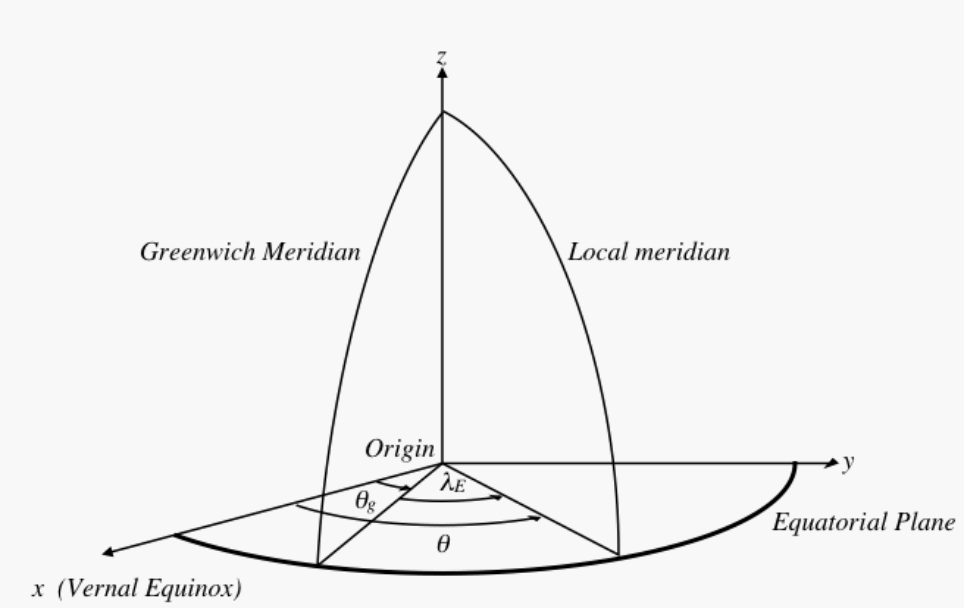

Figure 8.9: Sidereal time and Local Sidereal time.

$$
\begin{aligned}
i &= 51.6378^o \\
\omega &= 75.0551^o \\
\Omega &= 162.2458^o + v(deg/s) \cdot \Delta t
\end{aligned}
$$

From the Equatorial to the Geographical Reference System

The computation of the Local Sidereal Time Θ (Fig. 8.9) is needed for this transformration. It has been performed as follows:

$$\Theta = \Theta_g + \lambda_E \tag{8.18}$$

where:

$$\Theta_g = \Theta_{g_0} + \Delta t \cdot \frac{d\Theta}{dt}$$

$$\Theta_{g_0} = (99.69098329 + 36000.76893 \cdot T_u + 3.87080 \times 10^{-4} \cdot T_u^2)^o$$

$$\frac{d\Theta}{dt} = \frac{1}{240}\left(1 + \frac{1}{L}\right) deg/s$$

with:

$$L = (365.24219879 - 6.14 \times 10^{-6} \cdot T_u) \text{ days}$$

$$T_u = \frac{\text{actual Julian date} - \text{Julian date at 1900}}{\text{number of days in a Julian century}} = \frac{\text{Julian date} - 2,415,020.0}{36,525}$$

and the *Julian Date* is defined as the unit of the Julian Calendar which counts days progressively starting since 1^{st} *Jan 4713 BC*.

Given the AMS coordinates (x, y, z) with respect to the Equatorial Reference System and the Sidereal Time Θ_g it is possible to extract the corresponding Geographical coordinates as follows:

- Geographical longitude λ_E:

  $\lambda_E = \Theta - \Theta_g \ \mathrm{mod} 360^o$
  where Θ is the Right Ascension and:

$$\sin\Theta = \frac{y}{\sqrt{x^2+y^2}} \qquad \cos\Theta = \frac{x}{\sqrt{x^2+y^2}}$$

- The geographical latitude Φ and the altitude H are calculated by iteration:

  1) Set $\Phi'_o = \delta$ at $k-0$
  2) $r_{c,k} = a_e\sqrt{\frac{1-(2f-f^2)}{1-(2f-f^2)\cos^2\Phi'_k}}$

     $\Phi_k = \arctan\left(\frac{1}{1-f^2}\tan\Phi'_k\right) \quad ; \qquad -90^o \leq \Phi_k \leq 90^o$

     $H_k = \sqrt{r^2 - r^2_{c,k}\sin^2(\Phi_k - \Phi'_k)} - r_{c,k}\cos(\Phi_k - \Phi'_k)$

     $\Phi'_{k+1} = \delta - \arcsin\left(\frac{H_k}{r}\sin(\Phi_k - \Phi'_k)\right)$

  3) if $\left|\frac{\Phi'_{k+1}-\Phi'_k}{\Phi'_{k+1}} < 10^{-5}\right|$ stop iteration otherwise $k \to k+1$ and go to 2)

  4) $H = H_k$

     $\Phi = \arctan\left(\frac{1}{(1-f)^2\tan\Phi'_{k+1}}\right)$

  with:

$$r = \sqrt{x^2+y^2+z^2}, \qquad \sin\delta = \frac{z}{r}, \qquad \cos\delta = \frac{\sqrt{x^2+y^2}}{r}$$

  and $a_e = 6.37815 \times 10^6$ m (major semiaxis), $f = 1/298.30$ (flattening).

The AMS-02 position with respect to the geographic, equatorial and galactic reference system for 1 year observation time and the exclusion of the SAA, are shown in Fig. 8.10 and Fig. 8.11.

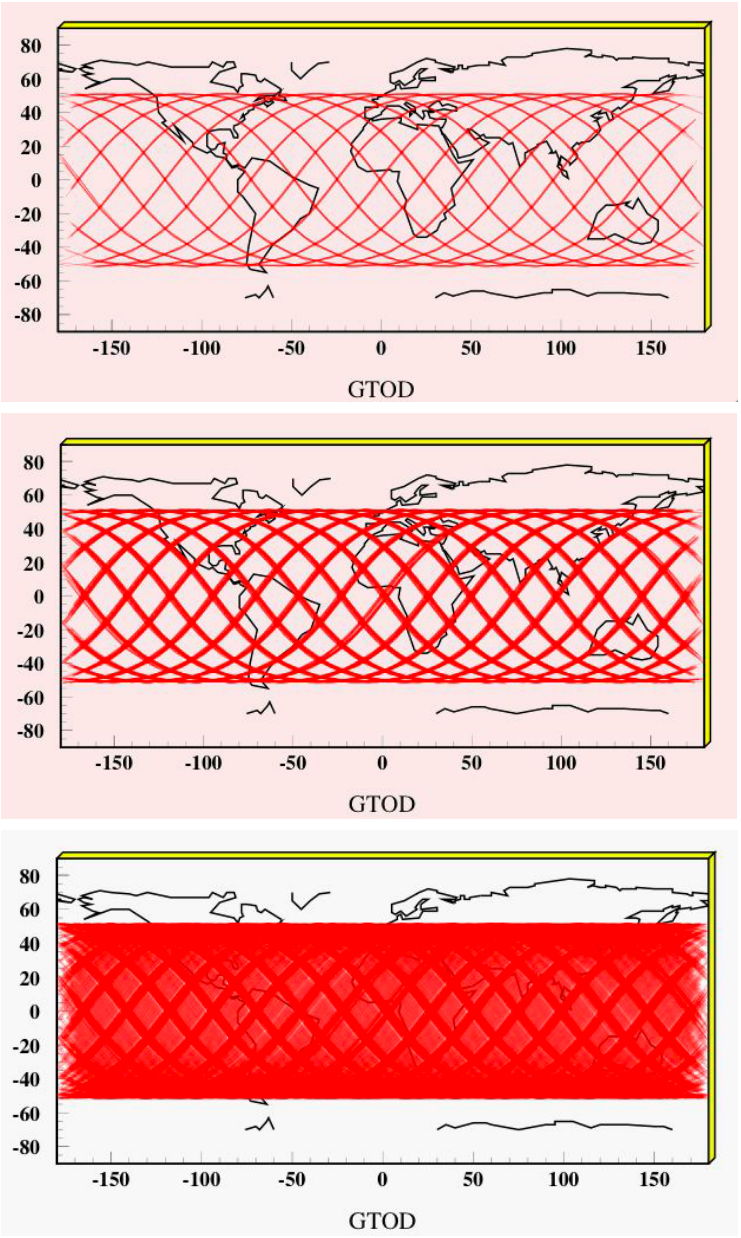

Figure 8.10: AMS position with respect to the geographical reference system for different orbiting times epochs: 7 days (top), 30 days (middle) and 90 days (bottom).

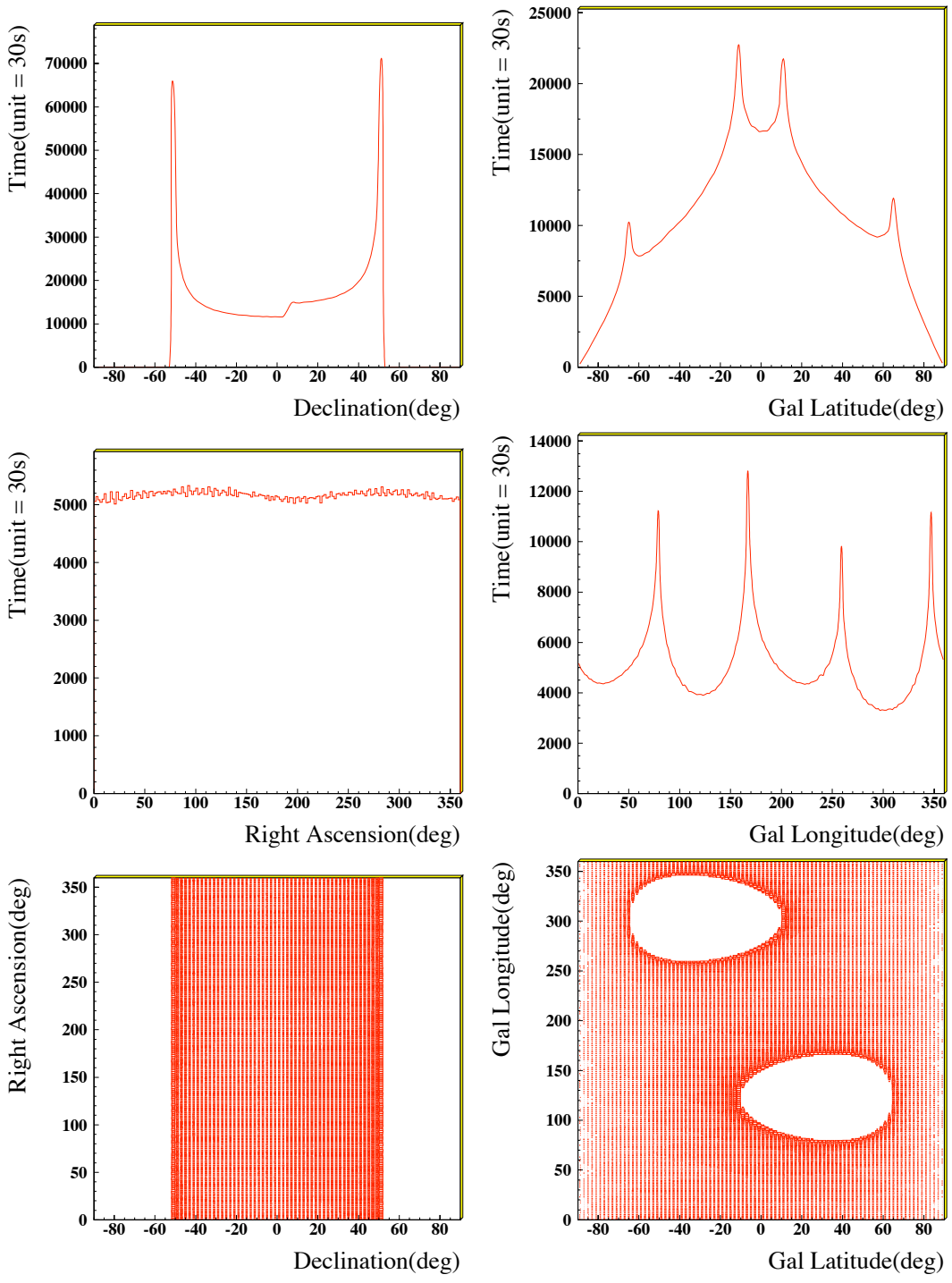

Figure 8.11: AMS position with respect to the equatorial (left column) and galactic (right column) reference system for 1 year observation time after the exclusion of the SAA.

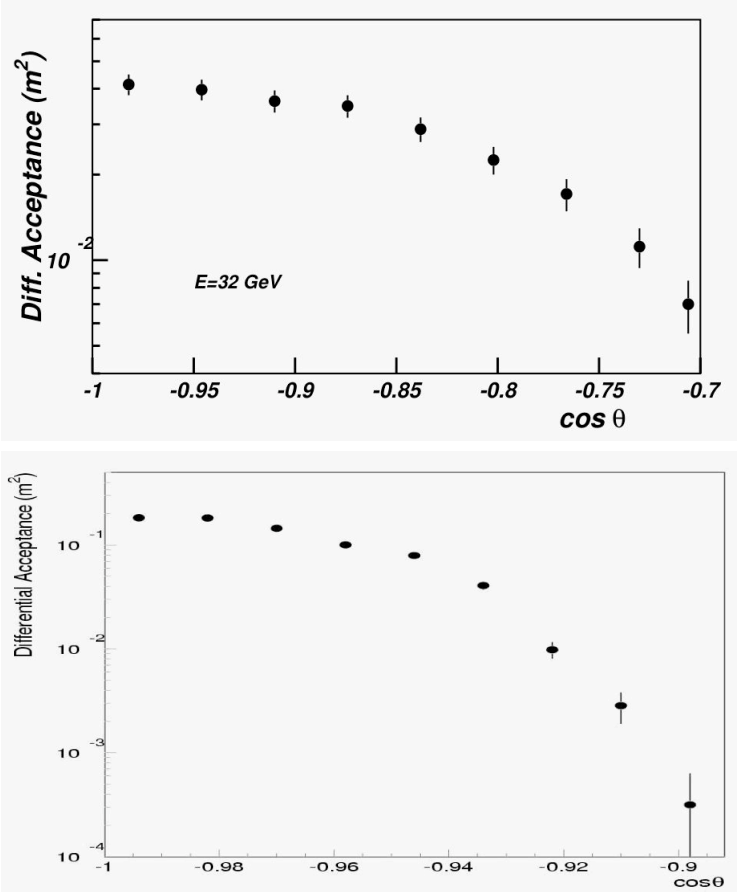

Figure 8.12: AMS-02 effective area. On the top for the Tracker (considering an observation cone with a $\sim 45°$ maximal half opening angle) and on the bottom for the ECAL (considering an observation cone with a $\sim 26°$ maximal half opening angle).

Integration over the Acceptance

Next step is to introduce the tracker Effective Area angular dependence shown in Fig. 8.12. It can be parametrized as a function of the polar angle θ with respect to the AMS vertical axis (zenith) while it is totally symmetric with respect to the angle ϕ around the same axis:

$$f(\theta) = A \cdot \cos\theta - B \tag{8.19}$$

with $A = 0.13$ m^2 and $B = 0.08$ rad for the Tracker and $A = 2.15$ m^2 and $B = 1.95$ rad for Ecal.

Considering AMS observing a source S at different epochs t_i $(0 \leq i \leq n)$ it is possible to compute the time exposure maps using the following constraints:

- The AMS position is calculated on its orbital trajectory each $\Delta t = 30$ s which means $\Delta\alpha \sim 2^o$, being α the angle spanned on the orbital plane.

Galatic North Pole	RA= $12:51,4 \sim 193^o$, δ= 27.07^o
Galactic Center	RA= $17:45,6 \sim 266^o$, δ= -28.56^o
Galatic Plane inclination w.r.t. Geograp. Equat. Plane	i = 62.9^o
Intersection between Galactic and Geograp. Equat. Plane	RA= $18:51,4 \sim 283^o$, δ= 0^o

Table 8.3: Some of the parameters used to convert the AMS-02 exposure maps from Equatorial to the Galactic reference system.

- The position coordinates are calculated both in the Equatorial and in the Galactic reference system.
- The SAA (*South Atlantic Anomaly*), defined inside the following geographical coordinates:

minimal latitude $\sim$	-51^o,	minimal longitude $\sim$	-85^o
maximal latitude $\sim$	+5^o,	maximal longitude $\sim$	-10^o

  is excluded.
- The θ angle is computed for each position and constrained to be inside the detector field of view: ECAL $\rightarrow$ $\leq 26^o$, Tracker $\rightarrow$ $\leq 45^o$
- The exposure is computed as the sum of the products between $A(\theta)$ and the corresponding Δt.

In Tab. 8.3 some useful parameters used in this analysis are reported and in Fig.8.13, 8.14 the results for the Tracker, ECAL and the sum of the two are shown. The integrated effective area in a year of observation is above 0.008 m^2 for most of the spanned sky area.
The AMS field of view is calculated for each 30-second step as the ISS progresses in its simulated orbit. This is done for a full Space Station precession period (2.26 months).

8.5 Astrophysical γ Ray Sources

From the photon detection capabilities of AMS-02 and from the known orbit of the ISS, it is possible to calculate the number of photons observed by AMS-02 from γ-ray sources for a given time of observation [256, 257].

Astrophysical γ ray sources can be classified into three categories as already described in Chap. 2:

1. *Galactic point-like sources* among which the pulsars are the most luminous ones for high energy photons [258].

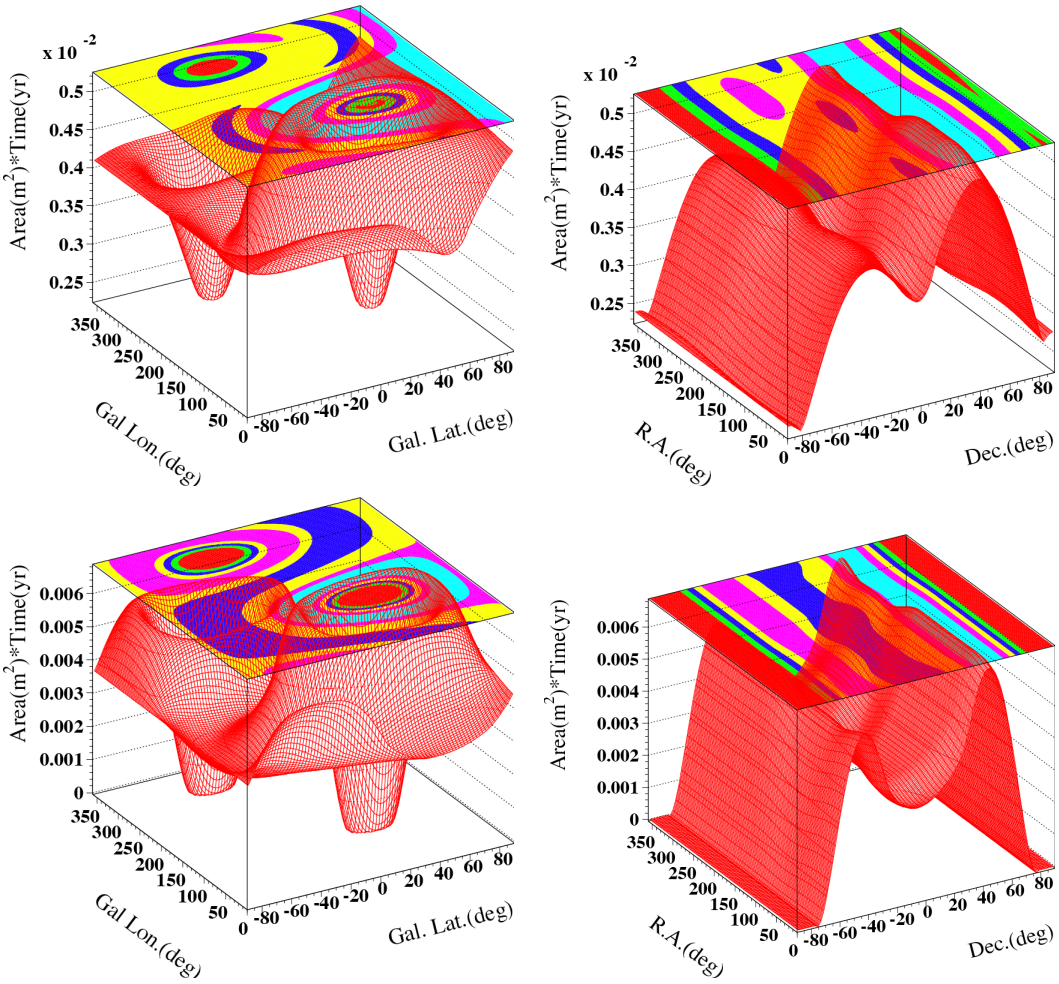

Figure 8.13: Upper: AMS Tracker exposure maps with respect to the galactic and equatorial reference system for 1 year observation time and the exclusion of the SAA. Lower: AMS Ecal exposure maps with respect to the galactic and equatorial reference system for 1 year observation time and the exclusion of the SAA.

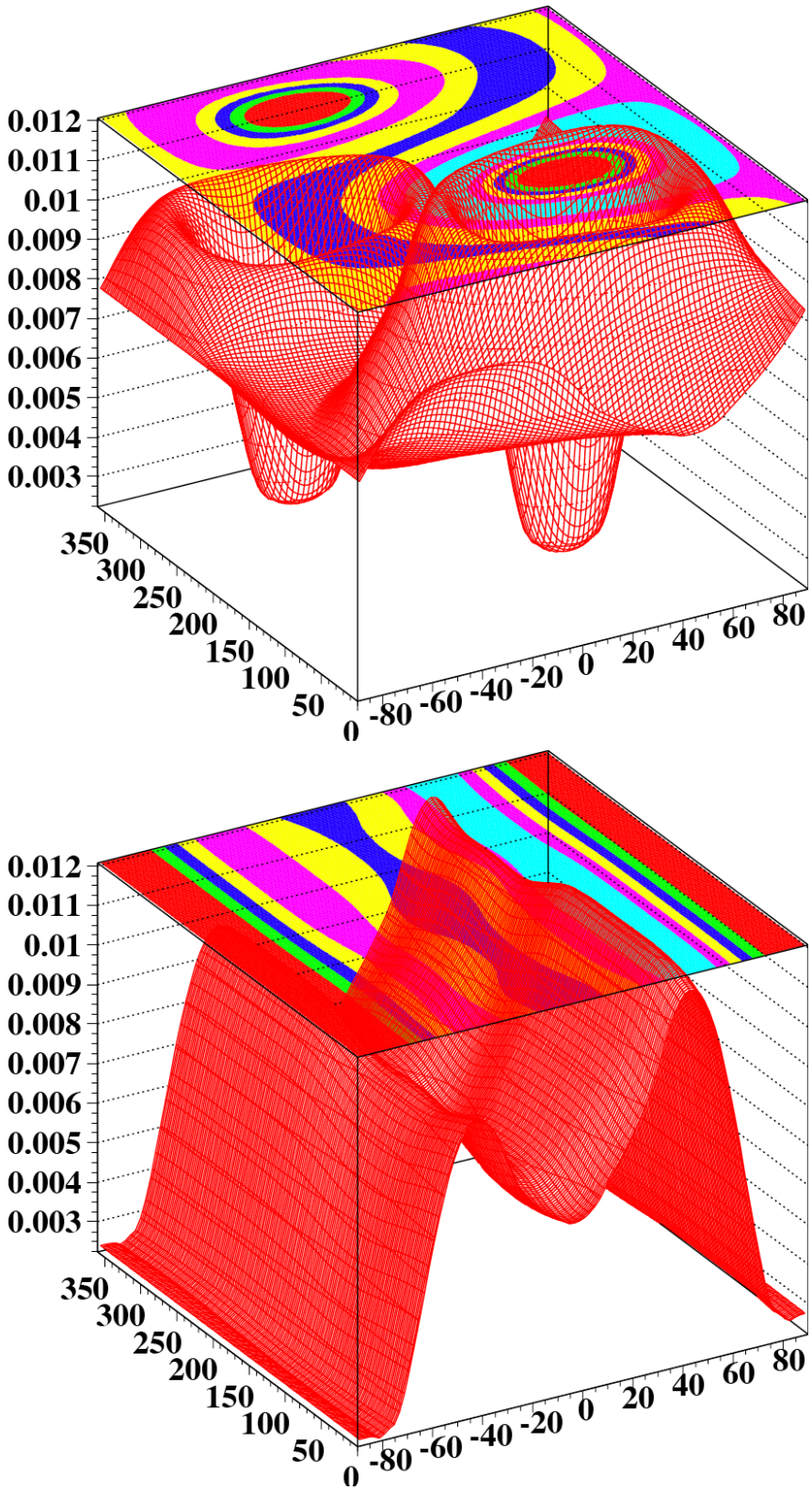

Figure 8.14: AMS total exposure maps (Tracker+ECAL) with respect to the galactic and equatorial reference system for 1 year observation time and the exclusion of the SAA.

They are rotating neutron stars from supernovae remnants [259]

An additional unpulsed emission is also possible. A long term observation of these sources in multiple frequency bands, including energies above 30 GeV, may reveal details of the acceleration mechanism involved in pulsars. Different high energy cut-offs are predicted by different models. The region from a few GeV to several hundred GeV is sparsely covered by experiments, yet important to fix the shape of the inverse Compton scattering contribution beyond the synchrotron radiation cut-off.

2. *Extragalactic point-like sources* among which the most spectacular astrophysical objects are the Active Galactic Nuclei, AGN [157].

   Photons are emitted by synchrotron radiation and then boosted in energy by Compton scattering off energetic charged particles. A contribution of hadronic jets with neutral pions is conceivable, the relative contribution of hadrons and electrons is under debate. The observational characteristics and classification of AGN vary with the angle between the line of site and the jet axis. When the jet points toward Earth, the resulting violent object is called a blazar. Their photon emission rate is highly variable, while the spectral index stays constant [197].

3. *Diffuse γ sources* which consist of the diffuse galactic background [152] of several 10^{-8} photons per $\mathrm{cm}^2 \cdot \mathrm{sr} \cdot \mathrm{s} \cdot \mathrm{MeV}$ observed above 1 GeV and of the diffuse extragalactic background, three orders of magnitude weaker than the galactic one, but characterized by the same spectral index as the blazar signal [83].

8.6 Detected Photons from a Point-like Source

Here a source S defined by its galactic coordinates, (l, b), and its differential flux F expressed in photons$/(cm^2 \cdot s \cdot GeV)$, as a function of energy, is considered:

$$F(E) = \frac{d\Phi}{dE}(E) = \Phi_0 E^{-\alpha} \tag{8.20}$$

where α is the spectral index and Φ_0 is a constant. To estimate the number of photons registered by AMS from a given point in the sky, the amount of time when the point is visible by the detector must be known. This information is included in the exposure maps. Each map stores exposure time (t_I) for a given bin I of the incident angle $\psi = cos(\theta)$. The total exposure for a given location in the sky or a source (S) is the sum of the exposures for different incident angle bins (I):

$$T(S) = \Sigma_I t_I(S) \tag{8.21}$$

In the case of AMSFS, the effective area parametrization assumes that the effective area $A(E, \theta)$ can be factorized as follows [261]:

$$A(E, \theta) = \frac{A_1(E) A_2(\theta)}{A_1(E_0)} \tag{8.22}$$

where $A_1(E)$ is a function of the energy and $A_2(\theta)$ is a function of the incidence angle [262]. E_0 is a constant which depends on the detection mode:

- conversion mode $\rightarrow$ E_0 =32 GeV
- calorimetric mode $\rightarrow$ E_0 =50 GeV

In [262] a parametrization for A_1 is given as:

$$A_1(E) = p_1 \cdot \exp(-\frac{y + e^y}{2}) \tag{8.23}$$

where $y = (x - p_2)/p_3$, $x = \log_{10}(E)$ and E is measured in GeV.
Concerning A_2, it is a function of $\psi = \cos\theta$:

$$A_2(\psi) = \frac{q_1}{1 + \exp((\psi - q_2)/q_3)} \tag{8.24}$$

Parameters p_1, p_2, p_3, q_1, q_2, q_3 are obtained via a fit on the full Montecarlo simulation. Tab. 8.4 gives these parameters with respect to the two detection modes.

Parameter	Conversion Mode	Calorimetric Mode
p_1	0.098 ± 0.005	0.111 ± 0.003
p_2	1.39 ± 0.11	1.62 ± 0.04
p_3	0.82 ± 0.10	0.62 ± 0.05
q_1	0.041 ± 0.004	0.18 ± 0.04
q_2	-0.79 ± 0.02	-0.951 ± 0.001
q_3	0.057 ± 0.01	0.010 ± 0.003

Table 8.4: Fit parameter values entering in Eq.(8.23) and Eq.(8.24) for the Conversion and Calorimetric Mode respectively.

The general formula to compute the total number of photons from a source S detected by a detector with the effective area A is:

$$N_\gamma(S) = \Sigma[t_I(S) \int_E < A(E,\psi) >_I \cdot F(E)dE)] \tag{8.25}$$

where the average effective area is expressed as:

$$< A(E,\psi) >_I = \frac{1}{\Delta\Omega_I} \int_{\Omega_I} A(E,\psi)d\Omega \tag{8.26}$$

Using the relation:

$$d\Omega = 2\pi \cdot d\psi_I \tag{8.27}$$

the average effective area becomes:

$$< A(E,\psi) >_I = \frac{1}{2\pi\Delta\psi_I} \int_{\psi_I} A(E,\theta)2\pi d\psi = \frac{1}{\Delta\psi_I} \int_{\psi_I} A(E,\theta)d\psi \tag{8.28}$$

Source	1-2 GeV		2-5 GeV		5-20 GeV	
	(Tracker)	(ECAL)	(Tracker)	(ECAL)	(Tracker)	(ECAL)
0208-512	13.8 ± 2.7	0.8 ± 0.2	14.7 ± 3.5	3.2 ± 0.8	10.7 ± 3.1	5.5 ± 1.6
0528+134	9.0 ± 1.7	0.5 ± 0.1	6.7 ± 1.5	1.6 ± 0.4	3.0 ± 0.8	1.7 ± 0.5
Crab	40.2 ± 5.6	2.3 ± 0.3	36.6 ± 5.7	8.3 ± 1.3	21.7 ± 3.8	11.7 ± 2.1
Geminga	82.5 ± 13.8	5.0 ± 0.9	87.1 ± 17.3	20.5 ± 4.1	62.9 ± 15.2	34.9 ± 8.5
Vela	149.3 ± 25.1	11.9 ± 2.1	157.6 ± 31.4	49.0 ± 10.0	113.9 ± 27.6	83.3 ± 20.4
3C279	44.5 ± 7.7	2.6 ± 0.5	48.4 ± 9.8	11.0 ± 2.3	36.5 ± 9.0	19.4 ± 4.9
1406-076	13.6 ± 4.7	0.8 ± 0.3	11.5 ± 5.0	2.5 ± 1.1	6.1 ± 3.5	3.2 ± 1.9
1633+382	24.1 ± 7.2	1.5 ± 0.5	22.7 ± 8.3	5.5 ± 2.1	14.0 ± 6.6	8.0 ± 3.8

Source	20-50 GeV		>50 GeV	
	(Tracker)	(ECAL)	(Tracker)	(ECAL)
0208-512	2.4 ± 0.9	1.8 ± 0.6	1.4 ± 0.6	1.0 ± 0.5
0528+134	0.4 ± 0.1	0.3 ± 0.1	0.1 ± 0.04	0.1 ± 0.03
Crab	3.8 ± 0.8	2.9 ± 0.6	1.7 ± 0.4	1.3 ± 0.3
Geminga	14.0 ± 4.1	11.0 ± 3.2	7.7 ± 2.7	6.3 ± 2.2
Vela	25.3 ± 7.4	26.3 ± 7.7	14.0 ± 4.9	15.1 ± 5.2
3C279	8.5 ± 2.5	6.4 ± 1.9	5.0 ± 1.8	3.9 ± 1.4
1406-076	1.0 ± 0.7	0.7 ± 0.6	0.4 ± 0.3	0.3 ± 0.3
1633+382	2.6 ± 1.5	2.1 ± 1.3	1.2 ± 0.9	1.0 ± 0.8

Table 8.5: Number of expected photons, in function of their energy, integrated over one year of AMS-02 operation and for different EGRET sources. For Vela and Geminga, the spectral index 2.00 ± 0.05 has been assumed[256].

It is convenient to modify variables considering a logarithmic variability of the effective area in function of energy, ie. $x = log_{10}E$. Eq.(8.25) becomes:

$$N_\gamma(S) = \frac{1}{\Delta\psi_I}\Sigma_I[t_I(S)\int_x\int_{\psi_I} A(x,\psi)F(x)K(x)dxd\psi] \tag{8.29}$$

where:

$$K(x) = 10^x ln(10) \tag{8.30}$$

Eq.(8.29) gives the number of photons detected from a source S. This equation is implemented in the AMSFS code. A summary of the expected AMS-02 photon yields, as a function of the photon energy and for one year of operation, is given in Tab. 8.5 for selected point-like sources. The integrated yields above 1 GeV is also reported in Tab. 8.6.

8.6.1 Point-like Source Sensitivity

The point-like source sensitivity is defined as the minimum source flux required to achieve a specified level of detection significance. It is calculated as the ratio of the total number of detected γ from a source, N, with energy $\geq E_t$ and the number of

Source	N_γ (Tracker)	N_γ (ECAL)	N_γ (Total)
0208-512	43.0 ± 10.7	12.3 ± 3.6	55.3 ± 11.3
0528+134	19.1 ± 4.0	4.2 ± 1.0	23.3 ± 4.1
Crab	103.8 ± 16.1	26.4 ± 4.6	130.2 ± 16.8
Geminga	253.9 ± 52.9	77.5 ± 18.9	331.4 ± 56.2
Vela	459.3 ± 96.2	185.1 ± 45.3	644.4 ± 106.3
3C279	142.6 ± 30.6	43.2 ± 10.8	185.8 ± 32.4
1406-076	32.6 ± 14.1	7.5 ± 4.0	40.1 ± 14.7
1633+382	64.4 ± 24.4	18.1 ± 8.3	82.5 ± 25.7

Table 8.6: Number of expected photons above 1 GeV integrated over one year of AMS-02 operation and for different EGRET sources. For Vela and Geminga, the spectral index 2.00 ± 0.05 has been assumed [256].

background photons , B, within the source direction with an energy $\geq E_t$:

$$S(\geq E_t) \sim \frac{N(\geq E_t)}{\sqrt{B(\geq E_t)}} \tag{8.31}$$

The numerator and denominator can be expressed as:

$$N(\geq E_t) = \int_{E_t}^{E_{max}} \frac{dN}{dE} \cdot A(E) \cdot t \; dE \tag{8.32}$$

$$B(\geq E_t) = \int_{E_t}^{E_{max}} \frac{dB}{dE} \cdot A(E) \cdot \Delta\Omega(E) \cdot t \; dE \tag{8.33}$$

where t is the viewing time, dN/dE and dB/dE are the differential source and background spectra, respectively, and the angular resolution is expressed as a solid angle $\Delta\Omega(E) = \pi\sigma_{68}^2(E)$. $A(E)$ is the effective detection area, where $\sigma_{68}(E)$ is the angular resolution quoted in Eq. 8.2.

8.6.2 Photons from Diffuse Gamma Background

The estimation of AMS sensitivity to the diffuse gamma ray background is based on results from EGRET on Compton Gamma Ray Observatory (CGRO) satellite. The background has two components: galactic and extragalactic. Their fluxes are shown in Fig. 8.15.

Diffuse Galactic Background

The galactic diffuse background is predominantly produced by the gas clouds of our galaxy. It is important especially when the central zones of the galaxy are observed. The Galactic diffuse background is highly anisotropic. The EGRET measurements

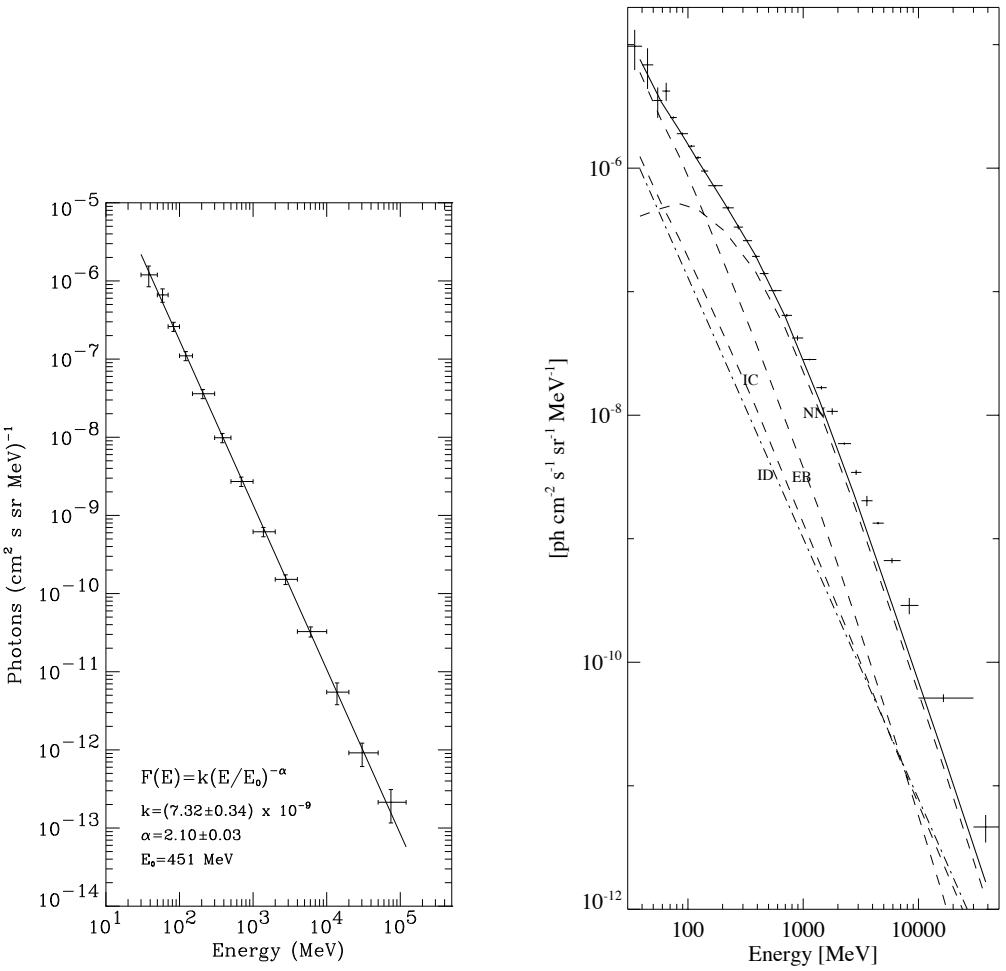

Figure 8.15: Flux of diffuse background as a function of energy: extragalactic (left) and galactic (right).

Source	$B_\gamma^{GAL\ EGRET}$ (Tracker)	$B_\gamma^{GAL\ EGRET}$ (ECAL)	$B_\gamma^{GAL\ EGRET}$ (Total)
Crab	22.3	0.4	22.7
Geminga	42.8	0.4	43.2
Vela	39.6	0.4	40.0

Table 8.7: Number of expected photons above 1 GeV from galactic diffuse background integrated over one year of AMS-02 operation.[256].

are presented in form of maps of sky with binning $l \times b = 10^o \times 4^o$. The maps cover only the part of the sky which contains the Galaxy, so the values of Galactic diffuse gamma background for $|b| > 10^o$ are neglected. Each bin of the map contains a value of the flux measured in a given energy range. Energy bins are defined by the following boundary values (in GeV): 0.03, 0.05, 0.07, 0.1, 0.15, 0.3, 0.5, 1, 2, 4, 10 and 30. AMS is sensitive to photons with energies above 1 GeV, so only the last 4 maps are taken into account. They contain fluxes in the energy bins (J): 1 to 2 GeV, 2 to 4 GeV, 4 to 10 GeV and 10 to 30 GeV.
To estimate the numbers of Galactic background photons detected from a given point of the sky the following formula is used:

$$N_\gamma(B_{gal}) = \Sigma_J \Sigma_I [t_I \int_{E_I} < A(E,\psi) >_I \cdot F(E_J) \cdot \Omega(E) dE] \tag{8.34}$$

where J is EGRET energy bin, $F(E_J)$ is the value of the flux read from a map which corresponds to energy bin J. The numerical value is:

$$N_\gamma(B_{gal}) = \frac{1}{\Delta\psi_I} \Sigma_J \Sigma_I [t_I \int_{x_I} \int_{\psi_I} A(E,\psi) \cdot F(x_J) \cdot \Omega(x) dx d\psi] \tag{8.35}$$

In Tab 8.7 the expected number of photons in one year of AMS-02 operation above 1 GeV from galactic diffuse background is given in regions around selected point-like sources.

Diffuse Extragalactic Background

The extragalactic component of the diffuse gamma ray background is isotropic. The flux of this background is parametrized in the following way [152]:

$$F(E) = k(\frac{E}{E_0})^{-\alpha} \qquad (cm^{-2} \cdot s^{-1} \cdot sr^{-1} \cdot GeV^{-1}) \tag{8.36}$$

where $k = 7.3210^{-6}$ $(cm^{-2} \cdot s^{-1} \cdot sr^{-1} \cdot GeV^{-1})$, $E_0 = 0.451$ GeV and the spectral index $\alpha = 2.1$.
To estimate the number of detected photons a formalism similar to the case of sources is used, but the detector angular resolution is added.

In the case of a diffuse source, it is important to take into account the detector

angular resolution. In AMSFS, the angular resolution at 68% confidence level is parametrized as follow:

$$\sigma_{68}(E) = \pi(\frac{\pi}{180})^2[a^2 + (\frac{b}{E})^2] \tag{8.37}$$

where a=0.9 and b=8.5 for calorimetric mode and a=0.015 and b=1.17 for conversion mode.

As the acceptance is usually known for the whole field of view, a scaling factor δ from $Acc(E)_{FOV}$ to $Acc(E)$ has to be introduced where the δ factor is the average differential acceptance:

$$N^p = T \int_{E_0}^{\infty} Acc(E)_{FOV} \cdot \delta \cdot \Phi(E) dE \tag{8.38}$$

The acceptance of protons mistaken as photons is usually known only as a lower limit of its ratio to photon acceptance. That is, this proton acceptance is usually expressed as the ratio of the gamma acceptance and the rejection factor R:

$$N^p = T \cdot \int_{E^0}^{\infty} Acc(E)^{\gamma}_{FOV} \cdot (1/R) \cdot \delta \cdot \Phi(E) dE \tag{8.39}$$

A lower limit for R has been found through Monte Carlo studies at the level of $2 \cdot 10^6$ and of $2 \cdot 10^4$ for the ECAL and Tracker entire range respectively. Note that these are lower bounds, limited by the statistics of these studies.

In conclusion, the number of background photons registered by a detector observing a defined point of the sky (source) is given by:

$$N_{\gamma}(B_{ex}) = \Sigma_I [t_I \int_E < A(E, \psi) >_I \cdot F(E) \cdot \sigma_{68}(E) dE]. \tag{8.40}$$

Following the same procedure as in case of sources for numerical calculation one uses:

$$N_{\gamma}(B_{ex}) = \frac{1}{\Delta\psi_I} \Sigma [t_I \int_x \int_{\psi_I} A(x, \psi) F(x) K(x) \sigma_{68}(x) dx d\psi] \tag{8.41}$$

This estimations give, for ECAL, 1 photon per year from diffuse extragalactic background and 18 photons per year from galactic background, all from the Galactic Center.

In Tab 8.8 the expected number of photons in one year of AMS-02 operation above 1 GeV from extragalactic diffuse background is given in regions around selected point-like sources.

Source	$B_\gamma^{EG\ EGRET}$ (Tracker)	$B_\gamma^{EG\ EGRET}$ (ECAL)	$B_\gamma^{EG\ EGRET}$ (Total)
0208-512	3.6	0.4	4.0
0528+134	5.6	0.4	6.0
Crab	5.6	0.4	6.0
Geminga	5.6	0.4	6.0
Vela	5.6	0.4	6.0
3C279	5.2	0.4	5.6
1406-076	5.2	0.4	5.6
1633+382	7.2	0.4	7.6

Table 8.8: Number of expected photons above 1 GeV from extragalactic diffuse background integrated over one year of AMS-02 operation.[256].

8.6.3 Proton Background

The number of protons detected as gamma photons for a solid angle Ω_0, an exposure time T, above a threshold energy of E_0, considering an exposure surface S is:

$$N^p = \int_T \int_{E_0}^{\infty} \int_{\Omega_0} \int_S \Phi(E)\varepsilon^p(E,\Omega,S)\vec{u}d\vec{S}d\Omega dE dt \tag{8.42}$$

where $\Phi(E)$ is the proton spectrum in $m^{-2}s^{-1}sr^{-1}GeV^{-1}$ assuming isotropy for the background; $\varepsilon^p(E,\Omega,S)$ is the detection efficiency for each energy, direction and surface element. The previous equation may be rewritten as:

$$N^p = T \cdot \int_{E_o}^{\infty} Acc(E) \cdot \Phi(E) dE \tag{8.43}$$

where $Acc(E) = \int_{\Omega_o} \int_S \varepsilon^p(E,\Omega,S)\vec{u}d\vec{S}d\Omega$ is called the acceptance at energy E and is measured in $m^2 sr$.

8.7 Upgrades to AMSFS

The AMSFS package, described in the previous paragraphs, did not have the possibility to select a specific position in the sky, i.e. a source location, in order to fold into the visibility maps the possible time dependences of a variable source. To do that, some modification to the original software were needed.

The goal is to estimate the AMS-02 sensitivity to detect any pulsed signal coming from a fixed point of the sky and observed inside the detector field of view. To accomplish these tasks, a new C++ algorithm has been developed and the steps followed to produce the final histograms are described.

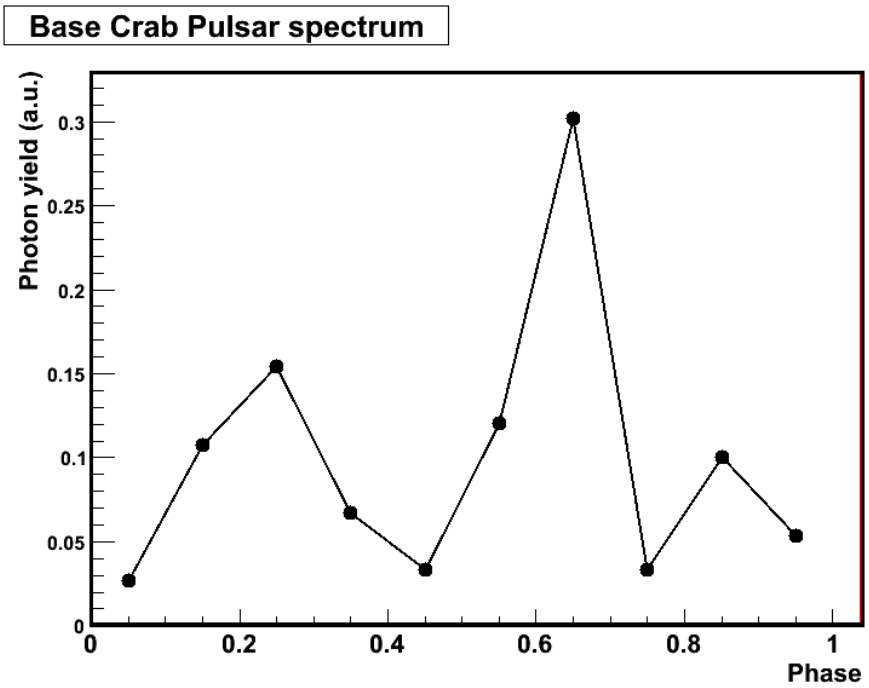

Figure 8.16: Time spectrum of the simulated Crab pulsar [263]. The time is normalized to the period.

The algorithm works using as inputs the total number of photons (from sources and backgrounds) with respect to a given observation period, estimated using the original AMSFS Package. A dedicated software module simulates, inside a visibility period of a point of the sky (source), a *pulsed signal* coming from it with a predefined period.
The arrival time of a photon from the source is generated following a defined time spectrum which is given as an input to the module. This procedure is repeated for all visibility periods. The goal of this study is two-fold:

- derive the sensitivity of AMS-02 to pulsed sources;
- enhance this sensitivity exploiting the periodic behaviour via time folding techniques.

As an example, the Crab pulsar, with a typical period of 30 ms is considered here. The time spectrum of this pulsar has been parametrized according to the findings in Ref. [263] and it is shown in Fig. 8.16. The time range has been normalized to its period (phase).

The number of expected signal photons in the visibility periods of the source, as calculated by AMSFS, is 130.2 with an average expected background of 28.7 (Tabs. 8.6,8.7,8.8).

To study the sensistivity of AMS to such a signal, several simulations have been performed varying the number of expected signal photons and keeping the background constant. The time folded distributions, shown in Fig. 8.17, are then

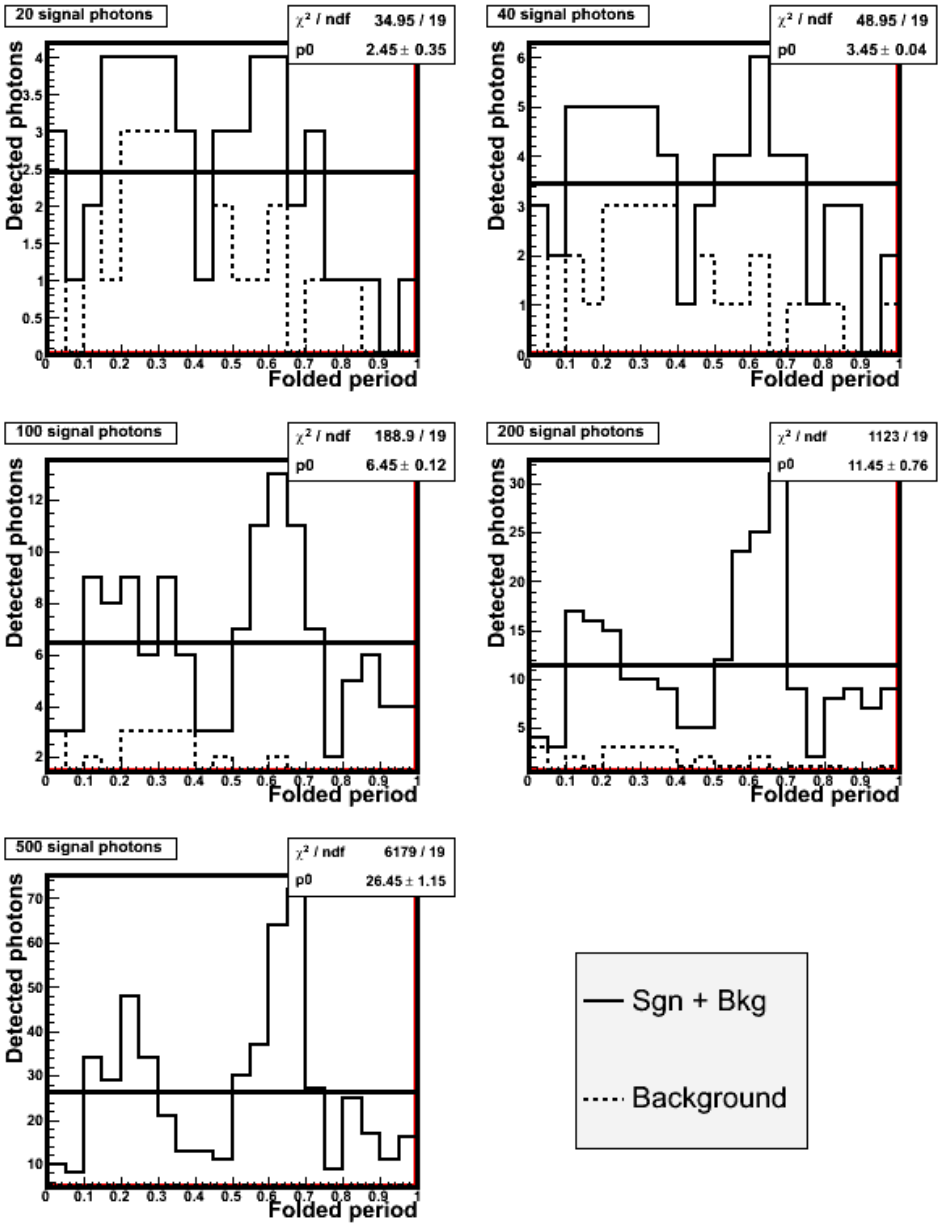

Figure 8.17: Photon yields as function of the folded arrival time. Both signal photons (varying from top-left to bottom-right) and a constant background are considered.

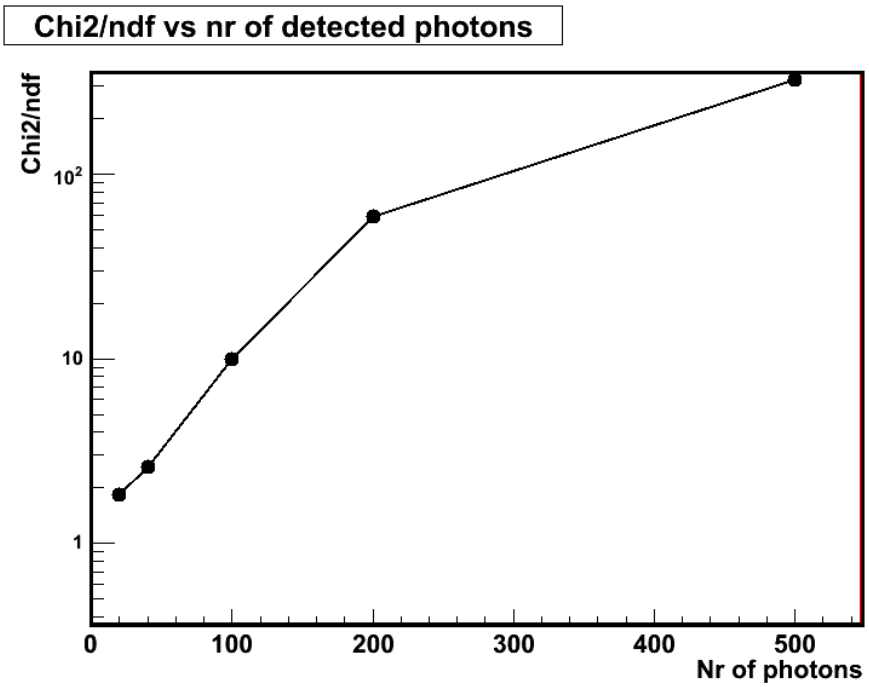

Figure 8.18: χ^2/degree of freedom from a "flat" hypothesis fit to the folded time spectrum of photons. The χ^2 is evaluated as a function of the number of signal photons.

fitted assuming only a flat background hypothesis. The corresponding χ^2/degree-of-freedom is then plotted in Fig. 8.18 as a function of the number of signal photons.

Clearly the folding technique enhances the signal/noise ratio for sources of known periods, given the flat time structure of the expected background. The capability of discriminating a pulsed signal in AMS-02 is verified with the "flat" background hypothesis. Large values of χ^2, indicating a non-flat photon yield, are obtained already with low number of photons as expected by a typical pulsar signal.

Conclusions

The present thesis find its place in the framework of a recent new branch of physics born from the fusion of particle physics and astrophysics and referred to as astroparticle physics.

During the last five years, I had the chance to work to the construction of the Silicon Tracker detector of the AMS-02 experiment and to perform analyses both on simulated and test beam data concerning the tracker and the whole experiment performance.

This thesis can be seen as the merging of three specific subjects:

1) the construction of the AMS-02 tracker detector through the clean room work on silicon ladders;

2) the test beam data analysis to test the performance of a "minitracker" in detecting converted photons and providing also the measurement of the momentum resolution and the validation of previous measurements on spatial resolution.

3) the computation of the exposure maps, with their usage inside a photon fast simulator program, and the AMS-02 sensitivy to detect gamma-ray sources, in particular pulsars.

All of these items contribute to an unique study: the AMS-02 capability to detect gamma-ray photons.

The AMS-02 experiment, conceived for the detection and the caracterisation of the cosmic radiation will have also good performances to detect photons in a range of energy from 1 GeV up to 1 TeV. This goal will be achieved by the the usage of two detectors: the silicon tracker, hosted in a magnetic field of 0.8 T provided by a superconductive magnet, and the electromagnetic calorimeter.

The silicon tracker ladder assembling and testing was performed at University of Geneva clean room. This job took into account both the mechanical and the electrical validation of modules and a extensive R&D activity was also needed in order to solve different problems arised during the production.
The test beam, which constitutes the second part of the work inside this thesis, was quite different from the previous ones because:

- it was the first time that silicon ladders were exposed to a beam of electrons;
- it was the first attempt to measure the "tracker" momentum resolution and its performance to converted photon detection;
- it was the first time that silicon ladders were mechanically arranged in order to reproduce the AMS-02 silicon tracker detector mechanical structure;
- it was the first time that part of the DAQ electronics was tested in realistic conditions.

All these aspects required a big effort of Geneva group and in particular the realization of two preliminary tests:

- the mapping of the magnetic field of the magnet to be used during the test beam. The collected data, measured by a 3D Hall probe, were taken for two different magnetic field intensities: 0.4 and 0.8 T. The measurement precision is 0.5 mm on the position and of the order of 10^{-3} mV on the voltage.
- the test of the two Čerenkov detectors to be used during the official test beam.

Concerning results obtained from the 2004 test beam, it can be concluded that even if AMS-02 was basically designed to detect cosmic charged particles, it shows good performance also in detecting photons above 1 GeV energy. Some of the performance predicted by the official simulation have been confirmed by this test using improved reconstruction and track fitting algorithm.

The obtained photon energy and angular resolutions in the energy range from 3 to 7 GeV, $\sigma_E/E \sim 0.015$ and $\sigma_\theta < 1^\circ$ respectively, are in good agreement with predictions. Results from previous test beams on silicon ladder spatial intrinsic resolution have been confirmed to be 10 μm and 30 μm respectively for p and n-type sensors.
The charged track momentum resolution of the order of 1.7% at 5 GeV, measured here for the first time, also confirmed predictions obtained using a different fit method for the track-finding algorithm.
The third part of the thesis was devoted to the estimation of AMS-02 sensitivity to the gamma-ray signals from point sources. This study started with production of the exposure maps for both the tracker and the electromagnetic calorimeter taking into account their effective area and the presence of the South Atlantic Anomaly. The usage of such maps, as inputs to a fast simulator, allows the predictions of photon yields for various types of gamma sources. A specific simulation verified the capability of AMS-02 to detect a pulsed signal as expected from pulsars.

Acknowledgements

Getting my PhD in Physics, a chapter of my life has been closed. I'm left with joy for this result but also a huge list of persons I should thank.

My PhD supervisor, Prof. Martin Pohl, who gave me the chance to reach this goal. He was not affected by my non standard career in Physics and helped me to join the Department of Physics at University of Geneva. He was always confident in my capabilities giving me the charge of many sensitive projects. Our discussions, sometimes so warm, were always led by the common aim to find the best solution of the problem.

The AMS Group at University of Geneva who helped me improving my scientific knowledges and not only.

Thanks to my *Maître* Philipp Azzarello, to Manfred Willenbrock and Philippe Bouvier. They were very patient to teach me silicon ladders and clean room "secrets". We spent nice days also discussing of trekking, sailing and French language grammar.

Thanks to Peggy Argentin, Catherine Blanchard, Pierre Béné, Florian Masciocchi, Yann Meunier and Jean-Pierre Richeux for their kindness and constant availability.

Thanks to all my collegues and friends for the nice time we spent together.

A very special thank to Silvia Borghi.

Last but not the least my Family.

Thanks to my parents who made me as I am.
Thanks to my father from whom I learnt to be realistic. Thanks to my mother from whom I learnt to be inspired and to think that sometime dreams can become reality. Thanks to my sister: a hidden but always constant supporter of my goals.

Thanks to my husband: my dear Luca, thanks to be unconditionally present in any moment of my life.

To my daughter Nora: the brightest light of my existence.

And now, what will happen?
For sure I will not give up.

I will face any future opportunity with the same enthusiasm and willness which brought me here because *lo spirto guerrier ch'entro mi rugge* is still alive!

Bibliography

[1] E. Hubble (1929), Proc. Nat. Acad.(15):168.

[2] A. A. Penzias and R. W. Wilson (1965), Astrophys. Journal(142): 419

[3] G. Gamow (1946), Phys. Rev.(70):572.

[4] G. Gamow (1948), Phys. Rev.(74):505.

[5] D. E. Groom et al. (2000), Eur. Phys. Journal C (15):1.

[6] T. K. Gaisser (1990), *Cosmic Rays and Particle Physics*.

[7] V. F. Hess (1912), Phys.Z(13):1084.

[8] W. Kohlhörster (1923), Phys.Z(14):1153.

[9] W. Bothe and W. Kohlhörster (1929), Phys.Z(56):571.

[10] C. D. Anderson (1933), Phys. Rev.(43):491.

[11] J. A. Simpson (1983), Ann. Rev. Nucl. Part. Sci.(33):323-81.

[12] R. A. Mewaldt (1983), Rev. Geophys. Space. Phys.(21):295-305.

[13] V. S. Ptuskin, H. J. Völk et al. (1997), Astrophys(321):434.

[14] S. Eidelman et al. (2004), Phys. Lett. B(592):1.

[15] Picture produced by S. Swordy, University of Chicago.

[16] A. D. Erlikin and A. W. Wolfendale (2001), J. Phys. G.(27):1005.

[17] E. Fermi (1959), Phys. Rev.(75):1169.

[18] R. Blandford and D. Eichler (1987), Phys. Rep.(154):1.

[19] R. Schlickeiser (2002), *Cosmic Rays Astrophysics*.

[20] M. G. Baring(1999), astro-ph./9912058v2.

[21] D. J. Bird (1993), Phys. Rev. Lett.(84):4276.

[22] M. Boezio (2005), *The* PAMELA *Space Experiment*, 29th International Cosmic Ray Conference, Pune, India.

[23] P. Maestro (2003), *Indirect search for dark matter by measurements of the cosmic ray positron spectrum with the AMS-02 experiment*. PhD Thesis, Universita' di Siena.

[24] R. Dawson, R. Meyhandan et al. (1998), Astroparticle Physics(9):331.

[25] V. L. Ginzburg, V. S. Berezinskii et al. (1990), Astrophysics of cosmic rays, Elsevier, Amsterdam.

[26] R. L. Golden, G. D. Badhwar et al. (1978), Nucl. Instr. and Meth.(148):179.

[27] Freely available data from the Swarthmore/Newark Neutron monitor, Univ. of Delaware.

[28] M. S. Longair (1997), High Energy Astrophysics, Cambridge University Press.

[29] A. Riotto and M. Trodden (1999), Ann. Rev. Nucl. Part. Sci.(49):35-75.

[30] E. A. Bogomolov, N. D. Lubyanaya et al. (1987), POCR 1, (72).

[31] L. C. Tan and L. K. Ng (1983), J. Phys. G: Nucl. Phys.(9):1289.

[32] V. F. Kuzichev et al. (1994), Nucl. Phys. Proc. Suppl.A(576):581.

[33] G. Batko et al. (1991), Phys. Lett.B(256):331.

[34] M. Simon et al. (1998), Astrophys. Journal(325):16.

[35] P. Kiraly et al. (1981), Nature(293):120.

[36] M. Turner (1982), Nature(297):379.

[37] K. Maki et al. (1996), Phys. Rev. Lett.(76):344.

[38] S. Rudaz and F. Stecker (1988), Astrophys. Journal(325):16.

[39] A. Bottino et al. (1998), Phys. Rev.D(58):123503.

[40] L. Bergström et al. (1999), Phys. Rev.D(59):43506.

[41] L. Bergström et al. (1999), Astrophys. Journal(526):215.

[42] M. Boezio et al. (1999), Astrophys. Journal(518):457.

[43] P. Ullio (1999), astro-ph./9904086.

[44] L. Bergström and A. Goobar (1999), *Cosmology and Particle Astrophysics*, Wiley.

[45] R. J. Protheroe (1982), Astrophys. Journal(254):391.

[46] I. V. Moskalenko and A. W. Strong (1998), Astrophys. Journal(493):694.

[47] S. A. Stephens and R. E. Streitmatter (1998), Astrophys. Journal(505):266.

[48] E. A. Baltz and J. Edsjö (1999), Phys. Rev.D(59):023511.

[49] S. W. Barwick et al. (1998), Astrophys. Journal(498):779.

[50] D. Muller and K. K. Tang (1990), 21st International Cosmic Ray Conference, Adelaide, Australia.

[51] K. A. Olive (2003), astro-ph/0301505.

[52] C. Alcock et al. (1997), Astrophys. Journal(491):L11.

[53] C. Renault et al. (1996), astro-ph/9612102.

[54] A. Udalski (1998), Acta Astron.(48):113.

[55] C. Alcock et al. (2000), Astrophys. Journal(542):281-307.

[56] B. J. Carr (2002), *Primordial Black Holes* Conference on Future Theoretical Physics and Cosmology, Cambridge - England.

[57] S. Fukuda et al. (2000), Phys. Rev. Lett.(85):3999-4003.

[58] Q. R. Ahmad et al. (2001), Phys. Rev. Lett.(87):071301.

[59] 2dFRGS experiment: `http://www.mso.anu.edu.au/2dFGRS/`.

[60] WMAP experiment: `http://map.gsfc.nasa.gov/m_mm.html`.

[61] D. N. Spergel et al. (2003), Astrophys. Journal. Suppl.(148):175.

[62] A. Pierce and Hitoshi Murayama (2003), hep-ph/0302131.

[63] R. D. Peccei and H. R. Quinn (1977), Phys. Rev. Lett.(38):1440-1443.

[64] C. Hagmann et al. (1998), Phys. Rev. Lett.(80):2043-2046.

[65] S. Asztalos et al. (2001), Phys. Rev.D(64):092003.

[66] I. Ogawa, S. Matsuki and K. Yamamoto (1996), Phys. Rev.D(53):1740-1744.

[67] K. Yamamoto et al. (2000), hep-ph/0101200.

[68] E. W. Kolb and M. S. Turner (1990), *The Early Universe*, Addison Wesley.

[69] K. A. Olive (1999), hep-ph/9911307.

[70] J. R. Ellis, J. S. Hagelin, D. V. Nanopoulos, K. A. Olive and M. Srednicki (1984), Nucl. Phys.B(238):453-476.

[71] T. K. Hemmick et al. (1990), Phys. Rev.D(41):2074-2080.

[72] A. Bottino, F. Donato, N. Fornengo and S. Scopel (2002), Nucl. Phys.B(Proc. Suppl.)(113):50-59.

[73] B. Moore et al. (1999), astro-ph/9907411.

[74] P. Belli et al. (2000), Phys. Rev.D(61):023512.

[75] A. Morales (2003), Nucl. Phys. Proc. Suppl.(114):39-57.

[76] EDELWEISS experiment: `http://edelweiss.in2p3.fr`.

[77] DAMA experiment: `http://people.roma2.infn.it/dama/web/hom.html`.

[78] R. bernabei et al. (2003), Riv. Nuovo Cim.(26N1):1-73.

[79] J. Silk, K. A. Olive and M. Srednicki(1985), Phys. Rev. Lett.(55):257-259.

[80] S. Desai et al. (2004), hep-ex/0404025.

[81] L. Bergström (2000), Rept. Prog. Phys.63(5):793.

[82] L. Bergström, J. Edsjö and P. Ullio (2001), Phys. Rev. Lett.(87):251301.

[83] P. Sreekumar et al. (1998), Astrophys. Journal(494):523-534.

[84] G. L. Godfrey. (1993), *Gamma Large Area Silicon Telescope (GLAST)*, Presented at 2nd Workshop: Towards a Major Atmospheric Cerenkov Detector, Calgary, Canada.

[85] R. A. Ong et al. (2003), astro-ph/0302610v1.

[86] F. Donato, N. Fornengo and P. Salati (2000), Phys. Rev.D(62):043003.

[87] M. S. Longair (2001), *Introduction to high energy astrophysics*, Prepared for Interna- tional School of Space Science, L'Aquila, Italy.

[88] G. Hartmann, D. Mueller and T. Prince (1977), Phys. Rev. Lett.(38):1368-1372.

[89] J. Nishimura et al. (1980), Astrophys. Journal(238):394-409.

[90] K. K. Tang (1984), Astrophys. Journal(278):881-892.

[91] H. Wilczynski et al. (1999), ICRC, Salt Lake City, Utah.

[92] M. Boezio et al. (2000), Astrophys. Journal(532):635-666699.

[93] R. L. Golden et al. (1996), Astrophys. Journal(457):L103-L107.

[94] M. A. DuVernois et al. (2001), Astrophys. Journal(559):296-303.

[95] S. W. Barwick et al. (1997), Astrophys. Journal(482):L191-L194.

[96] S. Profumo and P. Ullio (2004), JCAP,0407:006.

[97] C. Grimani et al. (2002), Astron. & Astroph.(392):287-294.

[98] R. L. Golden et al. (1979), Phys. Rev. Lett.(43):1196-1199.

[99] A. Buffington and S. M. Schindler (1981), Astrophys. Journal(247):L105-L109.

[100] A. Buffington, S. M. Schindler and C. R. Pennypacker (1981), Astrophys. Journal(248):1179-1193.

[101] M. H. Salamon et al. (1990), Astrophys. Journal(349):78-90.

[102] S. P. Ahlen et al. (1988), Phys. Rev. Lett.(61):145-148.

[103] R. E. Streitmatter et al. (1989), AdSR(9):65-69.

[104] F.Donato et al. (2001), Astrophys. Journal(563-1):172-184.

[105] T. Sanuki et al. (2000), Astrophys. Journal(545):1135.

[106] Y. Asaoka et al. (2002), Phys. Rev. Lett.(88):051101.

[107] S. Orito et al. (2000) Phys. Rev. Lett.(84):1078-1081.

[108] S. A. Stephens (1981), Astrophys. and Space Sci.(76-1):87-103.

[109] F. Taccetti et al. (1999), *The PAMELA silicon tracker*, Nuovo Cim.(A112):153-158.

[110] R. Battiston (1998), *The alpha magnetic spectrometer for the search for dark matter and antimatter in space and its first flight on the shuttle.*, Prepared for 2nd In- ternational Conference on Dark Matter in Astro and Particle Physics (DARK98), Heidelberg, Germany.

[111] K. Yoshimura et al. (1995), Phys. Rev. Lett.(75):3792-3795.

[112] M. Boezio et al. (1997), Astrophys. Journal(487):415-423.

[113] M. Boezio et al. (2001), Astrophys. Journal(561):787-799.

[114] F. Donato, N. Fornengo, D. Maurin and P. Salati (2004), Phys. Rev.D(69):063501.

[115] M. Aguilar et al. (2002), Phys. Rept.(366):331-405.

[116] T. Sjostrand (1995), Pythia 5.7 and JETSET 7.4: Physics and manual.

[117] P. Ruiz-Lapuente, A. Burkert and R. Canal (1995), Astrophys. Journal(447):L69.

[118] Galprop numerical package. http://www.mpe.mpg.de/ aws/propagate.html.

[119] L. J. Gleeson and W. I. Axford (1967), Astrophys. Journal(149):L115.

[120] C. E. Fichtel, D. A. Kniffen, H. B. Ögelman (1969),Astrophys. Journal(158):193.

[121] http://cossc.gsfc.nasa.gov/docs/cgro/cgro .

[122] T. H. Burnett et al. (1990) Astrophys. Journal(349):25.

[123] D. J. Thompson, M. Bailes, D. L. Bertsch et al. (1999), Astrophys. Journal(516):297.

[124] W. Hofmann (1997), Proc. of the Workshop *Towards a major atmospheric Cherenkov detector - V*, Kruger Park, O.C. de Jager (Ed.).

[125] A.Moralejo et al. (2004), Memorie della Societa Astronomica Italiana(75):232.

[126] M. Amenomori et al. (1994), Astrophys. Journal(429-2):634-637.

[127] R. Atkins (1999), astro-ph/9906417v1.

[128] Kraushaar and Clark (1962), Phy.s Rev. Lett.(8-3):106.

[129] W. L. Kraushaar, G. W. Clark, G. P. Garmire, H. Helmken et al (1965), Astrophys. Journal(357):638.

[130] Peterson et al. (1966), Phys. Rev. Lett.(16): 142.

[131] W. L. Kraushaar, G. W. Clark, G. P. Garmire et al (1972), Astrophys. Journal(177):341.

[132] C. R. Axtell, R. M. Potter ,(1965), DTIC, AD0483114.

[133] M. Casse, C. Cesarsky J. Paul (1977), La Recherche(8):112-121.

[134] K. Bennett (1990), Nucl. Phys. B (Proc. Suppl) (14B):23-34.

[135] M. Salvati (1983), Space Science Reviews, Springer.

[136] B. N. Swanenburget al. (1981), Astrophys. Journal(243):L69-L73.

[137] http://cossc.gsfc.nasa.gov/docs/cgro/osse/

[138] http://cossc.gsfc.nasa.gov/docs/cgro/batse/

[139] http://cossc.gsfc.nasa.gov/docs/cgro/comptel/

[140] http://cossc.gsfc.nasa.gov/docs/cgro/egret/

[141] D. J. Thompson et al. (1993), Astrophys. JournalS(86):629.

[142] R. C. Hartman et al. (1999), Astrophys. Journal Suppl.(123):79-202.

[143] D. Aitoff (1889), *Projections des cartes gographiques* In Atlas de Geographie Moderne, Paris, Hachette.

[144] R. C. Hartman, et al. (1999), Astrophys. Journal(123):203.

[145] R. C. Hartman et al. (2001), Astrophys. Journal(553):683.

[146] K. Hurley et al. (1994), Nature(372):652.

[147] D. J. Thompson (2001), Proc. of AIP Conf.(558):103.

[148] P. A. Caraveo, G. F. Bignami and J. Trümper (1996), A&A(7):209.

[149] P. Sreekumar et al. (1992), Astrophys. Journal(400):L67.

[150] P. Sreekumar et al. (1997), Astrophys. Journal(481):205.

[151] A. W. Strong, J. R. Mattox (1996), A&A(308):21.

[152] S. D. Hunter et al. (1997), Astrophys. Journal(481):205.

[153] M. Pohl and J. A. Esposito (1998), Astrophys. Journal(507):327.

[154] M. H. Salamon, and F. W. Stecker (1996), Astrophys. Journal(464):600.

[155] B. N. Swanenburg et al. (1978), Nature(275):298.

[156] J. Mattox, S. J. Wagner, M. Malkan et al. (1997), Astrophys. Journal(476):842.

[157] C. M. Urry and P. Padovani (1995), PASP(107):803.

[158] I. Robson (1997), *Active Galactic Nuclei*, ChiChester, Wiley.

[159] B.M. Peterson (1997), *An introduction to active galactic nuclei*, Cambridge Uni- versity Press.

[160] L. Woltier (1990), *Physical Processes in Active Galactic Nuclei*, In T. L. Courvoisier and M. Mayor eds., *Active Galactic Nuclei*, Saas-Fee Advanced Course 20. Springer-Verlag, Les Diablerets.

[161] V. Schönfelder (2002), *The history of gamma-ray astronomy*, Wiley Inter-Science.

[162] D. J. Thompson (1997), *Neutron Stars and Pulsars*, Tokyo: Univ. Acad. Press, 273.

[163] J. K. Daugherty and A. K. Harding (1996), Astrophys. Journal(458):278.

[164] R. W. Romani and I. A. Yadigaroglu (1995), Astrophys. Journal(438):314.

[165] G. H. Share (1976), Astrophys. and Space Sci.(42):29-33.

[166] L. Scarsi (1984), Proceedings of the COSPAR/IAU Symposium - Rojen, Bulgaria.

[167] E. Costa et al. (1997), Nature(387):876.

[168] P. A. Mazzali et al. (2003), Astrophys. Journal(599):95.

[169] T. Piran (1999), Phys. Rep.(314):575-667.

[170] G. Ghisellini (2001), Proc. of trso.conference, *A Relativistic Spacetime Odissey*, 381.

[171] P. Mészáros (2002), Annu. Rev. A&A(40):137.

[172] K. Belczynski, T. Bulik and B. Rudak (2002), Astrophys. Journal(571):394.

[173] K. Weiler and R. Sramek (1988), Ann Rev. Astron. Astrophys.(26):295-341.

[174] R. A. Chevalier (1977), Ann. Rev. Astron. Astrophys.(15):175-96.

[175] T. W. Jones et al. (1998), PASP(110):125.

[176] J.R. Mattox et al. (1997), Astrophys. Journal(481):95.

[177] N. Gehrels, D. J. Macomb, D. L. Bertsch, D. J. Thompson, R. C. Hartman (2000), Nature(404):363.

[178] P.A. Caraveo (2002), XXXVIIth Recontres de Moriond, Les Arcs, Savie, France.

[179] M. Aguilar et al. (2002), Phys. Rep.(366-6):331.

[180] Particle Data Group . Rev. of Particle Properties. Eur. Phys. J. C 3. (1988) 1.

[181] I. Frank, V. Ginzburg (1945), J. Phys. (9):353.

[182] T. Kirn and Th. Siedenburg (2004), Nucl. Instr. and Meth. A(535):165-170.

[183] D. Alvisi et al.(1999), Nucl. Instrum. and Meth. A(437):212.

[184] B. Blau et al. (2002), Nucl. Phys. Proc. Suppl.(113):125-132.

[185] W. J. Burger (2002), Nucl. Phys. Proc. Suppl.(113):139-146.

[186] J. Vandenhirtz, Ein Infrarot Laser Positions-Kontroll-System fr das AMS Experiment, 2001, PhD thesis - RWTH-Aachen.

[187] W.J. Burger etal., Nucl. Instr. and Meth. A 512 (2003) 517.

[188] J. Vandenhirtz et al., Proc. 27th International Cosmic Ray Conference (ICRC2001), D-Hamburg, session OG, 5(2001) 2197.

[189] W. Wallraff et al., Proc 7th International Conference on Advanced Technology and Particle Physics (ICATPP-7), I-Villa Olmo Como, M. Barone et al. (Eds.), World Scientific, Singapore, ISBN 981-238-180-5, (2002) 149.

[190] V. Vetterle, Silizium Alignment Sensoren fr den AMS-02 Tracker auf der ISS, 2001, Diplomarbeit, RWTH-Aachen.

[191] J. Casaus (2002), Nucl. Phys. Proc. Suppl.(113):147-153.

[192] P. Aguayo et al. (2004), Instr. and Meas. Tech. Conference, IMTC 04. Proceedings of the 21st IEEE (2):1135- 1139.

[193] J. Alcaraz et al. (2000), Phys. Lett.B(472):215.

[194] J. Alcaraz et al. (2000), Phys. Lett.B(494):193.

[195] J. Alcaraz et al. (2000), Phys. Lett.B(484):10.

[196] J. Alcaraz et al. (2000), Phys. Lett.B(495):440.

[197] R. Mukherjiee et al. (1997), Astrphys. Journal(490):116,135.

[198] R. Battiston et al. (2000), Astropart. Phys.(13):51-74.

[199] G. Lamanna et al. (2002), Nucl. Phys. Proc. Suppl.(113):177-185.

[200] J.G. Asbury et al.(1967), Phys. Rev. Lett.(18-2):65.

[201] J.G. Asbury et al. (1967), Phys. Rev. Lett.(19-15):869.

[202] U. Becker et al. (1968), Phys. Rev. Lett.(21-21):1504.

[203] H. Alvensleben et al. (1971), Phys. Rev. Lett.(27-13):888.

[204] R. Battiston (1995), Nucl. Phys. Proc. Suppl.(44):274.

[205] J. Alcaraz et al. (1999), Nuovo Cim.(112A):1325.

[206] M. Acciarri et al. (1994), Nucl. Instr. and Meth.A(351):300-312.

[207] G. F. Dalla Betta et al. (1999), Nucl. Instr. and Meth.A(431):83.

[208] Massachusetts Institute of Technology, M , Cambridge, MA02 , USA.

[209] Chungshan Institute of Science and Technology, Haidian District,Beijing 100080 - P.R.China.

[210] M. Cristinziani (2002), *Search for Heavy Antimatter and Energetic Photons in Cosmic Rays with the AMS-01 Detector in Space*, Ph.D. thesis, University of Geneva, Switzerland.

[211] G. Batignani et al. (1989), Nucl. Instr. and Meth.A(277):147.

[212] J.B.A. England et al. (1981), Nucl. Instr. and Meth.A(185):43.

[213] G & A Engineering, Localita' Miole I-67063 Oricola.

[214] J. B. Birk (1951), Proc. Phys. Soc.A(64):874.

[215] Colibrys SA, Maladière 83 CH-2007, Neuchâtel.

[216] ITC-irst, Via Sommarive 18 I-38050 Povo.

[217] Selmic Oy, Lumikontie 1 - 94000 Kemi, Finland.

[218] Airex R82, Alcan Airex AG Specialty Foam - CH 5643 Sins.

[219] M. Pauluzzi (2001), Nucl. Instr. and Meth.A(473):67.

[220] P. Azzarello (2004), *Tests And Production Of The AMS-02 Silicon Tracker Detectors*, PhD Thesis - Université de Genève.

[221] O. Toker et al. (1994), Nucl. Instr. and Meth.A(340):575-579.

[222] B. Alpat et al. (2000), Nucl. Instr. and Meth.A(446):552.

[223] G. Ambrosi (1999), Nucl. Instr. and Meth.A(435):215-223.

[224] IDE AS, Veritasveien 9 - N 1323 Hovik.

[225] G. Batignani et al. (1991), Nucl. Instr. and Meth.A(310):160164.

[226] E. Nygärd et al. (1991), Nucl. Instr. and Meth.A(301):506516.

[227] E. Beuville et al. (1990), Nucl. Instr. and Meth.A(288):157-167.

[228] R. Ansari (1990), Nucl. Instr. and Meth.A(288):240-244.

[229] IDEas, http://www.ideas.no. VAhdr9 V0.9 datasheet.

[230] M. Ionica (2003), Nucl. Instr. Meth. Phys. Research A(513):222-225.

[231] P. Holl et al. (1989), IEEE Trans. Nucl. Sci.(36):251.

[232] http://ps-div.web.cern.ch/ps-div/Welcome.html

[233] D. J. Simon and L. Durieu, PS/PA Note 93-21.

[234] http://ams.cern.ch/AMS/Tracker/tbeam04/beam/features/index.html.

[235] http://ab-dep-op-sps.web.cern.ch/ab-dep-op-sps/.

[236] http://ams.cern.ch/AMS/Tracker/tbeam04/magnet/features/features.html.

[237] http://ams.cern.ch/AMS/Tracker/tbeam04/cherenkov/cherenkov.html.

[238] R.Brun et al. GEANT3. CERN DD/EE/84-1 revised 87.

[239] R. Brun and F. Rademakers. (1997), Nucl. Instrum. Meth.A(389):8186.. See also http://root.cern.ch/.

[240] D. Caraffini (2004), *Anti-proton Flux Detection and Indirect Search for Dark Matter with the AMS-02 Experiment*. PhD Thesis - Universita' di Perugia.

[241] E. Choumilov (2001), *Mc simulation of AMS02 level-1 trigger*. AMS02 internal report.

[242] V. Choutko (2002), *AMS02 Charged Particles LVL1 Trigger Simulation*. Presentation at AMS TIM. Available at:
`http://ams.cern.ch/AMS/Analysis/hpl3itp1/ams02_lvl1.ps`.

[243] V. Choutko (2003), *Selected AMS Reconstruction Software Issues*. Presentation at AMS TIM. Available at:
`http://ams.cern.ch/AMS/Analysis/hpl3itp1/ams_rec_sel.ps`.

[244] V. Innocente, M. Maire, and E. Nagy, *Geane: Average tracking and error propagation package*. Proceedings, MC91: *Detector and event simulation in high energy physics* 58-78. (see HIGH ENERGY PHYSICS INDEX 30 (1992) No. 3237).

[245] J. Alcaraz et al. (2003), *The alternative track fitting method for AMS*. AMS02 internal note. Available at:
`http://ams.cern.ch/AMS/Analysis/hpl3itp1/ams_rec_sel.ps`.

[246] C. Zurbach (2004), *AMS-02 Tracker calibration with flags calculation*. AMS02 Tracker Group internal presentation.

[247] C. Zurbach (2005), *AMS-02 Tracker Data reduction*. AMS02 Tracker Group internal report.

[248] I. Sevilla Noarbe (2006), *El experimento AMS-02 como observatorio de rayos gamma desde la Estación Espacial internacional*, PhD Thesis - Universidad Complutense de Madrid.

[249] R. M. Green (1985), Spherical Astronomy, Cambridge.

[250] W. M. Smart(1977), *Textbook on Spherical Astronomy*, Cambridge.

[251] A. H. Murad, K. D. Jang, G. Atallah, R. Karne and J. Baras (1995), *A Summary of Satellite Orbit Related Calculations*, Tech. Research Report - CSHCN T.R. 95-12 (ISR T.R. 95-107).

[252] A. E. Roy (1998), *Orbital Motion*, Adam Hilger.

[253] `http://spaceflight.nasa.gov/realdata/elements/`.

[254] `http://groundstation.sourceforge.net/gpredict/index.php`.

[255] R. Harold, P. Nemeth and T. Mehta (2001), *AMS-02 Payload Integration Hardware Interfaces*, NASA Flight Project Division draft.

[256] J. Bolmont (2005), *Détection des gamma dans l'expérience AMS et analyse temporelle des sursauts gamma par la mission HETE-2*. PhD Thesis, Université de Montpellier II.

[257] L. Girard (2004), *Détection de rayons γ cosmiques et potentiel de découvertes avec le spectromètre AMS-02*. PhD Thesis, Université de Savoie.

[258] G. Kanbach et al. (1994), Astron. Astrophys.(289):855.

[259] B.W. Caroll and D.A. Ostlie (1996), *An Introduction to Modern Astrophysics*, Addison-Wesley Publishing Comp.

[260] J. Bolmont et al. (2004), *AMS-02 Fast Simulator*. AMS02 internal note.

[261] V. Choutko, G. Lamanna et A. Malinin (2001), *Cosmic photon and positron spectra measure- ments modelling with the AMS-02 detector at ISS*. In Matter, Anti Matter and Dark Matter, Trento - Italy).

[262] S. Sajjad (2002), *Étude de l'extraction d'un signal gamma pour la détection de sursauts gamma dans l'expérience AMS-02*. Rapport de stage de DEA, available in `http://www.lpta.in2p3.fr/ams/`.

[263] L. Kuiper et al. (2000), astro-ph/0005338.